Measurement of ν_μ Disappearance in the K2K Experiment With An Expanded Fiducial Volume at Super-Kamiokande

A Dissertation Presented

by

Ryan Vincent Terri

to

The Graduate School

in Partial Fulfillment of the

Requirements

for the Degree of

Doctor of Philosophy

in

Physics

Stony Brook University

December 2007

Stony Brook University

The Graduate School

Ryan Vincent Terri

We, the dissertation committee for the above candidate for the Doctor of Philosophy degree, hereby recommend acceptance of the dissertation.

Dr. Chang Kee Jung
Advisor
Professor of Physics, Department of Physics and Astronomy

Dr. George Sterman
Defense Committee Chairperson
Distinguished Professor of Physics, Department of Physics and Astronomy

Dr. Axel Drees
Professor of Physics, Department of Physics and Astronomy

Dr. Brett Viren
Advanced Technology Architect
Department of Physics, Brookhaven National Laboratory

This dissertation is accepted by the Graduate School.

Lawrence Martin
Dean of the Graduate School

Abstract of the Dissertation

Measurement of ν_μ Disappearance in the K2K Experiment With An Expanded Fiducial Volume at Super-Kamiokande

by

Ryan Vincent Terri

Doctor of Philosophy

in

Physics

Stony Brook University

2007

Measurements of two flavor ν_μ disappearance were made using K2K, the KEK to Kamioka long baseline neutrino oscillation experiment, data for three fiducial volume definitions at the far detector, Super-Kamiokande. A study was conducted on expanding the fiducial volume at Super-Kamiokande to show it is possible to expand it both symmetrically and shifted in the incoming neutrino beam direction. For the fiducial volume definitions, 112, 143, and 140 events are observed with an expectation of $158.1^{+9.2}_{-8.6}$, $183.3^{+10.7}_{-10.0}$, and $170.9^{+9.5}_{-9.0}$ events, respectively. A distortion is also seen in the reconstructed energy spectrum for single ring muon-like events for each fiducial volume. The probability that the observations are explained by no neutrino oscillations are 0.0021% (4.3σ), 0.018% (3.7σ), and 0.042% (3.5σ). The best fit values are $\sin^2 2\theta$=1.0 for all definitions and Δm^2=0.0027 eV^2, 0.0025 eV^2, and 0.0024 eV^2, respectively. All results are consistent with other disappearance measurements.

To my family

Contents

List of Figures

List of Tables

Acknowledgements

I thank the NN Group for allowing me to do this work. In particular, I would like to thank my advisor, Chang Kee Jung. Though insanely busy over these last five years, he has offered enough guidance to make my way through this process much easier than it could have been, especially with the amount of time we spent on different continents. I'd like to thank Clark McGrew and Chiaki Yanagisawa for their insights and, our former postdocs, Antony Sarrat and Kazuyoshi Kobayashi. I'd also like to thank my comrades Fumi Kato, Lisa Whitehead, Glenn Lopez, Dima Beznosko, and Trung Le.

This thesis doesn't exist without the K2K and Super-Kamiokande Collaborations. I would like to thank the 1KT group including Masato Shiozawa and Yoshitaka Itow, Makoto Miura, Asia Zalipska, Michael Smy, Jeremy Argyriades, Jun Kameda, and Shunichi Mine. I would also like to thank Tsuyoshi Nakaya, Gabriel Jover, Ana Rodriguez, Taku Ishida, Rik Gran, and Michel Sorel. Special thanks goes to Masaya Hasegawa. I would like to thank Kenji Kaneyuki as well as Yoshihisa Obayashi and Takeshi Nakadaira. Also, Yoshinari Hayato, Ko Abe, Yuskue Koshio, Yumiko Takenaga, Moto Ikeda, Jeff Wilkes, Parker Cravens, Aaron Herfurth, Wei Wang, Roger Wendell, Mike Litos, and Chris Regis. Lastly, I'd like to thank Yoichiro Suzuki and Koichiro Nishikawa as spokesmen of SK and K2K, respectively.

I'd like to thank the administrative staffs including Pat Peileker, Diane Siegal, Joan Napolitano, and Alice Dugan in the Department of Phyics and Astronomy and Eri Okada and Yukari Maeda in Super-Kamiokande.

I would never have gotten through my time in grad school without the help and humor of my friends in Tulare, Oxy, and Stony Brook.

I'd like to thank Ilektra Christidi for her love and support over the last year. I'm not even going to try to express what this meant to me since all attempts will fail miserably.

Lastly, I must thank my entire family for their years of love, support, and wondering what I've been up to without understanding it, especially my parents, Joe and Jennifer Terri, and my brother, Kevin.

Chapter 1

Introduction

The neutrino is an elusive particle. With over 20 years between its proposed existence and its first detection, this particle has been stubborn to give up its secrets in the face of scientific investigation. In the last decade has it yielded the fact that it has mass and mixes between its different flavors. Though one of the most common particles in the universe, only now are we beginning to understand the neutrino's effect in physics and cosmology, and how it may further yield keys to physics beyond the Standard Model.

1.1   History of the Neutrino

The neutrino was first proposed by Wolfgang Pauli in a letter to colleagues at a conference in December of 1930 [1]. His proposal called for the existence of a third particle that needed to be emitted to explain the observed energy distribution of the electron in β decay. If β decay were a two body process, as initially assumed, a nucleus A would decay to a lighter nucleus B and emit an electron

$$A \rightarrow B + e^- \tag{1.1}$$

with an energy

$$E_e = \frac{m_A^2 - m_B^2 + m_e^2}{2m_A}. \tag{1.2}$$

The observed decay electron energy spectrum tail ended at E_e, but the spectrum peaked at a lower value. Pauli said that the particle had to be chargeless, to conserve charge, have a very small, if not zero, mass, and have a very small cross section. This particle would eventually be named "neutrino," which is Italian for "little neutral one," by Enrico Fermi in 1934 in his successful theory of β-decay [2].

The first type of neutrino detected was the anti-electron neutrino by Reines and Cowan detected from inverse β-decay, $\overline{\nu}_e + p \rightarrow e^+ + n$, at the Savannah River Plant in 1956 [3, 4]. Their detector contained $CdCl_2$ dissolved in water surrounded by a liquid scintillator. The signal they were searching for was coincident gamma rays from pair annihilation and a delayed gamma from neutron capture of the inverse β-decay procoess.

The muon neutrino was discovered by Leon Lederman, Melvin Schwartz, and Jack Steinberger in 1962 [5] by the interaction

$$\nu_\mu + N \rightarrow \mu^- + X \tag{1.3}$$

from a neutrino beam at the Alternating Gradient Synchrotron (AGS) at Brookhaven National Laboratory.

With the discovery of the τ lepton in 1979 [6], the corresponding neutrino, ν_τ, was postulated to also exist. The tau neutrino was directly observed in 2000 by the DONUT experiment at Fermi National Accelerator Laboratory (FNAL) [7].

Neutrinos were also detected from sources in outer-space. R. Davis and his collaborators first detected neutrinos from the sun in 1968 from the Homestake mine [8]. The neutrinos from supernova SN1987a were detected by the Kamiokande [9, 10] and Irvine-Michigan-Brookhaven (IMB) [11, 12] experiments in 1987.

1.2 Neutrino Physics

1.2.1 Neutrinos in the Standard Model

In the Standard Model of particle physics (SM), there exists two classes of particles: fermions and bosons. Bosons are the force mediators for the three forces incorporated into the SM: the electromagnetic, weak nuclear, and strong nuclear forces. Fermions are grouped into two categories of particles, leptons (which include neutrinos), and quarks, each in three generations or flavors. Each particle in the SM also has an antiparticle. A summary of the particles in the SM is given in Table 1.1. The neutrinos come in three flavors: ν_e, ν_μ, and ν_τ, corresponding to their charged lepton, the electron (e), muon (μ), and tau (τ), respectively. The number of light neutrinos measured by the LEP experiment is three [13].

Because the neutrino is chargeless and colorless, it only interacts via the weak force. The two types of weak interactions that can occur with a neutrino are charged current (CC) interactions, involving a W boson exchange, and
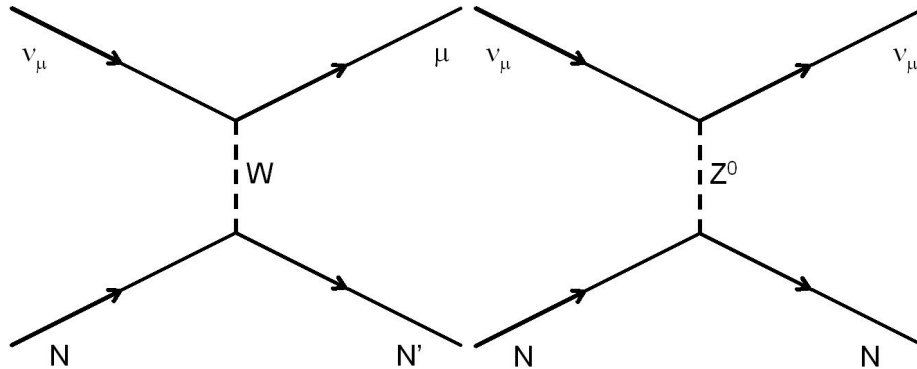
Figure 1.1: Left: CC interaction of a muon neutrino with a nucleon N. Right: NC interaction of a muon neutrino with a nucleon N.

Table 1.1: Summary of the Standard Model particles. Both fermions and gauge bosons are shown.

Particles	Flavor			Charge
Quarks	u	c	t	$+\frac{2}{3}$
	d	s	b	$-\frac{1}{3}$
Leptons	ν_e	ν_μ	ν_τ	0
	e	μ	τ	-1

Force	Electromagnetic	Weak	Strong
Mediator	γ	$W^\pm, Z^0$	g

neutral current (NC) interactions, which have a Z^0 exchange. A cartoon of a CC and a NC interaction can be seen in Figure 1.1.

The neutrinos in the SM are assumed to be massless particles. Direct measurements have placed limits on the mass of each flavor of neutrino, with $m_{\nu_e} < 2.2$ eV [13], $m_{\nu_\mu} < 0.17$ MeV [13], and $m_{\nu_\tau} < 15.5$ MeV [13]. The cosmological constraint, $\sum m_\nu < 0.42$ eV [13], is the most stringent, though. The massless assumption implies that the neutrinos are of left-handed helicity and anti-neutrinos are of right-handed helicity. This was measured by M. Goldhaber $et.$ al [14] in 1958.

1.2.2 Neutrino Oscillations

Neutrino oscillations are a quantum mechanical phenomenon. Oscillations can occur between two or more states if the states have different masses and those states are not eigenstates of some force. Generally speaking, the neutrinos created in weak interactions are not in mass eigenstates, but flavor eigenstates, represented as $|\nu_e\rangle$, $|\nu_\mu\rangle$, and $|\nu_\tau\rangle$, where the flavor eigenstates do not necessarily correspond to the mass eigenstates, $|\nu_1\rangle$, $|\nu_2\rangle$, and $|\nu_3\rangle$.

The flavor and mass eigenstates each form a complete basis to describe the set of neutrinos. Each basis can also be rewritten in terms of a linear combination of the other basis, such as:

$$|\nu_\alpha\rangle = \sum_i U_{\alpha i}^* |\nu_i\rangle \tag{1.4}$$

where $U_{\alpha i}^*$ relates the mixing between the two bases, $|\nu_\alpha\rangle$ is a flavor eigenstate and $|\nu_i\rangle$ is a mass eigenstate. If the off-diagonal coefficients describing the rotation amongst the two bases are not 0, then the states mix.

This mixing matrix between the generations was first proposed in 1962 by Z. Maki, M. Nakagawa, and S. Sakata [15], though the first proposal of neutrino mixing between neutrinos and anti-neutrinos was in 1957 by B. Pontecorvo [16]. The mixing matrix, known as the MNS (or PMNS) matrix, for three flavors is defined as:

$$U = \begin{pmatrix} U_{e1} & U_{e2} & U_{e3} \\ U_{\mu 1} & U_{\mu 2} & U_{\mu 3} \\ U_{\tau 1} & U_{\tau 2} & U_{\tau 3} \end{pmatrix}. \tag{1.5}$$

The mixing matrix can be decomposed to three matrices each involving two state mixing:

$$U = \begin{pmatrix} 1 & 0 & 0 \\ 0 & c_{23} & s_{23} \\ 0 & -s_{23} & c_{23} \end{pmatrix} \begin{pmatrix} c_{13} & 0 & s_{13}e^{-i\delta} \\ 0 & 1 & 0 \\ -s_{13}e^{i\delta} & 0 & c_{13} \end{pmatrix} \begin{pmatrix} c_{12} & s_{12} & 0 \\ -s_{12} & c_{12} & 0 \\ 0 & 0 & 1 \end{pmatrix} \tag{1.6}$$

where $c_{ij}\,(s_{ij}) = \cos\theta_{ij}(\sin\theta_{ij})$ and δ is the CP violating phase. The first matrix, starting on the left, relates to $\nu_\mu \to \nu_\tau$ mixing, the second matrix to $\nu_e \to \nu_\tau$ mixing, and the third matrix to $\nu_e \to \nu_\mu$ mixing. This form assumes the neutrinos are Dirac particles. In the case of Majorana neutrinos, an extra matrix with two Majorana phases, α_1 and α_2, is added.

The initial flavor state from Equation 1.4, created at time $t_0 = 0s$, has the time evolution operator applied to the mass eigenstates. Assuming the Hamiltonian is time-independent,

$$U(t; t_0) = \exp\left(\frac{-iEt}{\hbar}\right) = e^{\frac{-iEt}{\hbar}}$$

$$U(t)|\nu_\alpha; t_0\rangle = |\nu_\alpha; t\rangle$$

Equation 1.7 can be rewritten in terms of the mass eigenstates by substituting in Equation 1.4 for $|\nu_\alpha\rangle$. This state becomes:

$$|\nu_\alpha; t\rangle = \sum_i U_{\alpha i}^* e^{-iE_i t} |\nu_i\rangle \tag{1.7}$$

where natural units with $\hbar = c = 1$ are being used.

To find the time dependent probability that a neutrino of flavor α, ν_α, changes to a neutrino with flavor β, ν_β, we initially calculate the amplitude of the flavor state transition $\alpha \rightarrow \beta$ as:

$$A_{\alpha \rightarrow \beta}(t) = \langle \nu_\beta | \nu_\alpha; t\rangle = \sum_i U_{\beta i} e^{-iE_i t} U_{\alpha i}^*. \tag{1.8}$$

The probability is then:

$$P_{\alpha \rightarrow \beta} = |A_{\alpha \rightarrow \beta}|^2 = |\sum_i U_{i\beta} e^{-iE_i t} U_{\alpha i}^*|^2. \tag{1.9}$$

This term expands giving:

$$P_{\alpha \rightarrow \beta} = \sum_i \sum_j U_{i\beta} U_{\beta j}^* U_{\alpha i}^* U_{j\alpha} e^{-i(E_i - E_j)t} \tag{1.10}$$

as a general form for neutrino oscillations.

In this thesis, mixing between only two states (ν_μ, ν_τ) is assumed, and is thus defined as a simple two state rotation matrix:

$$U = \begin{pmatrix} \cos\theta & \sin\theta \\ -\sin\theta & \cos\theta \end{pmatrix} \tag{1.11}$$

The neutrino mixing probability in the two flavor mixing case is:

$$P_{\alpha \rightarrow \beta} = \sin^2(2\theta) \sin^2\left(\frac{1}{2}(E_1 - E_2)t\right) \tag{1.12}$$

Since it can be assumed $E_i \gg m_i$, we can use the ultra-relativistic approximation:

$$E_i = p + \frac{m_i^2}{2p} = E + \frac{m_i^2}{2E}$$

to substitute for E_i. Also using the fact that $L = t$, and taking into account all $\hbar$'s and c's, the probability in the case of a two flavor oscillation is:

$$P_{\alpha \rightarrow \beta} = \sin^2(2\theta) \sin^2\left(1.27\frac{\Delta m^2 L}{E}\right) \tag{1.13}$$

where L is the distance traveled by the neutrino in km, E is the energy of the neutrino in GeV, $\Delta m^2 = m_i^2 - m_j^2$ is in units of eV^2, and 1.27 is from the $\hbar$'s and c's being substituted in and converted for the units of km, GeV, and eV^2.

1.3 Atmospheric Neutrinos

1.3.1 The Atmospheric Neutrino Problem

Atmospheric neutrinos are created from cascading decays involving interactions of cosmic rays with the Earth's atmosphere. Cosmic rays, mostly protons and helium nuclei, interact with the atmosphere creating hadronic showers consisting mostly of pions [17]. The pions decay into muons and muon neutrinos; the muons subsequently decay into an electron, electron anti-neutrino, and muon neutrino:

$$\pi^+ \rightarrow \mu^+ + \nu_\mu; \ \mu^+ \rightarrow e^+ + \nu_e + \overline{\nu}_\mu \tag{1.14}$$

$$\pi^- \rightarrow \mu^- + \overline{\nu}_\mu; \ \mu^- \rightarrow e^- + \overline{\nu}_e + \nu_\mu \tag{1.15}$$

The neutrino flavor ratio is expressed as

$$N_\mu/N_e = \left(\nu_\mu + \overline{\nu}_\mu\right) / \left(\nu_e + \overline{\nu}_e\right) \tag{1.16}$$

and is expected to be close to 2. A more precise determination of N_μ/N_e can be calculated taking into account kaon production and the energies of both kaons and pions produced from the atmospheric hadronic interactions.

The first atmospheric neutrino detectors to measure the flavor ratio, which were water Cherenkov detectors, were the IMB [18, 19] and Kamiokande [20, 21] experiments. Though both were proton decay experiments, atmospheric neutrinos were considered the primary background source to be studied. When studying the flavor ratio from Equation 1.16, they measured a value different from 2. In practice, a double ratio R between the number of data (N_{data}) and the number expected (N_{MC}),

$$R \equiv \left(N_\mu/N_e\right)_{data} / \left(N_\mu/N_e\right)_{MC}, \tag{1.17}$$

was calculated in order to cancel detector systematic uncertainties and atmospheric flux uncertainties. In the absence of any new physics, R should equal 1. IMB and Kamiokande both measured values less than 1 for R, as seen in Table 1.2. This deficit in R became known as the "atmospheric neutrino problem." Later experiments using iron calorimeters, NUSEX [22] and Fréjus [23], reported no deviation from unity, but had a smaller data sample. Soudan 2 [24, 25], which was also an iron calorimeter, but with a larger event sample, measured a smaller value of R. Super-Kamiokande (SK), the successor to Kamiokande, also measured the flavor ratio to be smaller than 1.

Table 1.2: Flavor ratio summary from water Cherenkov and iron calorimeter experiments. S (M) is the Sub-GeV (Multi-GeV) data sample used in the flavor ratio analysis.

Experiment	Method	Exposure (kt $*$ yr)	Flavor Ratio (R)
IMB	Water Cherenkov	7.7	$0.54 \pm 0.05 \pm 0.012$ (S)
		2.1	$1.41^{+0.41}_{-0.30} \pm 0.3$ (M)
Kamiokande	Water Cherenkov	7.7	$0.60^{+0.06}_{-0.05} \pm 0.05$ (S)
		8.2	$0.57^{+0.08}_{-0.07} \pm 0.07$ (M)
NUSEX	Iron Calorimeter	0.74	$0.96^{+0.32}_{-0.28}$
Fréjus	Iron Calorimeter	1.56	$1.00 \pm 0.15 \pm 0.08$
Soudan 2	Iron Calorimeter	5.1	$0.68 \pm 0.11 \pm 0.06$
Super-Kamiokande	Water Cherenkov	92	$0.658 \pm 0.016 \pm 0.05$ (S)
		92	$0.702^{+0.032}_{-0.030} \pm 0.101$ (M)

1.3.2 Previous Atmospheric Neutrino Oscillation Results

Super-Kamiokande's measurement of the flavor ratio in Table 1.2 was also checked as a function of zenith angle. Neutrinos created in the atmosphere can travel anywhere from 15 km to 13,000 km to a detector near the Earth's surface. This is closely related to the zenith angle, θ, of the events, where the cosine is normally taken. If $\cos\theta=-1$, it considered to be going in the upward-direction, which is through the Earth; if $\cos\theta=0$, it is coming from the horizontal direction and part of the Earth's crust; if $\cos\theta=1$, it is a downward-going, where the neutrino is only going through the Earth's atmosphere. Super-Kamiokande noticed that there was a zenith angle dependence for a deficit for muon neutrinos and no deficit for electron neutrinos. This signal was the first compelling evidence for neutrino oscillations and resulted in the first measurement of the atmospheric neutrino oscillation parameters [26]. Since this publication, Super-Kamiokande has published a zenith angle [27] and L/E analysis [28], with the results summarized in Table 1.3.

Table 1.3: Current best fit results of atmospheric neutrino oscillation parameters from Super-Kamiokande from Refs. [27] and [28], K2K [35], and MINOS [29]. All results are in the physical region.

Analysis	$\sin^2 2\theta$	Δm^2 (eV^2)	Δm^2 (eV^2) (90% C.L.)
SK Zenith Angle	1.00	2.1×10^{-3}	$1.5 \times 10^{-3} < \Delta m^2 < 3.4 \times 10^{-3}$
SK L/E	1.00	2.4×10^{-3}	$1.9 \times 10^{-3} < \Delta m^2 < 3.0 \times 10^{-3}$
K2K	1.00	2.8×10^{-3}	$1.9 \times 10^{-3} < \Delta m^2 < 3.5 \times 10^{-3}$
MINOS	1.00	2.7×10^{-3}	$2.3 \times 10^{-3} < \Delta m^2 < 3.4 \times 10^{-3}$
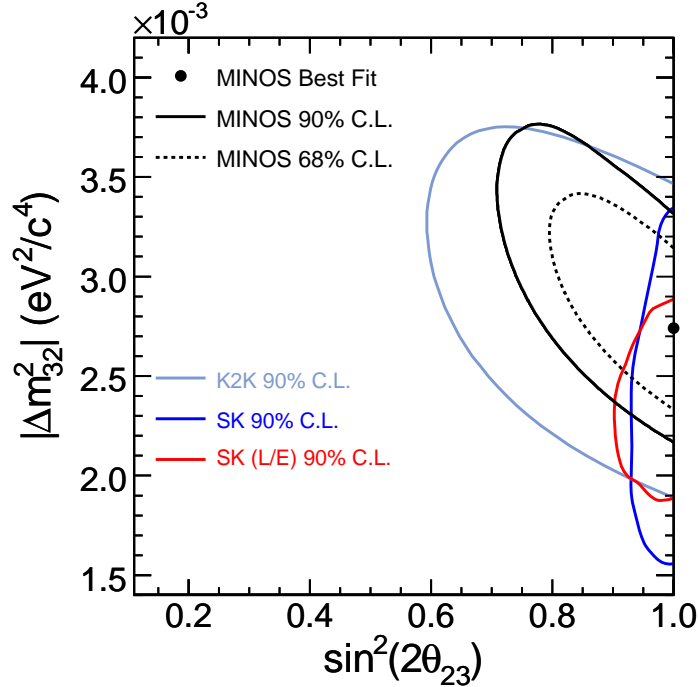
Figure 1.2: Allowed regions for the SK zenith angle analysis [27] and L/E analysis [28], K2K [35], and MINOS [29].
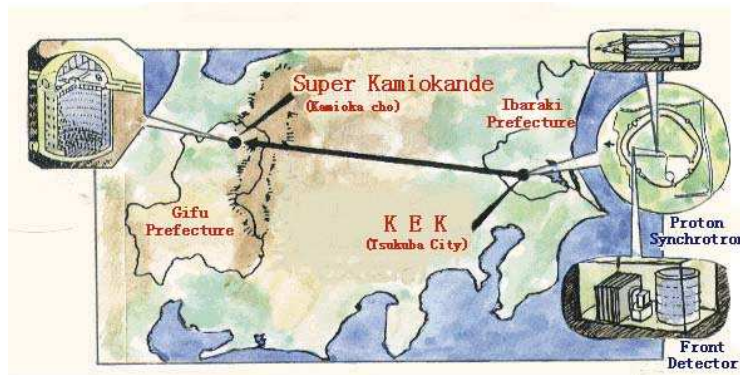
Figure 1.3: Location of the K2K experiment.

1.4 The K2K Experiment

The KEK to Kamioka (K2K) Long Baseline Neutrino Experiment was proposed to confirm the atmospheric neutrino oscillation results by Super-Kamiokande with an accelerator-based neutrino beam. Data taking began in June 1999 and ended in November 2004. Over 200 collaborators from 27 institutions in Japan, the U.S. including Stony Brook, Canada, Korea, and Europe participated in the experiment. This is the first neutrino oscillation experiment to use an accelerator-based neutrino source over a long baseline and was successful in making a measurement. This type of experiment is already ushering in an age of precision measurements of atmospheric neutrino oscillation parameters with the MINOS [29], OPERA [32], and, starting in 2009, the T2K [30] experiments.

At KEK in Tsukuba, Japan, a proton beam collides with an aluminum target producing charged particles. Most of the charged particles produced are pions. Positively charged pions are focused by two horns into a decay pipe, where they undergo a two body decay. The products of this decay are a positively charged muon and a muon neutrino. At the end of the decay pipe, 200 m downstream, is a beam dump which absorbs the muons and remaining pions and protons.

At this point, the muon neutrinos that have been produced have not yet oscillated. Three hundred meters from the pion production point, there is a suite of detectors that measure the flux, energy spectrum, and total number of interactions of the unoscillated muon neutrino beam. These measurements are used to calculate the expected number of neutrino beam events and the energy spectrum shape of those events at the far detector.
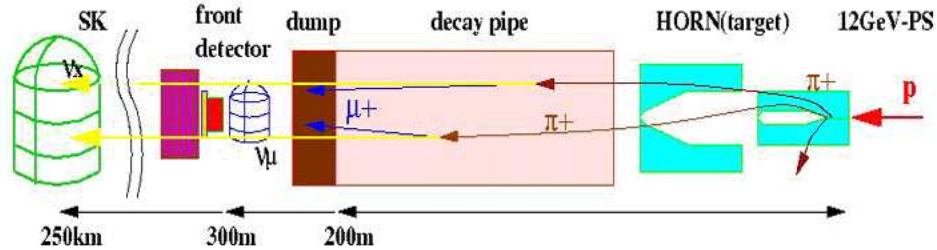
Figure 1.4: K2K detection principle (from right to left) from the proton beam colliding with the aluminum target, to the creation of the neutrino beam, to detection at the near and far detectors.

The muon neutrino beam then travels 250 km through Japan to Super-Kamiokande, the far detector. At SK, the total number of events produced from a muon neutrino is counted and the energy spectrum shape is measured. A cartoon from the pion production point to Super-Kamiokande is shown in Figure 1.4.

K2K's analysis is called a disappearance analysis since the observed events are from the same flavor of neutrino that were initially produced. The expected signal in K2K is a deficit of the total number of observed events from muon neutrino interactions compared to the number expected if there are no neutrino oscillations and a distortion of the reconstructed neutrino energy spectrum as compared to no neutrino oscillations. Figure 1.5 shows the K2K reconstructed neutrino energy with MC expectation in the case of no oscillations and the best fit oscillation parameters given in Table 1.3.

1.5 Current Atmospheric Neutrino Oscillation Experiments

The MINOS experiment [29] is a long baseline experiment with a baseline of 735 km from the target located at Fermilab to the far detector located in the Soudan iron mine in northern Minnesota. The neutrino beam is created from 120 GeV protons from the Main Injector hitting a target, producing mainly pions, which are focused into a 675 m long, 2 m diameter, decay pipe. For most of the data taken, the neutrino energy production was maximized to be in the 1-3 GeV range. The MINOS near detector (ND) and far detector (FD) are both steel-scintillator tracking calorimeters in a toroidal magnetic field.
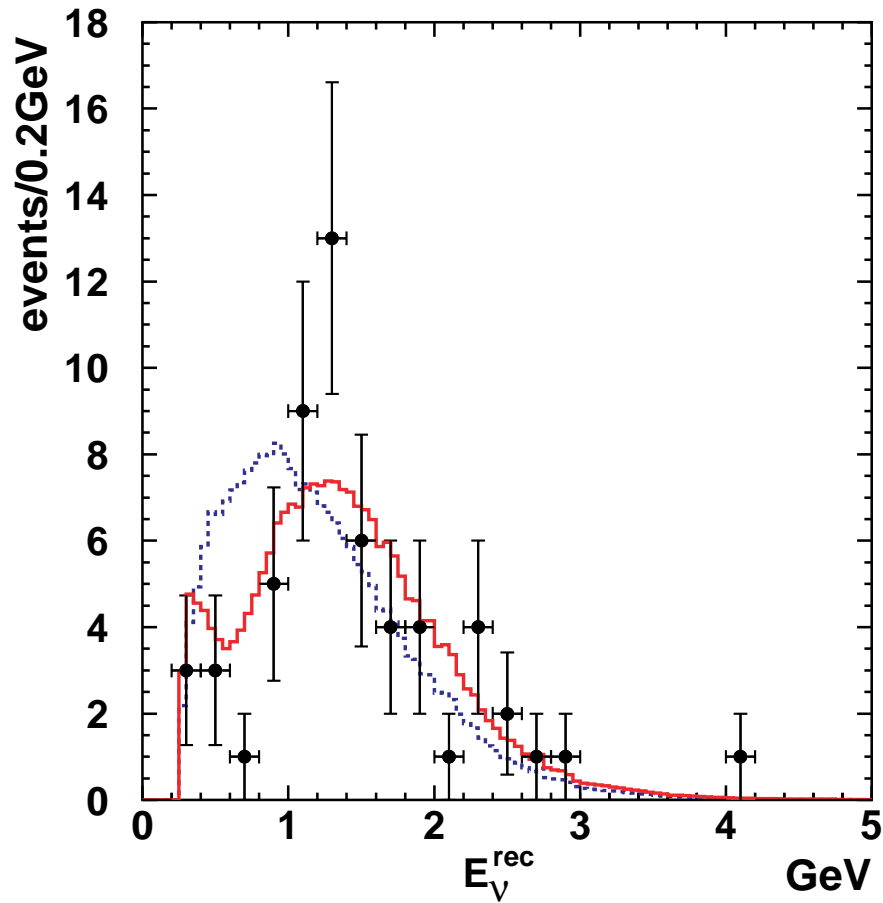
Figure 1.5: Reconstructed neutrino energy for the K2K single ring muon-like event sample. The blue histogram is the expected spectrum in the case of no neutrino oscillations. The red histogram is the oscillated spectrum with Δm^2=0.0028eV^2 and $\sin^2 2\theta$=1.0. The MC is normalized to the number of data events observed (58).

The ND has a fiducial mass of 0.98 ktons and the FD has a fiducial mass of 5.4 ktons.

MINOS, like K2K, is a ν_μ disappearance experiment. For MINOS's initial analysis, 336.0±14.4 unoscillated events below 30 GeV were expected with 215 observed. MINOS's best values for $\sin^2 2\theta$ and Δm^2 were 1.00 and 0.00274 eV^2, respectively. These results are in Table 1.3. The 90% C.L. region for MINOS, K2K, and the two SK analyses are shown in Figure 1.2. More recently [31], these best fit values were updated to 1.00 and 0.00238 eV^2 from an increase in statistics roughly twice their original data set and improvements in event reconstruction, event selection, and shower modelling.

The CERN Neutrinos to Gran Sasso (CNGS) experiment is another long baseline experiment searching for ν_τ appearance from a ν_μ beam with a 730 km baseline. The far detector for CNGS is the OPERA [32, 33] detector using target trackers with a lead target and photographic emulsion plates to identify τ decays from ν_τ interactions and a spectrometer to identify muons along with their charge and momentum. A first run was tested in August 2006, successfully collecting data statistically consistent with the integrated beam intensity [34]. Data taking started again in October 2007 with plans for a full physics run in 2008.

1.6 Motivation

The motivation for this thesis is to make a measurement of the atmospheric oscillation parameters $\sin^2(2\theta)$ and Δm^2 with an increased K2K data set at the far detector as compared to the published K2K analysis [35]. Because of the small sample size, an increase in statistics at the K2K far detector may increase the significance of the oscillation parameter measurement, with the resulting significance of one expansion is shown in Figure 1.6, and improve the event quality of the K2K oscillation analysis. The method for increasing the data sample may also be helpful for future neutrino oscillation and proton decay experiments using water Cherenkov detectors.

Chapter 2 will discuss the experimental setup, Chapters 3-6 will discuss measurements and experimental techniques necessary for the oscillation parameter measurement, as well as how to increase the number of events observed, and Chapter 7 will discuss the oscillation analysis and the results of the analysis. Finally, Chapter 8 will summarize the results and discuss future experiments.
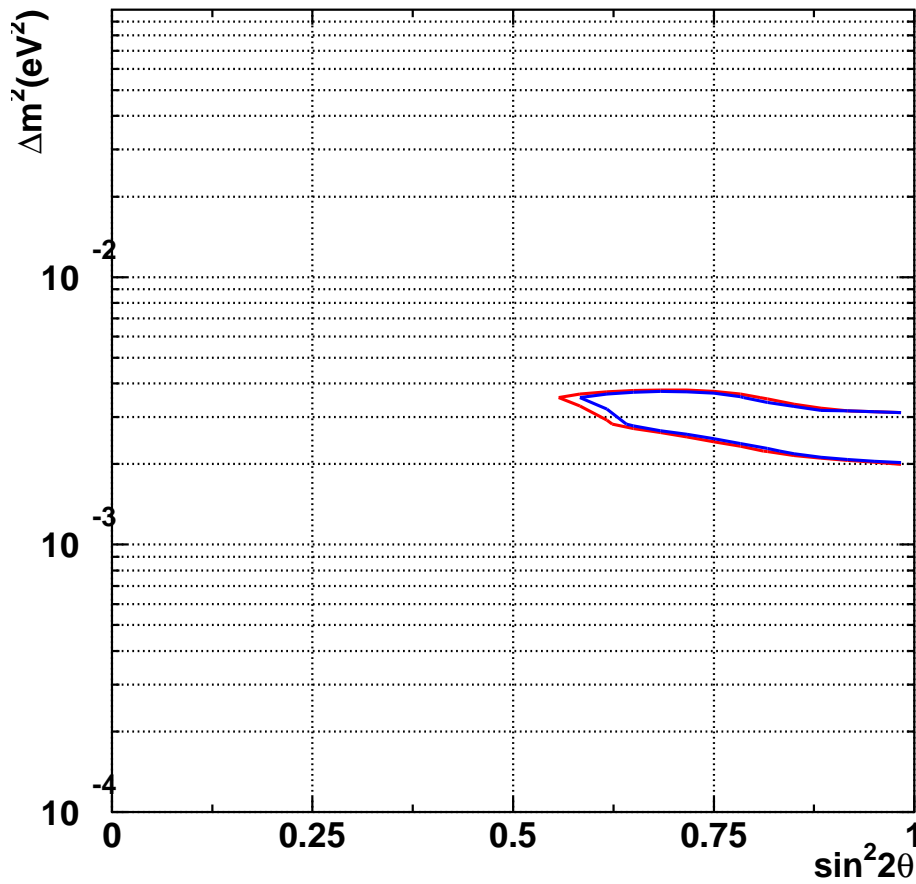
Figure 1.6: Sensitivity plot of effect of an increase in statisitics at the K2K far detector. The red(blue) line is the 90% C.L. for the normal(expanded) event selection with best fit at $\sin^2 2\theta$=1.0 and Δm^2=0.0025eV^2 with 1×10^{20} protons hitting the target.

Chapter 2

The K2K Long Baseline Experiment

2.1 The Beamline and Beam Monitors

2.1.1 Proton Beam

Protons are accelerated in the KEK proton synchrotron (KEK-PS) to an energy of 12 GeV and extracted into the neutrino beam line. The protons are extracted in a a single turn every 2.2 s where each extraction, or "spill," lasts 1.1 μs. Each spill has 9 bunches with 125 ns between each bunch. The beam is bent $90°$ toward the direction of Super-Kamiokande (SK) and $1°$ downward with respect to the horizontal. A diagram of the KEK-PS and beam line is in Figure 2.1.

The proton beam intensity is monitored by 13 current transformers (CTs) along the beamline to measure the beam transportation efficiency. The overall efficiency of the beamline is about 85%. One of the CTs is placed just before the target and is used to estimate the total number of protons delivered to the target. Typically, the beam intensity is roughly 5×10^{12} protons per spill. In total, 104.90×10^{18} protons were delivered by the KEK-PS for the duration of the K2K experiment. This, along with the average number of protons delivered per spill per day, is shown in Figure 2.2.

To measure the beam profile and position, 28 segmented plate ionization chambers are also installed along the beamline. Each chamber consists of three 28 μm thick copper sheets. The gaps between each sheet are 1 cm and are filled with helium gas. The central sheet acts as the anode and is supplied with roughly -1000 V while the two outer sheets have vertical or horizontal cathode strips. Each segmented plate ionization chamber is used to monitor and steer the beam, with the last two placed just before the target and used to estimate the beam size and divergence. The information from the last two chambers is used in the beam Monte Carlo (MC) simulation.
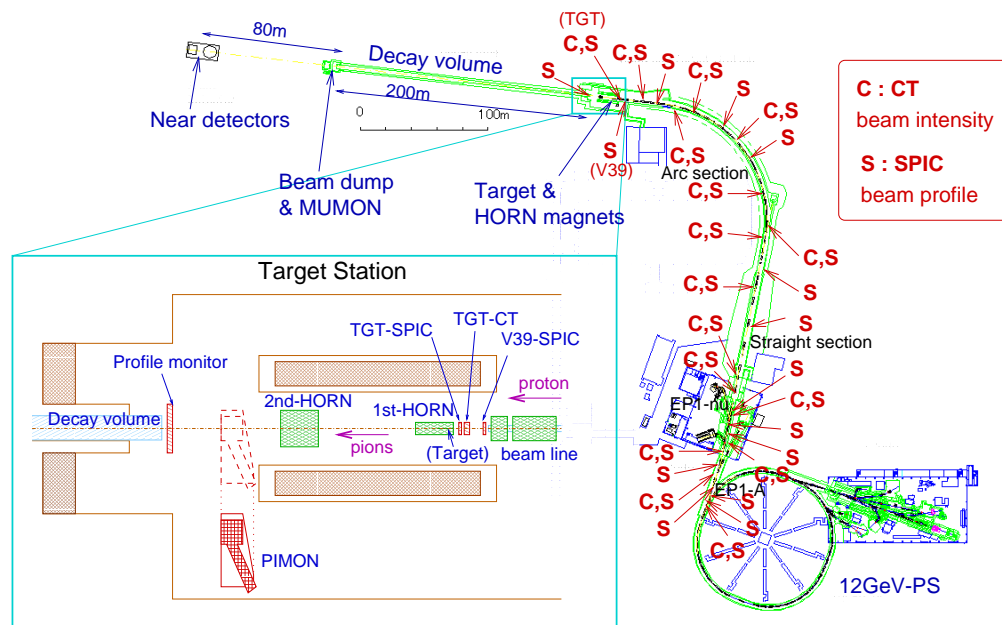
Figure 2.1: Upper right: Schematic of the KEK-PS and beam extraction line. Lower left: Diagram of the target station.
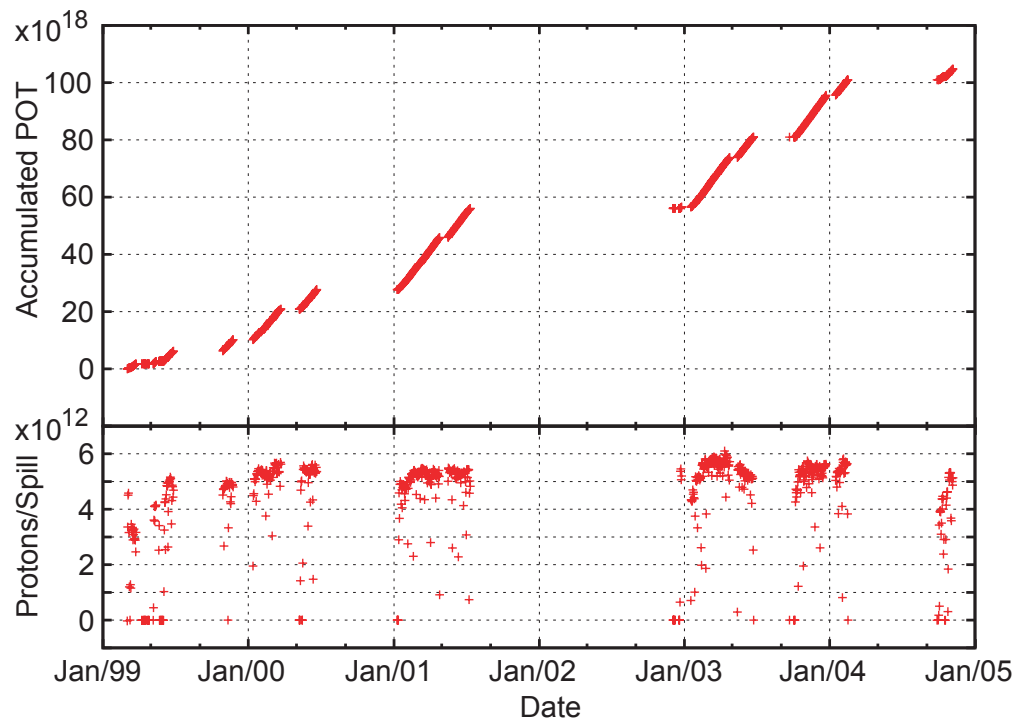
Figure 2.2: Integrated delivered protons on target (POT) (top) and the average protons per spill per day (bottom) during K2K data taking.
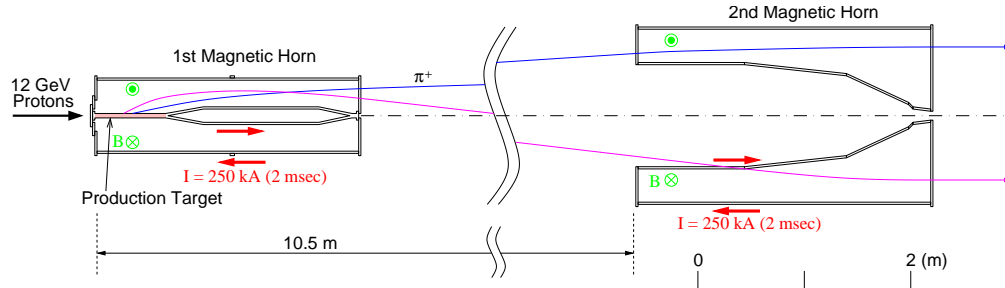
Figure 2.3: Diagram of the K2K target and horn system. The current direction and magnitude are given in the figure, as well as the magnetic field direction.

2.1.2 Target and Horn Monitors

The proton target is an aluminum cylinder 66 cm in length and 3 cm in diameter (2 cm before November 1999). Protons from the beam hit the target producing hadrons, mostly pions. The target is located in the first of two magnetic horns. The purpose of the horns is to select positively charged particles and focus them in the forward direction using a toroidal magnetic field. The current through the horns is pulsed for a duration of 2 ms at an amplitude of 250 kA (200 kA before November 1999) every 2.2 s in time with the beam arrival. The first horn is 0.70 m in diameter with a length of 2.37 m. The second is 1.65 m in diameter, 2.76 m in length, and 10.5m downstream from the the first horn; its purpose is to refocus over-bent low energy pions and further focuses under-bent high energy pions. Both horns are cylindrical. Figure 2.3 shows a diagram of the target and horn system with the current magnitude and direction labeled. For a target of diameter 3 cm and current of 250 kA, the maximum magnetic field on the horn surface at the target is 33 kG.

The transverse momentum focused by the horn magnets is roughly 100 MeV/c per meter. The momenta of the focused pions is 2-3 GeV/c, which makes the daughter neutrino's energy 1.0-1.5 GeV in the forward direction. According to MC simulation, the neutrino flux above 0.5 GeV is 22 times greater with the 250 kA horn current than without.

2.1.3 Decay Pipe and Beam Dump

The focused pions then go into a 200 m long decay pipe, which starts 19 m downstream from the target, where they decay through the process $\pi^+ \rightarrow \mu^+ + \nu_\mu$. The decay pipe is cylindrical and is separated into three sections

with different dimensions. The diameter of each section going downstream are 1.5 m in the first 10 m, 2 m in the next 90 m, and 3 m in the final 100 m. The pipe is filled to pressure of 1 atm of helium gas to reduce pion loss as compared to air in the decay volume.

The beam dump is located at the end of the decay pipe and is designed to stop all particles in the pipe except neutrinos. The dump, starting 200 m downstream of the target, consists of 3.5 m of iron, 2 m of concrete, and 60 m of soil.

2.1.4   Beam Monitors and Beam Direction/Stability

MUMON

Just downstream of the iron and concrete shields of the beam dump, the muon monitor (MUMON) monitors the beam stability and direction of every spill. Muons from pion decay with a momentum greater than 5.5 GeV/c can penetrate the iron and concrete with a flux of roughly 10^4 muons/cm^2/spill. The neutrino beam direction can be inferred by monitoring the muon direction because of the fact the neutrinos and muons are from a two body decay of the parent pion. Thus, the center of the muon profile can be assumed to be the center of the neutrino beam. The beam as designed needed to stay within ± 3 mrad of the direction of SK. During data taking, the beam direction was stable within ± 1 mrad of SK, performing better than the needed ± 3 mrad.

The MUMON consists of two detectors, an ionization chamber (ICH) and an array of silicon pad detectors (SPDs), as can be seen in Figure 2.4. The ICH is a 190 cm (horizontal) $\times$ 175 cm (vertical) segmented plate chamber. The ICH has one anode plane and two cathode planes where one cathode plane has 32 vertical strips and the other has 36 horizontal strips. The spacing between cathode strips is 5 cm, while the gap between each cathode plane and the anode is 1 cm. There are six 60 cm $\times$ 90 cm modules, with three in the horizontal direction and two in the vertical. The space between the modules is 25 cm horizontally and 15 cm vertically, but the corresponding cathode strips are electrically connected on adjacent modules to make the strips roughly 180 cm in length. The gaps between the cathode and anode are filled with Argon gas. The anode has a voltage of -500 V applied.

Figure 2.5 shows the center of the muon profile measured by the ICH. The upper(lower) figure shows the profile center in the horizontal(vertical) direction. The black line shows the direction to SK and the red lines show ± 1 mrad in the direction to SK as measured by GPS.

The silicon pad array is located downstream of the ICH. There are a total
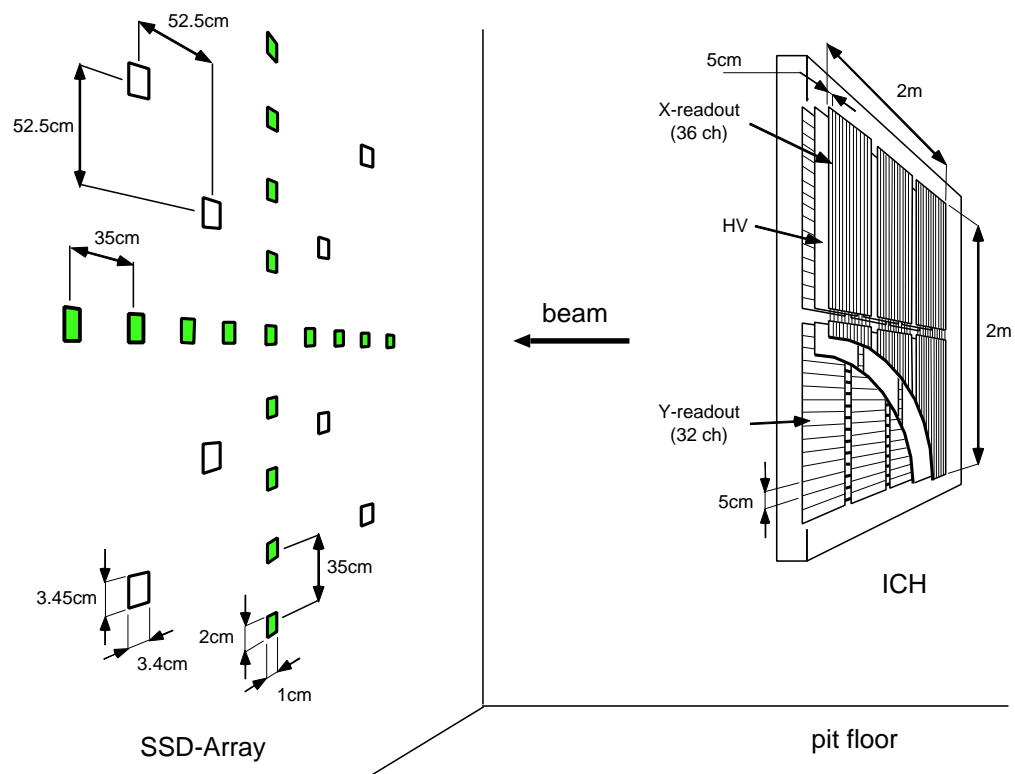
Figure 2.4: Schematic of the MUMON. The ionization chamber is on the right, the silicon pad array is on the left.
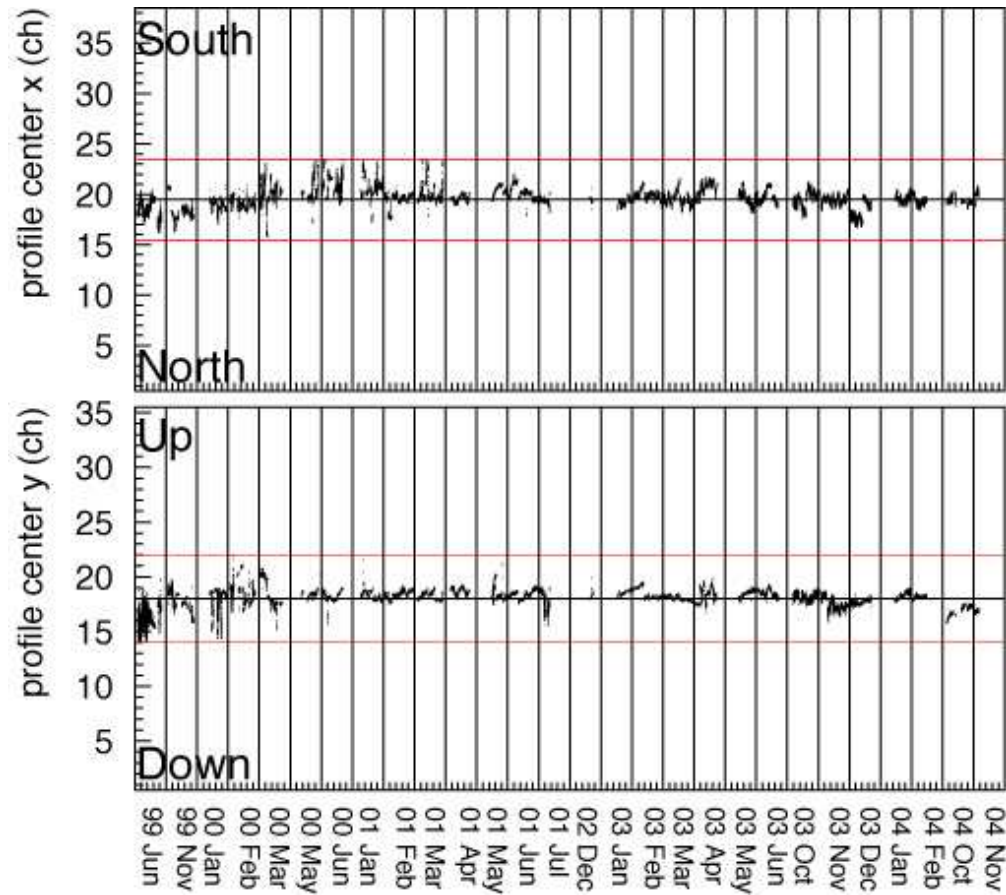
Figure 2.5: Stability of the muon beam as measured by the MUMON's ionization chamber. Upper figure: horizontal direction. Lower figure: vertical direction. The red lines are ±1mrad of SK.

of 17 SPDs each with a sensitive area of 1 cm × 2 cm with a depletion layer thickness of 300 μm and a spacing of 35 cm between them arranged along the horizontal and vertical directions. On the diagonals, 9 larger SPDs are arrayed 74.2 cm apart with a sensitive area of 3.4 cm × 3.05 cm and depletion layer thickness of 375 μm. A bias voltage of 100 V (70-80 V) is applied for the smaller (larger) pads.

PIMON

A pion monitor (PIMON) is installed just downstream of the horns, to measure the momentum (p_π) versus angle (θ_π) distributions of the focused pions. For the pion decay that goes into a muon and muon neutrino, the neutrino's energy can be calculated given the momentum of the pion and the angle θ of the outgoing neutrino with respect to the pion's initial direction in the lab frame,

$$E_\nu = \frac{m_\pi^2 - m_\mu^2}{2\left(E_\pi - p_\pi \cos\theta\right)} \tag{2.1}$$

where m_μ is the muon mass, m_π is the pion mass, and $E_\pi = \sqrt{p_\pi^2 + m_\pi^2}$ is the pion energy in the lab frame. With Equation 2.1 and the fact that pion decay is isotropic in the pion's rest frame, the neutrino energy spectrum at any distance can be extrapolated from the (p_π, θ_π) distributions. The extrapolation will be explained in more detail in Chapter 4. PIMON measurements were made twice: once during June 1999 with the 200 kA horn current and 2 cm target diameter and once in November 1999 with the 250 kA horn current and 3 cm target diameter. Measurements were never made during neutrino data taking.

To make the (p_π, θ_π) measurement, the PIMON is built as a gas Cherenkov imaging detector consisting of a gas vessel, a spherical mirror, and an array of 20 photomultiplier tubes (PMTs). A schematic of the PIMON is given in Figure 2.6. Cherenkov photons from the pions strike the mirror and are reflected to the PMT array. Because of the spherical mirror characteristics, photons propagating in the same direction are focused to the same focal plane position, thus giving information on the pion's direction. The direction is therefore determined by the Cherenkov ring's location and the momentum is determined by the size of the Cherenkov angle.

The gas vessel of the PIMON is filled with freon gas (C_4F_8). The index of refraction n of the gas can be changed by changing the pressure; the gas pressure sets the momentum threshold for pions to emit Cherenkov radiation. At refraction indices above n=1.00242, the 12 GeV primary photons emit Cherenkov photons, becoming a significant source of background to the pion
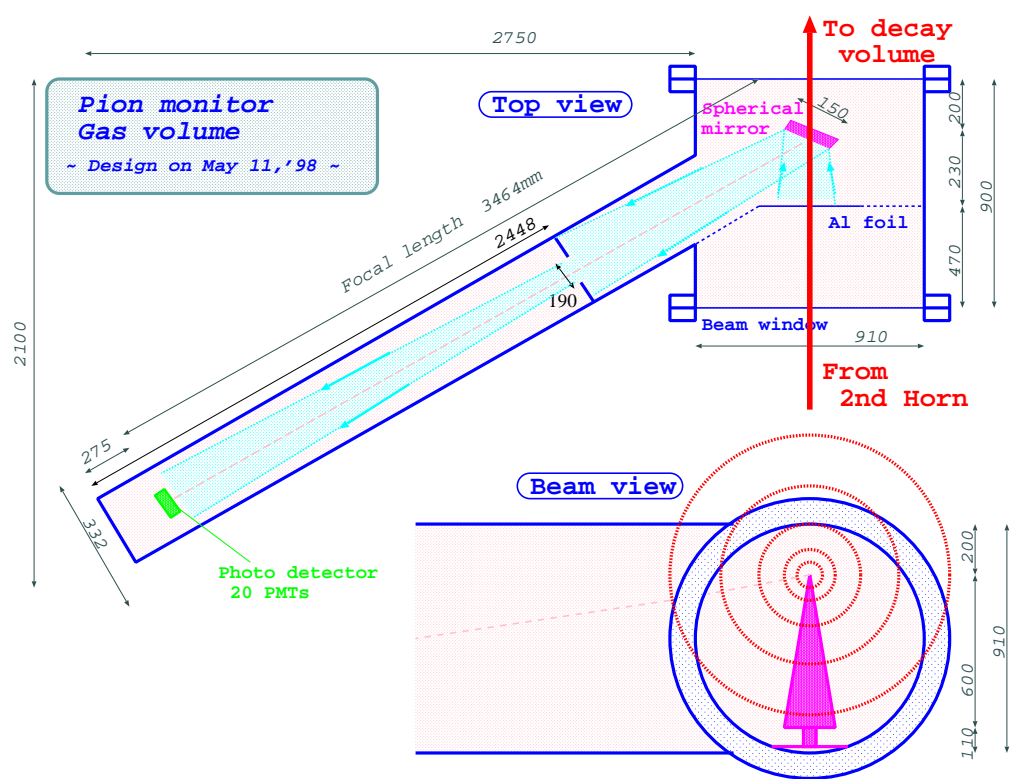
Figure 2.6: Schematic of the PIMON. The upper part of the figure shows the PIMON from above, with the arrow indicating the beam direction. The lower part of the figure shows the beam view of the PIMON, with the beam going into the page.

measurement. The spherical mirror is wedged-shaped, covering 1/30 of the beam, with the assumption that the beam is azimuthally symmetric. The reflection angle is 30° with respect to the beam direction. The PMT array is set 3 m away from the beam to minimize radiation damage. The sensitive area of the photocathode for each PMT is 8 mm in diameter with the PMTs arranged vertically spaced 35 mm apart.

2.1.5 Run Periods and Beam Summary

The neutrino beam line finished construction in early 1999 and started commissioning that March. The beam line and its components were aligned to within 0.1 mrad of the nominal beam axis as determined by a GPS survey between KEK and Super-Kamiokande [37] that had an accuracy of 0.01 mrad. Data was taken from June 1999 until November 2004 and divided into five run periods corresponding to different experimental configurations. The run periods are defined as K2K-Ia (June 1999), K2K-Ib (November 1999 to July 2001), K2K-IIa (December 2002 to June 2003), K2K-IIb (October 2003 to February 2004), and K2K-IIc (October 2004 to November 2004)[1]. K2K-Ia had a target diameter of 2 cm and horn current of 200 kA, which went up to 3 cm and 250 kA, respectively, for all subsequent run periods. This change took into account the size of the profile of the proton beam with respect to the target diameter. Super-Kamiokande had full PMT coverage during the K2K-I run periods, but only half during the K2K-II periods (see below). The Lead Glass Calorimeter operated during K2K-I in K2K's Near Detector, but was replaced by SciBar (the Scintillating Bar Detector) for the K2K-II run period. Finally, the Scintillating Fiber Detector used a water target except for K2K-IIc, where the water was drained and replaced with aluminum. This is, as well as the corresponding number of protons delivered (also known as protons on target, or POT) is given in Table 2.1.

The number of protons delivered shown in Table 2.1 mentions protons used for physics analysis as well as total number of protons delivered. Spills that are used for physics analysis must satisfy four criteria. The first is that the spill must have normal machine status. Any spill that occured during a beam study, beam tuning, or machine study cannot be used. Secondly, a spill with trouble in the beam components or data acquisition systems can not be used. The third criteria is the the spill must have a proton intensity greater than 1×10^{12} protons. Lastly, the beam spill must have a horn current greater than 190 kA for K2K-Ia and greater than 240 kA for the rest of K2K data taking.

---

[1]I was monitoring the Near Detector for shift when K2K stopped data taking.

Table 2.1: Summary of the number of protons on target and the experimental configuration for each running period. The row labeled "LG/SciBar configuration" indicates the detector installed between the SciFi and MRD detectors. For the row "SK configuration", "SK-I" refers to the configuration with full PMT density while "SK-II" refers to that with half density. The delivered shown in the table includes the beam delivered during commissioning and beam tuning work before the physics runs. Mini-Scibar is the the SciBar detector with only 4 layers.

Periods	Ia	Ib	IIa	IIb	IIc
Delivered POT ($\times 10^{18}$)	6.21	49.85	24.91	20.15	3.78
POT for analysis ($\times 10^{18}$)	3.10	44.83	22.57	18.61	3.12
Horn current (kA)	200	250	250	250	250
Target diameter (cm)	2	3	3	3	3
SK configuration	SK-I	SK-I	SK-II	SK-II	SK-II
LG/SciBar configuration	LG	LG	mini-SciBar	SciBar	SciBar
Target material in SciFi	water	water	water	water	Al

This gives a total of 1.049×10^{20} protons delivered for K2K with 9.22×10^{19} used for physics analysis.

2.2 The Far Detector (Super-Kamiokande)

In order to discuss the 1KT Water Cherenkov Detector with little confusion, it is a good idea to discuss the principles of a water Cherenkov detector as well as the premier water Cherenkov detector, and far detector of K2K, Super-Kamiokande, concurrently.

2.2.1 Location

Super-Kamiokande (SK) is located at the Kamioka Observatory, the Institute for Cosmic Ray Research, University of Tokyo, in a zinc mine under Mt. Ikeno in Kamioka, Gifu Prefecture, Japan. The mine is owned and operated by the Kamioka Mining and Smelting Company. SK's location is roughly 250 km west of KEK (which is slightly north of Tokyo) and geographically at 36°25'33" N, 127°18'37" E, and 371.8 m above sea level. This region is known as the Japanese Alps, which is known for its skiing and hot springs.

2.2.2 Overview

SK was built as a successor to the Kamiokande experiment [20]. The primary research goals of SK are to measure not only the lifetime of the proton, but also neutrino physics, making its name an acronym of **Super-Kamioka Nucleon Decay Experiment** or **Super-Kamioka Neutrino Detection Experiment**. The detector is covered by an average of 1000m (2700 meter water equivalent) rock overburden, which reduces cosmic ray background rate by roughly 10^5 compared to the Earth's surface, or approximately 2.2Hz at the detector. A side tunnel houses the water purification system, and another contains the control room where shift takers monitor the detector. The detector cavity and control room both have an over-pressure of fresh air with low radon content blowing from outside into the mine. Also, all exposed mine rock near the detector and in the control room has been coated with Mine Guard®, a polyurethane-like material, to reduce the amount of radon, dust, and debris. A schematic of the detector is in Figure 2.7 and a cross section view is in Figure 2.8.

SK, like the PIMON above and 1 Kiloton Water Cherenkov Detector below, detects Cherenkov radiation. Cherenkov radiation occurs when a particle's speed is greater than the speed of light of that medium (i.e. $v > c/n$) and is the optical equivalent to a sonic boom. The emitted radiation forms a cone along the particle direction with a angle θ_C:

$$\cos\theta_C = \frac{1}{n(\lambda)\beta} \tag{2.2}$$

where $n(\lambda)$ is the wavelength-dependent index of refraction and $\beta = v/c$. In SK, $n = 1.34$ consistently over most of the sensitive region of PMTs, giving a Cherenkov angle of $\theta_C \approx 42°$. The number of Cherenkov photons (dN) emitted per unit wavelength $(d\lambda)$ per unit distance (dx) the charged particle travels is:

$$\frac{d^2N}{dxd\lambda} = \frac{2\pi\alpha}{\lambda^2}\left(1 - \frac{1}{(n(\lambda)\beta)^2}\right) = \frac{2\pi\alpha}{\lambda^2}\sin^2\theta_C \tag{2.3}$$

where α is the fine structure constant. This makes the photon production rate roughly $dN/dx \approx 575$/cm.

By placing light sensors in the path of the Cherenkov radiation and measuring the number of photons deposited and the time they were deposited, it is possible to reconstruct the position, direction, and type of the original charged particle, see Appendix A for more details. From the total number of photons deposited, it is possible to estimate the energy of the particle as well.
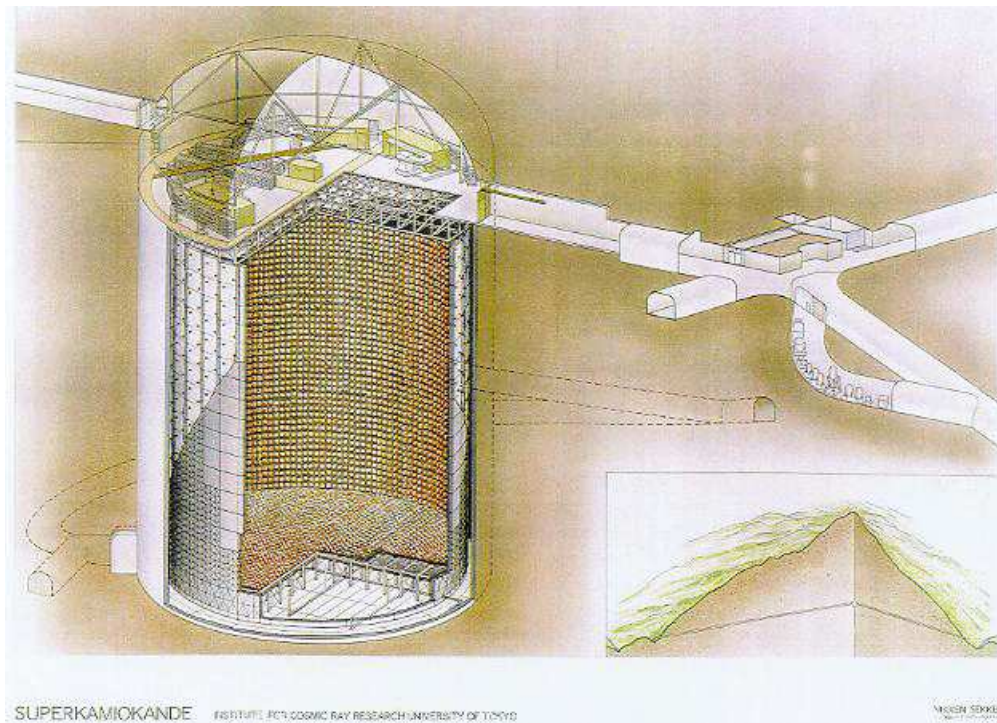
Figure 2.7: Drawing of Super-Kamiokande. The electronics huts on top of the tank, water purification system, and control room are also in the figure.
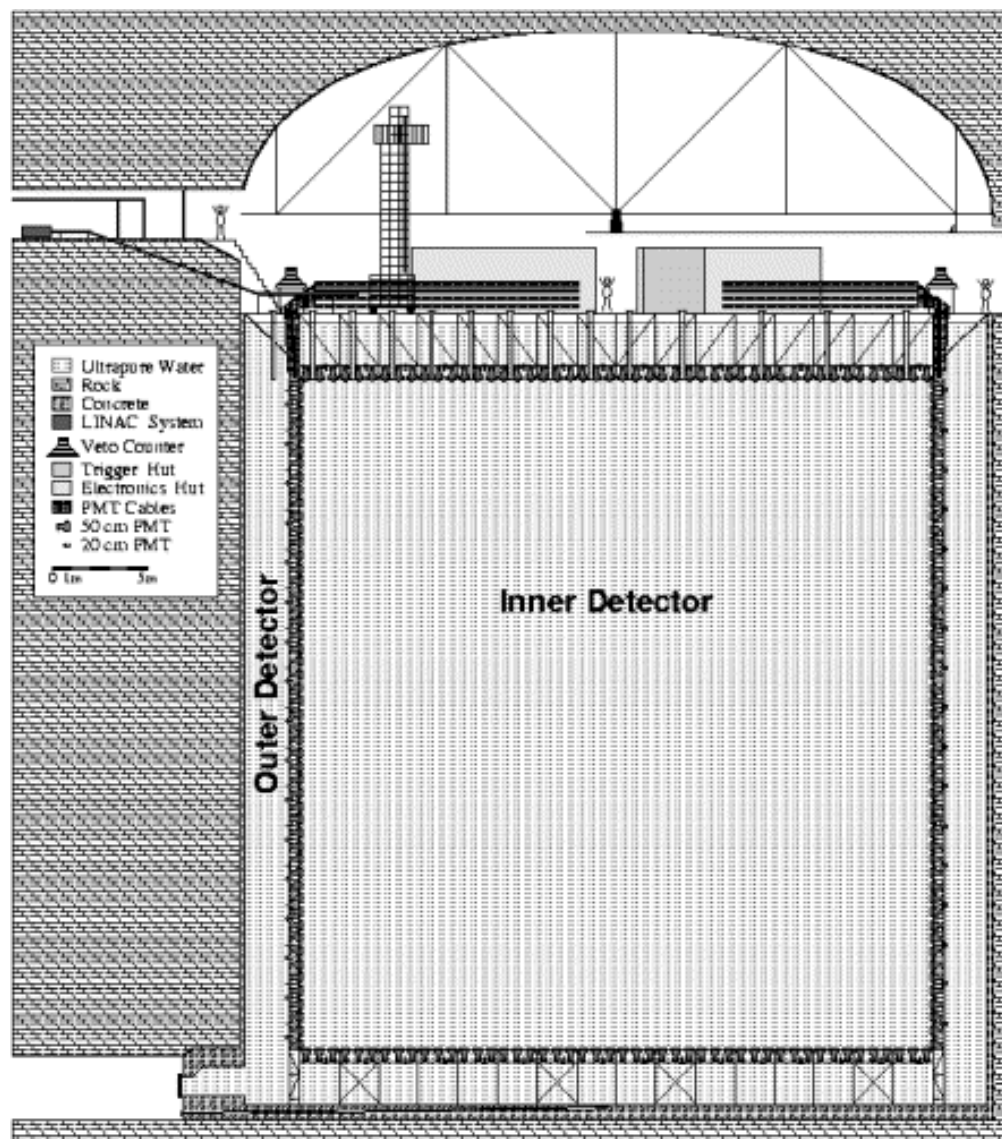
Figure 2.8: Cross section of Super-Kamioknade.

2.2.3 The Inner Detector

The Inner Detector (ID) is the primary detection volume for SK. It is cylindrically shaped with a height of 36.2 m and a 33.8 m diameter with 32.5 kton of water. Viewing the ID detector volume are 20" PMTs. In K2K-I, 11146 PMTs were set on a 70 cm grid, giving a 40% photocathode coverage of the wall, as in Figure 2.9. A schematic of the ID PMT is given for Figure 2.10. The remaining 60%, which covers mainly the gaps in the PMTs, is covered by black opaque polyethylene telephthalate sheets. These sheets help the optical separation between the ID and OD as well as suppress low energy events due to residual radioactivity behind the PMTs.

For K2K-II, there were 5181 ID PMTs with an acrylic shield giving a 19% photocathode coverage because of a shockwave released from an imploded PMT that destoyed over half of the ID PMTs in October 2001. These PMTs have since been replaced for SK-III, which has been taking data since July 2006.

An ID PMT works by converting a photon into a measurable electric pulse. Using the photo-electric effect, a photon incident on a deposited layer of bialkali (Sb-K-Cs) on the inner surface of the PMT glass kicks off an electron. This layer is called the photocathode. The peak quantum efficiency of this process is roughly 21% from wavelengths of 360 nm to 400 nm, as shown in Figure 2.11. The photoelectron is accelerated by roughly 800 V and strikes the first dynode. From this interaction, more electrons are produced and accelerated about another 300V to the second dynode. The electron showering continues through 9 more dynodes about 100 V larger than the previous dynode resulting in a gain of order 10^7 over the initial photoelectron. The voltage applied to each ID PMT ranges from 1700 V to 2000 V. For a single photoelectron (p.e.), the typical transit time is 100 ns with a $\sim$2.5 ns spread. The ID PMTs were made by the Hamamatsu Corporation for the Kamiokande experiment, with design improvements [38] for SK. The high voltage signal is carried through a 70 m co-axial cable to one of four quadrant electronics huts located directly above the tank. Details of the electronics and data acquisition system are given in Ref. [39].

2.2.4 The Outer Detector

The outer detector (OD), or anti-detector, is primarily used as a veto against cosmic rays. It is a cylindrical shell which varies in thickness of 2.2 m at the top and bottom of the tank to 2.0 m at the barrel and completely surrounds the ID with 14.7 kilotons of water. Mounted on the wall of the
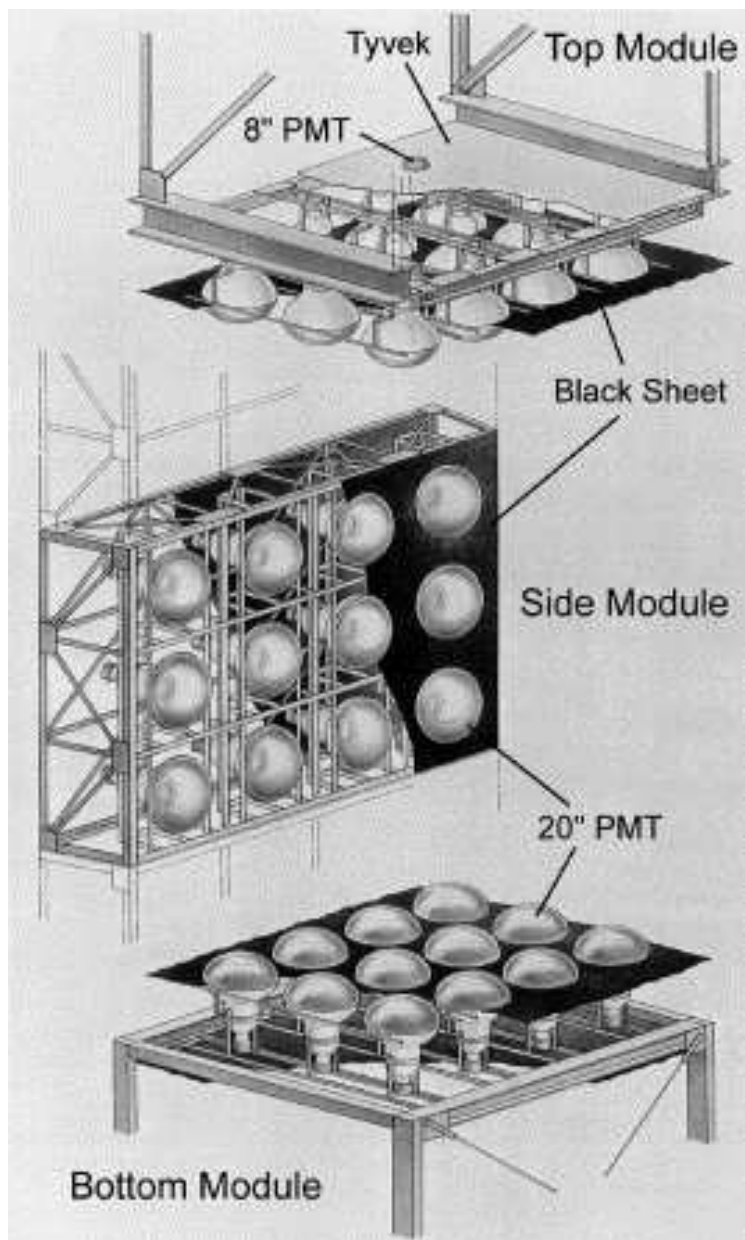
Figure 2.9: Schematic of support structures in SK and PMT array for a top, barrel, and bottom module.
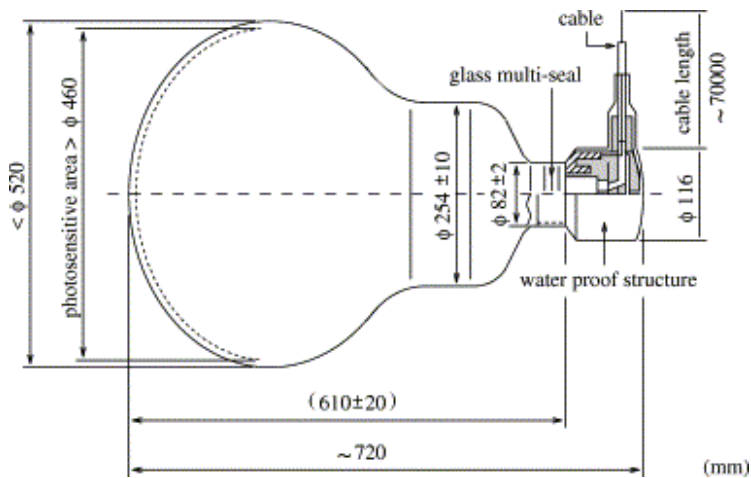
Figure 2.10: Schematic of the 20 inch ID PMT.
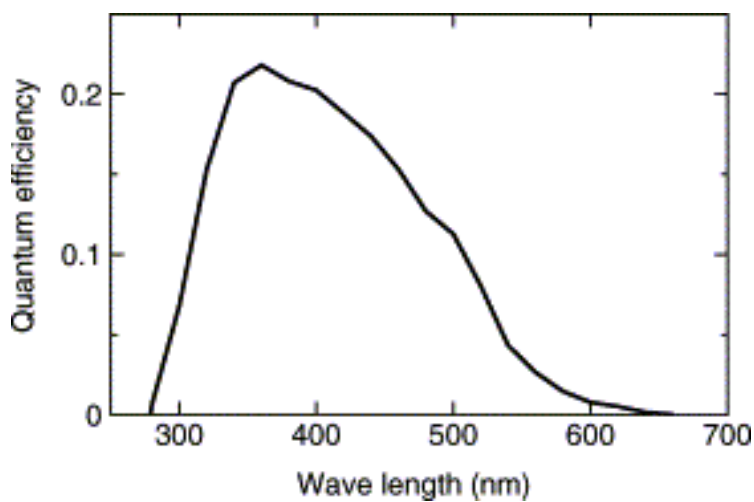
Figure 2.11: The quantum efficiency of the ID PMT photocathode as a function of wavelength

OD are 1885 8" Hamamatsu R1408 PMTs recycled from the IMB experiment [18]. Because of the small number of PMTs, acrylic wavelength shifting plates (WSPs) doped with 50mg/l of bis-MSB (60 cm×60 cm×1.3 cm) are attached to each face of the OD PMTs [36]. The outer edges of each plate are lined with reflective aluminum mylar tape. The WSPs absorb UV light and emit photons in the blue-green wavelength, matching the peak sensitivity of the OD PMTs. The plates increase the light detection efficiency by 60% as compared to having only PMTs. Overall, the timing resolution of the PMTs with WSPs is about 15 ns, with the PMTs having a 13 ns timing resolution.

In between the OD PMTs is white Tyvec bonded with black low density polyethylene. The white Tyvec side facing the OD region increases the Cherenkov light collection while the polyethylene helps the optical separation between the ID and OD.

2.2.5   Event Classes

SK was designed to be able to detect a variety of event classes. These are described below roughly in order of ascending energy from a few MeV to tens of GeV. Events are normally classified as e-like, or showering, events, or μ-like (non-showering) events. Due to the electromagnetic shower and multiple scatterings from electrons or gamma rays, e-like events have diffused ring patterns in the ID. Non-showering (μ-like) rings are produced by muons or charged pions and have sharper ring edges.

At the low energy end are solar events and their backgrounds of radon and spallation events. While far below the neutrino energies of K2K, there are decay electrons from muons which range in measured energy up to 60 MeV, which includes the upper theoretical energy of 52.8 MeV and energy resolution effects. These decay electrons are used as a calibration source for the energy scale systematic error.

Slightly higher in energy are the atmospheric neutrino induced events. Atmospheric neutrinos interact via NC or CC weak interactions with either oxygen or hydrogen nuclei. It is also possible to interact with the electrons in the water molecule, but is a much more rare case than the nuclei interactions. Observable NC interactions yield at least one pion from inelastic interactions, or a proton above the Cherenkov threshold. Observable CC interactions usually produce a single observable lepton, and in the case of higher energy events, at least one visible pion. In the NC or CC case, pions may be absorbed by the nucleus, undergo charge exchange in the nucleus, or are scattered before escaping. In the case the pion is a π^0, a showering event is usually observed from the two decay photons; it may be hard to detect both Cherenkov rings

from the electromagnetic shower of the decay photons because of the asymmetry of the decay in the lab frame. This asymmetry results in either a dim second ring, or the overlapping of both rings from the decay photons. The induced atmospheric events are fully contained within the ID. If the incident neutrino energy is high enough, the outgoing lepton can exit the detector, making it a partically contained (PC) event. PC events are mostly from CC ν_μ interactions. Atmospheric events will behave in a similar fashion as K2K events since they are in the same energy range, thus making it necessary to distinguish between the two (see Section 5.1). Also in this energy range may be nucleon decay events, which is limited in total energy to 1 GeV.

At the high end of observable energies, two SK event classes are normally observed. Cosmic-ray muons or muons from neutrino interactions in the rock below the detector can produce stopping or through-going muon events. The cosmic-ray muon flux goes to zero as the origin of the muons goes below the horizon. Any upward going muon are considered to be from neutrino interactions in the rock. The longest tracks of through-going muons deposit 10 GeV of energy in the detector. More energy can be deposited if the muon undergoes bremsstrahlung.

2.3   The Near Detector

A suite of detectors, known as the Near Detector (ND) and shown in Figure 2.12, is 300 m downstream of the target. The purpose of these detectors is to measure the neutrino energy spectrum, direction, and flux before oscillations occur. They are divided into the 1 Kiloton Water Cherenkov Detector (1KT), and the Fine Grained Detector (FGD), which consists of a Scintillating Fiber Detector (SciFi), a Lead Glass Calorimeter (LG) for the K2K-I run period, a Scintillating Bar (SciBar) detector for the K2K-II run period, and a Muon Range Detector (MRD). Details for each are given below.

2.3.1   The 1 Kiloton Water Cherenkov Detector

The 1KT is the upstream detector of the ND. It is a miniature version of Super-Kamiokande, using the same target material and instrumentation. The primary role of the 1KT is to measure the ν_μ interaction rate and energy spectrum and flux which will be extrapolated to Super-Kamiokande to provide a reference for the neutrino oscillation analysis. A secondary role is to provide high statistics for neutrino-water interaction measurements. An example of a 1KT event from the event display can be seen in Figure 2.13.
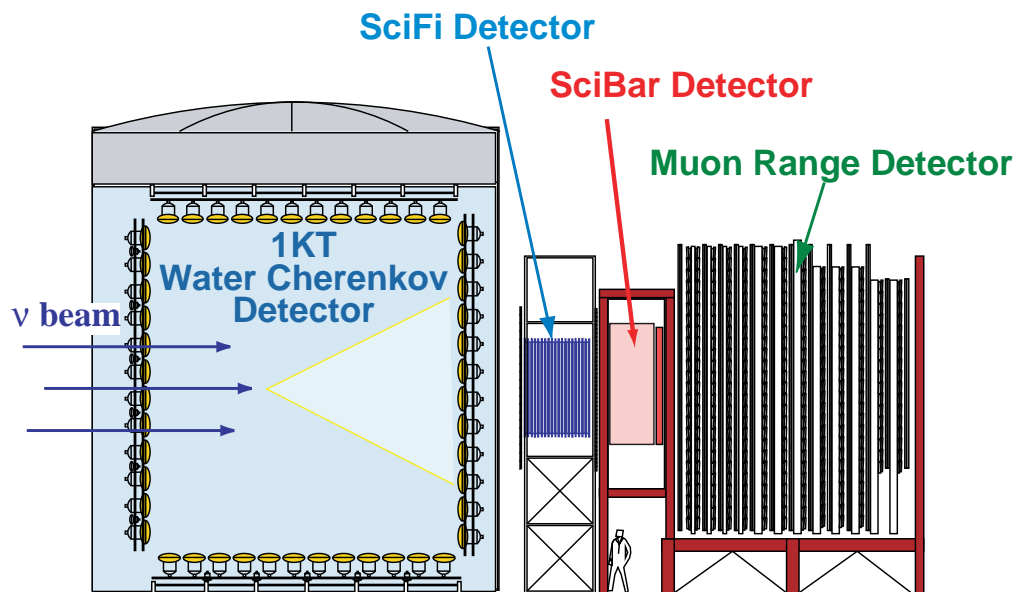
Figure 2.12: The ND for the K2K-IIb run period. From the left: the 1KT, the SciFi, the SciBar, and the MRD. For the K2K-I run period, the LG occupied the space that the SciBar currently occupies.
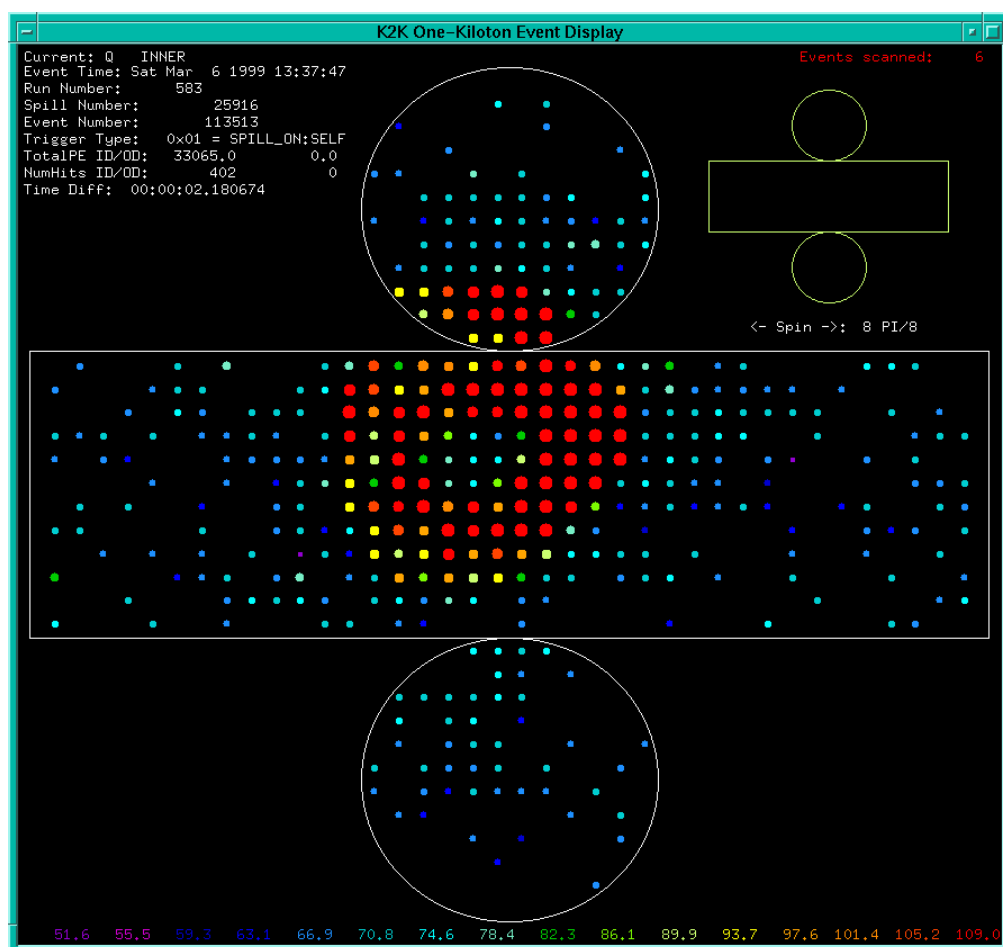
Figure 2.13: Muon neutrino event from 1KT event display.

The 1KT is a cylindrical tank 10.8 m in height and 10.8 m in diameter, holding approximately 1000 tons of pure water. The center of the tank is 294 m downstream of the pion production target. The tank is optically separated into an inner detector (ID) and outer detector (OD) by black opaque sheets and reflective Tyvek. The ID's dimensions are a cylinder of 8.6 m in height and a 8.6 m diameter. The 1KT has 680 inward-facing 20" PMTs which are used to detect Cherenkov light from neutrino events in the ID. The PMTs are spaced 70 cm apart and are the exact same type used in SK, giving the same 40% photocathode coverage as SK. The OD has 68 8" outward-facing PMTs covering the upstream third of the barrel and the whole bottom. These PMTs are used to veto incoming particles from beam induced interactions and cosmic-rays. To compensate for the Earth's magnetic field, which affects PMT response, 9 horizontal and 7 vertical Helmholtz coils surround the 1KT tank. The water purification system for the 1KT circulates roughly 20 tons of water per hour, while keeping the electrical resistance at ~ 10 MΩ/cm and the water temperature at $\sim 11^\circ$C.

The data acquisition (DAQ) system is also similar to SK. ATMs, a custom electronic board which processes the PMT signals, are used to record the digitized charge and timing information for each PMT hit over a threshold of 1/4 p.e. The DAQ trigger threshold is 40 PMT hits within a 200 ns time window within the 1.2 μs beam spill. The 40 hit threshold is roughly equivalent to the signal of 6 MeV electron. The pulse shape of the analog sum of all 680 PMTs (PMTSUM) is also recorded. The PMTSUM is recorded for every beam spill using a 500 MHz flash analog to digital converter (FADC) which enables the identification of multiple interactions in a spill. The number of interactions in each spill is determined from counting the peaks in the PMTSUM greater than a threshold equivalent to a 100 MeV electron signal.

The physical parameters of a 1KT event, such as vertex position, momentum, number of Cherenkov rings, and particle type, are determined using the same algorithms as SK (see Appendix A). The vertex position of an event is determined from the PMT timing information. With this knowledge, the number of Cherenkov rings and the direction of each ring are determined using a maximum likelihood procedure. Each ring is then classified as e-like, which are showering particles ($e^\pm$, γ) or μ-like, which are non-showering particles ($\mu^\pm$, $\pi^\pm$, p) using the ring pattern and Cherenkov opening angle. From this information, the vertex position of single ring event is further refined. The momentum corresponding to each ring is determined from the Cherenkov light intensity. Events are also divided into fully contained (FC) events and partially contained (PC) events by the number of photoelectrons deposited in a single PMT. A FC event is defined as no PMT having more than 200 p.e. de-

posited in it; a PC event has more than 200 p.e. deposited because a muon going through wall will deposit a lot of light in the nearest PMT. Because of this, the 1KT is sensitive to lower energy muons because they will stop in the detector, while the 1KT loses sensitivity to the high energy tail of the neutrino beam.

The reconstruction quality for event information was checked using a MC simulation. The vertex resolution for single ring events is 14.7 cm (12.5 cm) for FC (PC) events; for multi-ring events, the FC (PC) vertex resolution is 39.2 cm (34.2 cm). The angular resolution for single ring charged current quasi-elastic (CCQE) events is estimated to be 1.05° (0.84°) for FC (PC) events. As for particle identification, 0.3% of muon single ring CCQE events are misidentified as e-like while 3.3% of electron single ring CCQE events are misidentified as μ-like. The muon momentum resolution is estimated to be 2.0-2.5% over the whole 1KT momentum range.

The PMT gain and timing calibrations use a Xe lamp and N_2 laser as light sources, respectively. The absorption and scattering coefficients of water are measured using laser calibration while the coefficients are further tuned in the detector simulation by reproducing the charge pattern of cosmic-ray muons. The energy scale is calibrated from cosmic-ray muons and their decay electron as well as NC π^0 from the neutrino beam. The absolute energy scale uncertainty is $^{+3}_{-4}$% while the vertical/horizontal asymmetry is about 1.7%. The energy scale was stable within 1% from 2000 to 2004.

2.3.2   The Scintillating Fiber Detector

The SciFi detector is a 6 ton tracking detector with integral water target layers. See Figure 2.14 for a schematic. The SciFi serves as a compliment to the 1KT because of greater sensitivity to higher energy events. SciFi consists of 20 2.6 m×2.6 m layers of tracking modules that are 9 cm apart. Each layer has a double layer of sheets of scintillating fibers arranged in either the horizontal or vertical directions where each sheet is two fibers thick. The diameter of each fiber is 0.692 mm. Between each fiber module, there is a water target contained in an extruded aluminum tank, making 19 in total. Measurements made of the SciFi mass give a fiducial mass of 5590 kg. More details can be found in References [41, 42].

The fiber sheets are coupled to an image intensifier tube (IIT) with a CCD readout system. The relative position between the CCD coordinate system and the fibers is monitored by illuminating every 10th or 20th fiber periodically with and electro-luminescent plate placed at the edge of each fiber sheet. In addition to this check, cosmic-rays were used to monitor the system's gain on
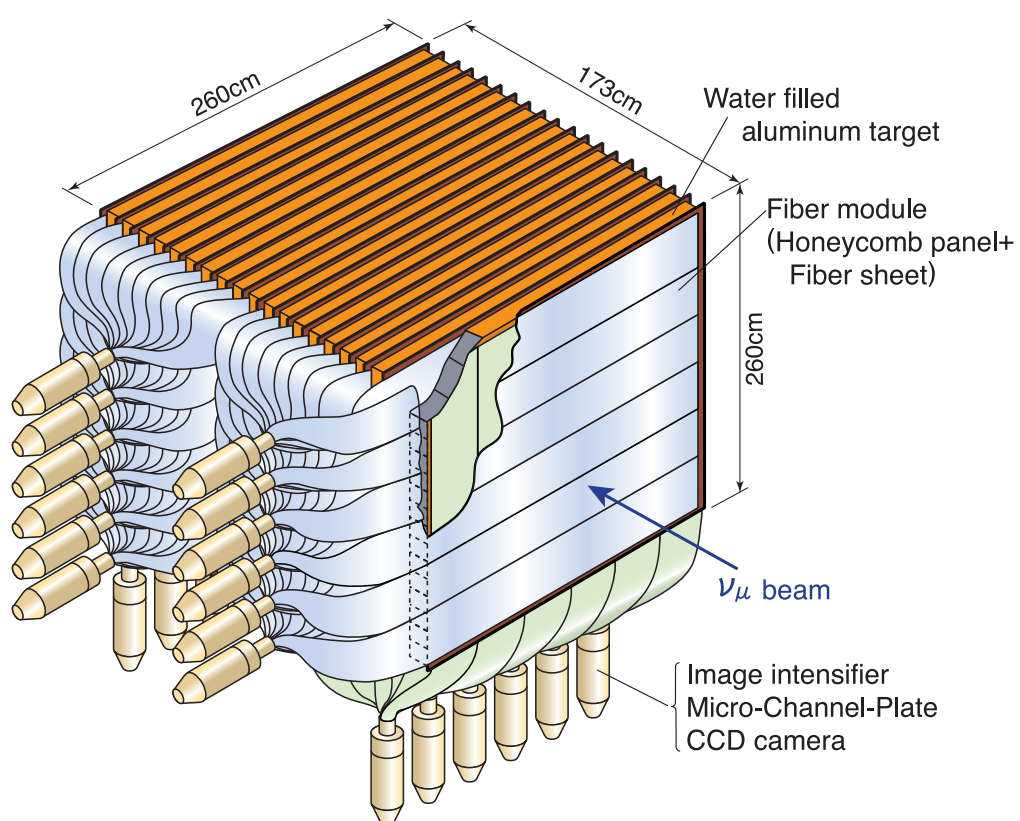
Figure 2.14: Drawing of the SciFi detector.

a weekly basis.

Fibers that are hit are extracted using the CCD images. Raw data consists of the hit pixels and their digitized brightness of the CCD with the neighboring hit pixels grouped to make a pixel cluster. The clusters are then combined and matched to specific scintillating fibers. The efficiency of identifying a fiber which had a charged particle pass though it is estimated to be about 95% using cosmic-ray muons, but closer to 90% at angles within 30° of the beam. After the hit fibers are reconstructed, tracks with at least three layers are reconstructed using conventional fitting techniques. Also using cosmic-ray muons, the track-finding efficiency is ∼70% for tracks of three layers, ∼87% for four layers, and close to 100% for longer tracks.

Two plastic scintillator hodoscope systems surround the SciFi. One is placed downstream of the SciFi and gives the track timing and position information. It is also a pre-shower detector for the LG. The other is placed upstream and used to veto muons, other particles from the beam, including interactions in the 1KT, and cosmic rays. The downstream system has 40 scintillator units with a total height of 4 m. Each unit is 466 cm long, 10.4 cm high, and 4 cm thick. The horizontal position of a charged particle in the downstream system can be resolved to 5 cm from PMT readouts at both ends of the scintillator. Upstream is similar, but pairs of scintillator are joined by optical cement, which share a single light guide for each PMT, giving a vertex resolution twice as bad. Between the two systems, there are a total of 120 PMTs. The energy resolution of the hodoscopes is estimated to be 7.4% from cosmic-ray muons for minimum ionizing particles. More details of the hodoscope system can be found in [43].

2.3.3   The Lead Glass Calorimeter

The LG calorimeter was located between the SciFi and MRD detectors during the K2K-I run period before being replaced by SciBar in K2K-II. Its purpose was to distinguish between muons and electrons from the deposited energy. The detector itself is made of 600 cells, where each cell is approximately 12 cm×12 cm×34 cm and viewed by a 3" PMT (a Hamamatsu R1652) though a light guide cylinder also made of lead glass. The LG was used in the TOPAZ experiment [48] and reused in K2K.

The LG readouts only read the charge information of each cell. The absolute energy scale of 9 standard LG cells out of 600 were calibrated using an electron beam from an electron synchrotron before installation. The energy range of the synchrotron was from 50 MeV to 1.1 GeV. The resolution estimated from the pre-calibration was 10% at 1 GeV. The position dependence

for energy resolution was measured to be 4%. The other cells were relatively calibrated to the standard cells using cosmic-ray muons.

Responses for muons were also calibrated from cosmic-ray muons prior to installation at KEK. The relative peak pulse height in each PMT was adjusted to each other within 2%. The charged pion responses were checked at momenta ranging from 0.3 GeV/c to 2.0 GeV/c by using the KEK test beam. These were confirmed to be in agreement with MC expectation.

2.3.4   The Muon Range Detector

The MRD's purposes are to monitor the stability of the neutrino beam and to identify muons produced in the upstream detectors and measure their energy and angle in combination with other detectors in the FGD system.

The MRD is made of 13 sets of vertical and horizontal drift-tube layers with 12 layers of iron absorber sandwiched in between. Each layer is approximately 7.6 m×7.6 m. The upstream 4 layers of iron plates are 10 cm thick and the remaining iron layers are 20 cm thick, giving a total iron thickness of 2.00 m and a mass of 864 tons. This covers muon energies up to 2.8 GeV. The MRD has 6,632 drift tubes, each one made of aluminum with a cross section of 5 cm×7 cm, and filled with P10 gas (Ar:CH_4 = 90%:10%). The maximum drift time is roughly 1μs. 20 MHz 6-bit TDCs are used to digitize the drift time. The total MRD mass is 915 tons.

Using a conventional track finding algorithm, the track finding efficiency for one, two, and three traversed iron plates is 66%, 95%, and 97.5%, respectively. For longer tracks, the efficiency goes up to 99%. The range of the track is estimated using the reconstructed path length in iron.

Knowing the iron-plate weight is necessary for measuring the track range and the neutrino interaction rate. The relative thickness of each plate was studied by comparing the event rate using the neutrino beam data. Using the same iron as in the MRD, the density was also measured directly. This lead to being able to quote the iron plate mass to within an accuracy of 1%. Using a GEANT based MC, the relation between the muon range and energy was calculated, giving a 1.7% difference in the muon range. The energy scale error of 2.7% is determined through the linear addition of the 1.7% range error and the 1% iron plate mass.

The energy acceptance and resolution of the MRD were studied using MC simulations. The acceptance ranged from 0.3 GeV to 2.8 GeV while the resolution is 0.12 GeV for forward-going muons. The angular resolution for the tracks is roughly 5° and the vertex point resolution perpendicular to the beam direction is 2 cm.

2.3.5 The Scintillating Bar Detector

The SciBar detector [45] was constructed as an upgrade of the ND during the K2K-II run period. It replaced the LG calorimeter, which is explained above. A drawing of the SciBar detector is in Figure 2.15.

SciBar is made of extruded scintillator strips, where each strip is 1.3 cm thick, 2.5 cm wide, and 300 cm long. There are 64 layers of alternating vertical and horizontal planes, using a total of 14,848 strips. This gives a detector size of 3 m×3 m×1.7 m and a total mass of roughly 15 tons. The scintillated light is guided to a multi-anode PMT (MAPMT) by wavelength shifting fibers inserted into a hole in the middle of each strip. A total of 64 fibers are bundled together and glued to the photo cathode of one MAPMT (see Figure 2.16). Both charge and timing of the MAPMT outputs are recorded using custom-made electronics [44] giving a noise level and timing resolution for a minimum-ionizing particle of about 0.3 p.e. and 1.3 ns, respectively.

An electromagnetic calorimeter (EC), also known as "the electron catcher," is installed at the downstream end of the SciBar. The main purpose of this detector is to study the beam ν_e contamination and π^0 production in neutrino interactions. The EC, which was originally built for the "spaghetti" calorimeter in the CHORUS experiment at CERN [47], is made of bars of dimension 262 cm×8 cm×4 cm. For the SciBar-EC, 32 bars are assembled to form a vertical plane followed by 30 bars for a horizontal plane. Each of these are 4 cm thick. They cover an area of 270 cm×262 cm and 262 cm×250 cm, respectively. This added 11 radiation lengths to the tracker part, which has about 4 radiation lengths. The response linearity of the EC is understood to be better than 10% and the energy resolution measured by a test beam is roughly $14\%/\sqrt{E(GeV)}$.

For neutrino event reconstruction, scintillating strips with at least two photoelectrons are selected. This corresponds to roughly 0.2 MeV. Using a cellular automaton algorithm [46], charged particles are reconstructed by searching for track projections in each of two dimensional views ($x-z$ and $y-z$). The candidates are combined based on matching the track edges in the z-direction and using the timing information. Tracks are required to have hits in at least three consecutive layers, corresponding to a minimum reconstruction length of 8 cm. This is equivalent to a 450 MeV/c proton. The reconstruction efficiency for an isolated track of at least 10 cm is 99%.
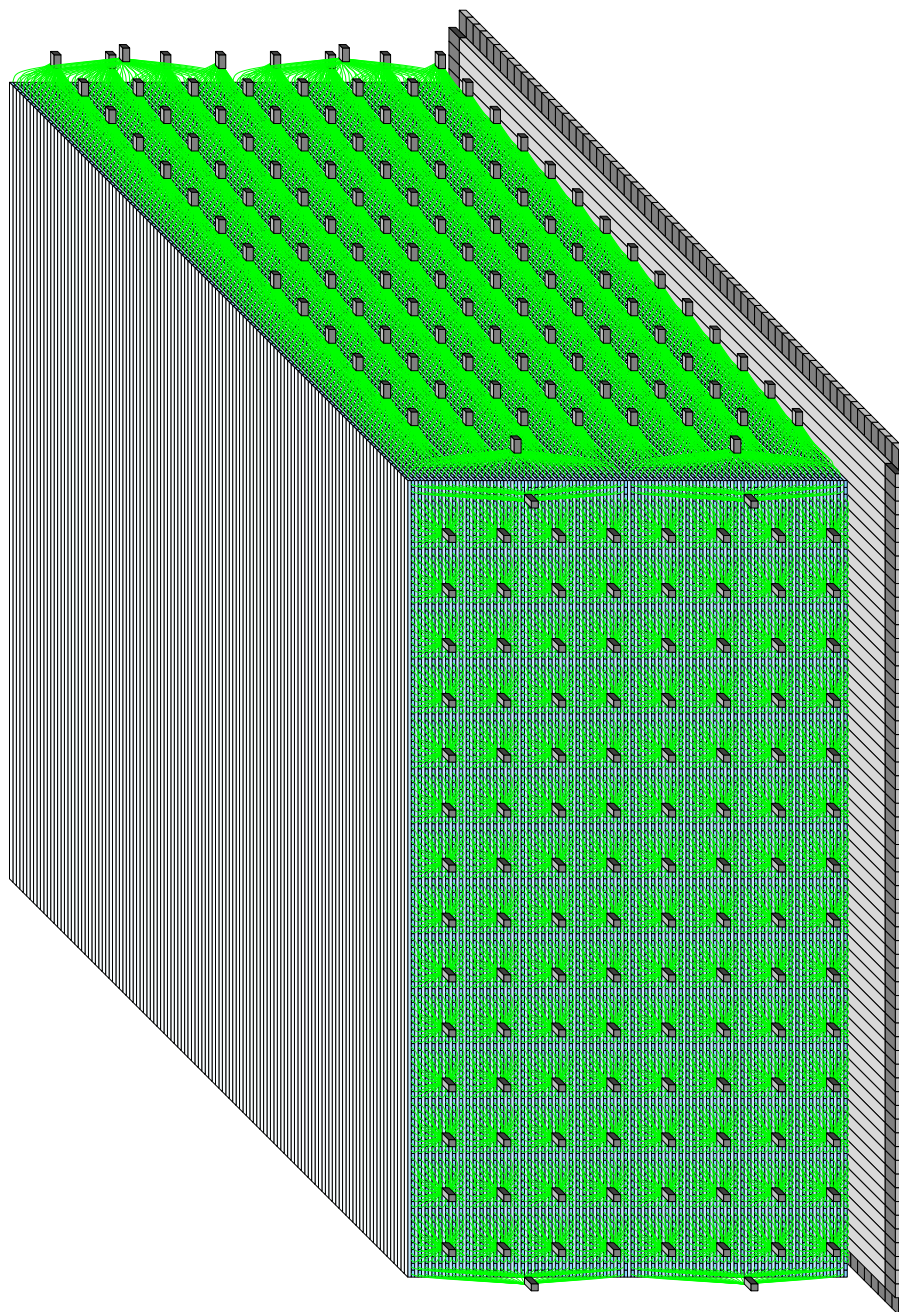
Figure 2.15: The SciBar detector with EC. The beam direction is going from left to right.
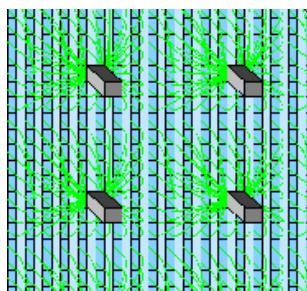
Figure 2.16: Close-up sketch of four fiber bundles. 64 fibers are grouped together and glued to a 64-channel MAPMT.

Chapter 3

The Near Detector Spectrum Analysis

The primary purpose of the Near Detector (ND) is to measure the neutrino energy spectrum from the neutrino beam. This measurement is used to extrapolate to the far detector both the expected number of events and the expected neutrino energy spectrum in the neutrino oscillation analysis. The neutrino energy is calculated assuming a CCQE interaction on a stationary nucleon:

$$E_\nu^{rec} = \frac{m_N E_\mu - m_\mu^2/2}{m_N - E_\mu + p_\mu \cos\theta_\mu}, \tag{3.1}$$

where m_N is the nucleon mass and E_μ, p_μ, $\cos\theta_\mu$, and m_μ are the energy, momentum, cosine of the angle with respect to the neutrino beam, and mass, respectively, of the muon.

In order to obtain the neutrino energy spectrum, a (p_μ, θ_μ) distribution is fit with the MC expectation as shown in Fig. 3.1. The neutrino energies are divided into eight bins as described in Table 3.1. For the MC expectation, a (p_μ, θ_μ) distribution is prepared separately for QE and non-QE interactions for each E_ν bin, making 16 distributions in total for each event sample. In the energy spectrum measurement, QE events are comprised of events from CCQE interactions and NC elastic interactions. Non-QE events are defined as CC or NC interactions where at least one hadron is produced.

The free parameters in the fit are the neutrino energy spectrum parameters for the eight neutrino energy bins and the parameter R_{nQE} that represents the relative weighting of CC non-QE events to CCQE events. The systematic uncertainties, such as nuclear effects, the energy scale, and other detector related systematics, are also incorporated as the fitting parameters ($\boldsymbol{f}$). The contents of the (m, n)-th bin of the (p_μ, θ_μ) distribution, $N_{m,n}^{\mathrm{MC}}$, is expressed

Table 3.1: The E_ν interval of each bin for the spectrum analysis.

	f_1^ϕ	f_2^ϕ	f_3^ϕ	f_4^ϕ
E [GeV]	0.0−0.5	0.5−0.75	0.75−1.0	1.0−1.5
	f_5^ϕ	f_6^ϕ	f_7^ϕ	f_8^ϕ
E [GeV]	1.5−2.0	2.0−2.5	2.5−3.0	3.0−

with the 16 templates and the fitting parameters as

$$N_{m,n}^{\mathrm{MC}} \equiv P \cdot \sum_{i=1}^{8} f_i^\phi \cdot \left[N_{m,n,i}^{\mathrm{MC(QE)}} + R_{\mathrm{nQE}} \cdot N_{m,n,i}^{\mathrm{MC(nQE)}} \right], \qquad (3.2)$$

where P, $N_{m,n,i}^{\mathrm{MC(QE)}}$ and $N_{m,n,i}^{\mathrm{MC(nQE)}}$ are a normalization parameter, the number of expected contents in the (m, n)-th bin for the QE interaction and that for the non-QE interaction for the i-th neutrino energy bin, respectively. The χ^2 is taken between the observed distributions, $N_{m,n}^{\mathrm{obs}}$, and $N_{m,n}^{\mathrm{MC}}$. During the fit, the flux in each energy bin and R_{nQE} are re-weighted relative to the nominal values in the MC simulation, except for the fourth energy bin ($E_\nu = 1.0 - 1.5$ GeV) which is fixed to unity for the normalization, and another set of parameters are prepared for the relative normalization of each detector.

The χ^2 functions are separately defined for each detector and then summed to build a combined χ^2 function as

$$\chi_{\mathrm{ND}}^2 = \chi_{\mathrm{1KT}}^2 + \chi_{\mathrm{SF}}^2 + \chi_{\mathrm{SB}}^2. \qquad (3.3)$$

Finally, a set of the fitting parameters $(f_i^\phi, R_{\mathrm{nQE}} : \boldsymbol{f})$ is found by minimizing the χ^2 function. The best fit values, their error sizes and the correlations between them are used as inputs to the oscillation analysis, as described in Chapter 7. The following subsections will describe the event selection, systematic error concerns, and the definition of the χ^2 for each subdetector. Lastly, the results of the fit will be given as well as a check against previous fits.

3.1 The 1 Kiloton Spectrum Measurement

3.1.1 Event Selection

Events in the 1KT spectrum analysis must satisfy certain criteria before being used. The main goal is to select a QE enriched data set. Using the
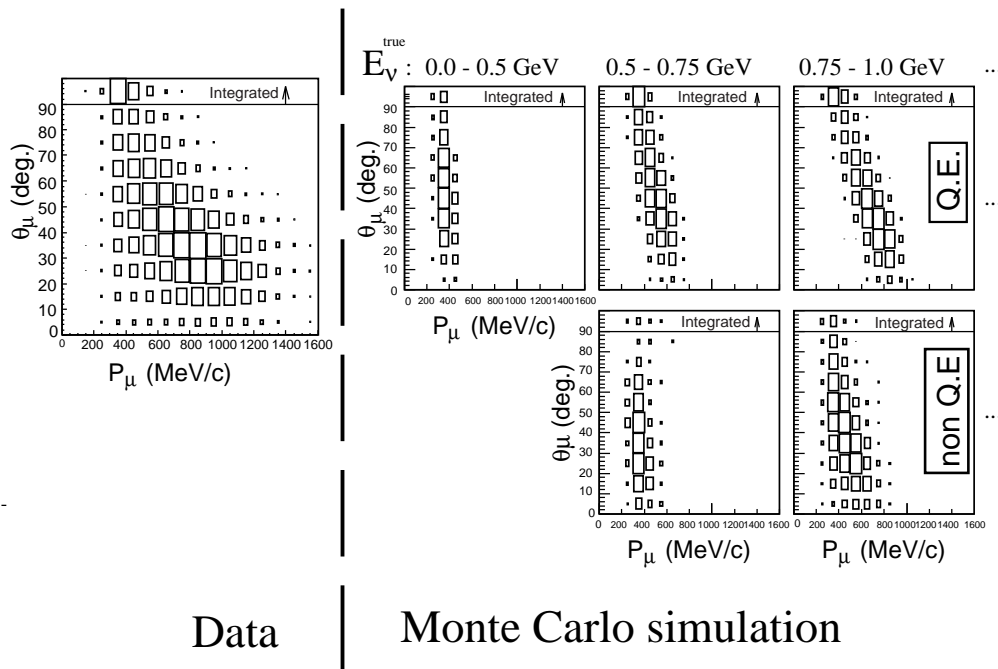
Figure 3.1: Schematic view of the binning of the data and Monte Carlo events for the spectrum fit. The left plot shows the p_μ vs. θ_μ distribution for FC1Rμ events in the 1KT data used for the spectrum fit. The right plots show those for the MC sample separately prepared for each true neutrino energy bin with either QE or non-QE interactions.
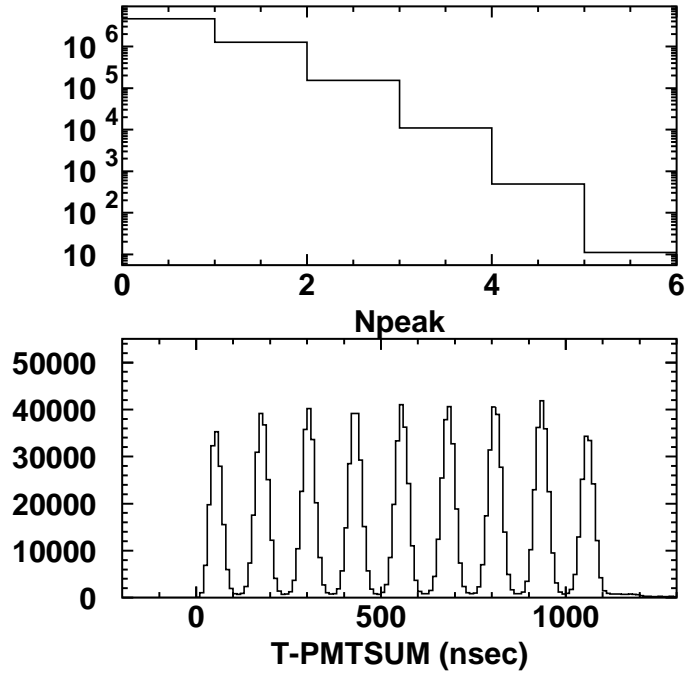
Figure 3.2: The upper figure shows the number of neutrino interactions in a spill. Zero peaks is defined as the left-most bin in the histogram. The lower figure shows the time distribution of peaks of PMTSUM signal which are recorded by FADC. The beam's nine micro bunch structure can be seen clearly.

PMTSUM mentioned in Section 2.3.1, events with a single interaction are selected. A single interaction is defined as a single peak from PMTSUM after a threshold of 1000 p.e. has been applied. The number of peaks from the PMTSUM and timing information is shown in Figure 3.2. This rejects low energy events, such as decay electrons from stopped muons in the detector. Events that have been selected so far then have their vertex position checked to see if it is in the fiducial volume (FV). The 1KT FV is defined as a cylinder 2 m in diameter around the beam along the z (or beam) axis. In z, the length of the cylinder is 2 m starting 2 m upstream and going to the center of the 1KT, or -2 m$<z<$0 m. The 1KT FV is 25 tons. Those events that are within the FV are potentially selected for the analysis.

In addition to the selection criteria given, additional selections are used

Table 3.2: The summary table for the number of observed events in the FC1Rμ sample, the efficiency and the purity of the CCQE events estimated with the MC simulation.

	# of events	CCQE efficiency (%)	CCQE purity (%)
FC1Rμ	52110	53.7	57.9

to enrich the sample. The first is that the event is fully contained (FC) as explained in Section 2.3.1. Events also must have a single reconstructed Cherenkov ring (1R) and that ring must be considered muon-like (μ-like). Finally, to ensure the quality of event reconstruction, the reconstructed muon momentum must be greater than 200 MeV/c. After these events are selected, the fraction of CCQE events is about 60%. See Table 3.2 for the data summary and CCQE fraction. Figures 3.3, 3.4, and 3.5 show the ring number likelihood, particle identification likelihood, and the fully contained versus partially contained event (FC/PC) separation, respectively, used in the single ring fully contained μ-like (1RFCμ) event selection.

3.1.2 Systematic Error Evaluation

The systematic errors that are introduced in the fit come mainly from the event selection. Those errors are from the ring counting likelihood, the particle identification likelihood, the FC/PC separation, the event vertex and direction reconstruction, fiducial volume, and the energy scale. The other systematic errors are from the detector calibration and the axial mass (M_A), which is used for modeling neutrino interactions.

For each systematic effect evaluated, a 1σ difference is determined using a basic χ^2,

$$\chi^2 = \sum_{i=0}^{n} \frac{\left(N_i^{data} - N_i^{MC}\right)^2}{N_i^{data} + N_i^{MC}} \tag{3.4}$$

where N_i^{data} and N_i^{MC} are, respectively, the number of data and weighted MC events in the ith bin. The 1σ limit is determined from the χ^2 difference between the default MC and MC that has been changed to measure the particular systematic error being measured. Finally, this limit is used to calculate the effect of each systematic error on the (p_μ, θ_μ) distribution used in the analysis.

The particle identification is estimated by calculating a likelihood L, with $L \leq 0$ for electron-like events and $L > 0$ for μ-like events. The $\pm 1\sigma$ limit is
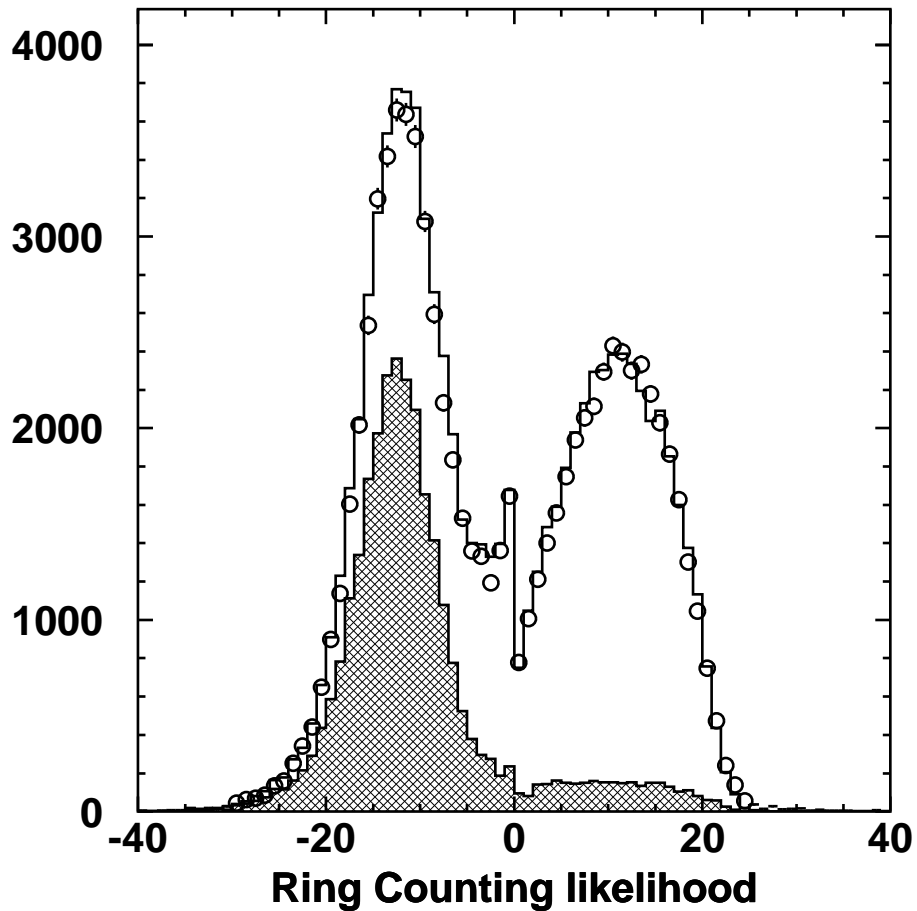
Figure 3.3: The distribution of ring counting likelihood for the 1KT. Those events that have a likelihood less than or equal to 0.0 are considered to have one ring; those above 0.0 are considered to be multi-ring. In this plot, data are the circles and the MC simulation is the histogram. The hatched histogram shows the CCQE component. Only statistical errors are shown for data.
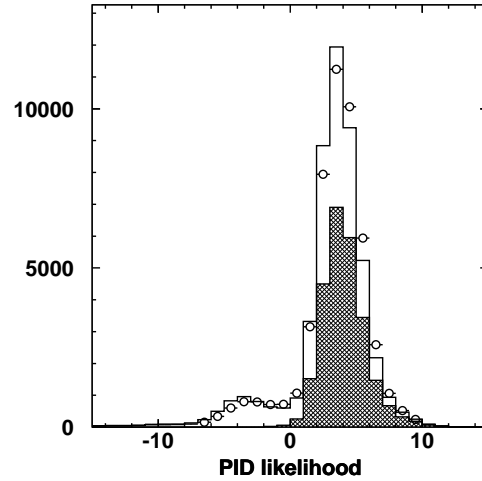
Figure 3.4: The distribution of particle identification likelihood for the 1KT. The events with a likelihood greater than 0.0 are μ-like while those less than or equal to 0.0 are e-like. Data are the circles and the MC simulation is the histogram with the CCQE component shown as the hatched area.
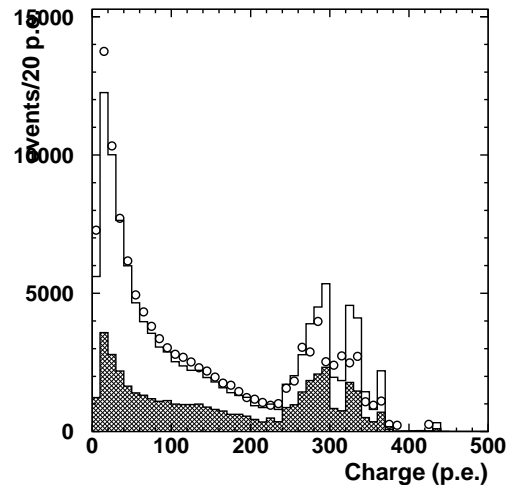
Figure 3.5: The largest charge in a PMT for a 1KT event. Events that have a PMT with charge less than 200 p.e. are considered FC events. The rest are PC events. Data are the circles and the MC simulation is the histogram, with the CCQE component shown as the hatched area.

evaluated by shifting the value of L in the MC. It is found to be $\delta L = \pm 0.25$, corresponding to a systematic error of about 1%.

The number of rings is also estimated from a different likelihood L, with $L \leq 0$ for single ring events and $L > 0$ for multi-rings events. This systematic depends on θ_μ, the particle direction with respect to the beam, and it is estimated for three different regions: $\theta_\mu < 50°$, $50° \leq \theta_\mu < 80°$ and $\theta_\mu \geq 80°$. Using the likelihood distribution, the ring counting systematic error is estimated to be 1%, 2% and 5%, respectively.

The selection of fully-contained versus partially-contained events is made by using the maximum value of photoelectrons seen by a PMT in the detector. The error is estimated to be 10 p.e., corresponding to a 5% systematic error.

The energy scale systematic error is determined by changing p_μ $\pm 5\%$ in the MC. For each analysis bin, the ratio of events is taken for the $\pm 5\%$ shifted MC against the unshifted MC. The average difference for each bin is the energy scale systematic error.

For the vertex fitting bias systematic error, the fitted vertex of the particle is shifted by 0 cm, ± 5 cm, ± 10 cm, and ± 20 cm along its direction. A 1σ difference is found between the unshifted vertex and the vertex shifted +5 cm. The angular fit systematic error shifted the fitted vertex transversely to the particle direction. The transverse shifts of the vertex are the same magnitudes as the vertex fitting bias systematic error above with the same result. The FV systematic error shifts the FV's radius and length ± 5 cm for a 1σ effect.

The angular resolution systematic error is calculated by smearing the fitted angle by 1°, 2°, and 3°. As with the fitting bias systematic error, the difference between the χ^2 of the smeared MC and the unsmeared MC is calculated. The 1σ shift is taken as an average of the 1° and 3° smearings.

In QE scattering, the value of the axial vector mass, M_A, in the dipole formula affects the Q^2 dependence of the cross-section, thus it affects the (p_μ, θ_μ) distribution used in the analysis. The systematic effect on the 2-dimensional distribution is calculated for a central value of 1.1 GeV/c^2 varied by 10% [40].

Finally, we estimated a systematic error coming from change in the detector calibrations and event reconstructions. We compared the 2D distribution of Data/MC ratio between two sets of data and MC analyzed by different versions of the event reconstruction procedure and calibration.

3.1.3   1KT χ^2 Definition

Both data and MC are binned into 2-dimensional distributions of muon momentum versus the scattered angle. The momentum is divided into 16 100

MeV/c bins from 0 - 1600 MeV/c. The scattering angle (θ_μ) is divided into 10 bins where the first nine are in increments of 10 degrees from $0° - 90°$ and the final bin contains all events that are greater than $90°$. The data are all placed in the same 2-dimensional histogram while the MC are separately filled into histograms according to the parent neutrino energy and the interaction mode. The parent neutrino energy is divided into eight energy bins as given by Table 3.1. The two interaction modes are QE, which include CCQE and NC elastic events, and non-QE, which includes all other interaction modes. Figure 3.1 shows the schematic view of the binning.

The neutrino spectrum is derived by comparing the observed data and weighted sum of MC expectations using a χ^2 test. The χ^2 is defined as:

$$\chi^2_{KT} = \sum_{m,n} \frac{\left(N^{obs}_{m,n} - N^{MC}_{m,n}\right)^2}{\sigma^2_{m,n}} + \frac{(1 - \epsilon)^2}{\sigma^2_{energy}} \tag{3.5}$$

where $N^{obs}_{m,n}$ is the number of observed events for data for (m, n)-th bin, $N^{\mathrm{MC}}_{m,n}$ is the number of MC events given in equation 3.2, ϵ is the fitting parameter for energy scale, where $\epsilon = 1$ is the nominal value that scales the muon momentum, $\sigma_{m,n}$ is the error including statistical and systematic errors, and σ_{energy} is the estimated uncertainty of the energy scale, $^{+3}_{-4}\%$.

3.2 SciFi and LG Spectrum Measurement

3.2.1 Data Selection and Systematic Uncertainties

The SciFi data can be divided into a total of nine categories based on event type and when the data was collected. Event types consist of one-track, two-track QE, and two-track non-QE events. The data collection periods are divided into K2K-I SciFi events, K2K-I LG events, and K2K-IIa SciFi events. SciFi events are defined as events whose reconstructed vertex is in the SciFi fiducial volume and the muon stops at least two layers into the MRD; LG events are events whose vertex is reconstructed in the SciFi fiducial volume and stop in the LG calorimeter. The FV is defined to be a rectangle 1.1m to each side of the detector's center in x and y, and going 17 layers deep from the front of the detector while the upstream hodoscope system also must not have been hit before the event was seen in SciFi. This gives a total fiducial mass of 5.59±0.07 tons.

Single track events are defined as having hits along one reconstructed track or two fitted tracks where the second track has hits in only two layers. The

LG sample has an additional requirement that the z vertex in the LG must be less than 115.0 cm; this removes events that are being reflected or rescattered backward through the SciFi detector and causes the vertex to be badly reconstructed. The two track QE selection and non-QE have all but one of their selection criteria the same. In both cases, there needs to be two tracks reconstructed where the second track has more than two layers with a hit. The definition of a QE event in the SciFi is one where the difference between the measured and expected angle of the second track, $\Delta\theta_p$, is less than 25°, assuming the second track is a proton. An example of a SciFi QE event is given in Figure 3.6. Non-QE events are defined with $\Delta\theta_p >25°$. The QE/non-QE selection is shown in Figure 3.7 for the SciFi two-track events. Again, the LG QE data sample has additional selection criteria. Depending on whether the second track is contained, there is a cut with the event's angle with respect to the beam of 30 or 40 degrees.

To calculate the momentum of the muon passing through the detector, the muon's energy is calculated by adding the energy deposited in the SciFi, LG (SciBar for K2K-IIa), and MRD detectors. From there, the neutrino energy is reconstructed assuming the event is CCQE.

The SciFi has a series of systematic uncertainty terms, all but two that are unique to it. The two that are common to the other detectors are the energy spectrum and R_{nQE} parameters. Three systematic errors relate to uncertainties in an event's reconstructed energy. The muon energy scale has an uncertain of $\pm2.7\%$ applied to the measured muon momentum. For events in K2K-Ib, there is an uncertainty of $\pm5\%$ of muon energy loss from going though the LG, which is considered an uncertainty in the LG density. The final error related to energy applies to energy reconstructed from visible energy clusters in the LG for events that stop in the LG. Two other systematic parameters relate to the migration between one track and two track events, taking into account the tracking efficiency for short second tracks, and a migration between two track QE and non-QE samples which can be a manifestation of proton rescattering as it leaves the nucleus after a QE interaction. There is a 5% uncertainty attached to the track migration and 2.5% to the rescattering.

3.2.2 SciFi Spectrum Fit Criteria and χ^2 Definition

For the neutrino analysis, data and MC events are chosen based on the bins in the $(p_\mu,\ \theta_\mu)$ distribution. Each data sample was divided into seven angle bins from 0 to 60 degrees in 10 degree increments and into eight muon momentum bins using the same binning as Table 3.1.

There are 286 bins used in the SciFi spectrum fit, as well as six systematic

Run 2279 Spill 18568 TRGID 1
100 1 24 14 21 23 0
Nvtx 0

Top View
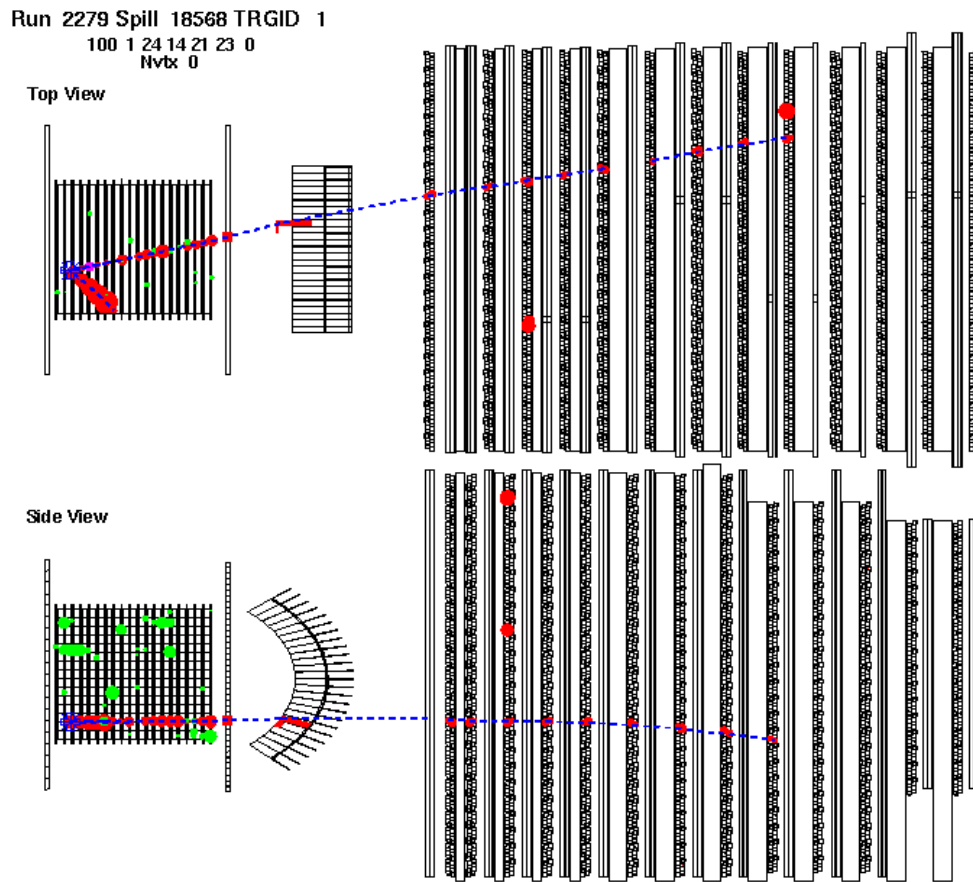
Side View

Figure 3.6: Example of a SciFi CCQE candidate event from K2K-Ib (top and side views). The three detectors are, from left to right, SciFi, LG, and MRD.
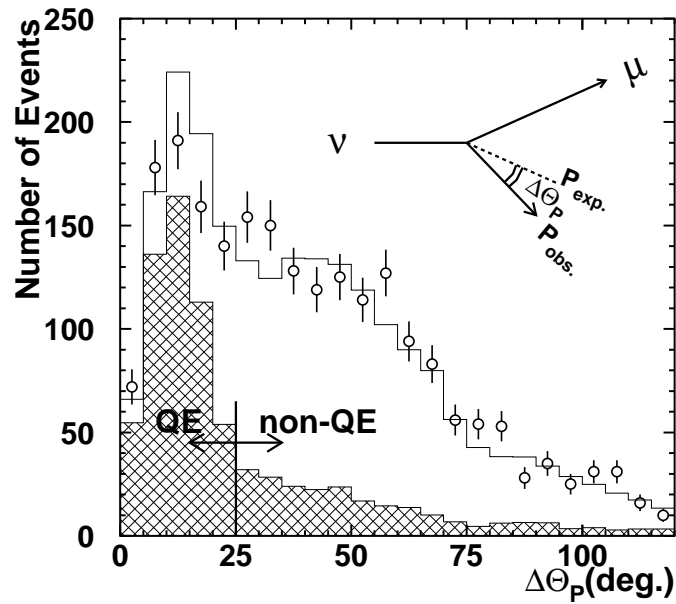
Figure 3.7: Example of the distribution of $\Delta\theta_P$, the difference between the observed and predicted (assuming QE interaction) angle of the second track. This distribution is for SciFi two-track events in K2K-Ib. The data (circles) and the MC(histogram) are shown, with the shaded region showing the QE fraction of the MC.

errors including the normalization. The χ^2 minimizes the negative logarithm of the Poisson likelihood for the binned data, plus χ^2 terms for the systematic pulls not including the normalization. The χ^2 is defined as:

$$
\begin{aligned}
\chi^2 &= -2\ln\lambda(\theta) \\
&= 2\sum_{m,n}[N_{m,n}^{\mathrm{MC}}(\theta) - N_{m,n}^{\mathrm{obs}} + N_{m,n}^{\mathrm{obs}}\ln(N_{m,n}^{\mathrm{obs}}/N_{m,n}^{\mathrm{MC}}(\theta))] \\
&+ \chi^2_{\mathrm{Escale}} + \chi^2_{\mathrm{LG\ density}} + \chi^2_{\mathrm{LG\ cluster\ energy}} \\
&+ \chi^2_{\mathrm{2nd\ track\ eff}} + \chi^2_{\mathrm{Rescattering}}
\end{aligned}
\tag{3.6}
$$

where $N_{m,n}^{obs}$ and $N_{m,n}^{MC}(\theta)$ are the observed and predicted values in the (m,n)-th bin for some values of the parameters θ. This is the simplified version given in Reference [13] with the χ^2 terms arising from the systematic errors.

3.3 The SciBar Spectrum Measurement

3.3.1 Event Selection and Systematic Errors

The SciBar, like the SciFi, divides its events into three classes: one-track, two-track QE, and two-track non-QE. All events used in the spectrum analysis have a vertex reconstructed in SciBar's fiducial volume, which is defined as a 2.6 m×2.6 m rectangle in x and y around the beam center, and between the 2nd and 53rd layers in the beam direction z. This gives a total fiducial mass of 9.38 tons. Single track events are events that have only one reconstructed track in a SciBar event whereas the two-track events require two. Similar to the SciFi detector, QE events have the additional requirement that the difference between the expected and measured proton angle, $\Delta\theta_p$, be less than or equal to 25° and non-QE events must have an angular difference greater than 25°. Figure 3.8 shows an example of a QE event. All events must have either a matched track or hits in the MRD to be used in the analysis. The energy deposited in the SciBar, EC, and MRD from a SciBar event is used to calculate the momentum of the muon passing through the detector.

The systematic error terms that the SciBar uses are the one-track/two-track, the QE/non-QE, and the momentum scale. The momentum scale error was measured to be 2.7%, which is the same as SciFi. The one-track/two-track systematic error was determined to be 5.9% while the QE/non-QE systematic error is 5.8%. The two previous systematic errors were found to have a 1.7% correlation between them. This is put into a covariance matrix given below.
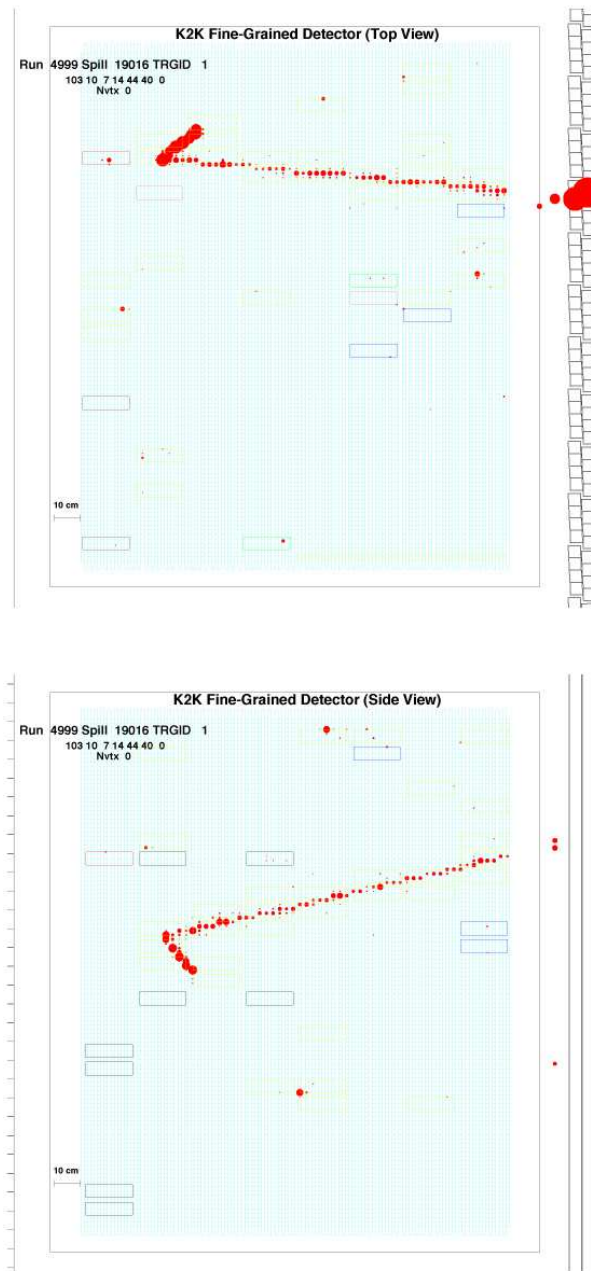
Figure 3.8: Top (top) and side (bottom) view of a CCQE candidate in SciBar. The track continues into the MRD, allowing the event to be used in the neutrino analysis.

3.3.2   SciBar Spectrum Fit Criteria and χ^2 Definition

The (p_μ, θ_μ) distributions are divided into 40 bins from 0 to 4000 MeV/c and 45 bins from 0 to 90 degrees, respectively. In the neutrino analysis, the bins chosen for the spectrum fit have at least five data events in each bin in the (p_μ, θ_μ) distributions.

The spectrum fit χ^2 for the SciBar detector has a Poisson convoluted with a Gaussian distribution with some systematic terms incorporated. Simplistically, it is defined as the addition of the χ^2 of the distribution with the χ^2 of the systematic errors

$$\chi^2_{SB} = \chi^2_{dist} + \chi^2_{syst}. \tag{3.7}$$

The χ^2 for the distribution, χ^2_{dist}, is defined as the logarithm of likelihood ratios defined as

$$\chi^2_{dist} = -2\sum_{m,n} \ln \frac{\mathcal{L}\left(N^{obs}_{m,n}; N^{MC}_{m,n}; \sigma\right)}{\mathcal{L}\left(N^{obs}_{m,n}; N^{obs}_{m,n}; \sigma\right)}, \tag{3.8}$$

where

$$\mathcal{L}\left(N^{obs}_{m,n}; N^{MC}_{m,n}; \sigma\right) \equiv \prod_{m,n} \int_0^\infty \frac{1}{\sqrt{2\pi}\sigma_{m,n}} \exp\left[-\frac{\left(x - N^{MC}_{m,n}\right)^2}{2\sigma^2_{m,n}}\right] \cdot \frac{x^{N^{obs}_{m,n}} e^{-x}}{N^{obs}_{m,n}!} dx.$$

For the systematic terms, χ^2_{syst} is calculated with constraint parameters, including their correlation:

$$\chi^2_{\text{syst}} = (\boldsymbol{P_{syst}} - \boldsymbol{P_0})^t \boldsymbol{V}^{-1}(\boldsymbol{P_{syst}} - \boldsymbol{P_0}) \tag{3.9}$$

where $\boldsymbol{P_{syst}}$ is the set of systematic parameters mentioned in the previous section, $\boldsymbol{P_0}$ are their nominal values, which is set to unity, and $\boldsymbol{V}$ is a covariance matrix. A total of three systematic parameters, $P^{\text{SB}}_{\text{p-scale}}$, $P^{\text{SB}}_{\text{2trk/1trk}}$, and $P^{\text{SB}}_{\text{nonQE/QE}}$ are included in $\boldsymbol{P_{syst}}$; they are defined as relative weighting factors to the nominal MC expectation. The uncertainties and correlation among the parameters are put in the covariance matrix $\mathbf{V}$, which is defined as

$$\mathbf{V} \equiv \begin{array}{c} \\ P^{\text{SB}}_{\text{p-scale}} \\ P^{\text{SB}}_{\text{2trk/1trk}} \\ P^{\text{SB}}_{\text{nonQE/QE}} \end{array} \begin{array}{ccc} P^{\text{SB}}_{\text{p-scale}} & P^{\text{SB}}_{\text{2trk/1trk}} & P^{\text{SB}}_{\text{nonQE/QE}} \\ \left(\begin{array}{ccc} +(0.027)^2 & 0 & 0 \\ 0 & +(0.059)^2 & +(0.017)^2 \\ 0 & +(0.017)^2 & +(0.058)^2 \end{array} \right) \end{array}. \tag{3.10}$$

The dominant error sources are the track finding systematic error $P^{\text{SB}}_{\text{2trk/1trk}}$ and the nuclear rescattering parameter $P^{\text{SB}}_{\text{nonQE/QE}}$.

3.4 Combined Near Detector Spectrum Measurement

The neutrino energy spectrum measurement is made for the 1KT, the SciFi, and the SciBar as well as the ND as a whole. The combined fit is necessary since none of the individual detectors is sensitive to the entire neutrino energy range. The 1KT is sensitive to low energy events that are above the Cherenkov threshold, but not to high energy events because of its FC requirement. The SciFi and SciBar are sensitive to the high energy region, but not to events with an energy below 400 MeV/c. A combined fit of the neutrino energy spectrum with all of these detectors allows for a measurement over the full energy range without the wekanesses in any one individual detector.

3.4.1 Results of the combined fit

The minimum χ^2 point in the multi-parameter space is found by changing the spectrum shape parameters, R_{nQE}, and the systematic parameters, fitting with the MINUIT program library [49]. The central values and the errors of the fitting parameters are summarized in Table 3.3. The result of the spectrum measurement is shown in Fig. 3.9 with the prediction of the beam MC simulation.

The results of the measurements with individual detector data are also shown in Table 3.3. In the fit with only 1KT data, the energy spectrum parameters are fixed to their default values for the high energy region, $E_\nu > 2$ GeV, where there is little or no acceptance because of the FC criteria. Also because of little to no acceptance, the low energy region is fixed for SciFi and SciBar. This is because the momentum threshold in SciFi is 675 MeV/c (400 MeV/c, 550 MeV/c) for K2K-I (K2K-I with LG, K2K-IIa) and 450 MeV/c in SciBar. All the fitting parameters are in good agreement, within their errors, with each other except for R_{nQE}.

The p_μ, θ_μ and q^2_{rec} distributions for the 1KT, SciFi and SciBar samples are shown in Figures 3.10–3.12. In these figures, the reconstructed Q^2 distributions (q^2_{rec}) are constructed by assuming that the interaction was CCQE and using the reconstructed energy under this assumption. The expected distributions of the MC simulation with the best-fit parameters are also shown.

The discrepancy in R_{nQE} is treated as a systematic error. However, the value of R_{nQE} is strongly correlated with the E_ν spectrum as well as the other systematic parameters such as $P^{SB}_{nonQE/QE}$. In order to evaluate R_{nQE} with each detector data set under identical fitting conditions, a second fit is performed.

In the second fit, the E_ν spectrum and the systematic parameters, except for the overall normalization, are fixed at the best fit values obtained with all the three detectors. The best fit value of R_{nQE} for each detector in the second fit is (1KT, SciFi, SciBar) = (0.76, 0.99, 1.06), respectively, while the fit result with three detectors is 0.96. Therefore, an additional error of 0.20 is assigned to R_{nQE} in order to account for the discrepancy.

The errors of the measurement are provided in the form of an error matrix. Correlations between the parameters are taken into account in the oscillation analysis with this matrix. The elements of the error matrix are shown in Table 3.4, where the elements in are the correlations between two parameters from the spectrum measurement.

3.4.2 Changes in the combined fit from the previous meaurement

The ND spectrum analysis had been measured for previous K2K results [50], the most recent before this analysis in 2004. Between 2004 and this analysis, two changes had been made. Those were including events with $\theta_\mu <$ 20° and excluding CC coherent pion (CCcohπ) events. The reason for the θ_μ selection in 2004 was because of a discrepancy between data and MC in low q^2, as in Figure 3.13. A supression in the data that was noticed for events in the forward direction. Because of this, it was found [51] that the discrepancy could be explained by having no CCcohπ interactions in the MC sample from a two track non-QE event sample analysis. For the result in the previous subsection, all of θ_μ was allowed for the analysis while the MC sample did not include CCcohπ events.

A comparison of the 2004 analysis and the current analysis was made in the 1KT to see the effects of the changed analysis criteria. The second and third columns of Table 3.5 report the best fit values of the 2004 and 2005 analyses. It should be noted that this comparison was done before the decision to fix bins with $E_\nu >$2 GeV in the 1KT. There is a large discrepancy in the lowest energy bin ($E_\nu < 0.5$ GeV) and a smaller one in R_{nQE}.

As an initial check, the CCcohπ events were put back into the MC sample. The fourth column of Table 3.5 shows that the CCcohπ event sample makes the fit worse for both R_{nQE} and $E_\nu < 0.5$ GeV. Thus, the CCcohπ sample is not driving the discrepancy. The 20° cut on θ_μ did have a small effect on increasing R_{nQE} as shown in the final column of Table 3.5. This slight increase is from the non-QE events in the low θ_μ region now included in the analysis, though not enough to be entirely inconsistent with the main result.

Table 3.3: Results of the spectrum measurement. The best fit value of each parameter is listed for the fits with all the detectors' data, with the 1KT data, with the SciFi data, and with the SciBar data, respectively. The reduced χ^2 ($\chi^2_{\text{total}}/\text{DOF}$) and the averaged χ^2 of each detector ($\chi^2/\text{N}_{\text{bin}}$) are also shown.

Parameter	Combined	1KT only	SciFi only	SciBar only
f_1^{ϕ}	$\mathbf{1.657 \pm 0.437}$	2.372 ± 0.383	$\equiv 1$	$\equiv 1$
f_2^{ϕ}	$\mathbf{1.107 \pm 0.075}$	1.169 ± 0.072	0.882 ± 0.317	1.166 ± 0.251
f_3^{ϕ}	$\mathbf{1.154 \pm 0.061}$	1.061 ± 0.065	1.157 ± 0.201	1.145 ± 0.134
f_4^{ϕ}	$\mathbf{\equiv 1}$	$\equiv 1$	$\equiv 1$	$\equiv 1$
f_5^{ϕ}	$\mathbf{0.911 \pm 0.044}$	0.709 ± 0.151	0.980 ± 0.107	0.963 ± 0.070
f_6^{ϕ}	$\mathbf{1.069 \pm 0.059}$	$\equiv 1$	1.188 ± 0.096	0.985 ± 0.086
f_7^{ϕ}	$\mathbf{1.152 \pm 0.142}$	$\equiv 1$	1.062 ± 0.230	1.291 ± 0.283
f_8^{ϕ}	$\mathbf{1.260 \pm 0.184}$	$\equiv 1$	1.323 ± 0.203	1.606 ± 0.749
R_{nQE}	$\mathbf{0.964 \pm 0.035}$	0.589 ± 0.071	1.069 ± 0.060	1.194 ± 0.092
$\text{P}^{\text{1kt}}_{\text{Norm}}$	$\mathbf{0.948 \pm 0.024}$	1.172 ± 0.046	—	—
$\text{P}^{\text{1kt}}_{\text{energy}}$	$\mathbf{0.984 \pm 0.004}$	0.993 ± 0.007	—	—
$\text{P}^{\text{SF}}_{\text{Norm}}$	$\mathbf{1.009 \pm 0.029}$	—	0.925 ± 0.058	—
$\text{P}^{\text{SF}}_{\text{Escale}}$	$\mathbf{0.980 \pm 0.006}$	—	0.980 ± 0.007	—
$\text{P}^{\text{SF}}_{\text{LG-density}}$	$\mathbf{0.929 \pm 0.012}$	—	0.928 ± 0.012	—
$\text{P}^{\text{SF}}_{\text{LG-cluster}}$ [GeV]	$\mathbf{-0.001 \pm 0.002}$	—	-0.002 ± 0.003	—
$\text{P}^{\text{SF}}_{\text{2nd-track-eff}}$	$\mathbf{0.959 \pm 0.014}$	—	0.932 ± 0.017	—
$\text{P}^{\text{SF}}_{\text{rescattering}}$	$\mathbf{1.048 \pm 0.055}$	—	0.993 ± 0.062	—
$\text{P}^{\text{SB}}_{\text{Norm}}$	$\mathbf{0.998 \pm 0.010}$	—	—	1.003 ± 0.011
$\text{P}^{\text{SB}}_{\text{p-scale}}$	$\mathbf{0.976 \pm 0.004}$	—	—	0.972 ± 0.004
$\text{P}^{\text{SB}}_{\text{2trk/1trk}}$	$\mathbf{0.953 \pm 0.021}$	—	—	0.961 ± 0.023
$\text{P}^{\text{SB}}_{\text{non-QE/QE}}$	$\mathbf{1.066 \pm 0.032}$	—	—	0.978 ± 0.040
$\chi^2_{\text{total}}/\text{DOF}$	$\mathbf{687.2 \ / \ 585}$	$46.8 \ / \ 73$	$328.7 \ / \ 273$	$253.3 \ / \ 228$
$\chi^2_{\text{1kt}}/\text{N}_{\text{bin}}$	$\mathbf{85.4 \ / \ 80}$	$47.7 \ / \ 80$	—	—
$\chi^2_{\text{SciFi}}/\text{N}_{\text{bin}}$	$\mathbf{335.6 \ / \ 286}$	—	$328.7 \ / \ 286$	—
$\chi^2_{\text{SciBar}}/\text{N}_{\text{bin}}$	$\mathbf{266.1 \ / \ 239}$	—	—	$253.3 \ / \ 239$
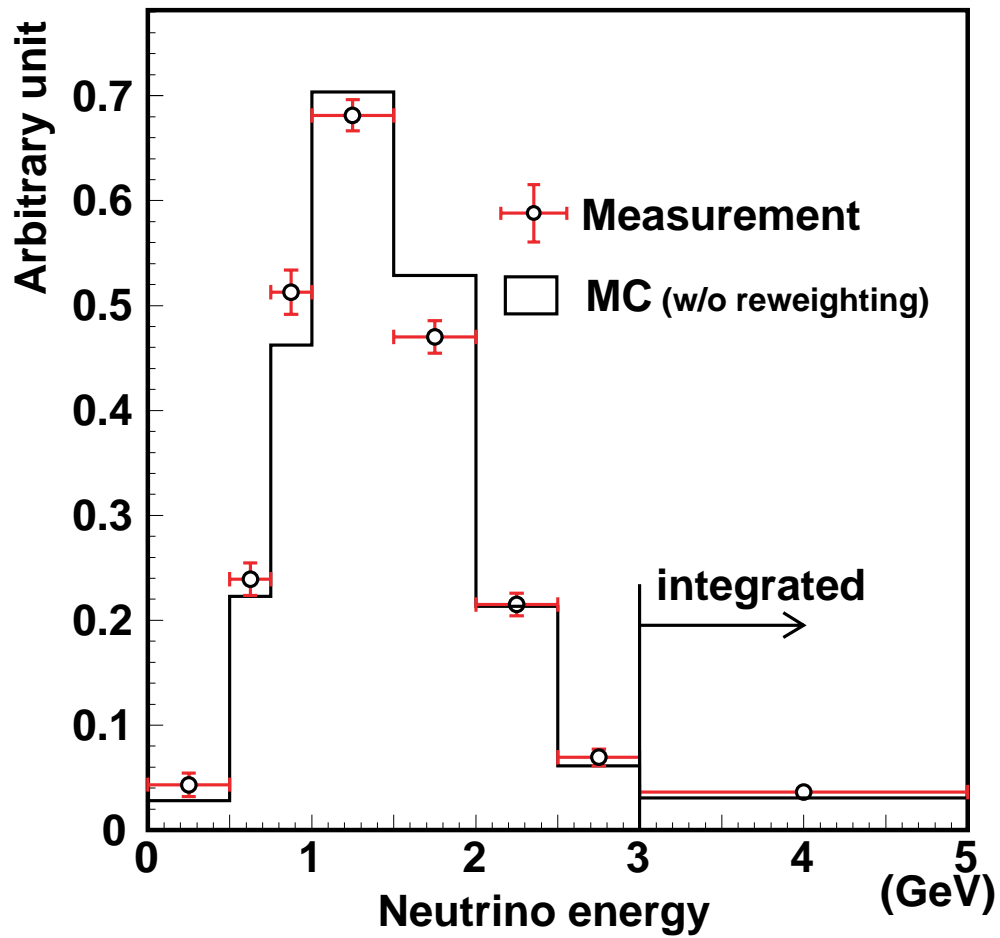
Figure 3.9: The neutrino energy spectrum measured at the near site, assuming CCQE. The expectation with the MC simulation without reweighting is also shown.

Table 3.4: The error matrix for f_i and R_{nQE}. The sign and square root of each error matrix element (sign $[M_{ij}] \cdot \sqrt{|M_{ij}|}$) is shown here in units of %.

	f_1	f_2	f_3	f_5	f_6	f_7	f_8	R_{nQE}
f_1	43.86	-3.16	7.28	-2.21	-0.76	-3.48	0.81	-8.62
f_2	-3.16	7.51	1.97	1.90	0.62	1.29	2.43	-5.68
f_3	7.28	1.97	6.00	3.38	1.63	3.44	1.71	-2.99
f_5	-2.21	1.90	3.38	4.04	-1.86	4.53	2.20	1.65
f_6	-0.76	0.62	1.63	-1.86	5.28	-5.85	5.11	0.94
f_7	-3.48	1.29	3.44	4.53	-5.85	13.67	-10.14	4.09
f_8	0.81	2.43	1.71	2.20	5.11	-10.14	18.35	-11.77
R_{nQE}	-8.62	-5.68	-2.99	1.65	0.94	4.09	-11.77	20.30
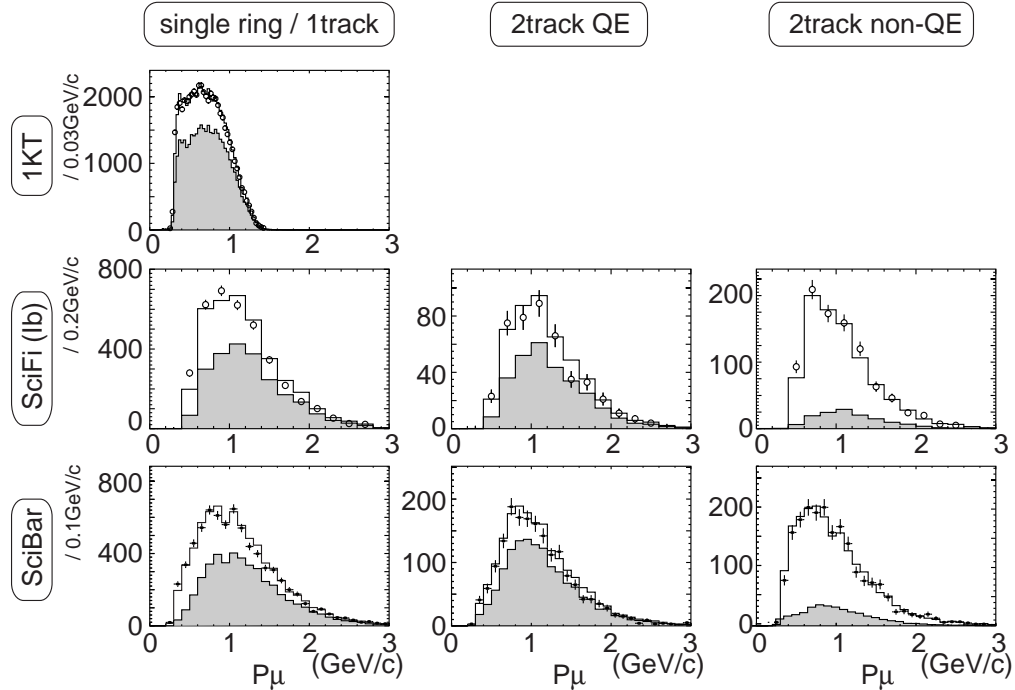
Figure 3.10: The p_μ distributions for each event sample of all near detectors with the MC simulation after fitting, given by open histograms. The hatched areas are the CCQE components in the MC distributions.
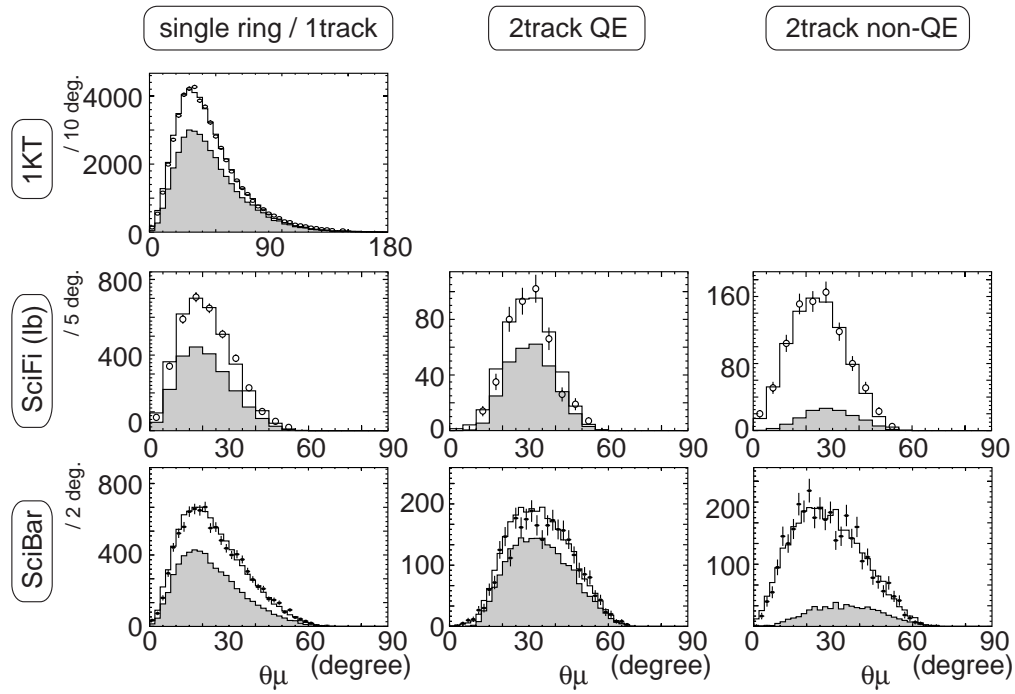
Figure 3.11: The θ_μ distributions for each event sample of all near detectors with the MC simulation after fitting, given by open histograms. The hatched areas are the CCQE components in the MC distributions.
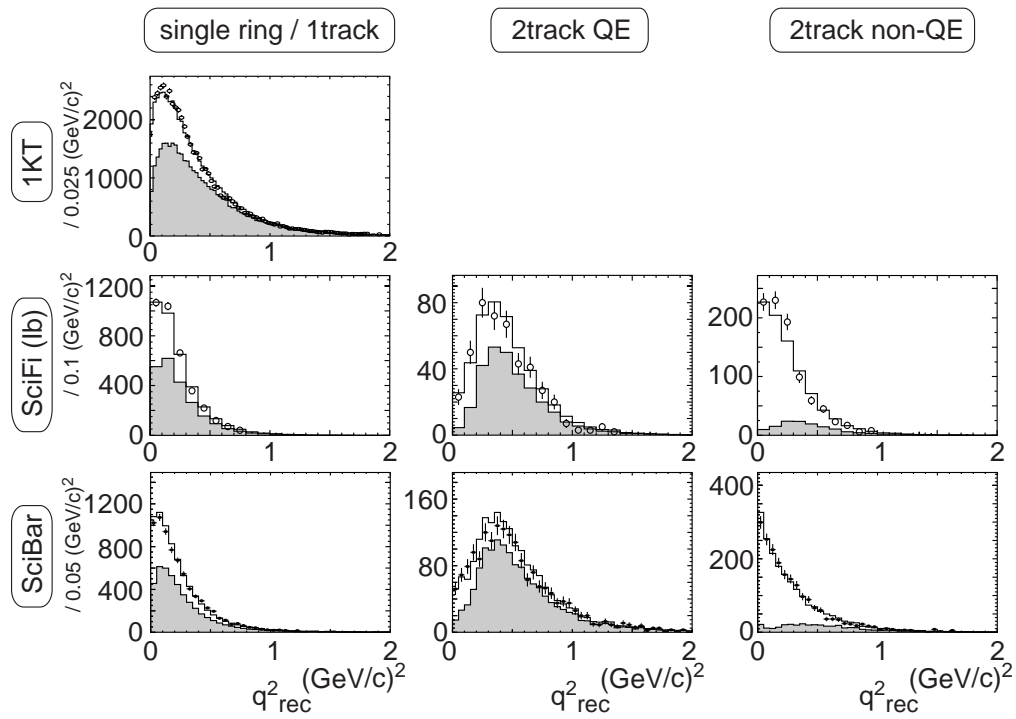
Figure 3.12: The q^2_{rec} distributions for each event sample of all near detectors with the MC simulation after fitting, given by open histograms. The hatched areas are the CCQE components in the MC distributions.
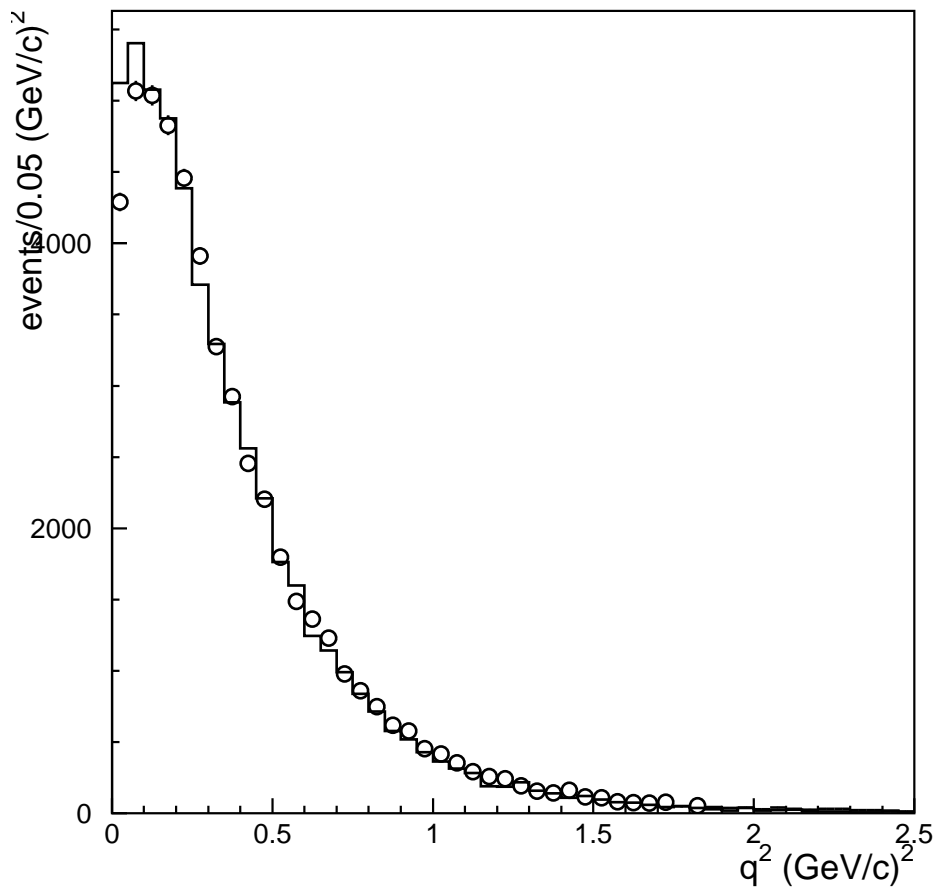
Figure 3.13: 1KT reconstructed q^2 distribution with charged current coherent pion interactions in the MC (histogram). The data are the circles. Note the discrepancy between data and MC with $q^2 < 0.2 (GeV/c)^2$.

66
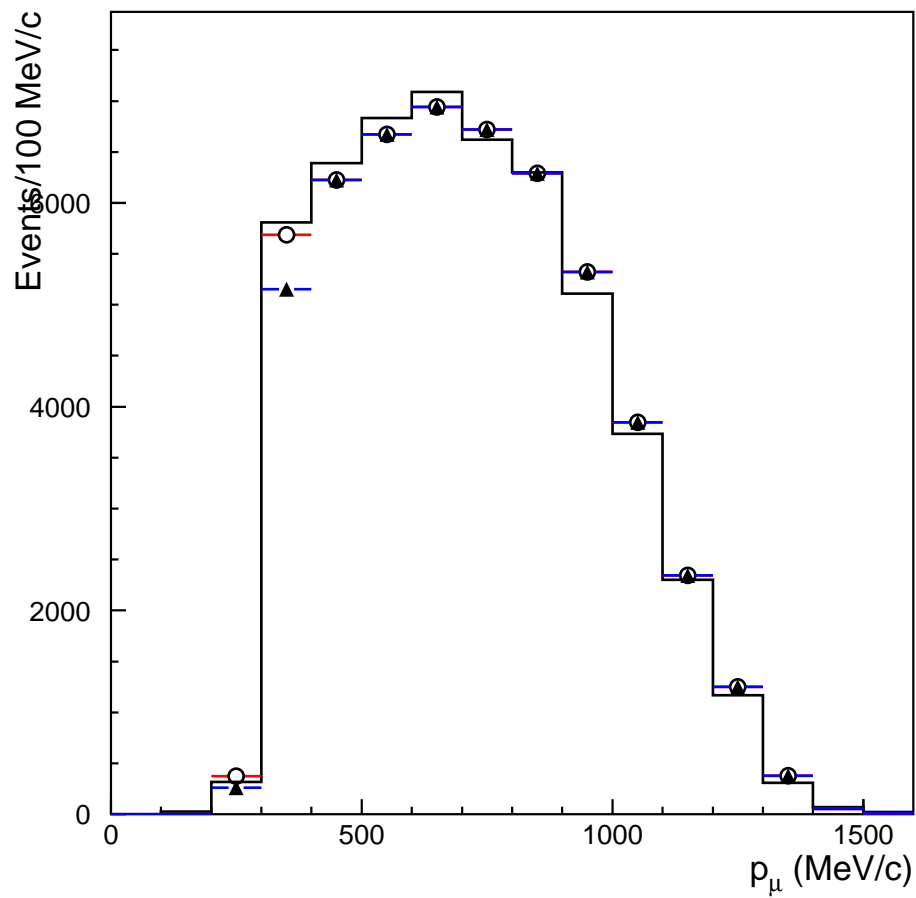
Figure 3.14: 1KT FC 1Rμ events for both data and MC. The MC is divided into events with (triangle) and without (circle) the FADC selection. The data is the histogram.

Table 3.5: Results of the spectrum measurement for the 1KT. The fit results from 2004 and 2005 are shown, with the 2005 results of including CCcohπ events in the MC and applying $\theta_\mu > 20°$ for data and MC, respectively.

Parameter	2004 Result	2005 Result	2005 w/ CCcohπ	2005, no θ_μ
f_1^ϕ	1.413±0.416	2.311±0.373	2.730±0.359	2.348±0.455
f_2^ϕ	1.136±0.103	1.178±0.071	1.257±0.067	1.116±0.089
f_3^ϕ	1.098±0.080	1.066±0.065	1.071±0.061	1.057±0.079
f_4^ϕ	≡1	≡1	≡1	≡1
f_5^ϕ	0.856±0.075	0.881±0.087	0.913±0.086	0.875±0.091
f_6^ϕ	0.936±0.172	0.908±0.176	0.930±0.176	0.910±0.176
f_7^ϕ	0.776±0.729	0.970±0.668	1.033±0.670	0.973±0.669
f_8^ϕ	≡1	≡1	≡1	≡1
R_{nQE}	0.705±0.113	0.556±0.062	0.420±0.045	0.696±0.110
$\mathrm{P}_{\mathrm{Norm}}^{\mathrm{1kt}}$	1.095±0.050	1.168±0.047	1.235±0.045	1.097±0.058
$\mathrm{P}_{\mathrm{energy}}^{\mathrm{1kt}}$	0.986±0.005	0.998±0.006	0.999±0.005	0.994±0.007

Though the cut on θ_μ did affect the R_{nQE} value, it did not solve the problem as to why the fit value for the lowest energy bin was higher than in 2004. This was a problem in one criterion that was not applied in the 2004 analysis. The MC normally has a function applied to lower energy events to mimic the effect of the FADC on the data. This cut affects MC events with $p_\mu < 500$ MeV/c, as seen in Figure 3.14. In 2004, this criterion was mistakenly not applied, lowering the lowest energy bin's fitted value in the 1KT spectrum analysis.

Chapter 4

Extrapolation of the measurements at the Near Detector to Super-Kamiokande

The expected number of events and the expected neutrino energy spectrum at Super-Kamiokande requires a measurement of the neutrino energy spectrum at the Near Detector, given in the previous chapter, and the near/far ratio. The expected flux at SK is defined as

$$\Phi^{SK} = \Phi^{ND}\left(E_\nu\right) \cdot R^{F/N}\left(E_\nu\right)\left(1 - P\left(E_\nu; \Delta m^2, \sin^2 2\theta\right)\right) \qquad (4.1)$$

where $\Phi^{ND}\left(E_\nu\right)$ is the measured neutrino energy flux from the previous chapter, $R^{F/N}$ is the far/near ratio, and P is the neutrino oscillation probability as described in Equation 1.13 with L equal to 250 km. This chapter will cover the K2K beam MC, the HARP experiment which evaluated the far/near ratio, and how the number of events and neutrino energy spectrum are extrapolated to SK once both the ND spectrum and far/near ratio are known.

4.1 K2K Beam Monte Carlo

A neutrino beam MC simulation program is used to study the neutrino beam properties. The beam line geometry is implemented in GEANT [52] and particles are tracked in materials until they decay into neutrinos or are absorbed in the material. The tracks of the neutrinos are extrapolated along a straight line to the ND and SK, and the fluxes and the energy spectrum at these locations are determined.

In the simulation program, protons with a kinetic energy of 12 GeV are injected into the aluminum target. The profile and divergence are assumed to be Gaussian-like and the values for the beam size and divergence measured by the two segmented plate ionization chambers, described in Section 2.1, in front of the target are used as inputs. An empirical formula for the differential

Table 4.1: The fitted parameters, C_i's, in the Sanford-Wang formula for the production of positively charged pions in the Cho-CERN compilation and for the HARP results [56]. The target nucleus is beryllium in Cho-CERN compilation while it is aluminum in the HARP results. The values in the table are before the nuclear scaling is applied.

	C_1	C_2	C_3	C_4	C_5	C_6	C_7	C_8
HARP	440	0.85	5.1	1.78	1.78	4.43	0.14	35.7
Cho-CERN	238	1.01	2.26	2.45	2.12	5.66	0.14	27.3

cross-section by J. R. Sanford and C. L. Wang [53, 54] is used to simulate the primary hadron production in the target. The Sanford-Wang formula is expressed as:

$$
\begin{aligned}
\frac{d^2\sigma}{d\Omega dp} \;=\; & C_1\, p^{C_2} \left(1 - \frac{p}{p_B}\right) \times \\
& \exp\left(-\frac{C_3\, p^{C_4}}{p_B^{C_5}} - C_6\, \theta\,(p - C_7\, p_B\, \cos^{C_8}\theta)\right),
\end{aligned}
\tag{4.2}
$$

where $d^2\sigma/d\Omega dp$ is the double differential cross section of particle production per interacting proton in units of mb sr^{-1} (GeV/c)$^{-1}$, θ is the angle between the secondary particle and the beam axis in the laboratory frame, and p and p_B are the momenta of the secondary particle and the incident proton, respectively. The C_i's are parameters fitted to existing hadron production data. C_i's obtained from a fit of proton-beryllium interactions by Cho *et al.* [55] designated the "Cho-CERN compilation" are used as a refernce model for the production of positively charged pions. Their values are shown in Table 4.1.

A nuclear rescaling is then applied to convert the pion production cross section on beryllium to that on aluminum. The scaling factor, w, is defined as

$$
w \equiv \left(\frac{A_{\mathrm{Al}}}{A_{\mathrm{Be}}}\right)^{\alpha(x_F)},
\tag{4.3}
$$

where A_{Al} and A_{Be} are atomic masses for aluminum and beryllium, respectively, and the index $\alpha(x_F)$ is expressed as

$$
\alpha(x_F) = 0.74 + x_F(-0.55 + 0.26x_F)
\tag{4.4}
$$

where x_F is the Feynman x variable.

Negatively charged pions, and charged and neutral kaons are also generated using the Sanford-Wang formula but with a different set of C_i's. For negative pion production, the parameters in [55] are used, while those described in [57] are used for the kaon production. Generated secondary particles are tracked by GEANT with the GCALOR/FLUKA [58, 59, 60] hadron model through the two horn magnets and the decay volume until they decay into neutrinos or are absorbed in materials.

Since GEANT treats different types of neutrinos identically, a custom-made simulation program to properly treat the type of neutrinos emitted in particle decays is used. Charged pions are treated so that they decay into muon and neutrino ($\pi^+ \to \mu^+ \nu_\mu$, $\pi^- \to \mu^- \overline{\nu}_\mu$, called $\pi_{\mu2}^\pm$) with a branching fraction of 100%. The kaon decays considered in the beam simulation are the so-called $K_{\mu2}^\pm$, $K_{e3}^{\pm,0}$ and $K_{\mu3}^{\pm,0}$ decays, where the subscripts give the lepton produced in the decay as well as the total number of particles. Their branching ratios are taken from the Particle Data Group [13]. Other decays are ignored. Neutrinos from K_S^0 are ignored since the branching ratio for K_S^0 decaying to neutrinos is quite small. The Dalitz plot density of $V-A$ theory [13, 61] is also employed in $K_{\ell3}$ decays. Muons are considered to decay via $\mu^\pm \to e^\pm \nu_e(\overline{\nu}_e) \overline{\nu}_\mu(\nu_\mu)$, called $\mu_{e3}^\pm$, with 100% branching fraction. The energy and angular distributions of the muon antineutrino (neutrino) and the electron neutrino (antineutrino) emitted from a positive (negative) muon are calculated according to Michel spectra of $V-A$ theory [61], where the polarization of the muon is taken into account.

The produced neutrinos are extrapolated to the ND and SK along a straight line and the energy and position of the neutrinos entering the ND and SK are recorded and used in later simulations for neutrino interactions and detector simulators.

The composition of the neutrino beam is dominated by muon neutrinos since the horn magnets mainly focus the positive pions. Figure 4.1 shows the energy spectra of each type of neutrino at ND and SK estimated by the beam MC simulation. About 97.3% (97.9%) of neutrinos at the ND (SK) are muon neutrinos decayed from positive pions, and the beam is contaminated with a small fraction of neutrinos other than muon neutrinos. At the ND, 2.7% of the events are not muon neutrinos compared to 2.1% at SK.

The validity of the beam MC simulation has been confirmed by both the HARP experiment and PIMON measurements, which will be described in detail in the next section.
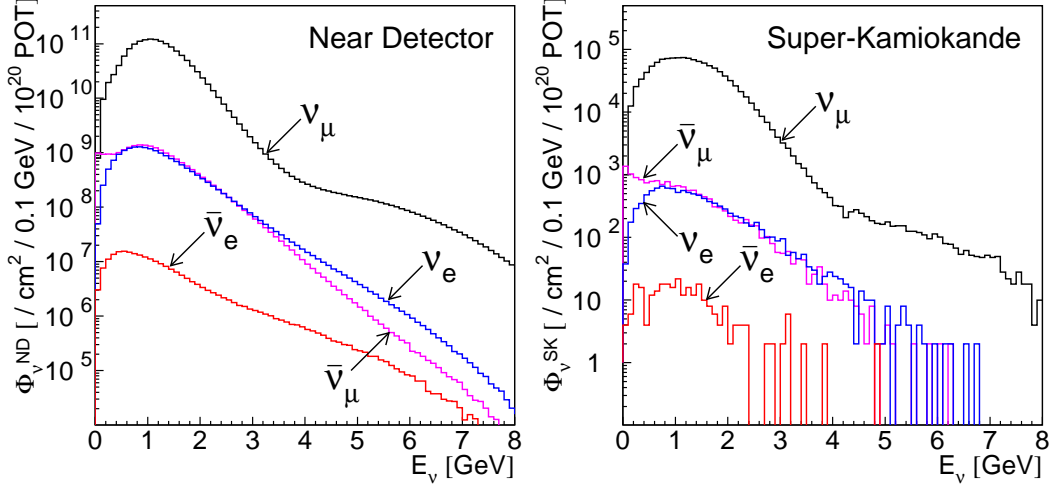
Figure 4.1: The energy spectrum for each type of neutrino at ND (left) and SK (right) estimated by the beam MC simulation. The neutrino beam is 97.3% (97.9%) pure muon neutrino with contaminated by $\nu_e/\nu_\mu \sim 0.013$ (0.009), $\overline{\nu}_\mu/\nu_\mu \sim 0.015$ (0.012), and $\overline{\nu}_e/\nu_\mu \sim 1.8 \times 10^{-4}$ (2.2×10^{-4}) at the ND (SK).

4.2 Far/Near Ratio

The neutrino flux at any distance from its source can be predicted when the geometry of the decay volume and the momenta and directions of the neutrino parents are known. Neutrinos are produced from an extended source because of the relatively long π^+ decay distance from the target and not produced from a point source, making the far/near flux ratio dependent on the neutrino energy. This energy dependence results from the ND viewing the neutrino beam as a line source weheas SK sees the production effectively as a point source. Therefore, the F/N flux ratio, $R^{\mathrm{F/N}}$, is defined as

$$R^{\mathrm{F/N}} = \frac{\Phi^{\mathrm{SK}}(E_\nu)}{\Phi^{\mathrm{ND}}(E_\nu)}, \qquad (4.5)$$

where $\Phi^{\mathrm{SK(ND)}}(E_\nu)$ is the neutrino energy spectrum at SK(ND).

The F/N flux ratio is estimated by the beam MC. In this simulation, while the Cho-CERN compilation is used as a reference model, the HARP experiment [56] result is an input for simulation of pion production. The pion production measurement done by HARP is of direct relevance for K2K, since it uses the same beam proton momentum, the same production target, and it covers a large fraction of the phase space contributing to the K2K neutrino

flux. The details of the HARP measurements are described in Section 4.2.2. The pion monitor (PIMON) measurement was performed as a confirmation of the validity of the beam MC simulation. It gives *in-situ* information on the momentum and the direction of pions entering the decay volume after they are focused by the horn magnetic fields. The PIMON, however, is not sensitive to pions below 2 GeV/c (corresponding to neutrinos below 1 GeV) due to the Cherenkov threshold. A description of the PIMON measurement is given in Section 4.2.1 first.

4.2.1 The PIMON Measurement

A measurement of the F/N ratio has been performed using *in-situ* pion monitor (PIMON) measurements. The PIMON was inserted into the beamline on two occasions just downstream of the horn magnets to measure the momentum (p_π) versus angle (θ_π) distribution of pions entering the decay volume.

As mentioned in Section 2.1.4, the index of refraction for the freon gas did not go above $n = 1.00242$ because the 12 GeV protons would also start to emit Cherenkov light. This limit on the index of refraction set a momentum threshold of 2 GeV/c for pions, which corresponds to an energy threshold of 1 GeV for neutrinos.

The (p_π, θ_π)-plane from the collected pion data by PIMON is binned into 5×10 bins; 5 bins in p_π above 2GeV/c with 1GeV/c slices (the last bin is integrated over $p_\pi > 6$ GeV/c) and 10 bins in θ_π from -50 mrad to 50 mrad in 10 mrad slices. Templates of the Cherenkov light distributions emitted by pions in these bins are produced for each refractive index using a MC simulation. Then, the weight of the contribution from each (p_π, θ_π) bin being the fitting parameter, the MC templates are fit to observed Cherenkov light distributions. The fitting is done for the data in June 1999 and in November 1999, separately. The resulting values of fitting parameters and errors on them in November 1999 run are shown in Fig. 4.2.

The neutrino energy spectra at ND and SK are derived by using the weighting factors obtained above and a MC simulation. The neutrino energy is binned into 6 bins: 0.5 GeV bins up to 2.5 GeV, and integrated above 2.5 GeV. The contribution of pions in each (p_π, θ_π) bin to the neutrino energy bins is estimated by a MC simulation, where to a good approximation it depends only on the pion kinematics and the geometry of the decay volume. Then, the neutrino spectrum is obtained by summing up these contributions weighted by fitted factors. Finally, the ratio of the neutrino spectra at SK to that at ND yields the F/N ratio.
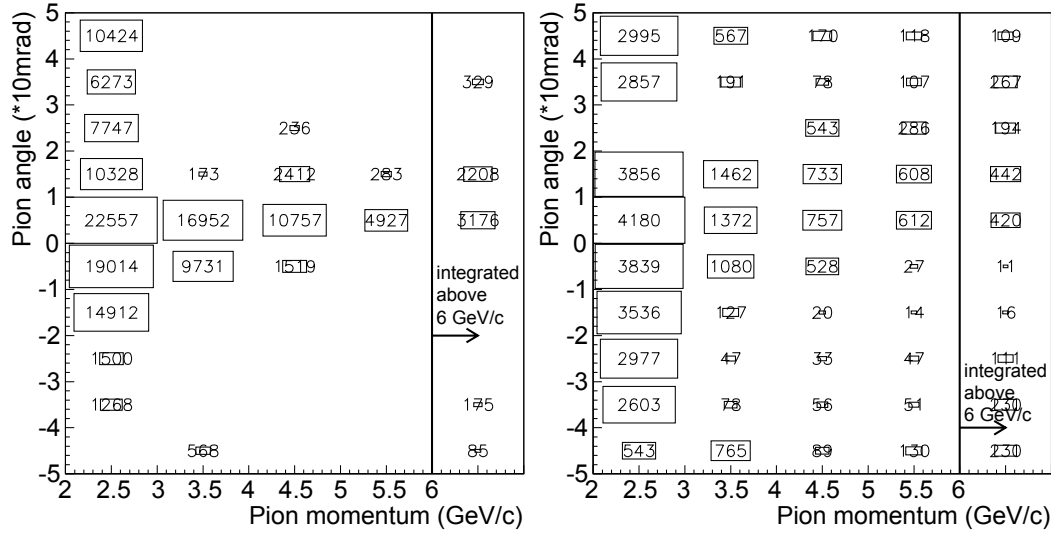
Figure 4.2: The fitting results of pion (p_π, θ_π) distribution in November 1999 run. The left figure shows the resulting central value of the weighting parameters and the right figure shows the estimated fitting errors on them (no box means fitting errors are negligibly small).

The F/N ratio from the PIMON data taken in November 1999 is shown in Figure 4.3 with empty squares and shaded error boxes. Systematic uncertainties in the PIMON measurement are included in the errors. The most dominant contributions to the error on the F/N ratio come from this fitting error, the uncertainty in the analysis methodology, and the uncertainty in the azimuthal symmetry of the horn magnetic field. Further details on the systematic uncertainties in the PIMON measurement are described in [64].

For neutrino energies below 1 GeV, the "Cho-CERN compilation" is used at K2K since the PIMON is not sensitive to those energies. It's prediction appears as the dotted histogram in Figure 4.3. In this case, the same Sanford-Wang functional form for π^+ production is employed to describe a CERN compilation of π^+ production measurements in proton-beryllium interactions, which is based mostly on Cho *et al.* data [55]. A nuclear correction to account for the different pion production kinematics in different nuclear target materials is applied. The predictions of F/N flux ratio by the PIMON and Cho-CERN are consistent with each other for neutrino energies above 1 GeV, as shown inn Figure 4.3. The results from HARP measurement is also overlaid, indicating that the results of PIMON measurements are consistent with both of them and confirming the validity of the F/N estimations.

4.2.2 The HARP Experiment

The dominant uncertainty in neutrino flux predictions for conventional neutrino beams is due to the pion production uncertainty in the hadronic interactions of primary beam protons with the nuclear target material. In this analysis, results provided by the HARP experiment at CERN are used as input to the pion production simulation. The HARP experiment precisely measured positively-charged pion production in the interactions of 12.9 GeV/c protons in a thin aluminum target [56]. The HARP experiment took data in 2001 and 2002 in the CERN PS T9 beamline, to systematically study hadron production for a variety of processes (pion and kaon in particular) with large phase space coverage. Secondary tracks from the decay products and interactions are efficiently reconstructed in the HARP forward spectrometer via a set of drift chambers located upstream and downstream with respect to a dipole magnet. Particle identification for forward tracks is obtained with a time-of-flight system, a Cherenkov threshold detector, and an electromagnetic calorimeter.

The HARP pion production measurement [56] is directly relevant for the K2K F/N flux ratio because it covers roughly the same proton beam momentum, 12.9 GeV/c, and uses a replica of the K2K target to produce the K2K neutrino beam. Moreover, beam MC simulations show that the forward pion production region measured in HARP, $30 < \theta_\pi < 210$ mrad, $0.75 < p_\pi < 6.5$ GeV/c, matches well the pion production phase space responsible for the dominant fraction of the K2K muon neutrino fluxes at both the near and far detector locations.

The result of the pion production measurements described in [56] is incorporated into the beam MC simulation to estimate the neutrino spectra at ND and SK and the energy dependence of the F/N flux ratio in the absence of neutrino oscillations. Uncertainties in the primary and secondary hadronic interactions, in the pion focusing performance in the horn magnetic fields, and in the primary beam optics, are considered. Here, primary hadronic interactions are defined as hadronic interactions of protons with more than 10 GeV total energy in aluminum, while secondary hadronic interactions are defined to be hadronic interactions that are not primary ones. In the following, the assumptions on systematic uncertainties affecting neutrino flux predictions are summarized.

The uncertainty in the multiplicity and kinematics of π^+ production in primary hadronic interactions is estimated based on the HARP results. In this case, the HARP π^+ Sanford-Wang parameters' uncertainties and correlations given in [56] are propagated into flux uncertainties using standard error matrix propagation methods: the flux variation in each energy bin is estimated by

varying a given Sanford-Wang parameter by a unit standard deviation in the beam MC simulation. An uncertainty of about 30% is assumed for the uncertainty in the proton-aluminum hadronic interaction length. The uncertainty in the overall charged and neutral kaon production normalization is assumed to be 50%.

The systematic uncertainty due to the incomplete knowledge of secondary hadronic interactions, such as π^+ absorption in the target and horns, is also considered. The relatively large differences between the GHEISHA [62] and GCALOR/GFLUKA [58, 59, 60] descriptions of secondary interactions, also in comparison to available experimental data, are used to estimate this uncertainty.

The uncertainties in the horn system's magnetic field were also evaluated. A 10% uncertainty is assumed in the absolute field strength, which is within the experimental uncertainty on the magnetic field strength and the horn current measured using inductive coils during horn testing phase [63]. Furthermore, a periodic perturbation in the azimuthal angle of up to $\pm15\%$ of the amplitude with respect to the nominal field strength is assumed as the uncertainty in the field homogeneity. This is also based on the experimental accuracy achieved in the measurement of the magnetic field mapping in azimuth during horn testing [64].

Finally, beam optics uncertainties are estimated based on measurements taken with two segmented plate ionization chambers located upstream of the target. An uncertainty of 1.2 mm and 2.0 mrad in the mean transverse impact point on target and in the mean injection angle, respectively, are assumed based on long-term beam stability studies [65]. The estimated uncertainty on the beam profile width at the target and angular divergence, based on the $\sim20\%$ accuracy with which the beam profile widths are measured at the segmented plate ionization chamber locations [65].

The F/N flux ratio, Φ^{SK}/Φ^{ND}, predicted by the HARP π^+ production measurement for primary hadronic interactions with the systematic error evaluation discussed above, in the absence of neutrino oscillations, is shown in Fig. 4.3 as a function of neutrino energy. The flux ratio uncertainty is estimated as a function of the neutrino energy. Below neutrino energies of ~1 GeV it is at the 2-3% level, while it is of the order of 4-9% above 1 GeV. The dominant contribution to the uncertainty in F/N comes from the HARP π^+ measurement itself. In particular, the uncertainty in the flux ratio prediction integrated over all neutrino energies is 2.0%, where the contribution of the HARP π^+ production uncertainty is 1.4%. Table 4.2 shows the contributions of all systematic uncertainty sources discussed above on the far-to-near flux
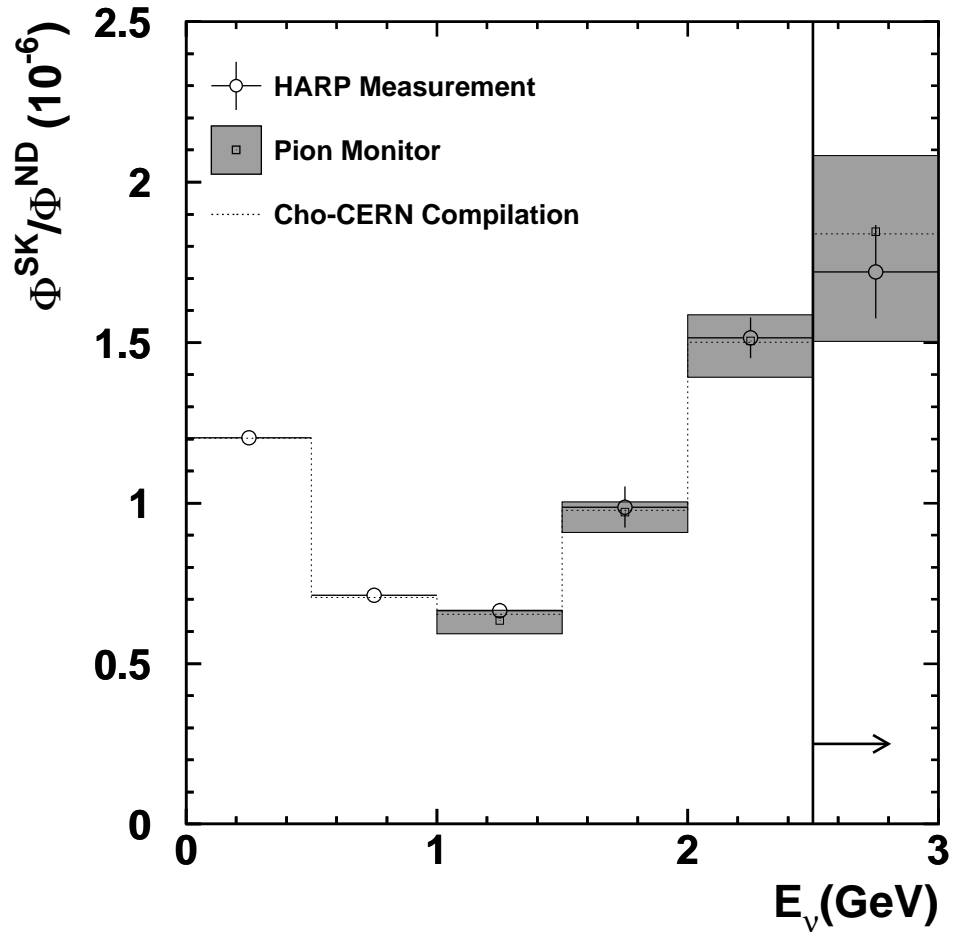
Figure 4.3: Prediction for the K2K muon neutrino F/N flux ratio in absence of oscillations. The empty circles with error bars show the central values with systematic errors on the muon neutrino flux predictions from the HARP π^+ production measurement, the empty squares with shaded error boxes show the central values and errors from the PIMON measurement, and the dotted histograms show the central values from the Cho-CERN compilation of older (non-HARP) π^+ production data.

Table 4.2: Contributions to the uncertainty in the far-to-near flux ratio prediction. The uncertainties are quoted in %. The six columns refer to different bins in neutrino energy, as shown in the table in units of GeV.

Source:	0.0-0.5	0.5-1.0	1.0-1.5	1.5-2.0	2.0-2.5	2.5-
Hadron interactions:						
Interaction rate	0.3	0.9	0.9	2.1	0.2	0.3
π^+ mult. & kinematics	0.7	2.0	1.8	2.1	2.9	4.7
Kaon multiplicity	0.1	<0.1	0.1	<0.1	0.1	4.9
Secondary interactions	0.3	1.2	2.0	2.1	0.4	0.7
Horn magnetic field:						
Field strength	1.1	0.8	1.4	4.2	2.8	3.9
Field homogeneity	0.3	0.2	0.5	0.3	0.6	0.3
Beam optics:						
Beam centering	0.1	<0.1	<0.1	<0.1	0.1	0.1
Beam aiming	0.1	<0.1	<0.1	0.1	0.4	0.2
Beam spread	0.1	0.7	1.7	3.4	1.0	3.2
Total	1.4	2.7	3.6	6.5	4.2	8.5

ratio prediction for each neutrino energy bin.

Prior to the availability fo the HARP results, the "Cho-CERN compilation" was used at K2K, and it's prediction appears as the dotted histogram in Figure 4.3. In this case, the same Sanford-Wang functional form for π^+ production is employed to describe a CERN compilation of π^+ production measurements in proton-beryllium interactions, which is based mostly on Cho *et al.* data [55]. A nuclear correction to account for the different pion production kinematics in different nuclear target materials is applied. The predictions of F/N flux ratio by HARP and Cho-CERN are consistent with each other for all neutrino energies. Note that the difference between Cho-CERN and HARP central values represents a difference in hadron production treatment only.

4.2.3   K2K's Far/Near ratio

The F/N flux ratio used to extrapolate the measurements in ND to the expectation at SK is obtained in three independent ways: using the HARP measurement, the Cho-CERN model, and the PIMON measurement, as described in the previous sections. All three predictions of the F/N ratio are consistent with each other within measurement uncertainties. Among these

Table 4.3: Predictions for the F/N muon neutrino flux ratio as a function of neutrino energy, for the HARP model for π^+ production in primary hadronic interactions. The neutrino energy binning is also indicated.

Energy Bin Number i	E_ν [GeV]	$\overline{R}_i$ ($\times 10^{-6}$)
1	0.0−0.5	1.204
2	0.5−1.0	0.713
3	1.0−1.5	0.665
4	1.5−2.0	0.988
5	2.0−2.5	1.515
6	2.5−	1.720

Table 4.4: Fractional error matrix $\langle \delta R_i \delta R_j \rangle / (\overline{R}_i \overline{R}_j)$ obtained from the systematic uncertainties on the F/N flux predictions. The neutrino energy binning is the same as in Tab. 4.3. The values are given in units of 10^{-3}.

Energy Bin	1	2	3	4	5	6
1	0.187	0.002	−0.036	−0.372	−0.281	0.240
2	0.002	0.728	0.868	1.329	0.698	−1.398
3	−0.036	0.868	1.304	2.122	1.041	−2.040
4	−0.372	1.329	2.122	4.256	2.165	−3.799
5	−0.281	0.698	1.041	2.165	1.779	−2.678
6	0.240	−1.398	−2.040	−3.799	−2.678	7.145

measurements, the HARP measurement gives the most precise measurements on hadron production.

The central values for the F/N flux ratio as a function of neutrino energy obtained from the HARP π^+ production results, $\overline{R}_i$, are given in Table 4.3, where the index i denotes an energy bin number. The total systematic uncertainties on the F/N flux ratio as a function of neutrino energy are given in Table 4.4, together with the uncertainty correlations among different energy bins, expressed in terms of the fractional error matrix $\langle \delta R_i \delta R_j \rangle / (\overline{R}_i \overline{R}_j)$. The F/N central values and its error matrix are used in the analysis for neutrino oscillation described later in Chapter 7.

While the neutrino flux predictions given here are appropriate for most

of the protons on target used in this analysis, a small fraction of the data was taken with a different beam configuration in K2K-Ia. As a result, the far/near flux ratio for K2K-Ia is separately estimated, in the same manner as described above for later run periods. The flux ratio predictions for the two beam configurations, integrated over all neutrino energies, differ by about 0.4%. The flux ratio prediction for the June 1999 beam configuration and the ND spectrum shape uncertainties are used to estimate the expected number of neutrino events in SK and its error for the June 1999 period.

4.3   Expected Number of Events at SK

The expected number of neutrino events in SK incorporates the elements of the spectrum extrapolation. The number of events is defined as:

$$N_{exp}^{SK}(\Delta m^2, \sin^2 2\theta) \equiv N_{int}^{1KT} \cdot \frac{\rho^{SK}}{\rho^{1KT}} \cdot \frac{M^{SK}}{M^{1KT}} \cdot \frac{POT^{SK}}{POT^{1KT}} \cdot C_{\nu_e}, \qquad (4.6)$$

where N_{int}^{1KT}, is the number of interactions measured by the 1KT, the variable M is the fiducial mass of each detector (25 tons for the 1KT), C_{ν_e} is the correction factor for the difference in electron neutrino contamination between the two detectors, and $\rho^{1KT(SK)}$ is the expected neutrino event rate per unit mass.

The number of interactions in the 1KT, N_{int}^{1KT}, is defined as

$$N_{int}^{1KT} = N_{obs}^{1KT} \cdot \frac{N_{peak}^{total}}{N_{peak}^{single}} \cdot \frac{1}{\epsilon^{1KT}} \cdot \frac{1}{1 + R_{BKG}} \cdot C_{multi} \qquad (4.7)$$

where N_{obs}^{1KT} is the number of events observed in the 1KT FV, N_{peak}^{total} is the total number of PMTSUM signal peaks above the 1000 p.e. threshold, and N_{peak}^{single} is the number of single peak events in the PMTSUM signal. The detector efficiency, ϵ^{1KT} is defined as the total number of events whose vertex is reconstructed in the 25 ton FV divided by the number of events whose true vertex is in the FV. R_{BKG} is the fraction of background events. The total background is estimated to be 1.5% (3.1%) for runs starting in (before) 2000. The main sources are cosmic rays (1.0%), beam induced events outside the detector (0.5%), and fake events from an impedance mismatch in the cables in 1999. C_{multi} is the correction factor for multiple interactions. This correction factor is from the fact the FADCs in the 1KT cannot indentify all the interactions in a beam spill. Accordingly, the number of interactions in the 1KT FV are underestimated by 2.3%. Multiple interactions making up

34% of the events, giving a value of $C_{multi} = 1.008$. The total systematic error for N_{int}^{1KT} is $\pm 4.1\%$.

The expected neutrino event rate per unit mass is defined as:

$$\rho = \int dE_\nu \cdot \Phi(E_\nu) \cdot \sigma(E_\nu) \cdot \epsilon(E_\nu) \tag{4.8}$$

where $\Phi(E_\nu)$ is the energy dependent neutrino flux, $\sigma(E_\nu)$ is the neutrino-water cross section, ϵ is the detector efficiency. The neutrino-water cross section is divided into three interaction types (CC QE, CC non-QE, and NC), which are summed together with relative weighting expressed as:

$$\sigma = \sum f^{CCQE}\sigma_{CCQE}^{MC} + f^{CCnonQE}\sigma_{CCnonQE}^{MC} + f^{NC}\sigma_{NC}^{MC}. \tag{4.9}$$

The flux term at the near detector, $\Phi^{ND}(E_\nu)$, is given as

$$\Phi^{ND}(E_\nu) = f^\phi(E_\nu) \cdot \Phi_{MC}^{ND}(E_\nu) \tag{4.10}$$

where f^ϕ is the relative energy dependent terms in Table 3.3 and $\Phi_{MC}^{ND}(E_\nu)$ is the flux of the beam MC before the spectrum measurement at the ND. For SK, $\Phi^{SK}(E_\nu)$ is given in Equation 4.1 with the F/N ratio multiplied by Equation 4.10.

Finally, C_{ν_e} has a simple determination. When electron neutrino component of the beam simulation is added to the muon neutrino simulation, the percent increase in the number of events at the 1KT (SK) is roughly 1.3% (0.6%). This gives a 0.996 correction factor for the extrapolation.

The systematic error in the expected number of events come from the ND spectrum measurement of the flux and the F/N ratio. The cross section errors are evaluated as the relative ratio between NC and CC non-QE neutrino-nucleus interactions and the CC QE neutrino-nucleus interactions. The CC non-QE/CC QE ratio error is taken from the ND spectrum fit. For NC interactions, 11% is assigned for the NC-π^0/CC QE interactions from [66] and 30% for all other interactions based on previous experiments [67]. In addition to the systematic errors given in the previous section, there is an additional 15% net uncertainty given to the NC/CC QE ratio which incorporates the detector efficiency. The largest systematic uncertainty contributors to the expected number of events are the FV systematic errors for the 1KT and SK, and the far/near ratio.

For K2K-Ia, there is not an energy spectrum measurement from the ND. In this case, the systematic errors are treated differently and incorporated into the error of a single normalization parameter. The total uncertainty is given

to be $^{+9.0\%}_{-9.8\%}$ from the HARP π^+ measurement ($^{+5.8\%}_{-7.0\%}$), the F/N ratio ($\pm4.3\%$), and the FV systematic errors in the 1KT ($\pm4.3\%$) and SK ($\pm3.0\%$).

For SK's official fiducial volume (defined in Section 5.2), a total of $158.1^{+9.2}_{-8.6}$ K2K beam neutrino events are exepected in the case of no neutrino oscillations.

4.4   Expected Spectrum at SK

The expected neutrino energy spectrum at Super-Kamoikande is calculated using:

$$\phi^{SK}_{exp} = \int dE_\nu \cdot \Phi^{SK}(E_\nu) \cdot \sigma(E_\nu) \cdot \epsilon^{SK}_{1R\mu}(E_\nu) \cdot r(E_\nu; E^{rec}_\nu) \tag{4.11}$$

where in this case $\epsilon^{SK}_{1R\mu}(E_\nu)$ is the detection efficiency of 1Rμ events in SK and $r(E_\nu; E^{rec}_\nu)$ is the probability of reconstructing an event with energy E_ν as E^{rec}_ν), where E^{rec}_ν is defined in Equation 3.1. The detector efficiency for 1Rμ events is evaluated in the same manner as the detector efficiency for the expected number of events, but with the single ring and μ-like events selected. The first two terms in the intergral, $\Phi^{SK}(E_\nu) \cdot \sigma(E_\nu)$, are the same as in the previous section.

Both the 1Rμ efficiency and r are estimated by MC simulation. The MC is binned in 50 MeV increments of the true neutrino energy, making the integral in Equation 4.11 a sum. The efficiency for 1Rμ events is calculated by comparing the number of 1Rμ events with their fitted vertex in SK's FV against the number of 1Rμ events with their true vertex in SK's FV.

The expected reconstructed energy spectrum is shown in Figure 4.4. The height of each box is the estimated error for each bin. The main uncertainties of the neutrino energy spectrum are the spectrum measurement at the ND, the far/near ratio, and cross section ratios, which are the same as those for the number of events extrapolation. The systematic errors for event reconstruction will be discussed in Chapter 7. In addition, the energy scale uncertainty at SK is 2.0% (2.1%) for K2K-I (K2K-II).
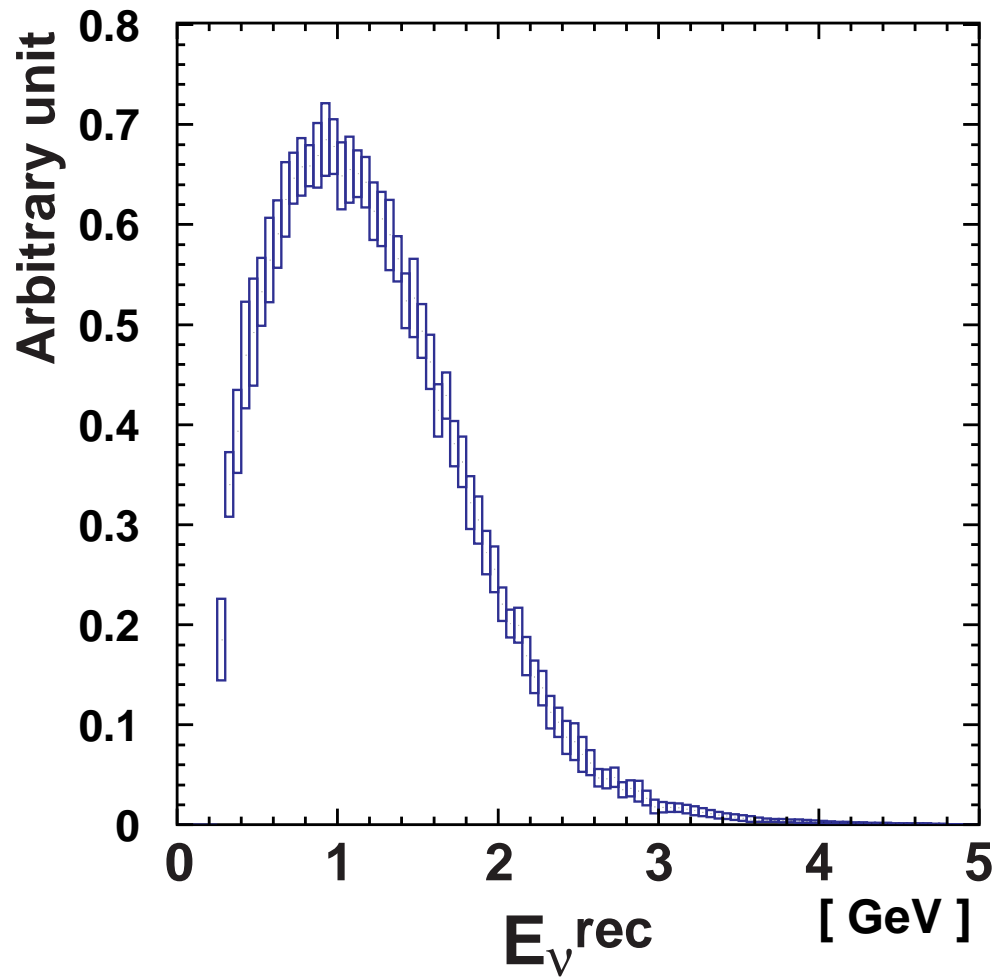
Figure 4.4: Expected reconstructed neutrino energy spectrum shape in the case of null oscillations. The height of the boxes indicates the error size.

Chapter 5

Super-Kamiokande Events

With the ability to extract the number of events and expected neutrino energy spectrum, it is time to see how events for the disappearance analysis are selected. The first section of this chapter will discuss the general selecton criteria that all candidate events must pass. The second section will discuss the event selection for events in Super-Kamiokande's official fiducial volume.

5.1   Inner Detector Event Selection

In order to select neutrino interaction events from the KEK neutrino beam at Super-Kamiokande, two Universal Time Stamps (UTSs) based on the GPS system are compared. The time stamp associated with the KEK-PS beam, T_{KEK}, that records when a spill occurred at the KEK site. At Super-Kamoikande, T_{SK} corresponds to the SK trigger time for an event. The time difference is calculated using the formula

$$\Delta T = T_{SK} - T_{KEK} - TOF, \tag{5.1}$$

where the time of flight, TOF, is the total time it takes a neutrino to go from the Near Detector site to the Far Detector. In the case of K2K, with a distance of 250 km and a speed that can be approximated as the speed of light, c, the TOF for neutrinos is roughly 833 μs. The range that ΔT can be expected to be distributed is at most 1.1 μs based on the length of the beam spill time. In order to account for an at most 200 ns difference in synchronization between the two clocks, events that are to be possibly included in the K2K analysis are selected if -0.2 μs$<\Delta T<$1.3 μs.

Next, within the timing window, six additional selection criteria are applied for the event sample used in the oscillation analysis, five of which are discussed here. The first is that there must be no activity in the detector 30 μs prior to

an event, which helps remove muon decay electrons from the sample. This is also called the pre-activity cut. Within a 300 ns timing window, there must be a minimum of 200 (94) p.e. in SK's ID for K2K-I (K2K-II). Events need to be FC. This means that there are fewer than 10 (16) hits in the OD for K2K-I (K2K-II). At least 30 MeV are required to be deposited in the ID and finally, a flasher cut is applied to all events. A "flasher" is a PMT that produces light because of a spontaneous discharge around the dynode which are identified by a timing distribution that is broader than a neutrino event and a repeating light pattern in the detector. Flasher events are normally removed through hand scanning each K2K event.
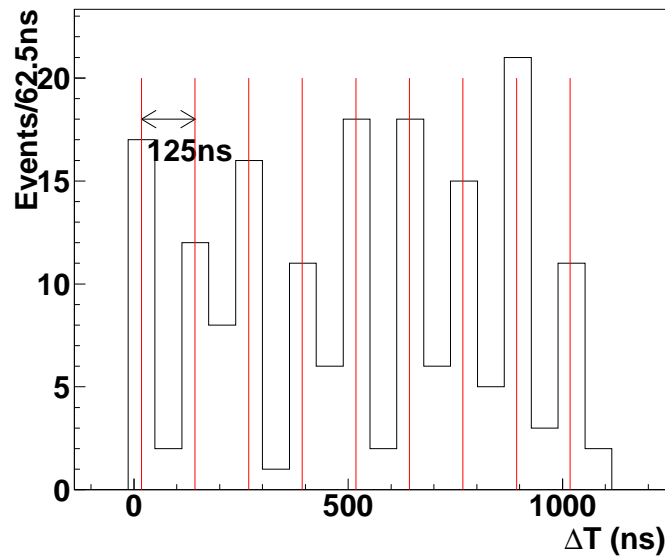
Figure 5.1: The ΔT distribution for all FC K2K events before the FV events are selected. The 9 microbunch structure of the K2K-PS beam can clearly be seen.

After these events are selected, there are 174 K2K events, 91 in K2K-I and 83 in K2K-II. The events in the timing window have the nine bunch structure of the K2K beam, as in Figure 5.1. The data reduction is summarized in Table 5.1.

Table 5.1: Super-Kamiokande event reduction summary before the fiducial volume selection.

Reduction step	K2K-I	K2K-II
$\|\Delta\text{T}\| < 500\mu\text{s}$	107892	470469
no pre-activity		
total number of p.e. within	36560	16623
300ns timing window		
>200 (K2K-I),94 (K2K-II)		
Fully contained event	153	99
flasher cuts	97	88
visible Energy >30 MeV	95	85
$-0.2\mu s \leq \|\Delta T\| \leq 1.3\mu s$	91	83

5.2 Official Fiducial Volume Event Selection

The final criterion applied to the data for the K2K analysis are events within the fiducial volume. The official FV is defined as having the reconstructed vertex of an event is at least 2 m away from the nearest ID wall in SK. This gives a total fiducial volume of 22.5 ktons with 112 events for the oscillation analysis. Of these events, 55 are from K2K-I and 57 are from K2K-II.

Figure 5.2 shows the event reduction with the FV selection being applied before the more stringent TOF cut. The wider timing window of -500 μs $< \Delta T < 500$ μs shows three events outside of the -0.2 μs$<TOF<$1.3 μs timing window, but within the FV. These events are consistent with the atmospheric neutrino background of two expected events.

From the 112 K2K events in the fiducial volume, 58 are 1Rμ events that are used in the comparison of the energy spectrum shapes and 9 events are 1R e-like events, which are candidate events in the ν_e appearance search. K2K-I has 30 (3) 1Rμ (1Re) events and K2K-II has 28 (6). For Equation 3.1, 1Rμ are used since they are more likely to be CCQE events and the proton from the interaction is below Cherenkov threshold. Figure 5.3 shows the reconstructed neutrino energy for all 1Rμ K2K data and the expected spectrum in the case of no oscillations. As shown, the data and MC do not agree for the reconstructed neutrino energy spectrum. In Chapter 7, this discrepancy will be analysed as neutrino oscillations. A summary of the fiducial volume events is given in Table 5.2.
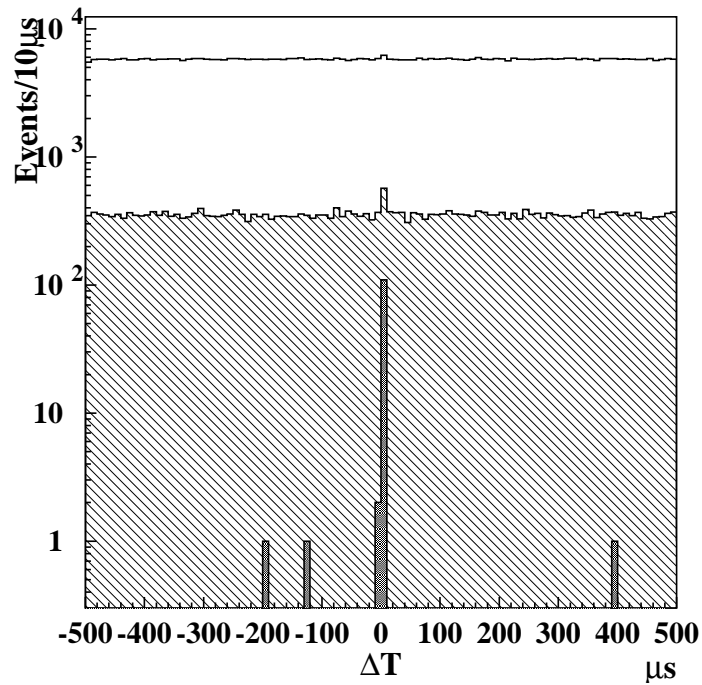
Figure 5.2: The ΔT distribution at three steps in the data reduction. Clear, hatched and shaded histograms are after pre-activity cut, total p.e. threshold has been applied, and official fiducial volume has been applied, respectively. The tighter ΔT selection has not yet been applied.

Table 5.2: SK event summary after the event selection has been applied, including the official fiducial volume.

	K2K-I	K2K-II
Fully contained event	55	57
1-ring	33	34
μ-like	30	28
e-like	3	6
multi-ring	22	23
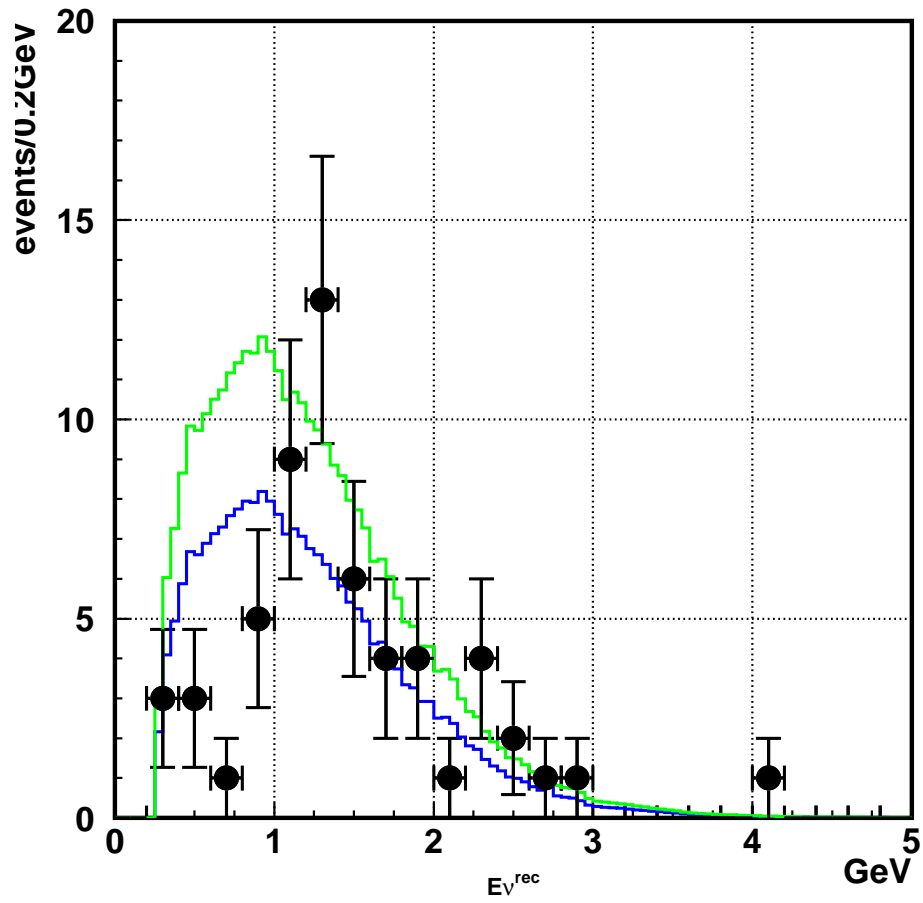
Figure 5.3: The reconstructed E_ν distribution for the SK single ring μ-like sample. Points with error bars are data. The histograms are the expected reconstructed neutrino energy spectrum without oscillation. The blue histogram is normalized to the observed 58 events and the green histogram is absolutely normalized.

Chapter 6

Expanded Fiducial Volume In Super-Kamiokande

6.1 Motivation

The fiducial volume normally used in K2K's analysis requires the reconstructed vertex of an event to be at least 2 m away from the nearest wall in Super-Kamiokande's ID (dwall>2 m) giving a fiducial mass of 22.5 ktons. For an event at the edge of SK's fiducial volume going directly into one of the Inner Detector walls, approximately 12 PMTs will have Cherenkov light deposited in them. This FV has been used in the analyses of the Kamiokande experiment (e.g. Reference [9]) and in Super-Kamiokande's proton decay [68, 69] and atmospheric neutrino analyses [27]. The one exception to the 2 m FV is SK's L/E analysis [28], where, to increase statistics in the region of interest, the radius was expanded to include events at least 1 m away from the wall of the barrel while the top and bottom were still 2 m away from the wall of the ID.

This 2 m FV is also used as part of the event selection in the K2K analysis, as mentioned in the previous chapter. Only 112 of 174 ID events are selected, and 22.5 kton out of 32.5 kton in the ID are being utilized. There has not been a systematic study to expand the FV for more events in both K2K and water Cherenkov detectors in general. In general, an expansion in the FV from having the vertex being at least 2 m away from the wall to at least 1 m away from the wall would increase the FV and event sample size 20%, since the two scale directly. An increase in the number of events in K2K using the first expansion given below would increase the sensitivity to the oscillation results, as in shown Figure 6.1. The best fit point was chosen to be at Δm^2=0.0025eV^2 and $\sin^2 2\theta$=1.0 for a run period of 10^{20} POT. Also, the increase in the number of events would improve the quality of the oscillation analysis because of more

information being used in fit.

6.2 Expansion Study

The MC used in the FV expansion study are fully contained (FC) events from K2K's beam MC and Super-Kamiokande's atmospheric neutrino MC for the SK-I and SK-II run periods. Three event samples (single ring muon-like events, single ring electron-like events, and multi-ring events) are used in the study.

Super-Kamiokande's ID is divided into four 0.5 m regions outside the official FV (dwall>2 m). These regions are defined as follows: Region 1 is the half meter closest to the FV (2 m>dwall>1.5 m); Region 2 is 1.5 m>dwall>1 m; Region 3 satisfies 1 m>dwall>0.5 m; and Region 4 has a vertex position of dwall<0.5 m. This is chosen so that the binning is larger than the vertex resolution. Each 0.5 m region is divided into two event categories: incoming and outgoing events. Outgoing (incoming) events are events whose reconstructed vertex position times their reconstructed direction are greater-(less-)than zero, or

$$\sum_i x_i \cdot \cos(\theta_i) > (<)0, \tag{6.1}$$

where x_i is defined as the z vertex position in the top and bottom of the ID or the x and y vertex position in the barrel comprising the radius r, and θ_i is the corresponding angle with respect to the axis that the particle direction is in. For the z vertex resolution, the radius was kept the same as the radius of the official FV (r_{FV}). For the r vertex resolution, the distance from the top and bottom of the tank were kept the same as that for the official FV. Events from each region are compared to a comparison region which satisfies 2 m<dwall<2.5 m, also defined as Region 0. The latter events that are at the edge of the official FV (OFV) and should have vertex reconstruction similar to that of events outside of the OFV. Each region is summarized in Table 6.1.

6.2.1 Single ring events

The vertex resolution is different between the incoming and outgoing events in z and r. In general, outgoing events have a worse reconstruction than incoming events because of fewer hit PMTs, making it difficult to reconstruct the interaction vertex. The incoming and outgoing vertex resolutions for each region are given in Tables 6.2 and 6.3 for SK-I and K2K-I and SK-II and K2K-II, respectively. Comparing the vertex resolutions in each region outside
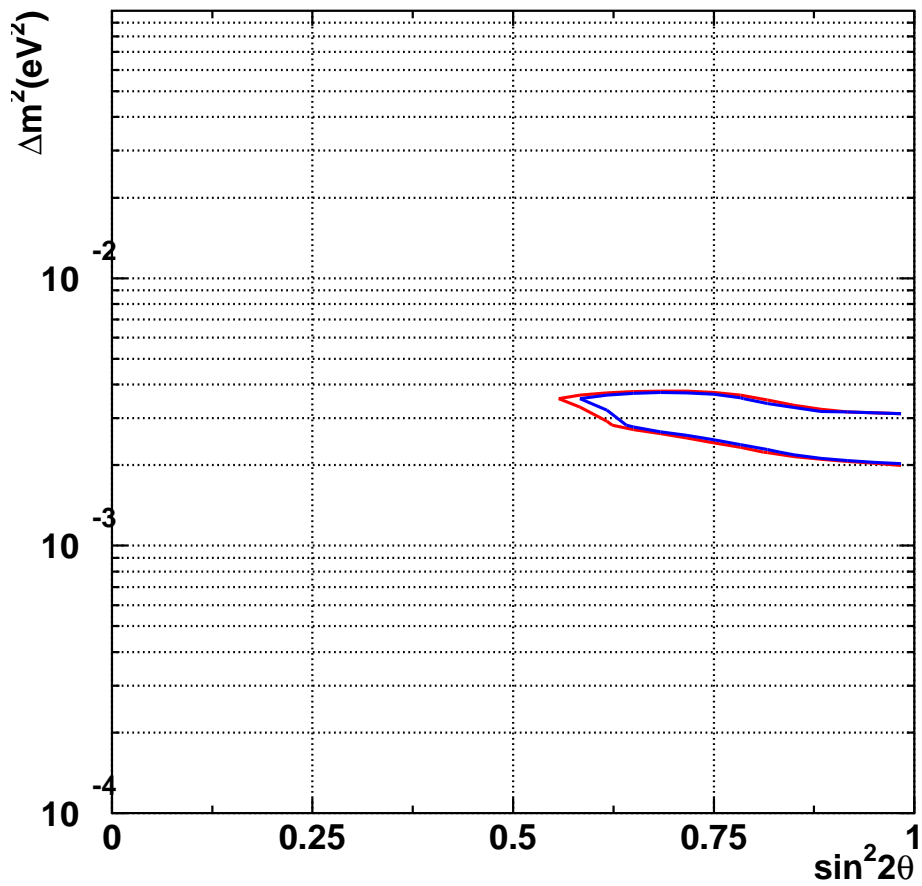
Figure 6.1: K2K sensitivity plot for the official (red) and an expanded (blue) fiducial volume for 1×10^{20} POT. The 90% confidence level lines are plotted for both.

Table 6.1: Definition of the regions outside of the official FV and of the comparison region. The official fiducial volume is defined as dwall>2 m.

Region	dwall (m)
0	2.5−2.0
1	2.0−1.5
2	1.5−1.0
3	1.0−0.5
4	0.5−0.0

Table 6.2: Reconstruction widths for incoming and outgoing SK-I (K2K-I) single ring events outside the official FV in z and r. These are compared to be compared to the comparison region, Region 0.

Region	Sample	σ_z^{in}(cm)	σ_z^{out}(cm)	σ_r^{in}(cm)	σ_r^{out}(cm)
0	SK 1Rμ	13.46±0.14	13.46±0.14	22.25±0.25	22.25±0.25
	K2K 1Rμ	11.34±0.18	11.34±0.18	18.50±0.50	18.50±0.50
1	SK 1Rμ	14.19±0.38	18.49±0.61	22.75±0.25	29.00±0.25
	K2K 1Rμ	15.25±0.49	16.16±0.49	20.50±0.50	21.00±0.50
2	SK 1Rμ	13.97±0.32	21.71±0.60	23.25±0.25	32.25±0.25
	K2K 1Rμ	14.10±0.41	17.26±0.46	21.50±0.50	26.50±0.50
3	SK 1Rμ	15.66±0.35	24.30±0.93	29.00±0.25	38.50±0.25
	K2K 1Rμ	15.25±0.49	17.81±0.96	23.00±0.50	30.50±0.50
4	SK 1Rμ	35.43±0.54	30.19±1.68	53.50±0.25	65.75±0.25
	K2K 1Rμ	36.78±1.06	15.04±1.33	49.00±0.50	42.50±0.50
0	SK 1R	18.34±0.24	18.34±0.24	32.50±0.50	32.50±0.50
	K2K 1Re	23.39±1.40	23.39±1.40	69.00±0.50	69.00±0.50
1	SK 1Re	19.25±0.58	18.70±0.68	36.50±0.50	40.00±0.50
	K2K 1Re	34.97±9.282	30.06±4.236	56.00±0.50	78.00±0.50
2	SK 1Re	20.66±0.57	20.79± 1.02	37.50±0.50	42.00±0.50
	K2K 1Re	45.69±18.90	35.10±4.781	61.00±0.50	61.00±0.50
3	SK 1Re	25.41±0.70	25.75±1.22	47.50±0.50	51.50±0.50
	K2K 1Re	32.88±5.228	27.61±3.838	63.50±0.50	54.00±0.50
4	SK 1Re	36.96±0.66	35.60±2.26	87.00±0.50	75.00±0.50
	K2K 1Re	36.84±2.16	246.3±194.9	98.00±0.50	60.50±0.50

Table 6.3: Reconstruction widths for incoming and outgoing SK-II (K2K-II) single ring events outside the official FV in z and r. These are to be compared to the comparison region, Region 0.

Region	Sample	σ_z^{in}(cm)	σ_z^{out}(cm)	σ_r^{in}(cm)	σ_r^{out}(cm)
0	SK 1Rμ	16.11±0.22	16.11±0.22	26.75±0.25	26.75±0.25
	K2K 1Rμ	13.81±0.20	13.81±0.20	22.00±0.50	22.00±0.50
1	SK 1Rμ	16.91±0.56	24.02±0.80	25.75±0.25	33.25±0.25
	K2K 1Rμ	14.39±0.46	20.45±0.57	23.50±0.50	27.00±0.50
2	SK 1Rμ	16.09±0.52	26.36±1.09	28.25±0.25	39.25±0.25
	K2K 1Rμ	13.32±0.36	20.54±0.58	22.50±0.50	30.50±0.50
3	SK 1Rμ	16.88±0.49	25.70±1.08	29.00±0.25	40.25±0.25
	K2K 1Rμ	15.04±0.43	22.42±0.79	26.00±0.50	33.00±0.50
4	SK 1Rμ	33.88±0.70	38.90±4.87	51.00±0.25	67.00±0.25
	K2K 1Rμ	33.58±0.85	19.31±1.81	49.50±0.50	50.00±0.50
0	SK 1Re	19.98±0.32	19.98±0.32	36.00±0.25	36.00±0.25
	K2K 1Re	27.94±1.46	27.94±1.46	67.00±0.50	67.00±0.50
1	SK 1Re	21.52±0.71	21.17±0.86	36.50±0.50	39.50±0.50
	K2K 1Re	34.97±9.28	30.06±4.24	56.00±0.50	78.00±0.50
2	SK 1Re	21.58±0.84	23.83±0.86	41.50±0.50	36.50±0.50
	K2K 1Re	45.69±18.90	35.10±4.78	61.00±0.50	61.00±0.50
3	SK 1Re	23.34±0.76	23.64±1.43	41.00±0.50	43.50±0.50
	K2K 1Re	32.88±5.23	27.61±3.84	63.50±0.50	54.00±0.50
4	SK 1Re	32.73±0.71	35.29±2.74	68.00±0.50	68.00±0.50
	K2K 1Re	36.84±2.16	246.3±194.9	98.00±0.50	60.50±0.50

the official FV with the comparison region yields the result: events that satisfy dwall>1 m and are incoming events are automatically included for the expanded FV. The vertex resolution for these event classes is consistent with the comparison region. For 1Re events, SK MC is better reconstructed than K2K MC since the K2K MC consists mostly of mis-dentified events from ν_μ interactions, making the vertex reconstruction worse than if they were events from ν_e interactions.

While it is reasonable to include incoming events based on their vertex reconstruction, there are events that are technically outgoing by Equation 6.1 that still deposit enough light to make their reconstructed vertex consistent the vertex resolution in the comparison region. In order to include these outgoing events, and to make a simply defined expanded FV, the function *towall* is used. *towall* calculates the distance to the wall from the vertex position along the particle direction. As an *a priori* assumption, it seems reasonable to assume that the detected particle should travel at least 200 cm. This would ensure that all events in the official FV are kept and that enough PMTs are hit in the outer FV region for the event vertex to be reconstructed. In SK-II, since it has half the photocoverage of SK-I, there is an extra factor of $\sqrt{2}$ for the Cherenkov light to hit 12 ID PMTs, implying that the *a priori towall* selection value may go as high as 300 cm.

The top row of Figure 6.2 gives a general procedure on how the *towall* criterion is determined. The vertex resolution in z and r for SK-I 1Rμ MC is plotted as a function of *towall* for events in the added region between 1 m and 2 m away from the ID wall. The vertex resolution is then compared to the vertex resolution in the comparison region and events in the comparison region with *towall*<250 cm, which comprise of events going perpendicularly into the wall. The vertex resolution in r is consistent with the vertex reconstruction of those events in the comparison region going directly towards the ID wall. In the SK-I 1Rμ sample, the r vertex does not drive the *towall* selection. For the z vertex reconstruction, there is a dependence on the distance the particle would travel. Events with *towall*>375 cm are consistent, or better, than the reconstructed vertex of the comparison region. Events with *towall*<200 cm are inconsistent with the comparison region. The events with 200 cm<*towall*<375 cm are accepted because the error of the resolution is consistent with the central value of the vertex resolution in the comparison region. Using similar arguments, the 1Re sample for SK-I also has a *towall* selection of 200 cm.

For SK-II, Figure 6.3 has the same selection criteria for μ-like events, though for e-like events, the top and bottom of the detector drives the cut value to *towall*>300 cm. For K2K-I and K2K-II 1Rμ (1Re) events, Figure 6.4, gives a *towall* selection of 200 cm (200 cm) and 200 cm (300 cm), respectively.
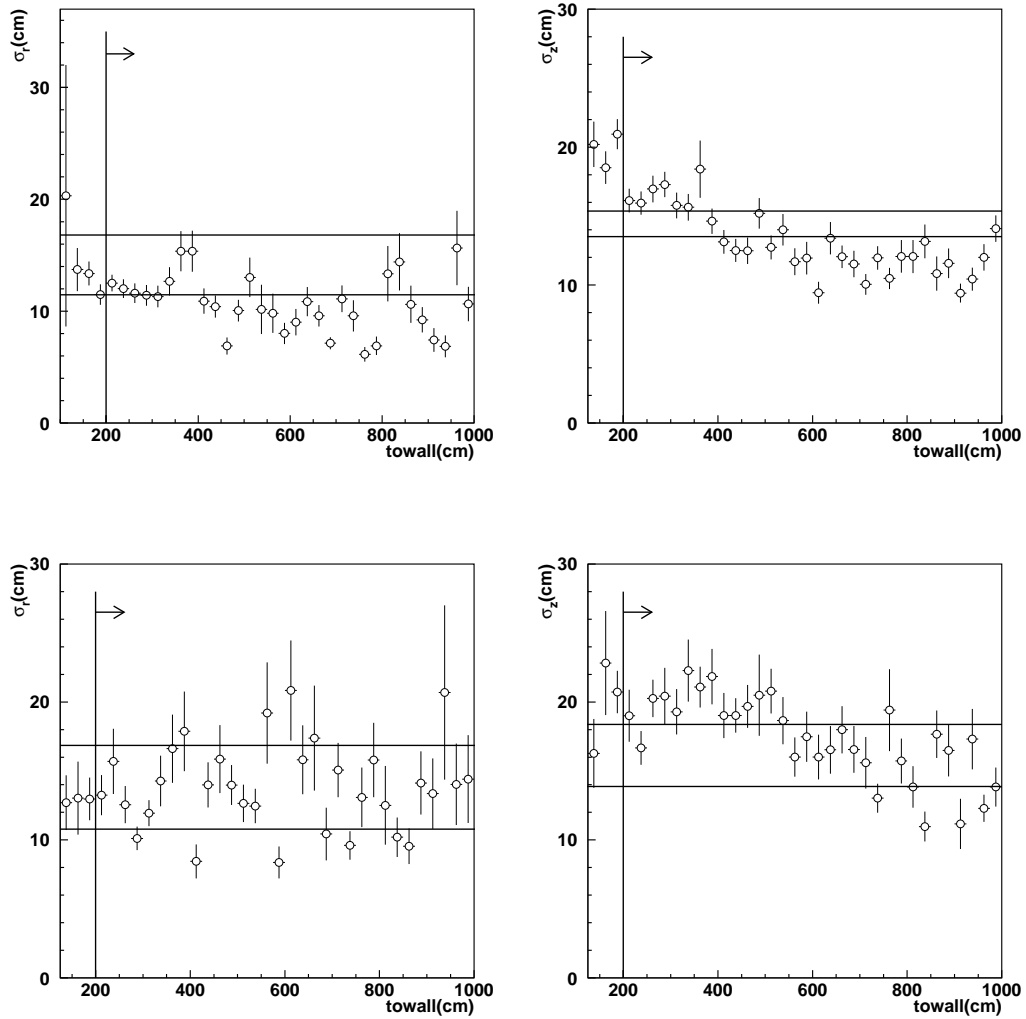
Figure 6.2: Vertex resolution vs. *towall* for the z and r coordinates in SK-I. The upper line is the width in the comparison region for events with *towall*<250 cm. The lower line is all events in the comparison region. The top (bottom) row is 1Rμ (1Re) events. The left column is the r vertex resolution; the right column is the z vertex resolution.

Figure 6.3: Vertex resolution vs. *towall* for the z and r coordinates in SK-II. The upper line is the width in the comparison region for events with *towall*<250 cm. The lower line is all events in the comparison region. The top (bottom) row is $1R\mu$ (1Re) events. The left column is the r vertex resolution; the right column is the z vertex resolution.
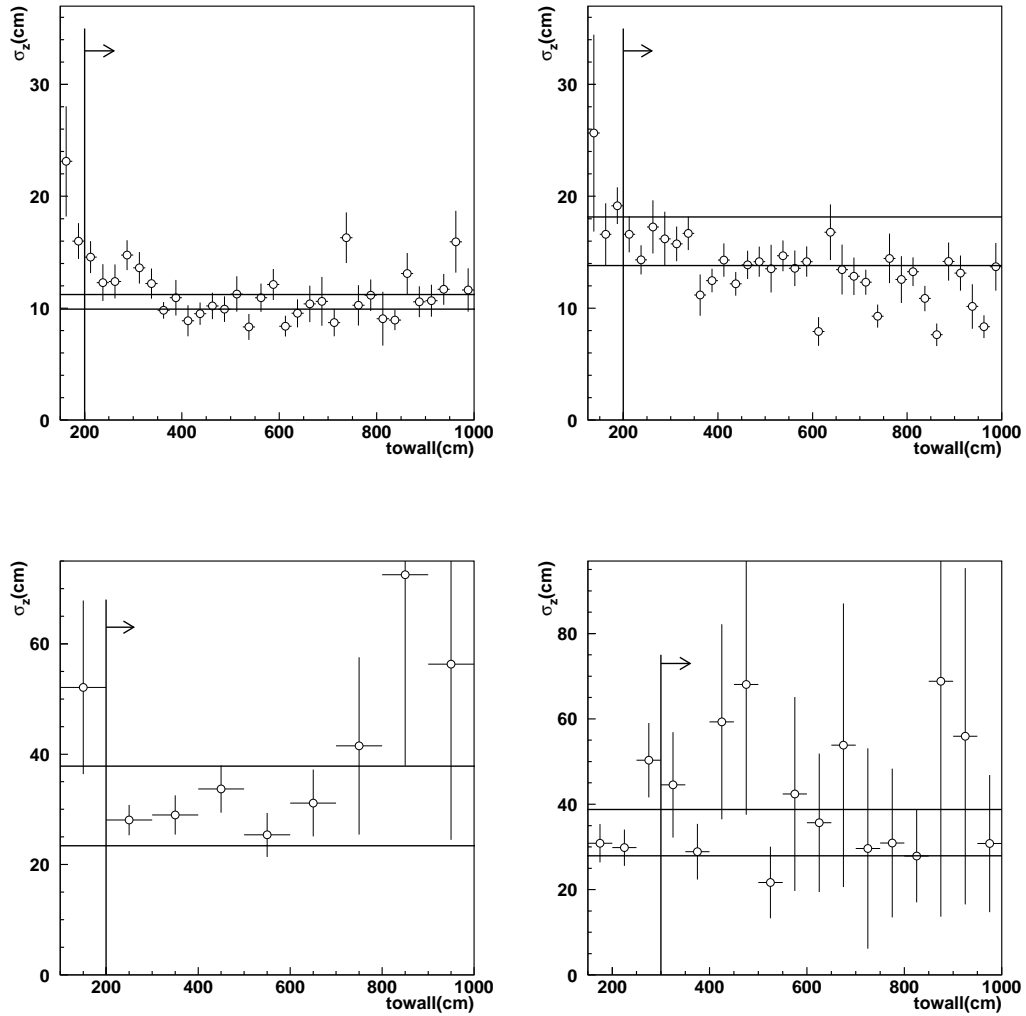
Figure 6.4: Vertex resolution vs. *towall* for the *z* coordinates in K2K. The upper line is the width in the comparison region for events with *towall*<250 cm. The lower line is all events in the comparison region. The top (bottom) row is the 1Rμ (1Re) sample. The left (right) column is K2K-I (K2K-II) *z* vertex resolution.

Table 6.4: Reconstruction widths for the official and new FVs. in SK and K2K with the percent change.

Sample	$\sigma_{Official}$ (cm)	σ_{New} (cm)	Difference (%)
SK-I 1Rμ z	12.43±0.04	12.65±0.04	1.8
SK-I 1Rμ r	20.50±0.25	20.75±0.25	1.2
SK-II 1Rμ z	14.97±0.06	15.29±0.06	2.1
SK-II 1Rμ r	24.25±0.25	25.00±0.25	3.1
K2K-I 1Rμ z	10.06±0.04	10.35±0.04	2.9
K2K-I 1Rμ r	18.25±0.25	17.50±0.25	-4.1
K2K-II 1Rμ z	12.12±0.05	12.40±0.05	2.3
K2K-II 1Rμ r	20.25±0.25	20.50±0.25	1.2
SK-I 1Re z	15.38±0.07	15.91±0.06	3.4
SK-I 1Re r	28.25±0.25	28.50±0.25	0.9
SK-II 1Re z	17.63±0.09	18.12±0.09	2.8
SK-II 1Re r	31.50±0.25	33.50±0.25	6.3
K2K-I 1Re z	23.20±0.57	24.75±0.53	6.7
K2K-I 1Re r	66.50±0.25	64.25±0.25	-3.4
K2K-II 1Re z	26.78±0.54	27.15±0.49	1.4
K2K-II 1Re r	75.75±0.25	75.00±0.50	-2.3

The lower right plot in Figure 6.4 is cut at 300 cm because of the fact that the first two bins have low statistics with a fitted vertex resolution much smaller than the number of events allows. The third bin is what drives the decision of whether the *towall* cut should be at 250 cm or 300 cm. Since it is above the comparison region resolutions, and the next bin is consistent with them, 300 cm is used in the selection criteria.

With these new events, the new and official FV vertex resolutions are then compared to see how much the vertex resolution changes from the added events and if the tails are significanctly affected. The increase of events, based only on the increase of the wall cut, is expected to be ∼20% because the number of events scales with the increase in fiducial mass, though this will be smaller because of the *towall* selection criteria.

In SK-I, there is a 16.0% increase in events from the new FV and a 16.4% in SK-II. In K2K, there is a 15.5% increase in K2K-I and 16.1% increase in K2K-II. In the K2K beam MC and the SK atmospheric MC, the discrepancy in the percent increase is an effect of how the event fitters recognize single or

Table 6.5: Percentage of events more than 3σ from the mean of the fitted reconstruction width for SK and K2K.

Sample	Over 3σ in z (%)	Over 3σ in r (%)
SK-I OFV1Rμ	8.06±0.08	7.24±0.14
SK-I New FV1Rμ	8.12±0.07	7.39±0.11
SK-II OFV1Rμ	7.49±0.09	6.63±0.13
SK-II New FV1Rμ	7.55±0.10	6.53±0.13
K2K-I OFV1Rμ	4.64±0.09	5.32±0.12
K2K-I New FV1Rμ	4.60±0.09	5.29±0.13
K2K-II OFV1Rμ	3.75±0.09	4.59±0.13
K2K-II New FV1Rμ	3.71±0.09	4.52±0.11
SK-I OFV1Re	8.68±0.10	6.79±0.13
SK-I New FV1Re	8.82±0.09	7.20±0.12
SK-II OFV1Re	7.87±0.13	6.12±0.12
SK-II New FV1Re	7.82±0.12	5.73±0.12
K2K-I OFV1Re	9.72±0.46	5.20±0.33
K2K-I New FV1Re	8.74±0.43	4.79±0.30
K2K-II OFV1Re	7.74±0.43	3.42±0.24
K2K-II New FV1Re	7.75±0.38	3.62±0.23

Table 6.6: Angular resolution for SK and K2K 1R μ-like and e-like events, respectively, with percentage increase in the resolution. Errors are one bin width.

Sample	$\sigma_{Official}$ (°)	σ_{New} (°)	Difference (%)
SK-I 1Rμ	1.96±0.02	2.16±0.02	10.2
SK-II 1Rμ	2.06±0.02	2.16±0.02	4.9
SK-I 1Re	4.78±0.02	5.00±0.02	4.6
SK-II 1Re	5.20±0.02	5.50±0.02	5.8
K2K-I 1Rμ	1.76±0.02	1.66±0.02	-5.7
K2K-II 1Rμ	1.82±0.02	1.88±0.02	3.3
K2K-I 1Re	4.78±0.02	5.50±0.02	15.1
K2K-II 1Re	5.72±0.02	5.56±0.02	-2.8

multi-ring events because of the difference in the photocoverage in SK-I and SK-II. Results on how the vertex resolution changed are given in Table 6.4. In order to ensure the tails are not significantly affected with the newly expanded FV, the percentage of events greater than 3σ from the mean is calculated for each coordinate. For the z vertex, 1σ is determined by a Gaussian fit of the vertex resolution. For the r vertex, 1σ was found by finding the number of bins that held the first 68% of events and making that value the vertex resolution, consistent with a single-sided Gaussian. The results of the tail check are in Table 6.5. The tails of the vertex resolution in the SK-I and SK-II run periods are consistent (see Figures 6.5 and 6.6).

In addition to the vertex tail comparison, three other checks were made with the new FV and compared to the official FV. These were the angular resolution, particle identification (PID) likelihood, and ring counting likelihood (DLFCT). These latter two are used in the event selection for the energy spectrum shape and differences may affect systematic errors.

The angular resolution is also checked between the new and official FV. $\Delta\theta$ was calculated by taking the fitted direction of the found Cherenkov ring and multiplying it by the true direction of the muon in case of 1Rμ events or the electron for 1Re events. There is a definite increase in the angular resolution, but as is shown in Table 6.6, it is not cause for concern. In all cases for SK, there is at most a 0.3° increase between the official and new FVs. K2K's increase in the angular resolution for the 1Re sample comes from the large number of muons or charged pions that are misidentified. This would lead to a larger discrepancy between the true direction and fitted direction of the ring
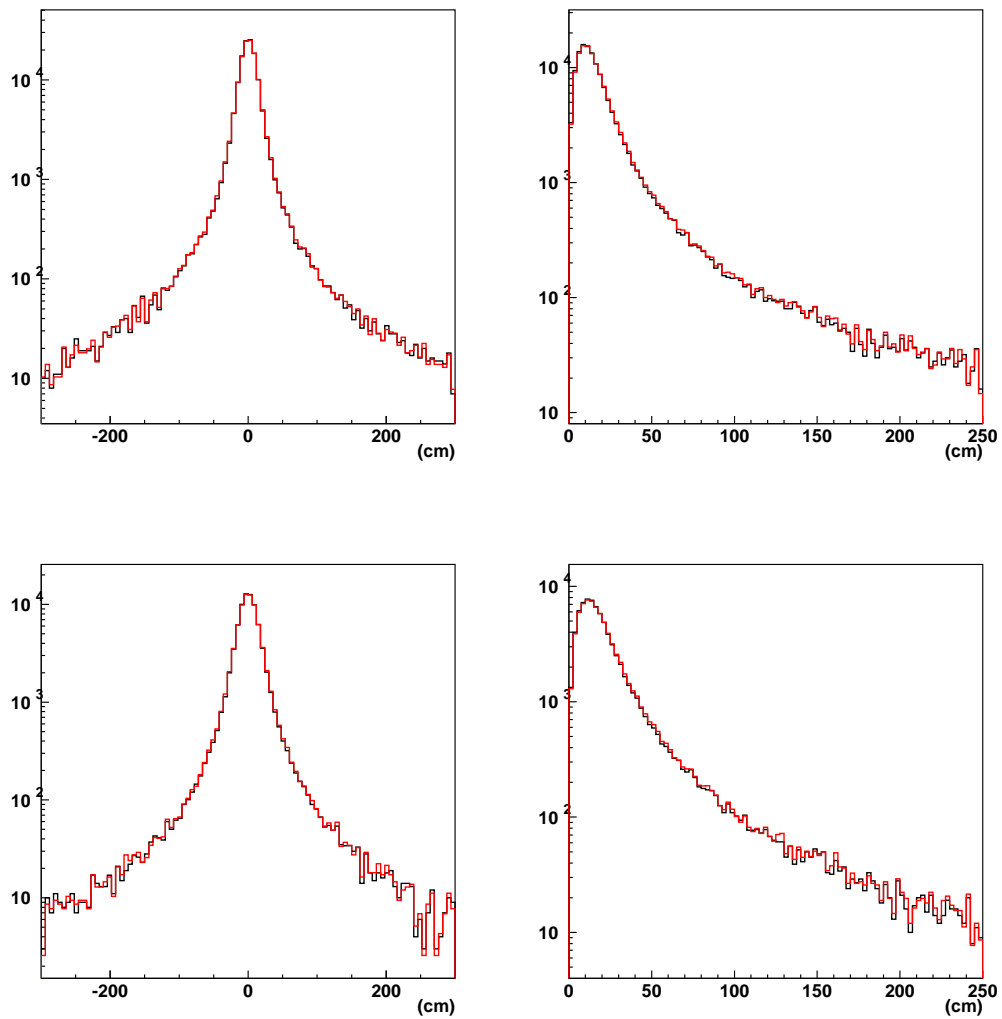
Figure 6.5: Overlay of the official FV (black) and new FV (red) vertex reconstruction for z (left) and r (right) for SK-I (top) and SK-II (bottom) 1Rμ events.
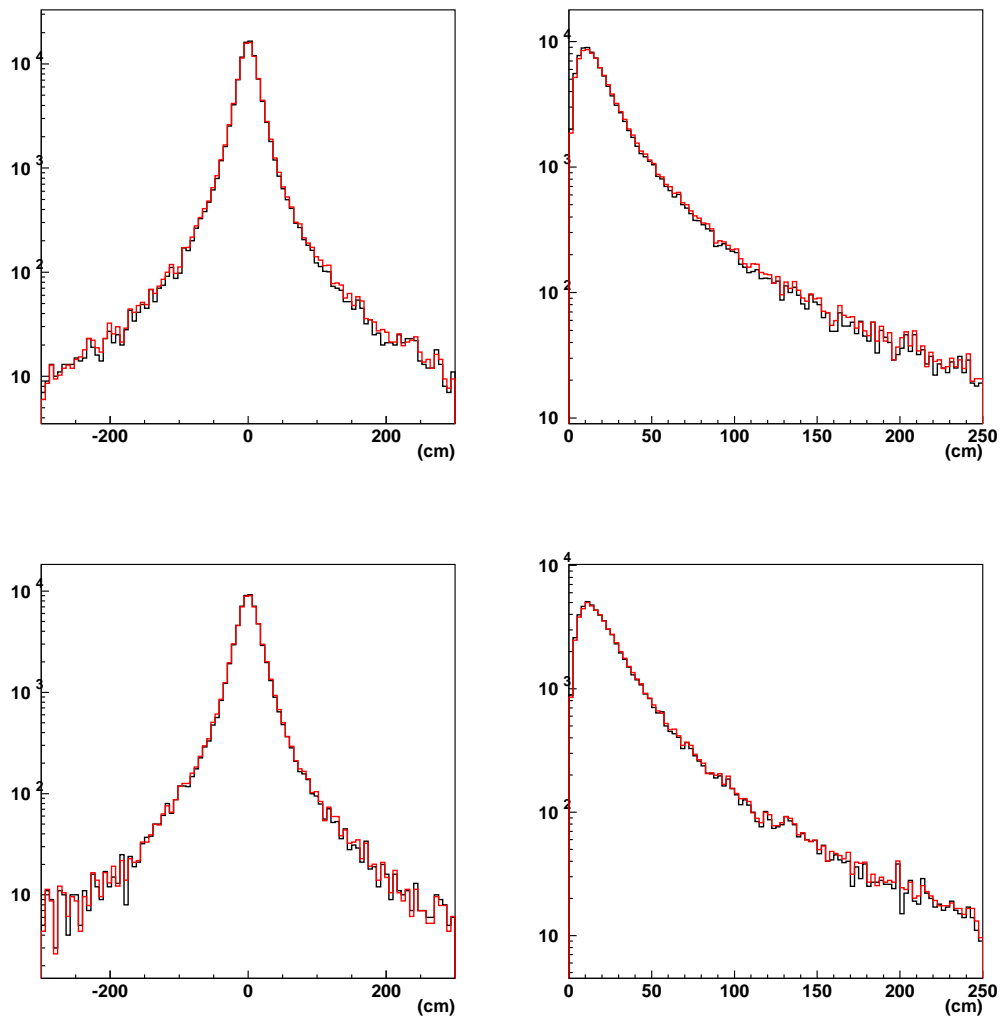
Figure 6.6: Overlay of the official FV (black) and new FV (red) vertex reconstruction for z (left) and r (right) for SK-I (top) and SK-II (bottom) 1Re events.

Table 6.7: Percentage of events greater than 3σ in $\Delta\theta$ for SK and K2K. Added Events are events that are in the new FV but not in the official FV.

Sample	Over $3\sigma_{1R\mu}$ (%)	Over $3\sigma_{1Re}$ (%)
SK-I OFV	9.30±0.10	19.34±0.12
SK-I Comparison Region	10.37±0.31	21.53±0.44
SK-I Added Events	11.42±0.23	23.40±0.32
SK-I New FV	9.26±0.09	20.00±0.12
SK-II OFV	8.61±0.11	20.60±0.16
SK-II Comparison Region	10.00±0.36	22.00±0.55
SK-II Added Events	10.72±0.27	24.00±0.43
SK-II New FV	8.76±0.10	20.94±0.15
K2K-I OFV	7.89±0.13	6.37±0.19
K2K-I Comparison Region	8.98±0.46	10.45±0.79
K2K-I Added Events	8.74±0.33	12.02±0.62
K2K-I New FV	8.48±0.14	6.54±0.18
K2K-II OFV	6.80±0.13	6.94±0.47
K2K-II Comparison Region	6.06±0.36	11.21±2.11
K2K-II Added Events	7.11±0.28	11.97±1.53
K2K-II New FV	6.74±0.11	7.09±0.44

Table 6.8: Percentage of CCQE events from ν_μ (ν_e) interactions misidentified as e-like (μ-like) for SK-I and SK-II. Added Events are events that are in the new FV but not in the official FV.

Sample	Mis-ID$_\mu$ (%)	Mis-ID$_e$ (%)
SK-I OFV	0.79±0.07	0.95±0.10
SK-I Comparison Region	2.74±0.45	2.81±0.55
SK-I Added Events	3.59±0.37	2.77±0.55
SK-I New FV	1.18±0.08	1.20±0.10
SK-II OFV	1.11±0.11	0.65±0.10
SK-II Comparison Region	1.51±0.42	1.88±0.59
SK-II Added Events	2.34±0.38	1.83±0.44
SK-II New FV	1.28±0.11	0.71±0.10
K2K-I OFV	1.21±0.17	0.73±0.23
K2K-I Comparison Region	4.00±1.05	1.57±1.10
K2K-I Added Events	4.94±0.84	2.34±1.03
K2K-I New FV	1.70±0.18	0.95±0.24
K2K-II OFV	1.01±0.14	0.42±0.42
K2K-II Comparison Region	0.97±0.48	0.00±0.00
K2K-II Added Events	2.79±0.84	0.00±0.00
K2K-II New FV	1.25±0.15	0.35±0.35

since the particle would be assumed to be an electron. The tails are checked using the same 1σ definition as the r vertex reconstruction. From Table 6.7, the tails of the angular resolution are consistent between the official and new FVs.

The PID misidentification is found by selecting single ring CCQE events in the K2K or SK MC that do not have a Δ resonance or pion exchange in the nucleus. For ν_μ interactions, CCQE events should be μ-like since the visible particle will have a sharp Cherenkov ring. For ν_e events, CCQE events have a visible electron, which has a showering ring. If the PID likelihood, defined in Appendix A is less than or equal to zero, the event is considered μ-like; if it is greater than zero, it is considered e-like. CCQE events from ν_μ (ν_e) interactions that are identified as e-like (μ-like) are considered mis-identified. The results for the official and new FVs are in Table 6.8. In the cases where the OFV sample and new FV sample do not have consistent PID misidentification, the comparison region and added events are consistent.

The ring counting likelihood mis-counting is calculated from CCQE events

Table 6.9: Number of events mis-identified as being multi-ring events from the CCQE ν_μ and ν_e samples.

Sample	Mis-counted$_\mu$ (%)	Mis-counted$_e$ (%)
SK-I OFV	4.53±0.16	7.89±0.26
SK-I Comparison Region	6.27±0.66	10.09±0.99
SK-I Added Events	5.78±0.47	11.16±0.76
SK-I New FV	4.70±0.16	8.34±0.25
SK-II OFV	3.76±0.19	7.65±0.32
SK-II Comparison Region	3.43±0.62	6.29±1.03
SK-II Added Events	4.71±0.53	7.14±0.83
SK-II New FV	3.90±0.18	7.38±0.30
K2K-I OFV	7.29±0.38	9.58±0.76
K2K-I Comparison Region	10.00±1.56	16.67±3.11
K2K-I Added Events	9.20±1.10	19.68±1.95
K2K-I New FV	7.54±0.36	11.02±0.75
K2K-II OFV	5.78±0.33	7.39±1.63
K2K-II Comparison Region	6.02±1.14	15.00±7.98
K2K-II Added Events	6.85±0.88	10.87±4.59
K2K-II New FV	5.93±0.31	7.92±1.55

that are μ-like (e-like) and that should only have one ring. The ring counting likelihood (DLFCT) calculates the likelihood that an event has one or many rings. If the likelihood is less than or equal to zero (DLFCT$\leq$0), it is defined to be a single ring event, otherwise it is a multi-ring event. Any CCQE events where the likelihood was greater than zero (DLFCT$>$0) were considered events that had the ring number mis-counted. These results are summarized in Table 6.9. For all of SK and K2K, the ring miscounting is consistent between the OFV and new FV CCQE samples.

6.2.2   Multi-ring events

The multi-ring events are treated slightly different than the single ring events. This section presents one treatment of the multi-ring event sample. In this study, because of the fact that all reconstructed rings are fitted to the same vertex and that each ring has a different *towall* value, an effective *towall* is created. For this study, the effective *towall* is calculated by adding vectorally the *towall* from each ring to get a net direction that the particles are traveling in. The new direction information is then used to recalculate the *towall* distance from the event vertex. The effective *towall* ($towall_{eff}$) is then used in the same manner as *towall* for the single ring events.

At this point, the same treatment is given to the multi-ring events as a single ring event. An initial check comparing the vertex resolution of incoming and outgoing events outside of the official FV using $towall_{eff}$ is performed. Incoming and outgoing events are defined based on the first ring's direction and the event's vertex using Equation 6.1. The events outside of the OFV were divided into the same four regions, while the comparison region remains defined as events whose vertex is inside the first 0.5m of the OFV. The events in the comparison region going perpendicularly into the wall have $towall_{eff}<250$ cm.

For the SK-I, K2K-I, K2K-II, and SK-II vertex resolution comparisons, the incoming events with dwall$>$1 m remain consistent with the vertex reconstruction for events in the comparison region. The outgoing events' r vertex resolution for the K2K-II Region 3 and 4 are consistent with the comparison region, though these regions have small statistics, making it difficult to determine the true vertex resolution. Incoming events in the region where 1 m$<$dwall$<$2 m, in addition to events in the official FV, are included in the data sample. See Table 6.10 and 6.11 for a summary of the vertex reconstruction widths for these regions.

To include as many events as possible, the events that satisfied 1 m$<$dwall$<$2 m were plotted with respect to $towall_{eff}$. Using the same criteria as the single ring events, multi-ring events with dwall$>$1 m are selected for the expanded

Table 6.10: Reconstruction widths for incoming and outgoing SK-I (K2K-I) multi-ring events outside the official FV in z and r. These are to be compared to Region 0.

Region	Experiment	σ_z^{in}(cm)	σ_z^{out}(cm)	σ_r^{in}(cm)	σ_r^{out}(cm)
0	SK	21.18±0.30	21.18±0.30	42.25±0.25	42.25±0.25
	K2K	15.49±0.33	15.49±0.33	39.25±0.25	39.25±0.25
1	SK	19.30±0.56	22.90±0.99	38.50±0.25	51.25±0.25
	K2K	12.94±0.54	18.00±1.12	33.00±0.25	39.00±0.25
2	SK	20.92±0.88	22.02±1.33	39.75±0.25	52.50±0.25
	K2K	16.56±1.06	17.72±1.20	31.75±0.25	42.25±0.25
3	SK	23.32±0.72	26.97±1.88	48.75±0.25	56.25±0.25
	K2K	18.28±1.05	18.62±1.34	37.00±0.25	27.00±0.25
4	SK	33.67±0.88	26.18±3.35	78.25±0.25	49.75±0.25
	K2K	29.92±1.53	17.70±2.56	52.00±0.25	13.50±0.25

Table 6.11: Reconstruction widths for incoming and outgoing SK-II (K2K-II) multi-ring events outside the official FV in z and r. These are supposed to be compared to Region 0.

Region	Experiment	σ_z^{in}(cm)	σ_z^{out}(cm)	σ_r^{in}(cm)	σ_r^{out}(cm)
0	SK	23.97±0.43	23.97±0.43	46.00±0.25	46.00±0.25
	K2K	18.79±0.34	18.79±0.34	39.75±0.25	39.75±0.25
1	SK	22.53±1.11	25.60±1.38	45.00±0.25	43.50±0.25
	K2K	17.10±0.60	22.16±1.00	35.25±0.25	43.25±0.25
2	SK	23.15±1.11	22.54±1.02	45.75±0.25	42.25±0.25
	K2K	18.11±0.86	20.22±0.96	37.50±0.25	43.25±0.25
3	SK	26.65±1.25	28.04±2.47	56.25±0.25	53.50±0.25
	K2K	21.85±1.05	22.70±1.56	40.50±0.25	41.25±0.25
4	SK	36.30±1.16	25.48±4.25	72.00±0.25	37.75±0.25
	K2K	29.71±1.46	28.56±6.69	51.75±0.25	20.00±0.25

Table 6.12: Reconstruction widths for the official and new FVs. in SK and K2K multi-ring events with the percent change.

Sample	$\sigma_{Official}$ (cm)	σ_{New} (cm)	Difference (%)
SK-I z	20.73±0.08	20.93±0.04	0.96
SK-I r	42.00±0.25	41.50±0.25	-1.19
SK-II z	23.89±0.13	24.01±0.12	0.50
SK-II r	48.25±0.25	47.50±0.25	-1.55
K2K-I z	14.88±0.09	15.14±0.09	1.75
K2K-I r	34.75±0.25	34.75±0.25	0.00
K2K-II z	17.27±0.10	17.57±0.09	1.74
K2K-II r	38.50±0.25	38.50±0.25	0.00

FV. For SK-I and SK-II, multi-ring events must also have $towall_{eff}$ >200 cm. In K2K-I (K2K-II), multi-ring events must also have $towall_{eff}$>250 cm (300 cm). See Figure 6.7 for the z vertex resolution as a function of $towall_{eff}$.

There were a series of checks with the proposed FV of dwall>1 m and $towall_{eff}$>200 cm for SK-I and SK-II. The first was an overlay of the vertex reconstruction plots for z and r in both SK-I and SK-II. As shown in Figure 6.8, there is a small change in the width for both of these. More importantly, the tails in each of the distributions match up well. As before with the 1R μ-like and e-like samples, to see if there was any increase of the number of events in the tail, the percentage of events more than 3σ in z and r for SK-I, K2K-I, K2K-II, and SK-II was calculated for the official and new FV. The results of the change of the reconstruction width and the tail check for the vertex reconstruction are summarized in Tables 6.12 and 6.13.

There are two other checks that can be done similarly to the μ-like and e-like samples in the two previous sections. The first is checking the angular resolution, $\Delta\theta$, and the other is the PID misidentification. For each of these checks, only CCQE events from ν_μ interactions are used. It is easy to check the mis-idenitfication of two ring events since the muon and proton are both categorized as μ-like. The angular resolution is checked using CCQE ν_μ events because the muon will be the more energetic of the two particles produced after the interaction, whereas for CC non-QE events, one of the hadrons produced could be the most energetic partcle. The most energetic particle is the first ring to be found. The angular resolution for SK and K2K experience a larger increase for the first particle than the error allows. The percentage of events
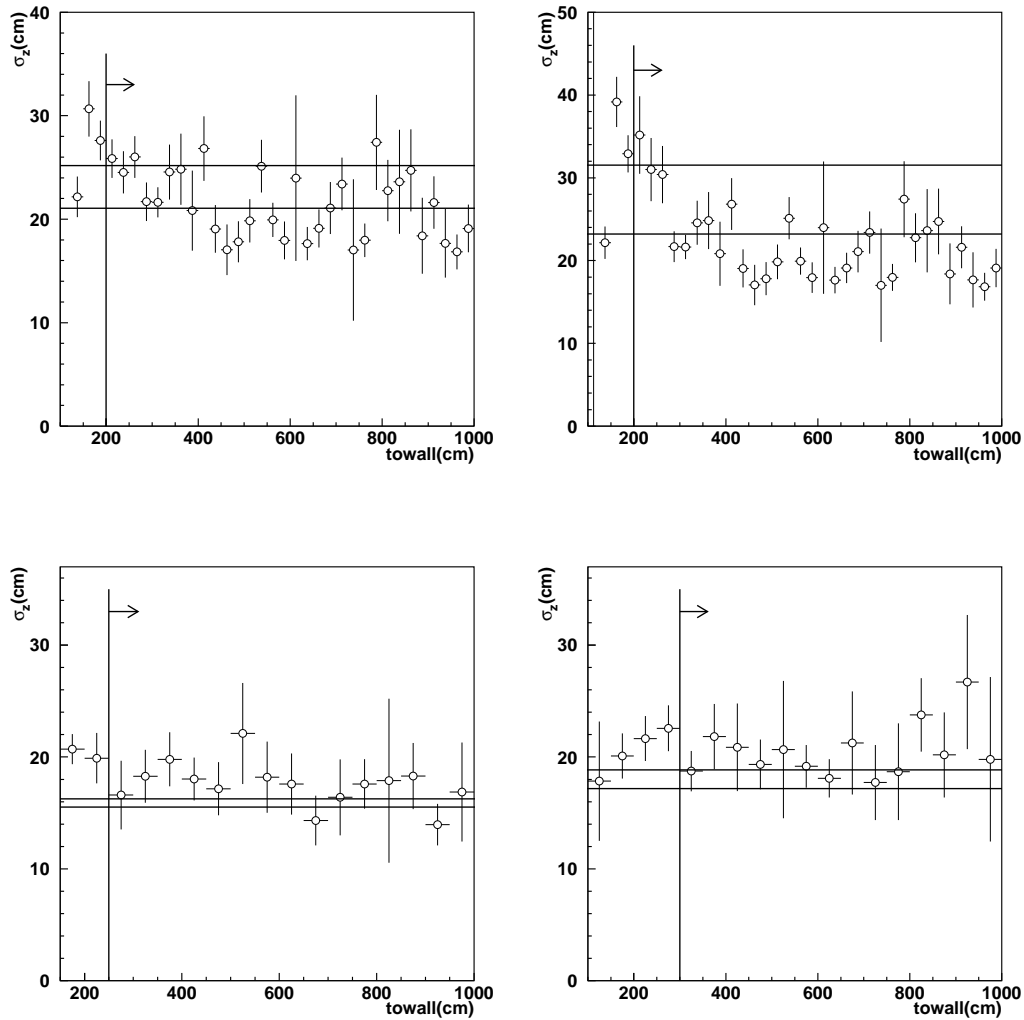
Figure 6.7: Vertex resolution vs. $towall_{eff}$ for the multi-ring z coordinate in SK (top) and K2K (bottom). The plots on the left (right) have the SK-I (SK-II) photocoverage. The upper line is the vertex resolution in the comparison region for events with $towall_{eff} < 250$ cm. The lower line is the vertex resolution of all events in the comparison region.

Table 6.13: Percentage of events greater than 3σ of the fitted reconstruction width for SK and K2K multi-ring events.

Sample	Over 3σ in z (%)	Over 3σ in r (%)
SK-I OFV	8.60±0.09	6.10±0.11
SK-I New FV	8.71±0.09	6.47±0.10
SK-II OFV	8.98±0.14	6.74±0.11
SK-II New FV	8.85±0.12	6.88±0.11
K2K-I OFV	4.16±0.14	4.59±0.13
K2K-I New FV	4.78±0.11	5.17±0.13
K2K-II OFV	4.20±0.13	5.11±0.12
K2K-II New FV	4.38±0.11	5.42±0.13

Table 6.14: Angular resolution for SK and K2K multi-ring events with percentage increase in the resolution. Errors are one bin width.

Reconstructed $\sigma_{\Delta\theta}$	$\sigma_{Official}$ (degrees)	σ_{New} (degrees)	Difference (%)
SK-I	4.88±0.02	6.38±0.02	30.7
SK-II	4.80±0.02	6.18±0.02	28.8
K2K-I	3.42±0.02	4.04±0.02	18.1
K2K-II	3.68±0.02	4.00±0.02	8.7

Table 6.15: Percentage of events greater than 3σ in $\Delta\theta$ for SK and K2K. OFV stands for official FV. The subscripts I and II represent the SK-I and SK-II photocoverages, respectively.

Sample	Over $3\sigma_I$(%)	Over $3\sigma_{II}$(%)
SK OFV	15.36±0.44	14.98±0.54
SK Comparison Region	20.60±1.35	20.51±1.79
SK Added Events	21.67±0.90	22.39±1.22
SK New FV	19.04±0.42	17.75±0.51
K2K OFV	12.66±0.88	14.13±0.80
K2K Comparison Region	22.04±2.65	25.87±3.09
K2K Added Events	21.87±1.84	23.77±2.11
K2K New FV	15.43±0.74	15.38±0.76

10 4
10 3
10 2
10
-200
0
200
(cm)
10 4
10 3
10 2
0
50
100
150
200
250
(cm)
10 4
10 3
10 2
10
-200
0
200
(cm)
10 3
10 2
0
50
100
150
200
250
(cm)
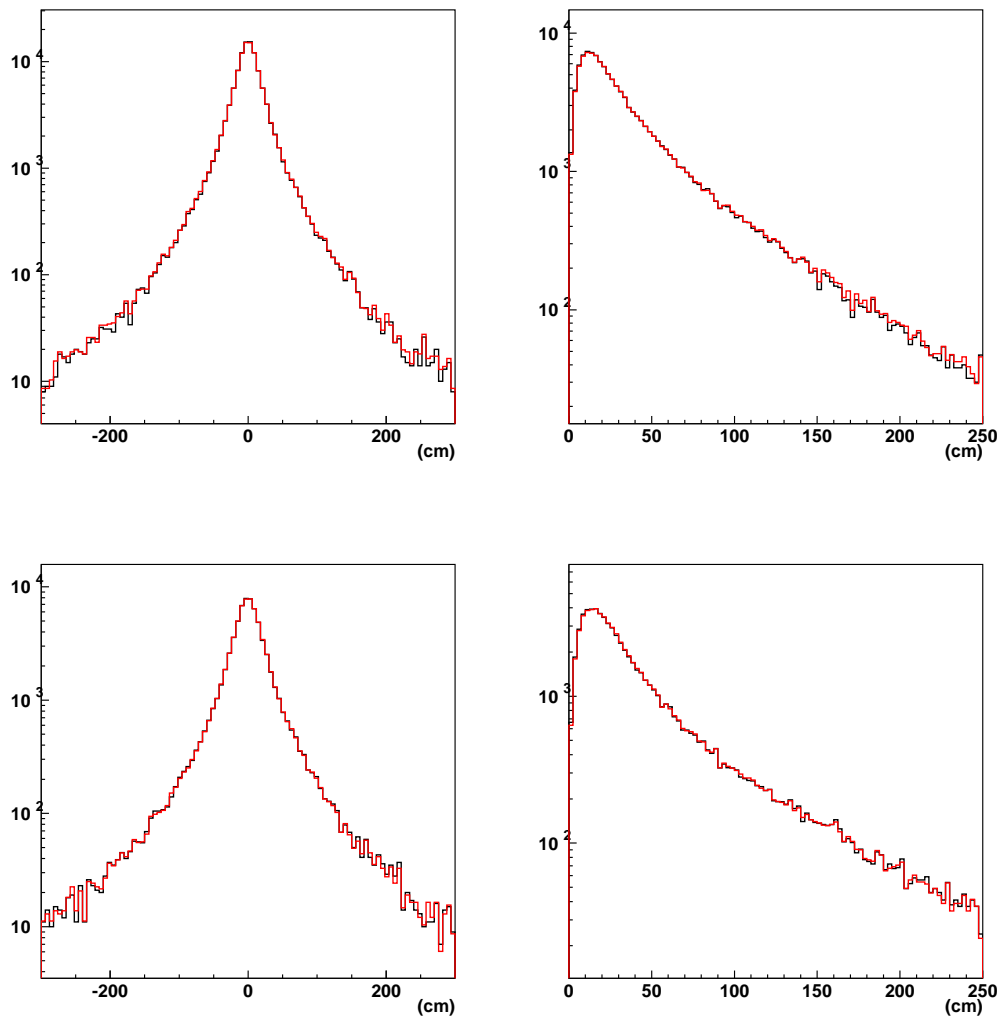
Figure 6.8: Overlay of the official FV (black) and new FV (red) vertex resolution for z (left) and r (right) for SK-I (top) and SK-II (bottom) multi-ring events.

Table 6.16: Percentage of CCQE events from ν_μ interactions misidentified as e-like for SK and K2K multi-ring events.

Sample	Mis-ID ring 1 (%)	Mis-ID ring 2 (%)
SK-I OFV	18.71±0.66	52.89±0.84
SK-I Comparison Region	33.33±2.15	37.29±2.21
SK-I Added Events	39.16±1.51	42.61±1.53
SK-I New FV	23.37±0.63	50.55±0.74
SK-II OFV	22.99±0.91	62.61±1.05
SK-II Comparison Region	29.33±3.04	55.11±3.32
SK-II Added Events	37.70±2.05	49.73±2.12
SK-II New FV	26.06±0.85	59.93±0.95
KK-I OFV	11.23±0.73	55.30±1.14
KK-I Comparison Region	22.86±2.68	48.57±3.19
KK-I Added Events	26.44±1.97	49.90±2.23
KK-I New FV	14.21±0.72	54.13±1.02
K2K-II OFV	11.84±0.74	55.02±1.15
K2K-II Comparison Region	22.89±2.96	50.75±3.53
K2K-II Added Events	22.06±2.05	55.15±2.46
K2K-II New FV	13.31±0.71	55.17±1.05

over 3σ, though, remains consistent between the two definitions.

The PID mis-identification was checked using a similar method to the one ring events. The mis-ID percentages can be seen in Table 6.16. For both rings, the mis-ID percentages are very high, but are consistent between the official FV and the new FV as well as the 0.5m inside the official FV and the added events from the New FV. The reason the events are so poorly identified is that the precision vertex fitter used on 1R events has not been applied and that the PID algorithm only uses the pattern information, not the pattern and opening angle information.

Ring Counting Test

There is an additional check on the ring counting efficiency between the comparison region in the OFV and the newly added region based only on the distance to the nearest wall in the FV; the *towall* selection criteria was not included in order to check the consistency of the ring counting algorithm between the different regions. The newly added region to the FV was divided into two

Table 6.17: Bin definition for the tracklength between a charged pion and its decay products.

Bin number	Track Length (cm)
1	0-20
2	20-40
3	40-60
4	60-80
5	80-100
6	100-150
7	150-200
8	200-

regions with 2 m>dwall>1.5 m and 1.5 m>dwall>1 m. Charged-current single charged pion (CC1π) events were selected from either the SK or K2K MC such that each event has a muon and a charged pion whose momenta was above the Cherenkov threshold and decaying somewhere in Super-Kamiokande's ID. The track length is defined as the distance between the true neutrino interaction vertex and the true decay vertex of the pion.

The track length is divided into eight bins based on length (see Table 6.17) with the percentage of single ring events placed into each bin. As seen in Figure 6.9, the percentage of events found for bins 1-5 are consistent. Bins 6-8 have low statistics, giving a larger variation between the different volumes. The high percentage of single ring events found for short track lengths is from the inability of the ring-finding algorithm to find the rings of both the muon and pion since the energy of the pion is at or below the detection threshold of SK.

6.3   Data Checks

6.3.1   Super-Kamiokande data

Using the new FV definition for SK-I and SK-II, the Super-Kamiokande atmospheric data and MC were compared. In principle, the basic distributions of data and MC should be consistent. Using the two flavor mixing neutrino oscillation parameters from Ref. [27], the MC was oscillated and normalized to the livetime for data taking in SK-I or SK-II. Figure 6.10 shows the SK-I
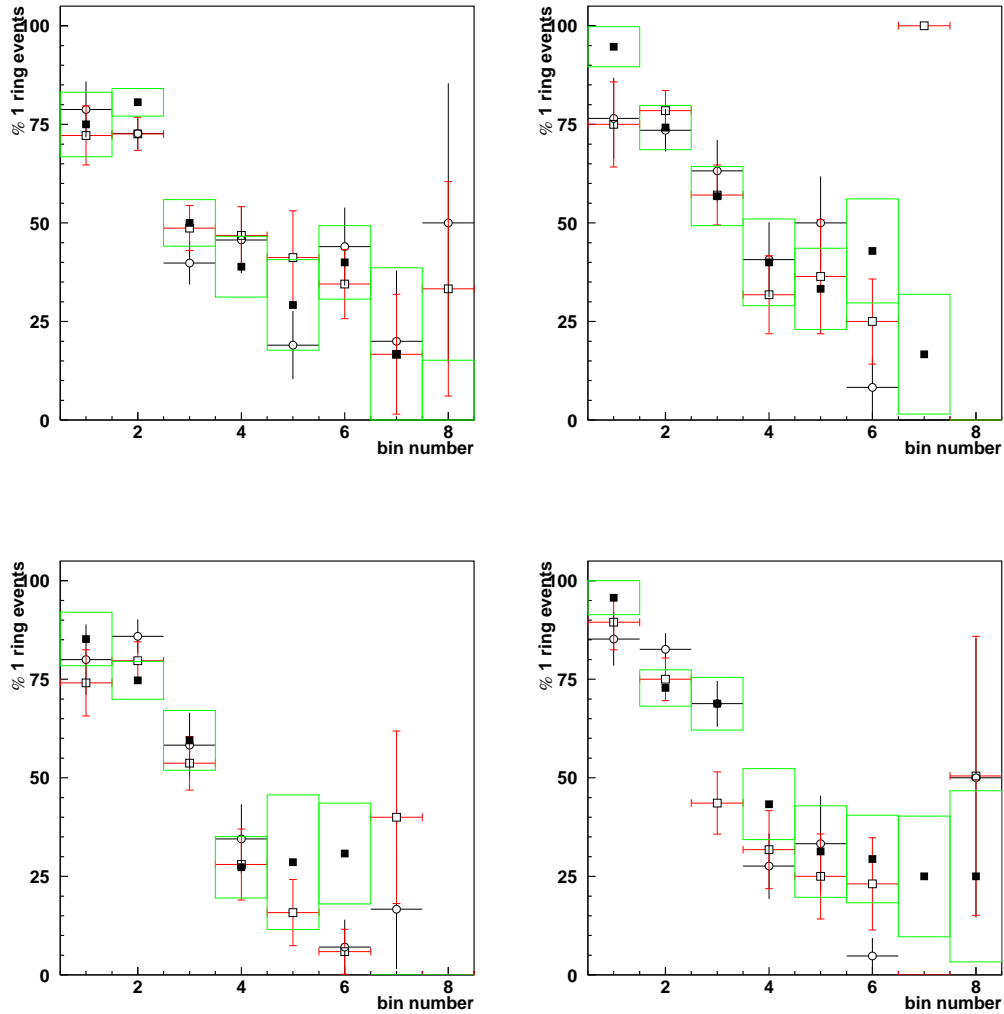
Figure 6.9: Percentage of single ring events found for CC1π events. The top (bottom) row is SK(K2K) MC. The left column has the SK-I photocoverage and right column has SK-II. White circles are the comparison region, white squares are the first 0.5m outside the OFV; black squares are the next 0.5m out from the OFV.

and SK-II z axis distribution in the region for events at most 3 m away from the wall with the new FV used. This allows for the effects of the new FV to be easily observed.

There is an excess in data events at the top of the tank for SK-I and SK-II. Figures 6.11 and 6.12 show there is some clustering at the top of the tank for SK-I. SK-II shows a similar effect in Figure 6.3.1. The lines in each figure show the distance to the wall cut at the top and bottom of the tank with the arrows pointing into the region selected. This clustering comes from cosmic ray muons going through the cable extraction holes at the top of Super-Kamiokande [70]. The cosmic ray muons that cause this are shielded from the outer detector by the cables before appearing in the ID. They are not simulated in the MC. In order to remove these events from the data sample, the following event selections are applied:

- the z vertex is 1.5 m from the top, $z > 16.6$ m
- the x vertex is $|x| > 13$ m
- the y vertex 2 m$< |y| < 6$ m

The agreement between data and MC is improved in the z vertex distributions for the new FV with the removal of these events, as seen in Figure 6.14. In general, the fully contained atmospheric data and MC z vertex distibutions are in good agreement, signifying that an expansion is consistent with the expectation.

6.3.2   K2K data

The K2K data is also put through a series of checks to test the event quality. The first checks involve the event timing and reconstructed energy distributions. The number of events added versus MC expectation is also compared. Finally, there is a check against the decay electron energy scale for K2K-II to see if there may be an effect on the energy scale.

The region added to the official FV has a total of 32 events before the 1.5 μs timing cut is applied to the data. Of these, 31 of the events survive. The other event is a decay electron from an invisible muon from the K2K-II run period. From a hand scan of the event, this decay electron is the only decay electron in the data set. The expectation for the atmospheric neutrino background events for the expanded FV is 2.3, consistent with the three events already seen in the $\pm 500 \mu$s timing window.

For 1Rμ events, there are 13 events added to the events sample, 9 to K2K-I and 4 to K2K-II. Monte Carlo expectation increases the percentage of events in K2K-I by 15.6% and K2K-II by 16.1% (15.8% overall). The expected number of added events is determined by multiplying the percentage increase obtained
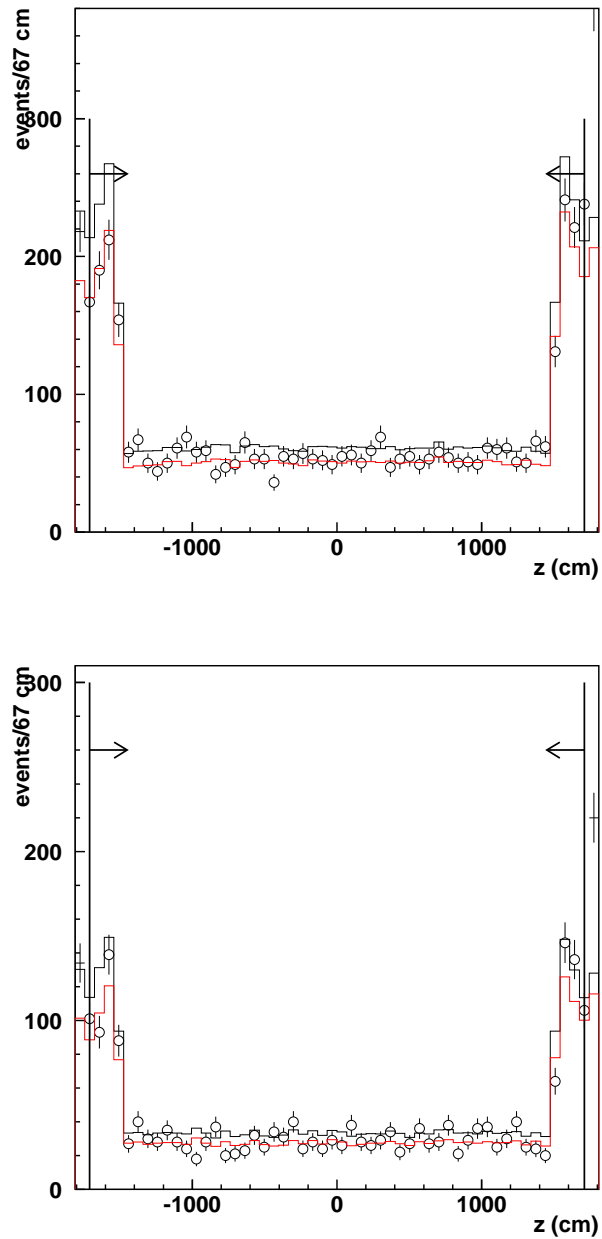
Figure 6.10: Vertex distributions of the z axis for SK-I (top) and SK-II (bottom) events. The radial and *towall* cuts are applied for the new FV. The lines show the region selected for the z coordinate.
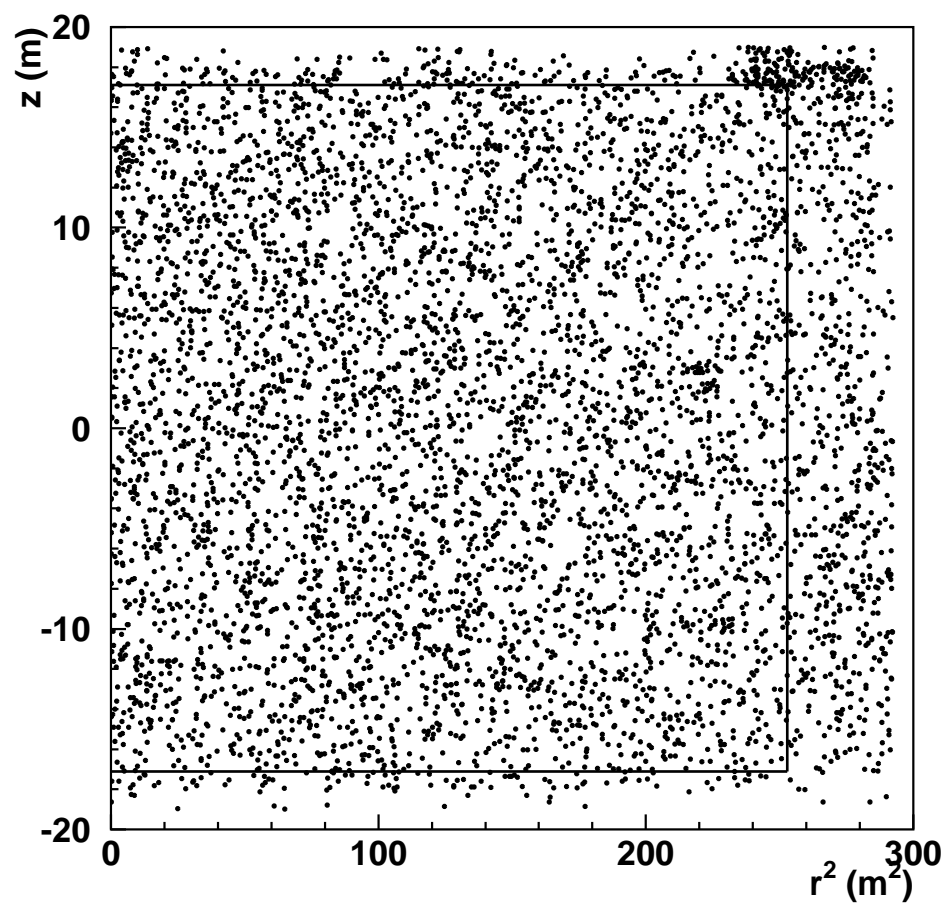
Figure 6.11: SK-I z vs. r^2 distribution. Lines mark the 1m distance from the wall according to the new FV.
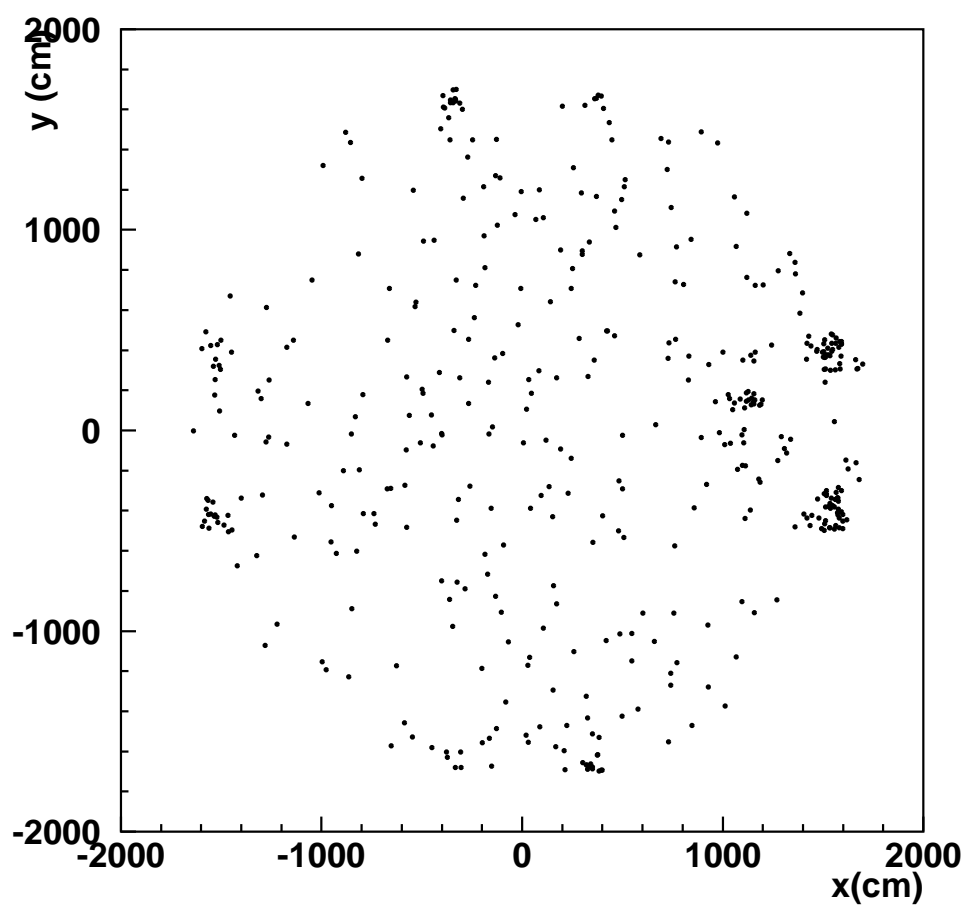
Figure 6.12: SK-I x vs. y distribution for events in the top 1.5m of the ID.
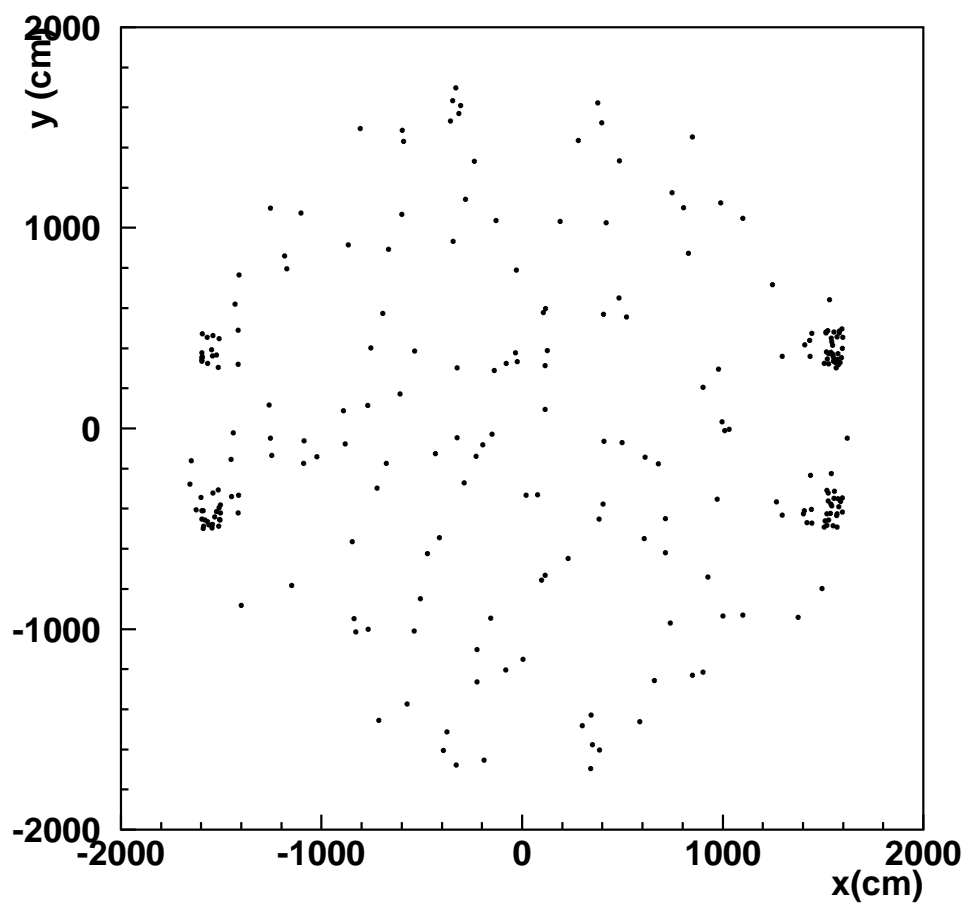
Figure 6.13: SK-II x vs. y distribution for events in the top 1.5m of the ID.
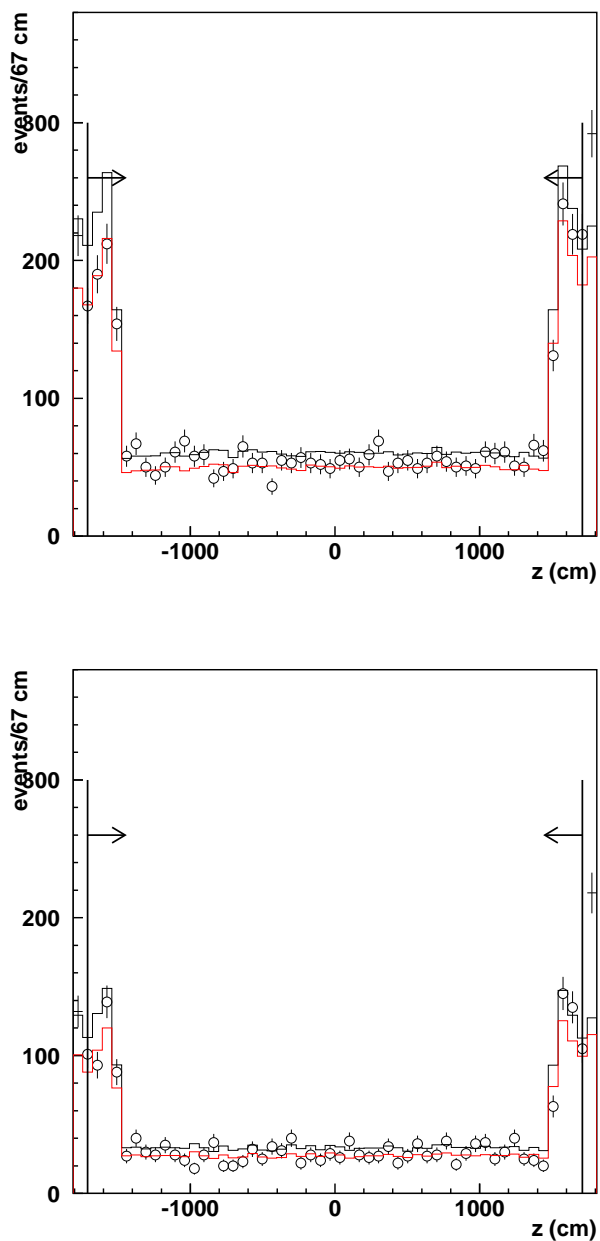
Figure 6.14: Vertex distributions of the z axis for SK-I (top) and SK-II (bottom) events with the events associated with the cable holes removed. The radial cut is applied for the new FV.
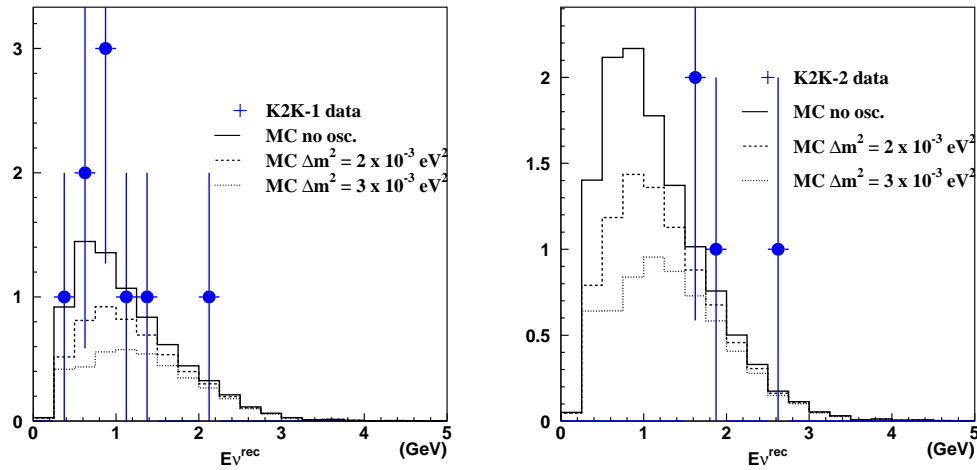
Figure 6.15: Left (Right): Reconstructed energy distribution of K2K-I (K2K-II) $1R\mu$ events. The circles are data while the solid, dashed, and dotted histograms are MC with no oscillations, $\Delta m^2 = 0.003 eV^2$ with maximal mixing, and $\Delta m^2 = 0.002 eV^2$ with maximal mixing, respectively.
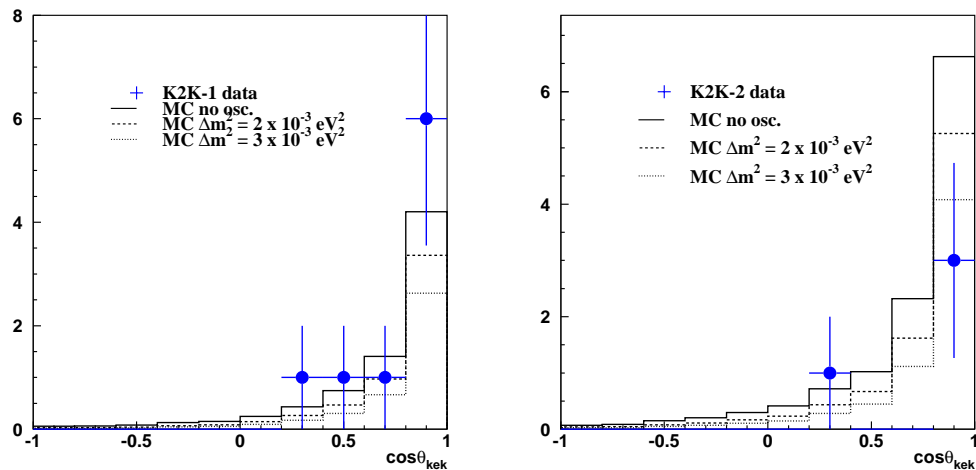
Figure 6.16: Left (Right): Cosine of the event angle with respect to KEK of K2K-I (K2K-II) $1R\mu$ events. The circles are data and the solid, dashed, and dotted histograms are MC with no oscillations, $\Delta m^2 = 0.003$ eV^2 with $\sin^2 2\theta = 1.0$, and $\Delta m^2 = 0.002$ eV^2 with $\sin^2 2\theta = 1.0$, respectively.
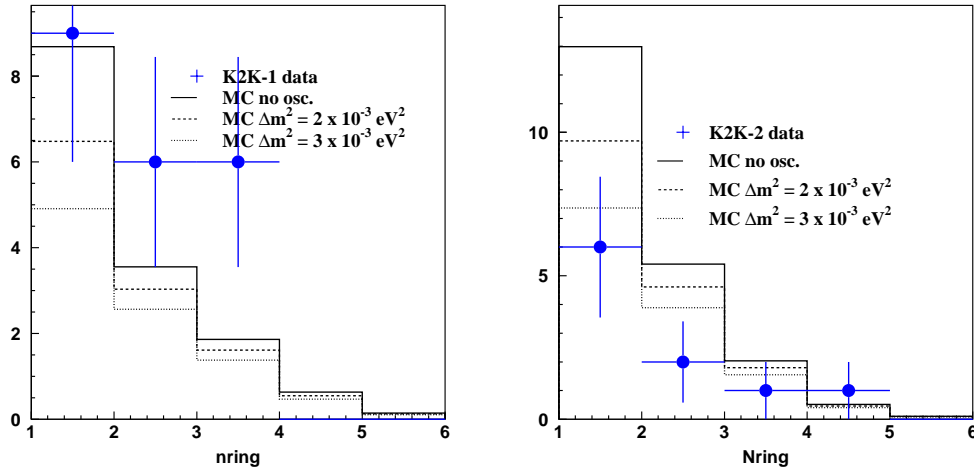
Figure 6.17: Left (Right): Number of rings in an event in K2K-I (K2K-II). The circles are data while the solid, dashed, and dotted histograms are MC with no oscillations, Δm^2=0.003 eV^2 with maximal mixing, and Δm^2=0.002 eV^2 with maximal mixing, respectively.

Figure 6.18: Left (Right): z vs. r^2(x vs. y) distributions of the events added by the new FV. The box represents the new fiducial volume dwall definition.

Table 6.18: Number of expected 1Rμ events in the added FV region versus the number observed. Errors are statistical.

Run Period	N_{exp}	N_{obs}	Discrepancy (σ)
K2K-I	4.67±0.85	9±3.00	1.4
K2K-II	4.50±0.85	4±2.00	-0.2
K2K-I&II	9.16±1.20	13±3.61	1.0

from the MC by the number of data events observed in the official FV. For K2K-I, the number expected is 4.67±0.85 events. Overall, a 1.4σ difference is seen between expectaton and data. K2K-II has 4.50±0.85 events are expected with 4 observed. In total, 9.16±1.20 events are expected from MC, with 13 observed. Table 6.18 summarizes this selection.

The 1Rμ event sample's reconstructed energy spectrum is also consistent with the MC expectaton. Figure 6.15 shows the reconstructed energy distribution to the added region data and MC. Figure 6.16 shows the angle of the event with respect to KEK.

The total data set has 21 events in the added FV for K2K-I; K2K-II has 10 added. None of these events are veto hole events using the selection criteria given in the previous section. The MC has a 17.6% increase for K2K-I and 17.4% for K2K-II (17.5% overall). As shown in Figure 6.17, the increase in multi-ring events for K2K-I is less than 2σ for each bin, whether or not the MC is oscillated. The same is true for the deficit observed for the K2K-II data and MC in Figure 6.17. In K2K-I, 9.69±1.31 additional events are expected with the increase in the FV. This gives a 2.4σ difference between data and expectation using just the statistical errors. Student's t-test gives a 2σ significance to the discrepancy. K2K-II has 9.93±1.32 events expected in the added FV and 10 observed. This difference between K2K-I data and expectation will cause a loss of significance in the normalization and total fit for the oscillation analysis. The difference between the number of observed events and the number expected are summarized in Table 6.19. For all events added to the official FV, Figure 6.18 shows the z vs. r^2 and x vs. y distributions. In all, there is less than a 2σ difference

Energy Systematic From Decay Electrons

The effect of an expanded FV on the K2K-II decay electron calibration data was the final check undertaken. Decay electrons from stopping muons

Table 6.19: Total number of expected events in the added FV region versus the number observed. Errors are statistical.

Run Period	N_{exp}	N_{obs}	Discrepancy (σ)
K2K-I	9.69±1.31	21±4.58	2.4
K2K-II	9.93±1.32	10±3.16	0.02
K2K-I&II	19.62±1.86	31±5.57	1.9

Table 6.20: Percentage difference between the data and MC decay electron energy means using Equation 6.2 for the new FV, official FV, the comparison region, and the events added by the new FV that are not in the official FV.

Event sample	D(%)
Official FV	1.9±0.6
Comparison Region	0.0±1.8
Added Events	1.1±1.5
New FV	1.8±0.5

are measured using a special trigger. MC was generated from the energy, direction, and stopping position from the parent muons. Single electrons with at least 30 PMT hits in a 50 ns timing window and a timing difference of 1.5 μs to 8 μs between when the muon decays and the daughter electron is observed are selected for the data sample in both data and MC.

The first step was to reproduce the decay electron component to the energy scale error for SK-II. The error is determined by calculating the percent difference of the mean energies of the data and MC by

$$D = \frac{E_{Data} - E_{MC}}{E_{Data}} \tag{6.2}$$

where D is the percent difference between the mean energy of the calibration data (E_{Data}) and the mean energy of the calibration MC (E_{MC}). The official FV has an error of 1.9% ± 0.6%.

Using the new FV criteria of dwall>1 m and *towall*>200 cm, the result was checked to see if there was any change in the energy scale systematic error. The energy systematic for the new FV was calculated using the same event selection described above and Equation 6.2. The systematic error slightly

decreases from 1.9±0.6% for the official FV to 1.8±0.5% for the new FV. The results are summarized in Table 6.20. While these numbers are completely consistent, the slight decrease in the central value is from the pull of the added events towards 1.1%, while the decrease in the error is due to an increase in statistics of the data and MC samples.

6.4 Alternative New FV

The expanded FV in the previous section for SK is useful in the cases of atmospheric neutrinos, proton decay, or any other analysis where the source does not include a bias in direction. It is also useful, as with K2K, in the case of trying to include as many events as possible when there are small statistics. But K2K is also a long baseline neutrino experiment, meaning that the neutrino direction is known for each event. Another possible way to expand the FV is to shift it upstream in the beam direction. This provides another way to increase the FV and take advantage of the beam direction.

6.4.1 Upstream Shift Study

In K2K, the neutrino beam is at an angle of $303.3°$ to SK's x-axis. An upstream shift of the FV has the requirement that the downstream edge of the FV remain 2 m away from the ID wall. As a consequence of this condition, any shift in the FV center must also be accompanied by an increase of the radius by the same distance. In order to keep some symmetry in the FV defintion, an increase of the radius is matched by the same increase in the top and bottom of the cylinder. From Tables 6.2, 6.3, and 6.10, an FV expansion from dwall>2 m to dwall>1 m is allowed for all event classes. Within the conditions given, and knowing how far the expansion is allowed, SK's FV can be shifted upstream 0.5 m, with a corresponding increase in the radius and top and bottom of 0.5 m. In addition, events that have $towall$<200 cm are removed from the data sample in order to ensure better vertex reconstruction than the case without (see Figure 6.19).

The checks on the data set are the same that were done for the new FV. The vertex resolution, in Table 6.21, is consistent with the official FV definition. The particle mis-identification (Table 6.22) is consistent between the added events and comparison region and the ring counting error (Table 6.23) is consistent with the official FV. The percentage of events with their vertex reconstruction greater than 3σ is also consistent, as shown in Table 6.24.
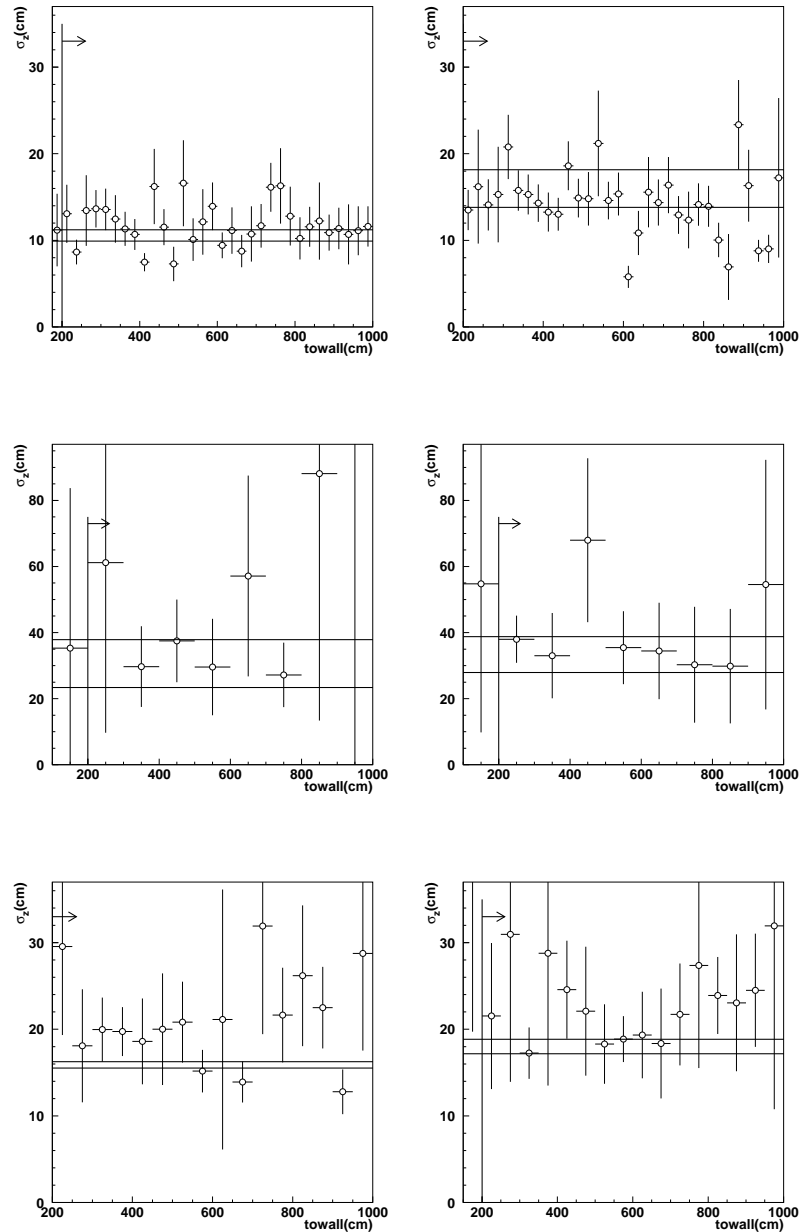
Figure 6.19: Vertex resolution vs. *towall* for the *z* coordinate of upstream shifted 1Rμ (top row), 1Re (middle row), and multi-ring events (bottom row) in K2K. The upper line is the width in the comparison region for events with *towall*<250 cm. The lower line is all events in the comparison region. The left (right) column is the K2K-I (K2K-II).

Table 6.21: Reconstruction widths for the official and shifted FVs. for single ring and multi-ring events in K2K with the percent change.

Sample	$\sigma_{Official}$ (cm)	σ_{New} (cm)	Difference (%)
K2K-I 1Rμ z	10.06±0.04	10.20±0.04	1.4
K2K-I 1Rμ r	18.25±0.25	16.50±0.25	-9.6
K2K-II 1Rμ z	12.12±0.05	12.26±0.05	1.2
K2K-II 1Rμ r	20.25±0.25	20.25±0.25	0.0
K2K-I 1Re z	23.20±0.57	23.68±0.54	2.1
K2K-I 1Re r	66.50±0.25	68.00±0.25	2.3
K2K-II 1Re z	26.78±0.54	26.78±0.50	0.0
K2K-II 1Re r	75.75±0.25	76.25±0.25	0.7
K2K-I multi z	14.88±0.09	14.99±0.09	0.7
K2K-I multi r	35.25±0.25	35.00±0.25	-0.8
K2K-II multi z	17.27±0.10	17.39±0.09	0.7
K2K-II multi r	42.25±0.25	40.25±0.25	-4.7

Table 6.22: Percentage of CCQE events from ν_μ (ν_e) interactions misidentified as e-like(μ-like) for SK-I and SK-II.

Sample	Mis-ID$_\mu$ (%)	Mis-ID$_e$ (%)
K2K-I OFV	1.21±0.17	0.73±0.23
K2K-I Comparison Region	4.00±1.05	1.57±1.10
K2K-I Added Events	3.20±0.87	3.25±1.60
K2K-I New FV	1.38±0.17	0.94±0.25
K2K-II OFV	1.01±0.14	0.42±0.42
K2K-II Comparison Region	0.97±0.48	0.00±0.00
K2K-II Added Events	1.27±0.51	0.00±4.08
K2K-II New FV	1.03±0.14	0.38±0.38

Table 6.23: Number of events mis-identified as being multi-ring events from CCQE ν_μ MC events.

Sample	Mis-counted$_\mu$ (%)
K2K-I OFV	7.29±0.38
K2K-I Comparison Region	10.00±1.56
K2K-I Added Events	9.88±1.08
K2K-I New FV	7.67±0.36
K2K-II OFV	5.78±0.33
K2K-II Comparison Region	4.02±1.14
K2K-II Added Events	8.70±0.95
K2K-II New FV	6.21±0.31

Table 6.24: Percentage of events greater than 3σ of the fitted reconstruction width for SK and K2K.

Sample	Over 3σ in z (%)	Over 3σ in r (%)
K2K-I OFV 1Rμ	4.64±0.09	5.32±0.12
K2K-I New FV 1Rμ	4.60±0.10	5.64±0.15
K2K-II OFV 1Rμ	3.75±0.09	4.59±0.13
K2K-II New FV 1Rμ	3.70±0.09	4.37±0.12
K2K-I OFV 1Re	9.72±0.46	5.20±0.33
K2K-I New FV 1Re	9.30±0.57	4.93±0.33
K2K-II OFV 1Re	7.74±0.43	3.42±0.24
K2K-II New FV 1Re	7.67±0.42	3.62±0.24
K2K-I OFV multi	4.16±0.14	4.59±0.13
K2K-I New FV multi	4.50±0.13	4.77±0.13
K2K-II OFV multi	4.20±0.13	5.11±0.12
K2K-II New FV multi	4.27±0.12	4.82±0.12
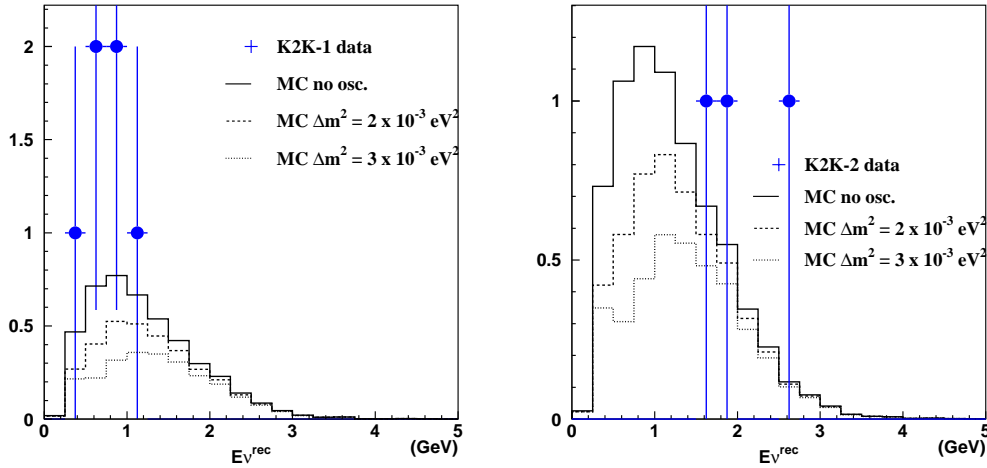
Figure 6.20: Left (Right): Reconstructed energy distribution of K2K-I (K2K-II) added 1Rμ events from the upstream shift. The circles are data while the solid, dashed, and dotted histograms are MC with no oscillations, Δm^2=0.003 eV^2 with maximal mixing, and Δm^2=0.002 eV^2 with maximal mixing, respectively.
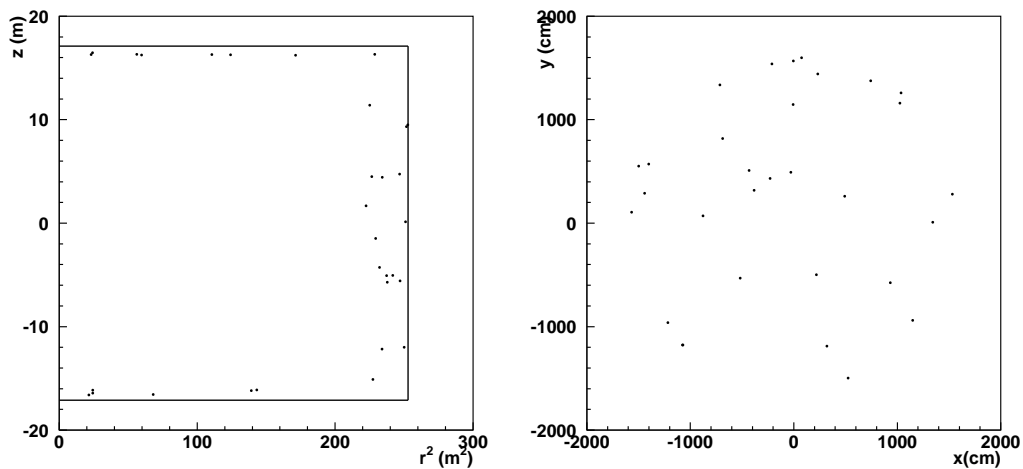
6.4.2 Data Checks

The data selected by the upstream shift is compared to the MC expectation. The reconstructed energy, direction with respect to KEK, number of rings, and vertex positions in the SK tank are given in Figures 6.20, 6.21, 6.22, and 6.23, respectively. The direction of the event with respect to KEK is consistent for K2K-I and K2K-II. The reconstructed energy in K2K-I is higher than the MC, but because of the small statistics of each bin, the results are consistent. The number of rings has an excess in multi-ring events, though again, the statistics are small enough to have less than a 2σ difference with MC in each bin. The percent increase in the event sample as given by MC is 9.6% for K2K-I and 9.6% for K2K-II.

For 1Rμ events, there are 9 events added to the events sample, 6 to K2K-I and 3 to K2K-II. Monte Carlo expectation increases the percentage of events in K2K-I by 9.5% and K2K-II by 9.7% (9.6% overall). The expected number of added events is the percentage increase given by the MC multiplied by the number of data events observed in the official FV. For K2K-I, the number expected is 2.84±0.52 events. Overall, only a 1.3σ difference is seen between
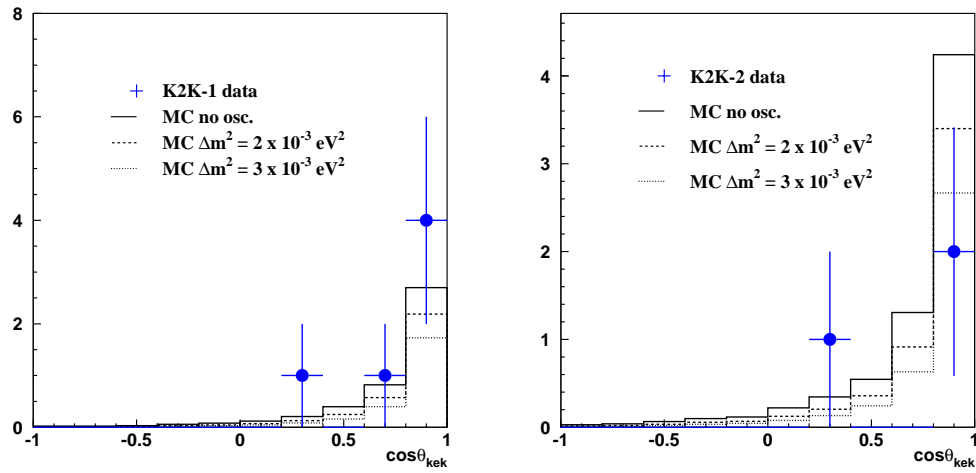
Figure 6.21: Left (Right): Cosine of the event angle with respect to KEK of K2K-I (K2K-II) $1R\mu$ added events for K2K from the upstream FV. The circles are data while the solid, dashed, and dotted histograms are MC with no oscillations, Δm^2=0.003 eV^2 with maximal mixing, and Δm^2=0.002 eV^2 with maximal mixing, respectively.
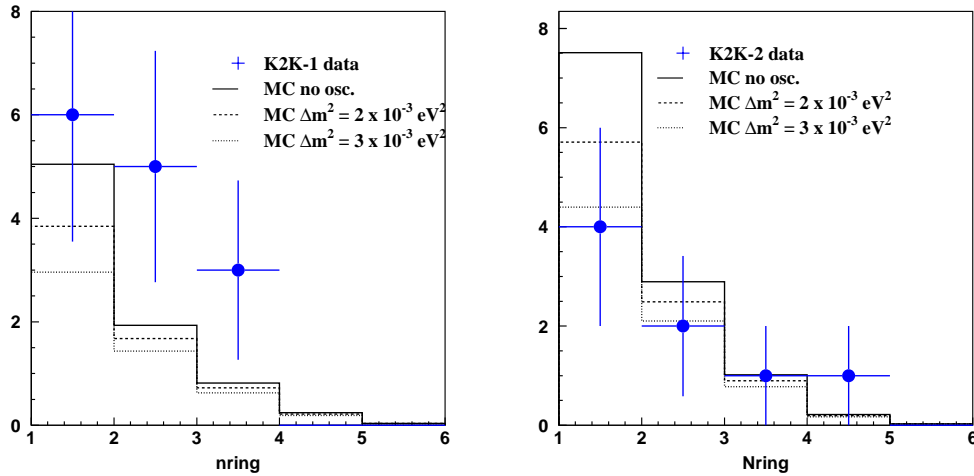
Figure 6.22: Left (Right): Number of rings for each event in K2K-I (K2K-II). The circles are data while the solid, dashed, and dotted histograms are MC with no oscillations, Δm^2=0.003 eV^2 with maximal mixing, and Δm^2=0.002 eV^2 with maximal mixing, respectively.
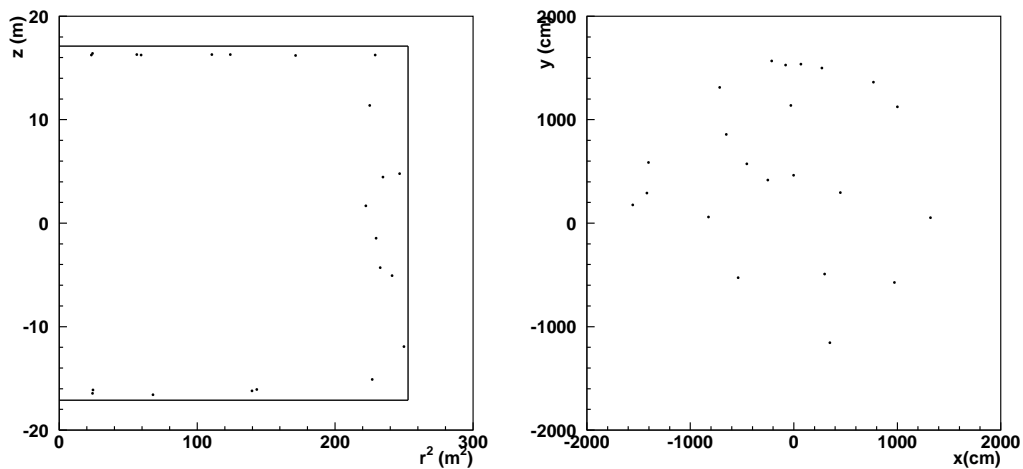
Figure 6.23: Left (Right): z vs. r^2(x vs. y) distributions of the events added by the new FV. The lines in the left plot represent the new FV dwall cut.

Table 6.25: Number of expected 1Rμ events in the added FV region versus the number observed. Errors are statistical.

Run Period	N_{exp}	N_{obs}	Discrepancy (σ)
K2K-I	2.84±0.52	6±2.45	1.3
K2K-II	2.73±0.52	3±1.73	0.1
K2K-I&II	5.57±0.73	9±3.00	1.1

Table 6.26: Total number of expected events in the added FV region versus the number observed. Errors are statistical.

Run Period	N_{exp}	N_{obs}	Discrepancy (σ)
K2K-I	5.26±0.71	14±3.74	2.3
K2K-II	5.50±0.73	8±2.83	0.9
K2K-I&II	10.76±1.02	22±4.69	2.3

expectation and data. K2K-II has 2.73±0.52 events expected with 3 observed. In total, 5.57±0.73 events are expected from MC, with 9 observed. Table 6.25 summarizes this selection.

For the total data set, there are 14 events in the added FV for K2K-I; K2K-II has 8 added. None of these events qualified as a possible cable hole event using the same selection criteria used on the SK data. The MC has a 9.6% increase for K2K-I and 9.6% for K2K-II (9.6% overall). In K2K-I, 5.26±0.71 additional events are expected with the increase in the FV. This gives a 2.3σ difference between data and expectation. Student's t-test gives a 1.7σ significance to the discrepancy. K2K-II has 5.50±0.73 events expected in the added FV and 8 observed. This difference between K2K-I data and expectation will cause a loss of significance in the normalization and total fit for the oscillation analysis. The difference between the number of expected events and the number observed are summarized in Table 6.26.

Table 6.27: K2K event summary after new or upstream FV definition has been applied. New (Up) is the new (upstream shifted) FV.

	K2K-I New	K2K-II New	K2K-I Up	K2K-II Up
FC events	76	67	69	65
1-ring	42	40	39	38
μ-like	39	32	36	31
e-like	3	8	3	7
multi-ring	34	27	30	27

6.5 K2K Expanded Fiducial Volumes Event Summary

The fiducial volume definitions presented in this chapter are applied to the K2K data. For the new FV, with an effective fiducial volume of 26.2 ktons, 143 events for all of K2K are selected. Of these events, 76 are from K2K-I and 67 are from K2K-II. For the upstream shifted fiducial volume, with an effective FV of 24.6 ktons, 134 events are selected with 65 from K2K-II and 69 from K2K-I. The total number of expected events with no neutrino oscillations for the new FV is $183.3^{+10.7}_{-10.0}$ events and $170.9^{+9.5}_{-9.0}$ for the upstream shifted FV.

Of the 143 K2K events in the new fiducial volume, 71 are $1R\mu$ events that are used in the comparison of the energy spectrum shapes. K2K-I has 39 $1R\mu$ events and K2K-II has 32. In the upstream shifted event sample, 67 of 134 events are $1R\mu$ with 36 coming from K2K-I and 31 from K2K-II. In order to use Equation 3.1, $1R\mu$ are used since they are more likely to be CCQE events than not. The proton from the interaction is below Cherenkov threshold. Figures 6.24 and 6.25 show the reconstructed neutrino energy for all $1R\mu$ K2K data and the expected spectrum in the case of no oscillations. The data shows a distorted spectrum as compared to the hypothesis of no neutrino oscillations as shown by the MC. A summary of the expanded fiducial volume event selection is given in Table 6.27.
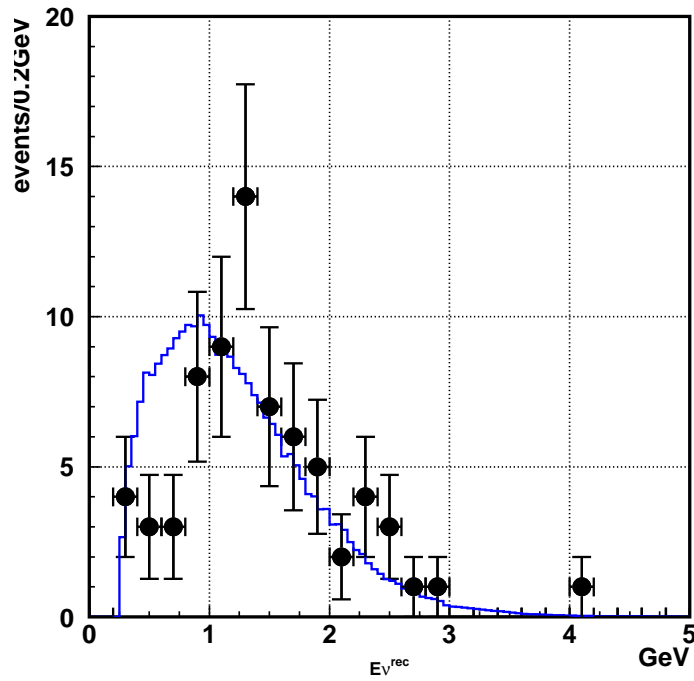
Figure 6.24: The reconstructed E_ν distribution for the SK single ring μ-like sample in the new FV. Points with error bars are data. The solid line (blue) is the expected reconstructed neutrino energy spectrum without oscillation. The histogram is normalized to the observed 71 events.
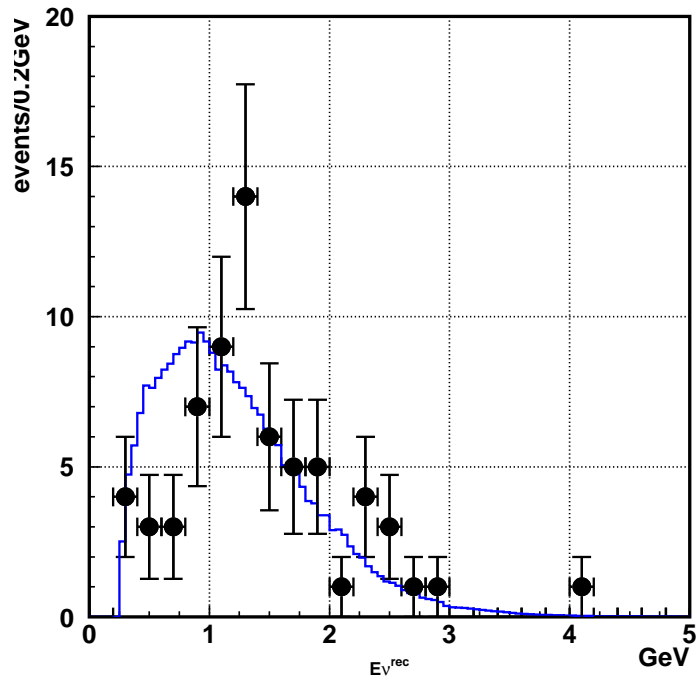
Figure 6.25: The reconstructed E_ν distribution for the SK single ring μ-like sample in the upstream shifted FV. Points with error bars are data. The solid line (blue) is the expected reconstructed neutrino energy spectrum without oscillation. The histogram is normalized to the observed 67 events.

Chapter 7

Oscillation Analysis

7.1 Likelihood Definition

Using the collected SK data during the K2K runs, the K2K oscillation analysis fits the two oscillation parameters from Equation 1.13 with a likelihood consisting of three terms:

$$\mathcal{L}(\Delta m^2, \sin^2 2\theta, f) = \mathcal{L}_{shape} \times \mathcal{L}_{norm} \times \mathcal{L}_{syst} \tag{7.1}$$

where Δm^2 and $\sin^2 2\theta$ are the two-dimensional oscillation parameters and f represents the systematic error terms. The first factor of the likelihood, $\mathcal{L}_{shape}$, relates to the energy spectrum shape, the second to the total number of events, while the third term is a pull on the likelihood from the systematic errors.

7.1.1 Energy Spectrum Shape

The energy spectrum shape likelihood, a probability distribution function (PDF), is defined as

$$\mathcal{L}_{shape} = \prod_{i=1}^{N_{1R\mu}^{Ib}} \phi_{exp,Ib}^{SK}(E_{\nu,i}^{rec}; \Delta m^2, \sin^2 2\theta) \times \prod_{i=1}^{N_{1R\mu}^{II}} \phi_{exp,II}^{SK}(E_{\nu,i}^{rec}; \Delta m^2, \sin^2 2\theta)$$

$$\tag{7.2}$$

where ϕ_{exp}^{SK} is defined similarly to Equation 4.11. The difference between Equation 7.2 and Equation 4.11 is that the probability r in Equation 4.11 is redefined to be the probability of measuring E_ν^{rec} as E_ν^{true}. $N_{1R\mu}^{Ib}$ and $N_{1R\mu}^{II}$ are the number for 1Rμ events in K2K-Ib and K2K-II, respectively. The neutrino energy is binned in 50 MeV increments making the integral from Equation 4.11 a summation. In addition, E_ν^{rec} is scaled by the energy scale parameter $f_{SK-X}^{E-scale}$ with a constraint of 2.0% (2.1%) for K2K-I (K2K-II) and the efficiency $\epsilon_{SK-X}^{1R\mu}$

is scaled by $f^{\epsilon_{SK-X}}$ taking into account the energy dependent systematic error terms for $1R\mu$ events. In the case of fitting for either K2K-I or K2K-II, the PDF for the other run period is removed from Equation 7.2.

7.1.2 Normalization

The normalization likelihood for the number of events is a Poissonian probability function, defined as

$$\mathcal{L}_{norm} = \frac{(N^{exp})^{N^{obs}}}{N^{obs}!} e^{-N^{exp}} \tag{7.3}$$

where N^{obs} is the number of observed events and N^{exp} is the expected number of events defined in Equation 4.6. $N^{obs(exp)}$ is the sum of all observed (expected) events for a given run period. For all of K2K, $N^{obs(exp)}$ is

$$N^{obs(exp)} = N^{obs(exp)}_{K2K-Ia} + N^{obs(exp)}_{K2K-Ib} + N^{obs(exp)}_{K2K-II}. \tag{7.4}$$

In the case of defining the likelihood for K2K-I or K2K-II, $N^{obs(exp)}$ only consists of the number of observed (expected) events for that run period.

7.1.3 Systematic Error Likelihood

Some of the systematic error terms in the likelihood analysis are treated as fit parameters. The parameters are assumed to follow a Gaussian distribution with the error constraint defined as

$$
\begin{aligned}
\mathcal{L}_{syst} &\equiv \exp\left[-\Delta f^{\phi,non-QE\ T} \cdot \left(M^{\phi,non-QE}\right)^{-1} \cdot \Delta f^{\phi,non-QE} - \frac{(\Delta f^{NC})^2}{2(\sigma^{NC})^2}\right] \\
&\times \exp\left[-\Delta f^{F/N\ T} \cdot \left(M^{F/N}\right)^{-1} \cdot \Delta f^{F/N}\right] \\
&\times \exp\left[-\sum \frac{(\Delta f_i^{\epsilon_{SK-X}})^2}{2(\sigma^{\epsilon_{SK-X}})^2} - \sum \frac{(f_{SK-X}^{E-scale})^2}{2(\sigma_{SK-X}^{E-scale})^2}\right] \\
&\times \exp\left[-\sum \frac{(\Delta f_{K2K-Y}^{norm})^2}{2(\sigma_{K2K-Y}^{norm})^2}\right], \tag{7.5}
\end{aligned}
$$

where $\Delta f = f - <f>$ is the difference between the fitted parameter and its nominal value; the parameter $M^{\phi,non-QE}$ is the R_{nQE} error matrix element given in Table 3.4; $M^{F/N}$ is the Far/Near ratio error matrix in Table 4.4; the systematic errors corresponding to the CC non-QE/CCQE and NC/CCQE cross section ratios are terms $f^{\phi,non-QE}$ and f^{NC}, respectively; SK's energy scale

Table 7.1: The number of envents and the percent difference in the number of entries for SK-I and SK-II $1R\mu$ atmospheric data and MC with wall>2m as well as the error.

Sample	# of *msfit* entries	# of *autofit* entries	Difference(%)
K2K-I data	1584	1597	0.82±0.23
K2K-I MC	128062	127730	-0.26±0.01
K2K-II data	1826	1813	-0.71±0.20
K2K-II MC	74488	75065	0.77±0.03

error and detection efficiency are $f_{SK-X}^{E-scale}$ and $f^{\epsilon_{SK-X}}$, respectively, where X is either the first or second run periods; and f_{K2K-Y}^{norm} is the systematic error for the overall normalization of the MC simulation to the 1KT prediction with Y defined as the Ia, Ib, or II run periods. Except for the terms related to the Near Detector spectrum measurement in Table 3.4, the nominal values of the systematic errors are set to 1.0.

7.2   Systematic Errors

7.2.1   Spectrum Shape Systematic Errors

The systematic errors for the energy spectrum is broken into five terms: the fiducial volume, ring counting, particle identification, events from the OD, and events in SK's dead region. These last two are specific to an expanded FV, while the first three are for either the official or expanded FVs.

The fiducial volume systematic error reflects the uncertainty in the vertex reconstruction algorithms used by Super-Kamiokande before events are selected inside the FV. If there is a systematic shift in event reconstruction, events can migrate into or out of the actual FV, affecting the number of events in the normalization likelihood or in the events selected for the energy spectrum shape PDF. The atmospheric neutrino data and MC from SK-I and SK-II use two different vertex fitters to determine the FV systematic term.

Fully contained $1R\mu$ events in the Inner Detector from SK's atmospheric data and MC are selected to determine the error. These events have had their vertex reconstructed using the initial vertex fitter *autofit* (which is also used for single ring e-like and multi-ring events) as well as the precision fitter, *msfit* (used also in single ring e-like events; see Appendix A for more details).

Table 7.2: Errors for data and MC for 1Rμ events used in the new FV systematic error.

Sample	percent difference data(%)	percent difference MC(%)
SK-I	1.48±0.35	-0.37±0.03
SK-II	-0.11±0.10	-1.06±0.04

Single ring mon-like events are selected to be in the FV using separately their *autofit* vertex position or *msfit* vertex position. The total number of entries is counted. The percent difference between these fitters is calculated for both data and MC (see Table 7.1 for the official FV). The difference between data and MC then gives the systematic error, which is then rounded up to the nearest whole percent.

For the new FV definition, the FV error is a little trickier to evaluate. The FV defintion involving only the wall distance is still evaluated for data and MC, but the function *towall* also needs to be accounted for. Since *towall* is a function of both vertex position and particle direction and *autofit* and *msfit* both have directional information for the particle, the position and vertex information are varied independently of each other. For example, the wall selection is made using the *msfit* vertex with dwall>1 m and the vertex information used in *towall* is also from *msfit*. The direction information used in *towall* is changed between the *autofit* and *msfit* values. The percent difference in the number of entries is then calculated. This procedure is repeated for each variation of the inputs for the *towall*. The error after each variation is then added in quadrature to give the total error for data or MC, given in Table 7.2. Since data and MC in each case have a combined error greater than 1%, but less than 2%, the FV systematic error term is rounded up to 2%, the same value for the official FV.

The ring counting systematic error is determined by shifting the single ring selection value of the ring counting likelihood in the K2K beam MC. The magnitude of the shift is found by fitting a double Gaussian to the likelihood distributions of fully contained sub-GeV and multi-GeV atmospheric μ-like events from SK. The dip location from both fits is then used as the upper and lower shifts for the μ-like beam MC, with their average position used as the central value for four different neutrino energy bins. The percentage of events that survive the upper and lower shifts relative to the average are calculated, with the larger of the two given as the error. These steps for the ring counting systematic error are repeated for different binnings of the likelihood function to

Table 7.3: Systematic errors for the ring counting likelihood.

Sample \ [GeV]	0.0-0.5	0.5-1.0	1.0-1.5	1.5-2.0	2.0-
K2K-I OFV	3.4%	2.7%	3.0%	4.5%	4.5%
K2K-II OFV	5.3%	4.1%	3.7%	3.8%	3.8%
K2K-I New	3.4%	2.7%	3.0%	4.5%	4.5%
K2K-II New	5.9%	4.1%	3.7%	3.8%	3.8%

minimize binning effects. The largest difference in the error calculated for the other binnings is added in quadrature to the error of the central binning. This combined error is used as the systematic error for the ring counting. For this analysis, the official FV systematic error is used only in the OFV oscillation analysis while the new FV systematic error is used for both expanded FV definitions. The systematic error for each energy bin is given in Table 7.3.

To determine the PID systematic error, the shift in the μ-like particle identification (PID) likelihood peak value for SK atmospheric FC 1R data and MC events is calculated. The shift in the likelihood is applied to the K2K beam MC μ-like selection criteria for each energy bin as given in Table 7.3. The percent difference in the number of events with no shift in the PID selection criterion and the shifted PID selection criterion give the systematic error in each bin.

In the region where the PID likelihood L≈0 there is a large charged pion background for events with $E_\nu <$500 MeV. This additional error is added by finding the shift between data and MC in the second ring PID likelihood peak for two ring events with both ring μ-like (2R$\mu\mu$) events in the SK atmospheric sample. This shift is then applied to the 1Rμ events in the K2K beam MC with $E_\nu <$500 MeV. The percent difference between no shift and the 2R$\mu\mu$ shift is then added quadratically to the $E_\nu <$500 MeV bin of the PID systematic error. The official FV PID systematic error is larger than the new FV PID systematic error. In order to be careful with the systematic error evaluation, the official FV systematic error is used in all analyses. The total PID errors are summarized in Table 7.4.

The second to last systematic error estimated, and one of two for only the new FV, relates to incoming events from the outer detector (OD) of Super-Kamiokande. The maximum number of hits allowed in the OD is 10 (16) for K2K-I (K2K-II) for fully contained events. Using the SK atmospheric data and MC, all 1Rμ event selection criteria except for the number of OD hits

Table 7.4: Systematic errors for the particle identification likelihood.

Sample \ [GeV]	0.0-0.5	0.5-1.0	1.0-1.5	1.5-2.0	2.0-
K2K-I	1.5%	0.3%	0.5%	0.4%	0.4%
K2K-II	2.6%	0.4%	0.3%	0.6%	0.6%

Table 7.5: Total systematic error for the K2K energy spectrum for the official and expanded fiducial volumes.

Sample \ [GeV]	0.0-0.5	0.5-1.0	1.0-1.5	1.5-2.0	2.0-
K2K-I OFV	4.1%	3.4%	3.6%	4.9%	4.9%
K2K-II OFV	6.2%	4.6%	4.2%	4.3%	4.3%
K2K-I New	4.2%	3.4%	3.6%	4.9%	4.9%
K2K-II New	6.8%	4.6%	4.2%	4.3%	4.3%

were applied. The OD hits were then varied from 10 (16) to 8 (10) for SK-I (SK-II). The total number of events were taken for each amount of OD hits and the percent difference was calculated, giving a systematic error of 0.2% (0.3%) for K2K-I (K2K-II).

Finally, K2K beam MC was used to find the number of events reconstructed in SK's dead area that survive the new FV. The K2K beam MC does not take into account the support structure of SK, the wires connecting the PMTs to the DAQ system, and the backs of the PMTs themselves, thus making it possible for the MC to generate an event in this region and not simulate it properly. The number of events with their true vertex in this region, though reconstructed in the new FV, was divided by the total number of events in the new FV. The systematic error for the contamination of events in SK's dead region is 0.1%.

Each of these systematic errors are then added in quadrature and put into the error matrix for the fit based on the neutrino energy. The total systematic error is given in Table 7.5 for the official FV and new FV.

7.2.2 Number of Events Systematic Errors

The systematic errors related to the number of events consists of four sources. For all but the last term, the SK atmospheric data and MC were

Table 7.6: Total systematic error for the K2K energy spectrum for the official and expanded fiducial volumes.

	K2K-I	K2K-II
Event reduction	<1%	<1%
FV cut	2%	2%
Decay e background	0.1%	0.1%
MC statistics	0.6%	0.6%
Total	3%	3%

used to estimate the systematic error. The dominant term is the FV systematic error, which is the same as the energy spectrum shape systematic error, 2%. The error on the data reduction, which is the process the raw data goes through to be classified as a FC event, is estimated to be less than 1%. In this case, there is no difference between the official and expanded FVs, making the error the same for both. The decay electron background is estimated to be 0.1%. The MC statistics systematic error is 0.6% from the number of MC events selected in the FV. For these two systematic terms, the official FV is evaluated to be slightly larger than the expanded FV, making the estimated values for the official FV the ones used for the systematic errors for all FV definitions. In all, the systematic error for the number of events is estimated to be 3% for K2K-I and K2K-II. The systematic errors are summarized in Table 7.6.

7.3   Analysis Method

The K2K oscillation likelihood is maximized in the entire Δm^2-$\sin^2 2\theta$ parameter space, a physical region where $\sin^2 2\theta \leq 1.0$, and the case where $\Delta m^2 = 0.0$ and $\sin^2 2\theta = 0.0$ to examine the no neutrino oscillation hypothesis. Fits are performed for the K2K-I, K2K-II, and K2K-I&II data sets for all combinations of likelihood terms and each set of constraints on the parameter space.

The probability and significance of the likelihood analysis are calculated using $\Delta \chi^2$, defined as:

$$\Delta \chi^2 = -2 \cdot \Delta \ln L = 2 \cdot (\ln L - \ln L_{phys}^{max}) \tag{7.6}$$

where L_{phys}^{max} is the maximum likelihood value in the physical region. The errors

Table 7.7: $\Delta\chi^2$ corresponding to a coverage probablility in a large data sample for a joint estimation of n parameters from Ref. [13]. In the contours, one half of the value is used in the confidence limit calculation.

(1-α) (%)	n=1	n=2
68.27	1.00	2.30
90.	2.71	4.61
95.	3.84	5.99
99.	6.63	9.21

for the fit are assumed to be Gaussian.

The $\Delta\chi^2$ from the difference between the best fit and null hypothesis is used to estimate the probability that the best fit is consistent with a statistical fluctuation of the null hypothesis. The probability α is defined as

$$\alpha = 1 - P(\Delta\chi^2, m) \tag{7.7}$$

where P is the incomplete gamma function and m is the number of parameters being estimated. In this analysis, m=2 to account for the two oscillation parameters in all fits except for the number of observed events. For the number of observed events there is only one measurement, making it impossible to fit the two oscillation parameters. From α, the significance in units of σ can be calculated as

$$\frac{\delta}{\sigma} = \sqrt{2} \cdot \mathrm{erf}^{-1}(1 - \alpha). \tag{7.8}$$

The confidence intervals for the contour plots in parameter space are calculated from Equation 7.6 and Table 7.7 for n=2 parameters. The likelihood is calculated for each point in parameter space with the contour being drawn along the curve of constant $\Delta\chi^2$. In the case where the best fit result is in the unphysical region, a correction is applied to the confidence intervals in Table 7.7 using a two-dimensional Gaussian approximation from the maximum in the unphysical region.

7.4 Results

7.4.1 Official Fiducial Volume

The best fit result in the physical region of the combined fit for all of K2K is Δm^2=0.0027 eV^2 and $\sin^2 2\theta$=1.00. The number of expected events with these
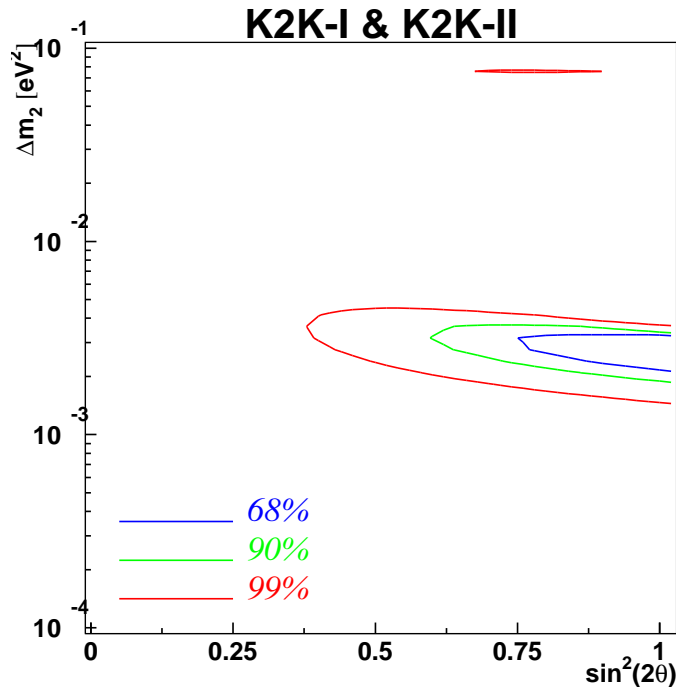
Figure 7.1: Allowed region of the official fiducial volume ν_μ disappearance analysis. The blue (green; red) line region allowed at 68% (90%; 99%) confidence level.

parameters is 107.2, consistent with the 112 observed for K2K's official fiducial volume. For the whole parameter space, $\sin^2 2\theta = 1.18$ and $\Delta m^2 = 0.0025$ eV^2. The contour of the allowed region in the parameter space for 68%, 90%, and 99% C.L.s are given in Figure 7.1. At $\sin^2 2\theta = 1.00$, Δm^2 ranges from 0.0019 eV^2 to 0.0035 eV^2 at 90% C.L. The probability that the data is consistent with no neutrino oscillations is 0.0021%, or 4.3σ.

The reconstructed energy spectrum is consistent between data and the physical region's best fit oscillation parameters, as in Figure 7.2. The consistency between the best fit energy spectrum shape and the observed spectrum shape is checked by the Kolmogorov-Smirnov (KS) test. For the best fit parameters in the physical region, the KS probability is 39%, while for the null oscillation hypothesis, it is 0.08%.

Using only the shape of the energy spectrum for all of K2K, the best fit in all parameter space is $\Delta m^2 = 0.0028$ eV^2 with $\sin^2 2\theta = 1.26$ while in the

Figure 7.2: Energy spectrum shape of 1Rμ events. Data are the circles, the best fit oscillation parameters is the red histogram, and null oscillations is the blue histogram. The histograms are normalized to 58 events.

Figure 7.3: Allowed region of the official fiducial volume ν_μ disappearance analysis for the number of events (left) and energy spectrum shape(right). The blue (green; red) line region allowed at 68% (90%; 99%) confidence level.

physical region, Δm^2=0.0029 eV^2 with $\sin^2 2\theta$=1.0. This disfavors the null hypothesis at 2.8σ. The number of events disfavors the null hypothesis by 3.4σ. The contours for the shape and number of events are in Figure 7.3. The K2K-I combined fit gives Δm^2=0.0028 eV^2 with $\sin^2 2\theta$=1.07 in all parameter space and Δm^2=0.0029 eV^2 with $\sin^2 2\theta$=1.0 in the physical region. K2K-II has Δm^2=0.0024 eV^2 with $\sin^2 2\theta$=1.33 in all parameter space and Δm^2=0.0026 eV^2 with $\sin^2 2\theta$=1.0 in the physical region. K2K-I and K2K-II reject the null hypothesis at 3.1σ and 2.7σ, respectively. The contours for K2K-I and K2K-II are in Figure 7.4.

The results of the oscillation analysis for the official FV are in Table 7.8 and probabilites for each fit in Table 7.9.

7.4.2 New Fiducial Volume

In the physical region for the new fiducial volume oscillation analysis, Δm^2=0.0025 eV^2 with maximal mixing. The number of expected events with the best fit oscillation parameters is 135.1, consistent with the 143 events observed in the new fiducial volume. The probability that this is consistent with the hypothesis of no neutrino oscillations is 0.0018%, or 3.7σ. The best fit parameters for the combined fit for all of K2K are Δm^2=0.0023 eV^2 with
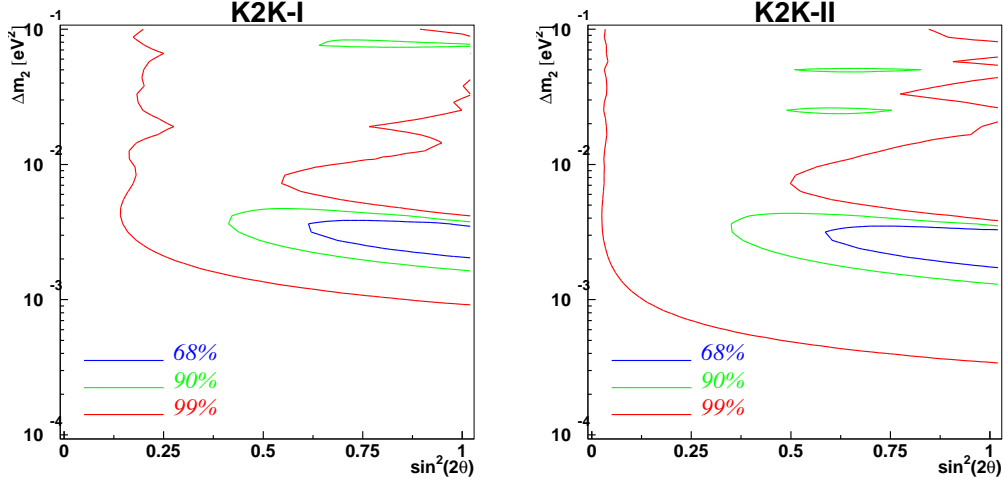
Figure 7.4: Allowed region of the official fiducial volume ν_μ disappearance analysis for K2K-I(left) and K2K-II(right). The blue (green; red) line region allowed at 68% (90%; 99%) confidence level.

Table 7.8: Summary of oscillation fit best fit parameters.

		All region		Physical region	
		Δm^2 [eV^2]	$\sin^2 2\theta$	Δm^2 [eV^2]	$\sin^2 2\theta$
All data	shape + norm.	0.00254	1.18	**0.00274**	**1.00**
	shape only	0.00276	1.26	0.00294	1.00
K2K-I	shape + norm.	0.00277	1.07	0.00287	1.00
K2K-II	shape + norm.	0.00236	1.33	0.00263	1.00

Table 7.9: Summary of null oscillation probabilities.

|	K2K-I+II	K2K-I	K2K-II
Shape + Norm.	0.0021% (4.3σ)	0.22% (3.1σ)	0.64% (2.7σ)
Shape	0.48% (2.8σ)	8.3%	5.4%
Norm.	0.07% (3.4σ)	0.63%	3.1%
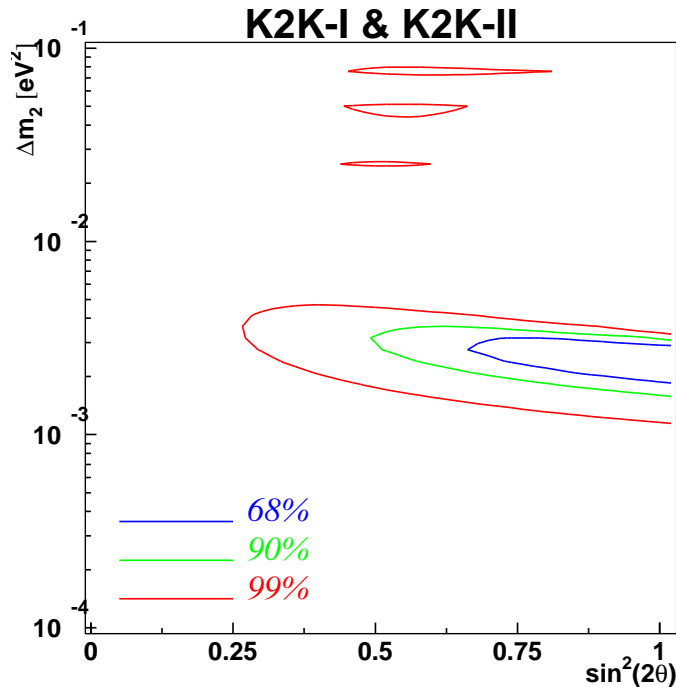
Figure 7.5: Allowed region of the new fiducial volume ν_μ disappearance analysis. The blue (green; red) line region allowed at 68% (90%; 99%) confidence level.

$\sin^2 2\theta$=1.12. The contour for the new FV analysis is in Figure 7.5. At 90% C.L. with maximal mixing, Δm^2 ranges from 0.0016 eV^2 to 0.0031 eV^2.

The shape of the reconstructed neutrino energy spectrum for data, the best fit oscillation parameters, the physical region oscillation parameters, and no neutrino oscillations are in Figure 7.6. The KS probability that the data and best fit results are consistent is 64%, while the data and null hypothesis is 0.04%. The best fit KS probability for the new FV at 64% is better than the official FV KS probability of 39%.

In K2K-I, the best fit is in the physical region with $(\Delta m^2,\ \sin^2 2\theta) = (0.0024$ eV^2, 0.85). This is inconsistent with the null oscillation hypothesis at 1.9σ, due to the smaller difference between the expected and observed number of events in K2K-I. K2K-II's combined fit yields $(\Delta m^2,\ \sin^2 2\theta) = (0.0024$ eV^2, 1.42) for all parameter space and $(\Delta m^2,\ \sin^2 2\theta) = (0.0027$ eV^2, 1.00) for the physical region. This differs from the null oscillation hypothesis by 3.2σ. The
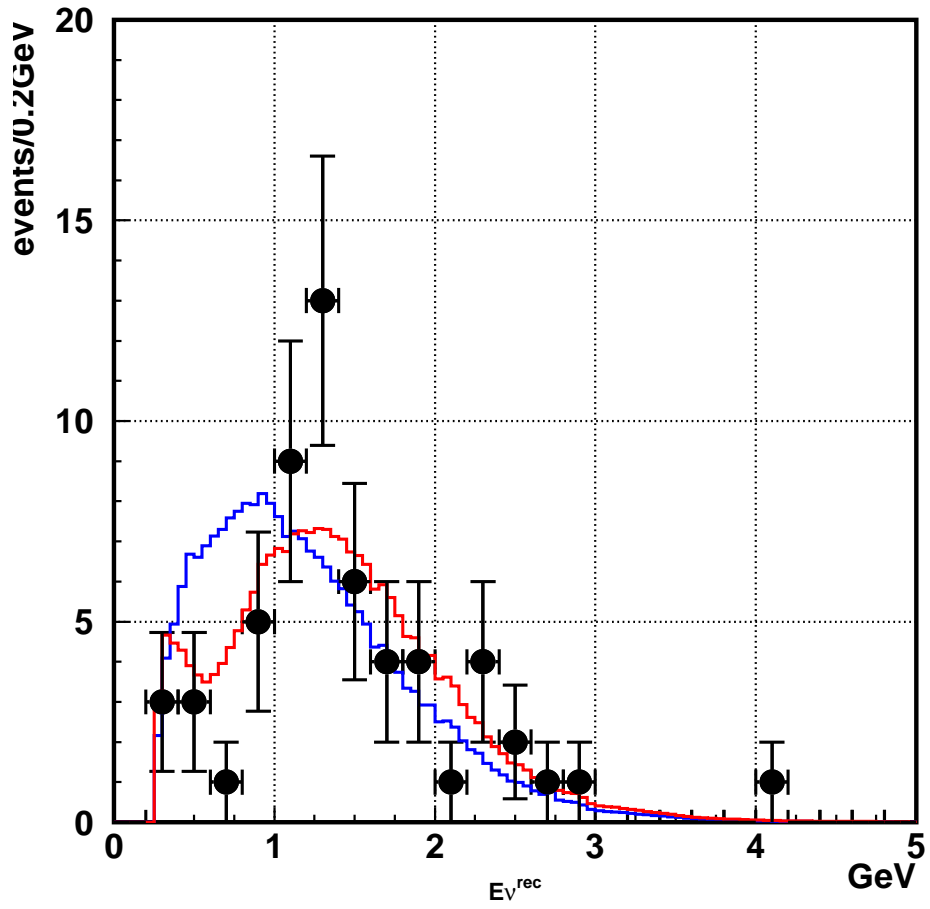
Figure 7.6: Energy spectrum shape of new FV 1Rμ events. Data are the circles, the best fit oscillation parameters is the red histogram, and null oscillations is the blue histogram. The histograms are normalized to 71 events.
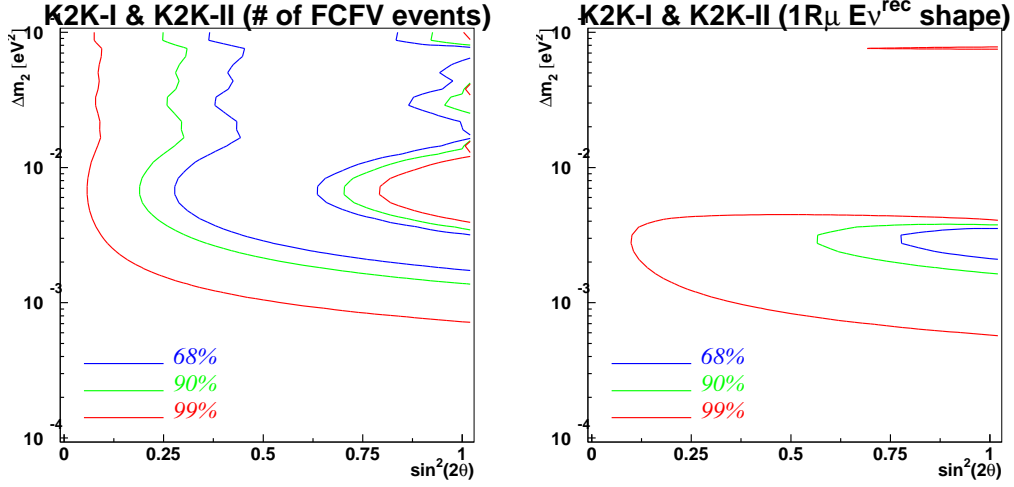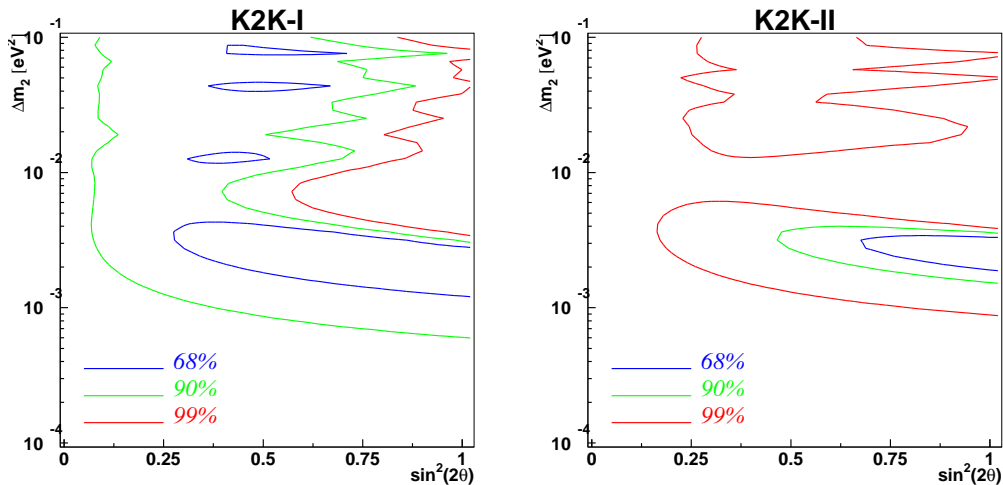
Figure 7.7: Allowed region of the new fiducial volume ν_μ disappearance analysis for K2K-I(left) and K2K-II(right). The blue (green; red) line region allowed at 68% (90%; 99%) confidence level.

contours for K2K-I and K2K-II are in Figure 7.7. The differences in the best fit values for K2K-I and K2K-II for the new FV as compared to the official FV is driven by the number of events added to each sample. In the case of K2K-I, the excess above expectation based on the FV expansion in the number of observed events caused a slight loss of significance with respect to the best fit value, as compared to the official FV. K2K-II, however, scaled to the increase in the FV size for the number of events, thus shrinking the allowed region with respect to the official FV.

The energy spectrum shape has $(\Delta m^2, \sin^2 2\theta) = (0.0026 \text{ eV}^2, 1.21)$ for all parameter space and $(\Delta m^2, \sin^2 2\theta) = (0.0028 \text{ eV}^2, 1.00)$ for the physical region for a 2.8σ difference with the null oscillation hypothesis. The expected number of events differs by 2.8σ. The contours for the energy spectrum shape and number of events are in Figure 7.8. The difference in the energy spectrum shape contours in the new and official FV were caused mainly by the increase in the systematic error for the lowest energy bin. The normalization contour increased because of the smaller difference between the number of expected and observed events from the added events to the new FV.

The results of the oscillation analysis for the new FV are in Table 7.10 and probabilites for each fit in Table 7.11.

Figure 7.8: Allowed region of the new fiducial volume ν_μ disappearance analysis for the number of events (left) and energy spectrum shape(right). The blue (green; red) line region allowed at 68% (90%; 99%) confidence level.

Table 7.10: Summary of oscillation fit best fit parameters for the new fiducial volume.

		All region		Physical region	
		Δm^2 [eV^2]	$\sin^2 2\theta$	Δm^2 [eV^2]	$\sin^2 2\theta$
All data	shape + norm.	0.00231	1.12	**0.00245**	**1.00**
	shape only	0.00261	1.21	0.00279	1.00
K2K-I	shape + norm.	0.00236	0.85	0.00236	0.85
K2K-II	shape + norm.	0.00238	1.42	0.00270	1.00

Table 7.11: Summary of null oscillation probabilities.

	K2K-I+II	K2K-I	K2K-II
Shape + Norm.	0.018% (3.7σ)	6.5% (1.9σ)	0.14% (3.2σ)
Shape	0.49% (2.8σ)	27%	1.4%
Norm.	0.52% (2.8σ)	7.5%	2.2%

7.4.3   Upstream shifted Fiducial Volume

The upstream FV given has a best fit of Δm^2=0.0024 eV^2 and $\sin^2 2\theta$=1.0. The 134 observed events is consistent with the 126.1 expected events with the best fit oscillation parameters. The best fit parameters in all parameter space for the combined fit for all of K2K are Δm^2=0.0024 eV^2 with $\sin^2 2\theta$=1.07. The probability that this is consistent with the hypothesis of no neutrino oscillations is 0.0063%, or 3.5σ. The contour for the new FV analysis is in Figure 7.9. The range of Δm^2 allowed for the upstream shifted FV at 90% C.L. is from 0.0015 eV^2 to 0.0031 eV^2.

The energy spectrum shape with the physical region's best fit parameters is also consistent with the shape of the 1Rμ data, as in Figure 7.10. The KS probability is 0.05% between the data and null hypothesis, while the data and best fit results have a KS probability of 68%. The KS probability for the upstream fiducial volume is is greater than the 39% probability given in the OFV.

In K2K-I, the best fit is in the physical region with $(\Delta m^2, \sin^2 2\theta) = (0.0025$ eV^2, 0.81$)$. This is inconsistent with the null oscillation hypothesis at 1.9σ, due to the smaller difference between the expected and observed number of events in K2K-I. K2K-II's combined fit yields $(\Delta m^2, \sin^2 2\theta) = (0.0023$ eV^2, 1.37$)$ for all parameter space and $(\Delta m^2, \sin^2 2\theta) = (0.0026$ eV^2, 1.00$)$ for the physical region. This differs from the null oscillation hypothesis by 2.8σ. The contours for K2K-I and K2K-II are in Figure 7.11. In the case of K2K-I, the excess above expectation based on the fiducial volume increase in the number of observed events caused a slight loss of significance with respect to the best fit value, as compared to the official FV. K2K-II, however, scaled to the increase in the FV size for the number of events, thus shrinking the allowed region further.

The energy spectrum shape has $(\Delta m^2, \sin^2 2\theta) = (0.0027$ eV^2, 1.18$)$ for all parameter space and $(\Delta m^2, \sin^2 2\theta) = (0.0028$ eV^2, 1.00$)$ for the physical region. The physical region is consistent at 2.7σ with the null oscillation hypothesis. The expected number of events differs by 2.7σ. The contours for the energy spectrum shape and number of events are in Figure 7.12. The difference in the energy spectrum shape contours in the new and official FV were caused mainly by the increase in the systematic error for the lowest energy bin. The normalization contour increased because of the smaller difference between the number of expected and observed events from the added events to the new FV.

The results of the oscillation analysis for the upstream shfited FV are in Table 7.12 and probabilites for each fit in Table 7.13.
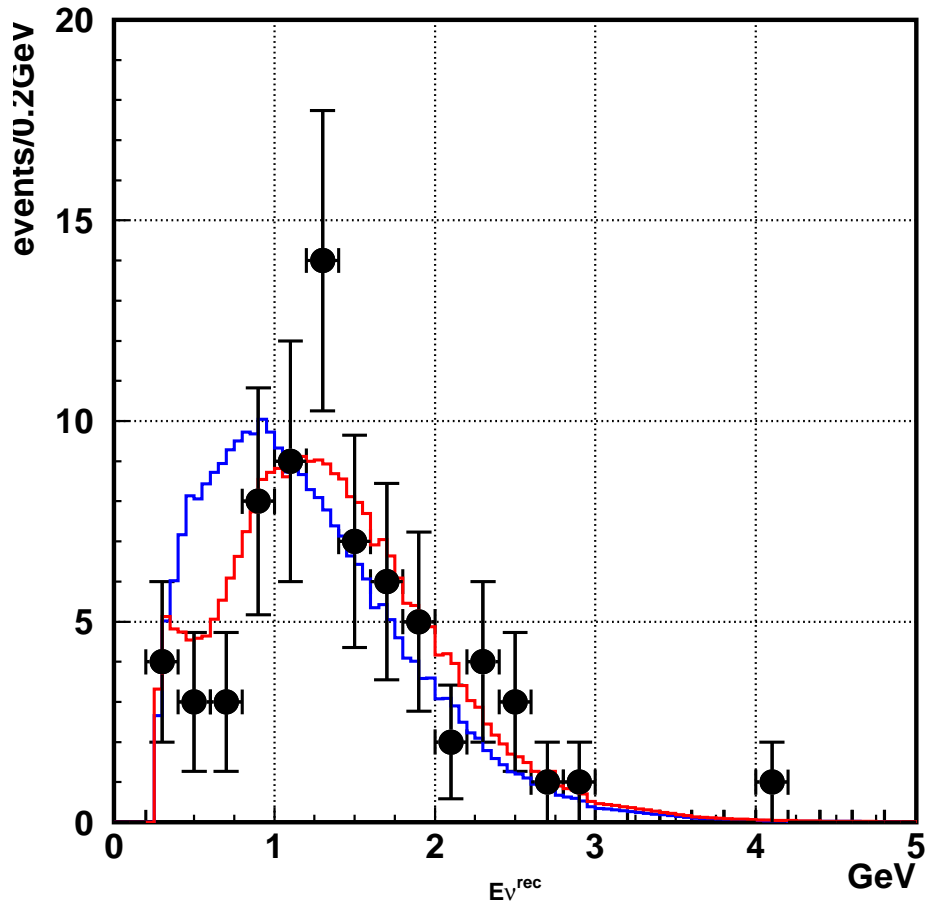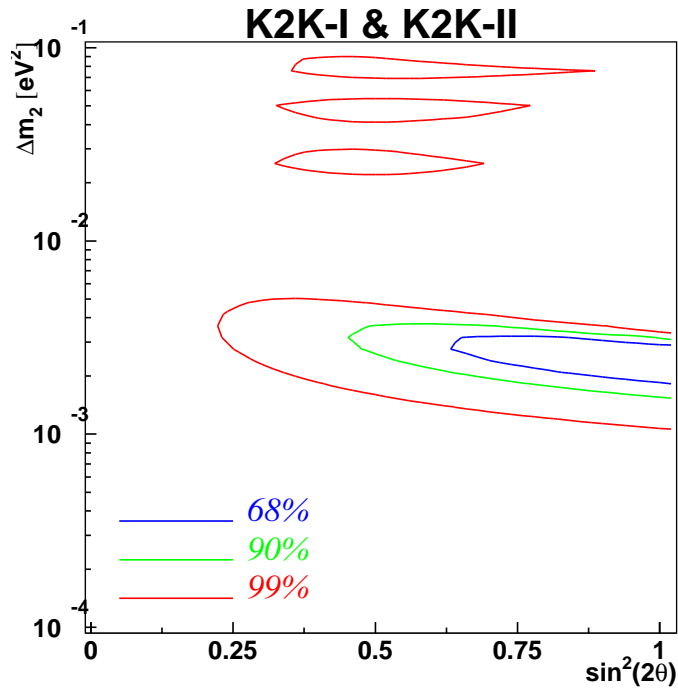
Figure 7.9: Allowed region of the upstream shifted fiducial volume ν_μ disappearance analysis. The blue (green; red) line region allowed at 68% (90%; 99%) confidence level.

Table 7.12: Summary of oscillation fit best fit parameters for the upstream fiducial volume.

		All region		Physical region	
		Δm^2 [eV^2]	$\sin^2 2\theta$	Δm^2 [eV^2]	$\sin^2 2\theta$
All data	shape + norm.	0.00236	1.07	**0.00244**	**1.00**
	shape only	0.00265	1.18	0.00281	1.00
K2K-I	shape + norm.	0.00254	0.81	0.00254	0.81
K2K-II	shape + norm.	0.00232	1.37	0.00261	1.00
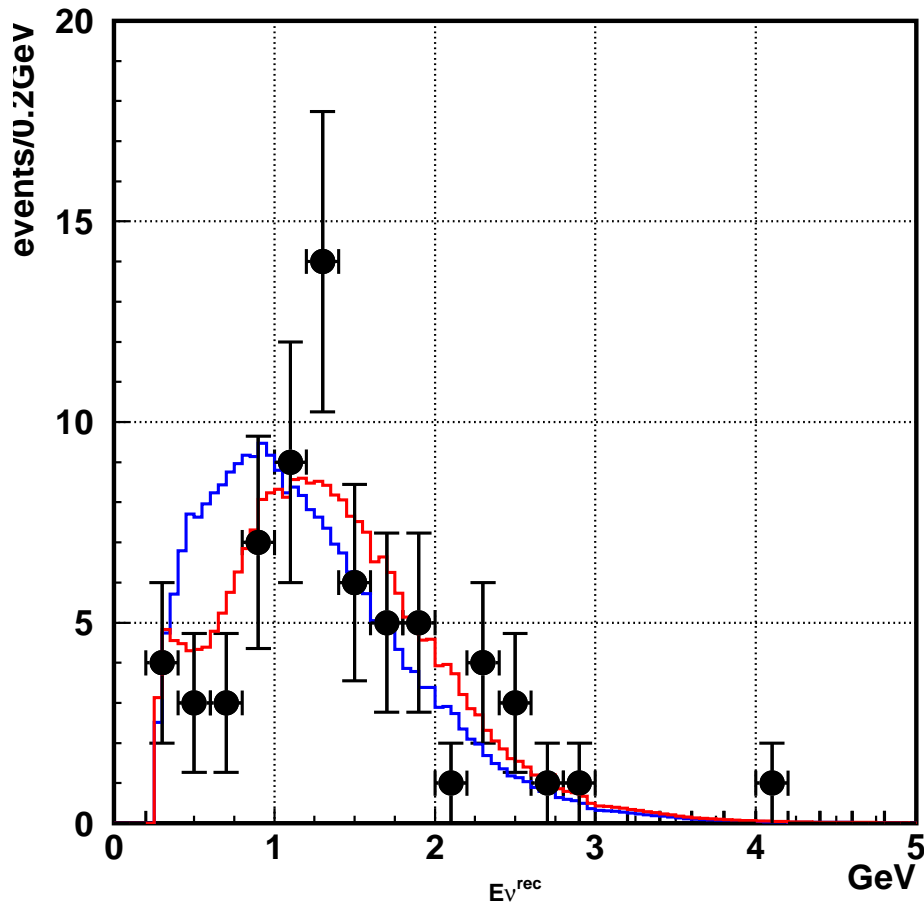
Figure 7.10: Energy spectrum shape of 1Rµ events. Data are the circles, the best fit oscillation parameters is the red histogram, and null oscillations is the blue histogram. The histograms are normalized to 67 events.

Table 7.13: Summary of null oscillation probabilities.

	K2K-I+II	K2K-I	K2K-II
Shape + Norm.	0.042% (3.5σ)	5.90% (1.9σ)	0.44% (2.8σ)
Shape	0.76% (2.7σ)	34%	1.8%
Norm.	0.76% (2.7σ)	5.6%	4.9%
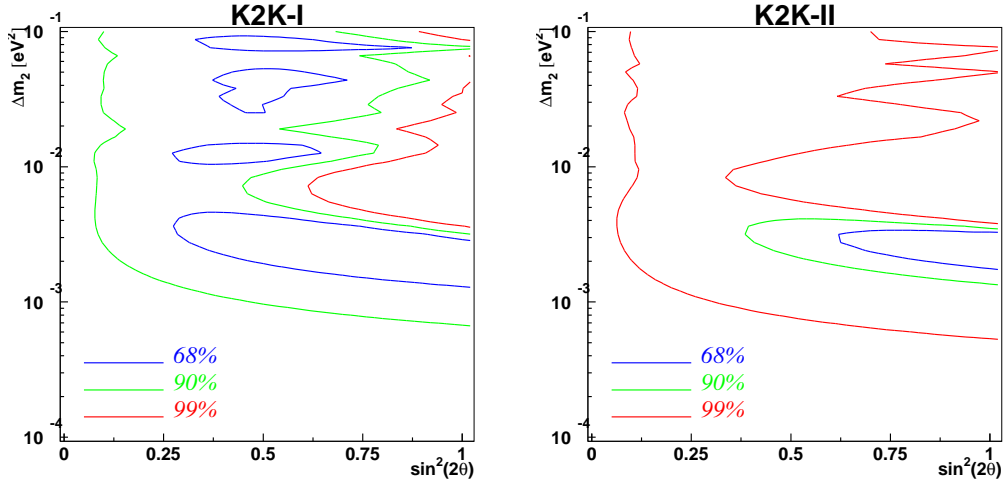
Figure 7.11: Allowed region of the upstream shifted fiducial volume ν_μ disappearance analysis for K2K-I(left) and K2K-II(right). The blue (green; red) line region allowed at 68% (90%; 99%) confidence level.
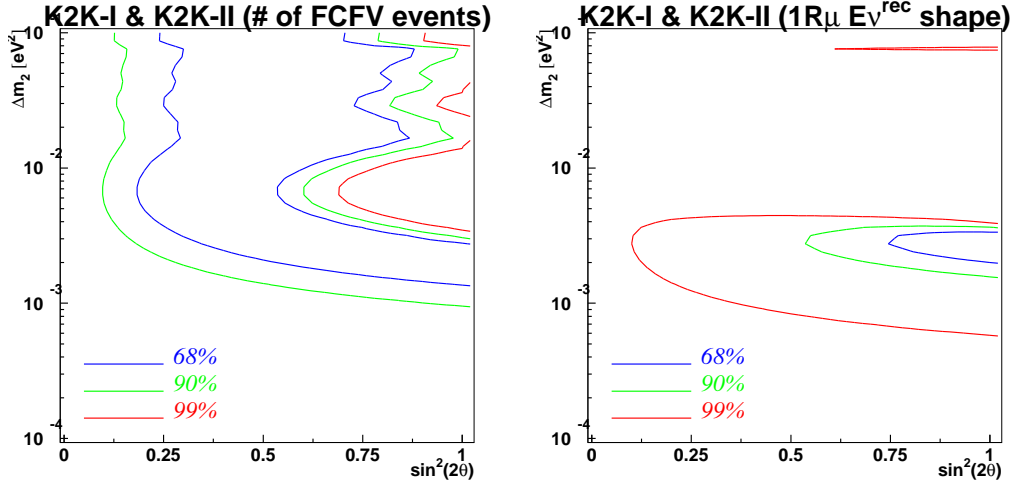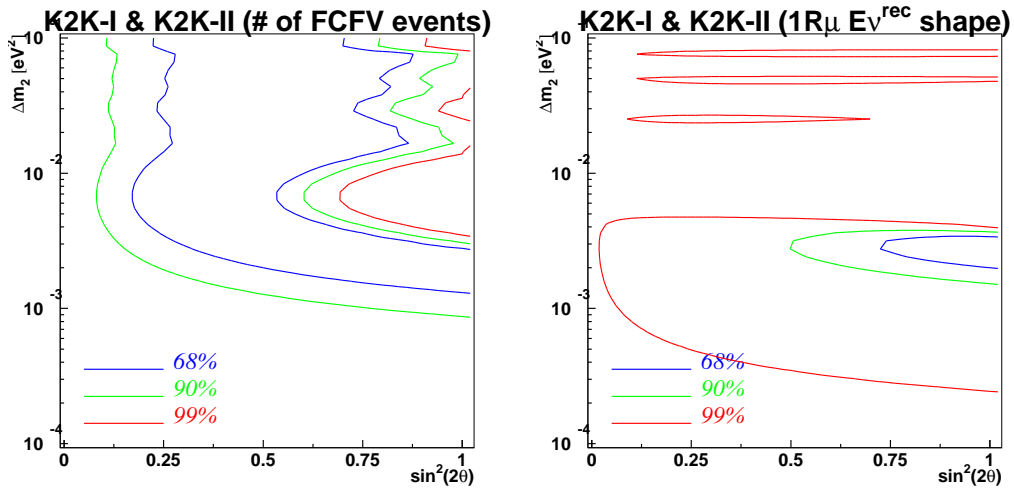

Figure 7.12: Allowed region of the upstream fiducial volume ν_μ disappearance analysis for the number of events (left) and energy spectrum shape(right). The blue (green; red) line region allowed at 68% (90%; 99%) confidence level.

Chapter 8

Summary and Implications For Future Experiments

8.1 Summary Of the K2K Oscillation Analysis

Data taken by the K2K experiment from June 1999 to November 2004 was used to determine the oscillation parameters using an accelerator-based neutrino beam and for different fiducial volumes at Super-Kamiokande. The neutrinos are measured first by the near detectors 300 m downstream from the proton target and then at Super-Kamiokande 250 km away from KEK. The three fiducial volume defintions examined were: events at least 200 cm away from Super-Kamiokande's inner detector wall, events at least 100 cm away from the wall and having to travel a distance of at least 200 cm or greater depending on their event class, and a fiducial volume shifted 50 cm upstream with a volume consistent with events at least 150 cm away from the wall and having to travel at least 200 cm. These obtained results are consistent with previous measurements of neutrino oscillation parameters made by the Super-Kamiokande collaboration [27, 28] and other atmospheric neutrino experiments [71, 72] and recent measurements made by the MINOS collaboration [29, 31].

For the different fiducial volume definitions, 112, 143, and 134 events were observed at Super-Kamiokande against the null oscillation expectations of $158.1^{+9.2}_{-8.6}$, $183.3^{+10.7}_{-10.0}$, and $170.9^{+9.5}_{-9.0}$, respectively. The spectrum distortion expected from oscillation is also observed in 58, 71, and 69 single ring muon-like events. From a likelihood analysis, the probability that the observations are a statistical fluctuation rather than neutrino oscillations is at the 4.3σ, 3.7σ, and 3.5σ for the order of fiducial volumes given in the previous paragraph. In the two flavor oscillation scenario, the allowed Δm^2 region at 90% C.L. is between 0.0019 eV^2 and 0.0035 eV^2, 0.0016 eV^2 and 0.0031 eV^2, and 0.0015 eV^2 and 0.0031 eV^2 for the three fiducial volumes, respectively. The best fit point for

the official fiducial volume at Super-Kamiokande is 0.0027 eV^2; the best fit point for the new fiducial volume is 0.0025 eV^2; and the best fit point for the upstream shifted fiducial volume is 0.0024 eV^2. The best fit for all cases is $\sin^2 2\theta = 1.0$ in the physical region.

8.2 Implications for Future Experiments

Future neutrino oscillation experiments, such as T2K [30] or a very long base line (VLBL) experiment [73] of over 1000 km with UNO [74] as the far detector, will be making precision measurements of the atmospheric neutrino parameters as well as attempting to measure the remaining oscillation paramters, such as θ_{13} and the CP violating phase δ_{CP}. It needs to be determined if an expanded fiducial volume on its own can improve the sensitivies of these analyses, or if additional studies need to be undertaken to retune the selection criteria with a new fiducial volume.

One of T2K's physics goals is to measure the mixing angle θ_{13} in a ν_e appearance analysis. The desired signal in this analysis is an excess of single ring e-like events compared to the expected number of background events at the far detector, Super-Kamiokande. The signal comes from $\nu_\mu \rightarrow \nu_e$ oscillations given by the probability:

$$P_{\nu_\mu \rightarrow \nu_e} = \sin^2(2\theta_{\mu e}) \sin^2 \left(1.27 \frac{\Delta m^2 L}{E} \right) \tag{8.1}$$

where $\sin^2(2\theta_{\mu e}) = \sin^2 \theta_{23} \sin^2 2\theta_{13}$. θ_{23} is assumed to be 45° from previous atmospheric measurements, making $\sin^2(2\theta_{\mu e}) = \frac{1}{2} \sin^2 2\theta_{13}$. Currently, the best limit for θ_{13} is set by the CHOOZ experiment [75].

The MC selected in a sensitivity study are fully contained fiducial volume single ring e-like events. The event must not be an electron from muon decay and must have deposited at least 100 MeV of visible energy in the Inner Detector. The reconstructed direction of the e-like event has a direction less than 25.8° with respect to the neutrino beam to remove intrinsic ν_e events. A selection based on a likelihood that determines whether a second Cherenkov ring is found from π^0 decays is applied. The MC is weighted by the far/near ratio for the fiducial volume definition used in the event selection and whether the event is to be signal or background. Finally, the reconstructed energy is constrained to be between 350 MeV and 850 MeV, to remove the low energy background peak and high energy tail that contains mostly background events.

The reconstructed neutrino energy with five years of data taking is shown for the official and new fiducial volumes in Figure 8.1 and official and upstream
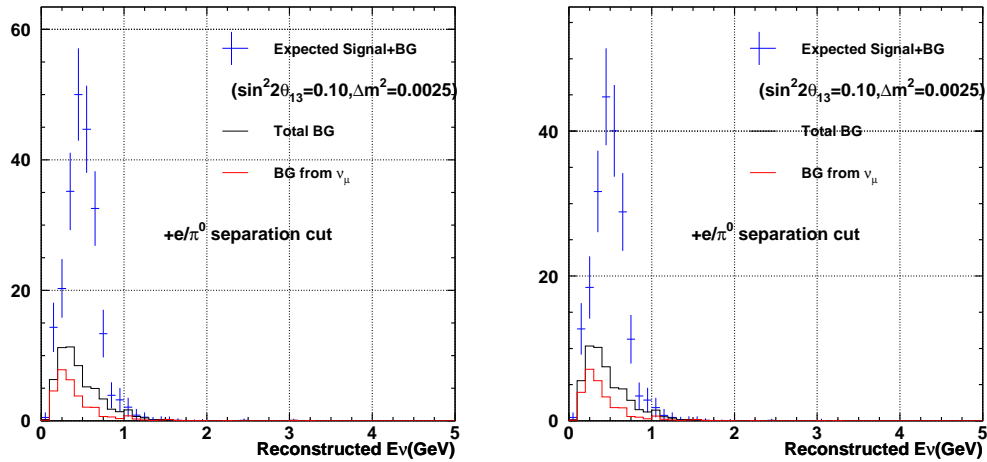
Figure 8.1: Reconstructed neutrino energy for the official fiducial volume (left) and new fiducial volume (right) without the reconstructed neutrino energy criterion.
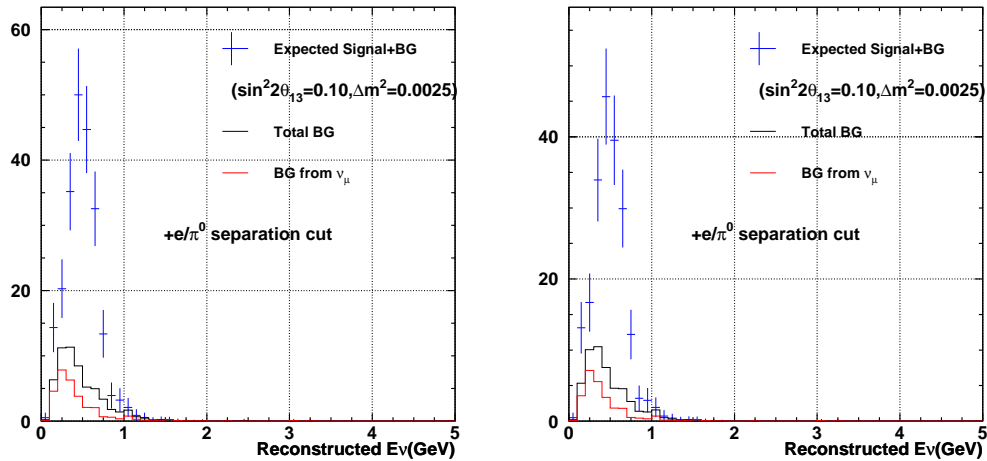
Figure 8.2: Reconstructed neutrino energy for the official fiducial volume (left) and upstream-shifted volume (right) without the reconstructed neutrino energy criterion.

shifted fiducial volumes in Figure 8.2. Each figure is weighted by the far-to-near ratio for their respective fiducial volumes. All other selection criteria are left the same. Relative to the official fiducial volume, the new fiducial volume has a smaller signal to background ratio from a percentage increase in background larger than the increase of signal events. The increase in background is partially from the increase in misidentified $NC\pi^0$ events. The efficiency to reconstruct the second Cherenkov ring from a π^0 decay decreases in the expanded region for two reasons. The first is that the two photons decay perpendicular to the boost direction of the π^0, making the two Cherenkov rings overlap. Because of a short time of flight until the Cherenkov photons hit the PMT plane, the rings do not separate. The second is the two photons from the decay are parallel to the boost direction, so one photon has its energy boosted in the direction the π^0 is traveling, while the other has a smaller energy. The second photon is not found because of absorption in the water from travelling a farther distance to the other wall as well as scattering.

This increase in the background affects the 90% C.L. contour for the expanded fiducial volume as compared to the official fiducial volume. The significance is calculated at each point in the Δm^2-$\sin^2 2\theta_{13}$ parameter space with a 10% systematic uncertainty in the background subtraction. As shown in Figure 8.3, the increase in background relative to the signal removes any gains from the overall increase in statistics.

In order to see if expanding the fiducial volume is an intelligent decision for the ν_e appearance search, a broader study with the likelihood selection must be undertaken. Only expanding the fiducial volume without taking into account the signal and background, as was done in this dissertation, does not lead to an improvement in the sensitivity. Additional studies should also be undertaken combining a new fiducial volume with the other selection criteria to see if it is possible to obtain better sensitivity to θ_{13}.

For physics at UNO, defining the fiducial volume similarly to the new fiducial volume at Super-Kamiokande increases the fiducial volume from 425 ktons to 470 ktons. In a disappearance analysis of ν_μ events, an expanded fiducial volume at UNO would not have an increase in background since the desired signal is single-ring muon-like events. This will be useful in determining if θ_{23} is maximal or not based on the energy spectrum shape.

If θ_{13} is known, δ_{CP} can be measured from the discrepancy between the number of events observed using a beam of muon neutrinos and the number of observed events with an anti-muon neutrino beam.

For future neutrino oscillation experiments using a large water Cherenkov detector, it appears that an expanded fiducial volume does not, by itself, yield an increased sensitivity to neutrino oscillation parameters not yet measured,
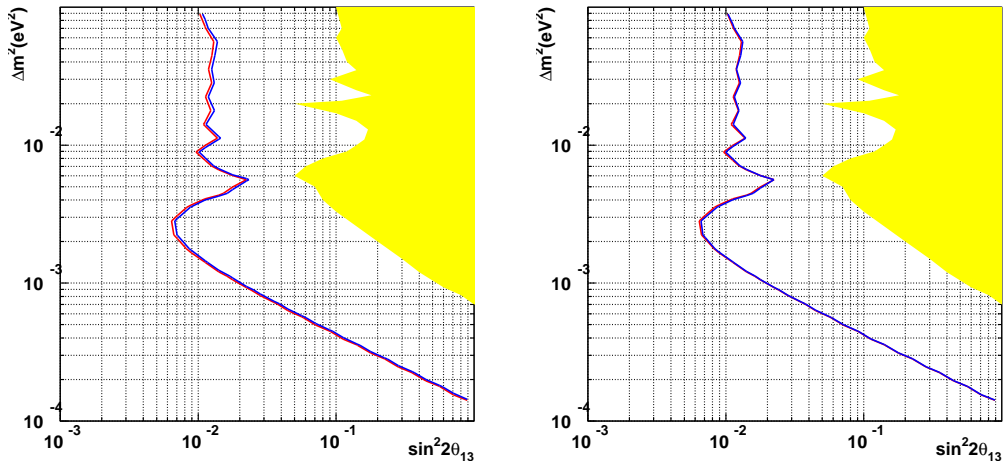
Figure 8.3: Sensitivity plots for T2K's ν_e appearance search. The 90% C.L. contour for the official fiducial volume is red. The 90% C.L. contour for the new (upstream-shifted) fiducial volume in the left (right) plot is blue. The yellow region is the 90% C.L. from the CHOOZ experiment [75].

namely $\sin^2 2\theta_{13}$ and δ_{CP}. To measure $\sin^2 2\theta_{13}$ and, further down the road, δ_{CP}, further studies are needed to gauge whether an expanded fiducial volume is beneficial to these analyses, and if so, exactly what definition to use to maximize the physics potential. In the case of measuring atmospheric neutrino oscillation parameters, an increase in the fiducial volume will yield more events without a significant increase in systematic errors. This will help in the determination if θ_{23} is maximal or not.

Appendix A

Appendix A: Event Reconstruction at Super-Kamiokande

The atmospheric neutrino data and MC at Super-Kamiokande, as well as the K2K data and MC, undergo an event reconstruction procedure to determine event properties such as the vertex position, the momenum, the number of Cherenkov rings, and the particle identification. With the reconstruction of the events, FC events are categorized into: the number of rings with single ring events having one Cherenkov ring and multi-ring events having more than one Cherenkov ring; particle identification, e-like events are showering ($e^{\pm}$, γ), μ-like events are non-showering events ($\mu^{\pm}$, $\pi^{\pm}$, p); and visible energy where sub-GeV events have $E_{vis} \leq 1.33$ GeV and multi-Gev events have $E_{vis} > 1.33$ GeV. The sub-/multi-GeV separation is not used as a determining factor in the K2K data and MC. All processes are automated.

A.1 Vertex Fitting

The event reconstruction process begins with vertex fitting. The vertex position is reconstructed using the timing information of each hit PMT in three steps. First, using the assumption that the Cherenkov light is emitted from a point-like source, a rough vertex position is found by minimizing the timing residual distribution. The timing residual is the arrival time of the Cherenkov photons subtracted by the time-of-flight (TOF). The goodness of fit G_p is defined and maximized:

$$G_p = \frac{1}{N} \sum_i \exp\left(-\frac{(t_i - t_0)^2}{2(1.5 \times \sigma)^2}\right) \tag{A.1}$$

where N is the number of hit PMTs, t_i is the time residual of the ith PMT, t_0 is the mean time residual, and σ is the timing resolution of the PMTs (2.5ns).

Once the vertex is determined, the particle direction is roughly estimated by summing the charge-weighted vector from the vertex to each hit PMT. Second, the outer edge of the most energetic Cherenkov ring is setimated by calculating the ovserved charge as a function of the Cherenkov opening angle from the particle direction. By changing the direction, the sharpest ring is found. Thirdly, instead of assuming a point-like source, the track length of the charged particle and the scattered Cherenkov photons are considered by modifying the goodness with the light inside and outside of the Cherenkov rings, which account for the track length and scattered photons, respectively. For the single-ring events, the vertex is more precisely fitted by the algorithm described in Section A.4.

A.2   Ring Counting

With the event vertex and first Cherenkov ring found, a ring counting algorithm is applied to search for any other Cherenkov ring in the event. The neutrino energy in the K2K event sample at SK is high enough to produce multiple particles, mainly pions, which can also emit Cherenkov light and thus give an event with multiple rings.

Cherenkov ring candidates are seached by an algorithm using a Hough transformation [76]. The center of a possible ring can be identified by putting a ring around a hit PMT with a Cherenkov opening angle of $42°$ from the event vertex, as in Figure A.1. In the algorithm, this is done by mapping the charge distibution on a (Θ, Φ) plane for each hit PMT. Peaks in the (Θ, Φ) plane, as in Figure A.2, are the directions of the identified Cherenkov rings.

After candidates for Cherenkov rings are found, they are tested using six evaluation functions to determine if the rings found are true rings. The evaluation functions are:

L_1: The probability that the observed charge distribution would match the expected p.e.'s with or without a candidate ring.

L_2: The charge density at the peak of the candidate ring.

L_3: The difference in p.e.'s between the peak of a candidate ring and the outside of the peak. The larger L_3 is, the more likely the candidate ring is a true ring.

L_4: The difference in p.e.'s between the peak of a candiate ring and the average of inside and outside the ring. The larger L_4 is, the more likely the candidate ring is a true ring.
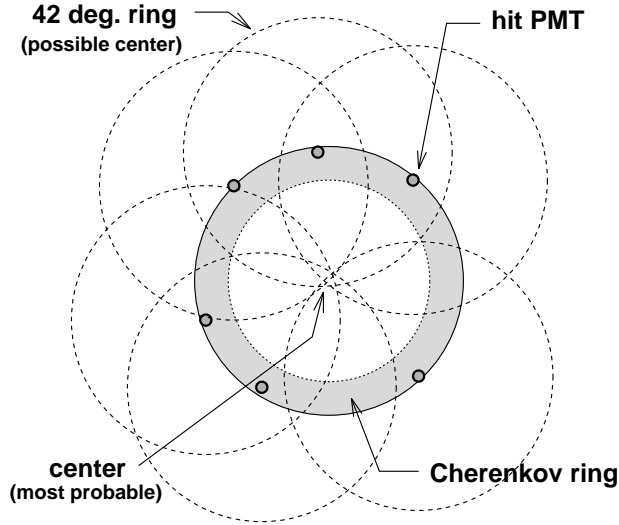
Figure A.1: Basic plan of finding ring candidates. By drawing rings around the hit PMT with Cherenkov angle 42° from the vertex, the center of the actual Cherenkov ring can be identified.

L_5: The residual p.e.'s which is a vector sum of the charge over all PMTs, between the observed and expected p.e.'s of the rings already found.

L_6: The azimuthal sysmmetry of ring with respect to the direction of the ring. An single ring event is more symmetric than a multi-ring event.

For SK-I, the likelihood is a linear combination of these six evaluation functions with optimized weights α_i:

$$\mathcal{L}_{SK-I} = \sum_{i=1}^{6} \left[\alpha_i L_i \right]. \tag{A.2}$$

For SK-II, the ring counting is modified to use a true log likelihood. Using MC samples of single-ring and multi-ring events, the probability desity functions (PDFs) for each evaluation function are determined, and the likelihood is calculated as:

$$
\begin{aligned}
\mathcal{L}_{SK-II} &= \sum_{i=1}^{6} \left[\mathcal{P}_i \right] \\
&= \sum_{i=1}^{6} \log \left[(\mathcal{P}_i)_{multi} \right] - \log \left[(\mathcal{P}_i)_{single} \right]
\end{aligned}
\tag{A.3}
$$
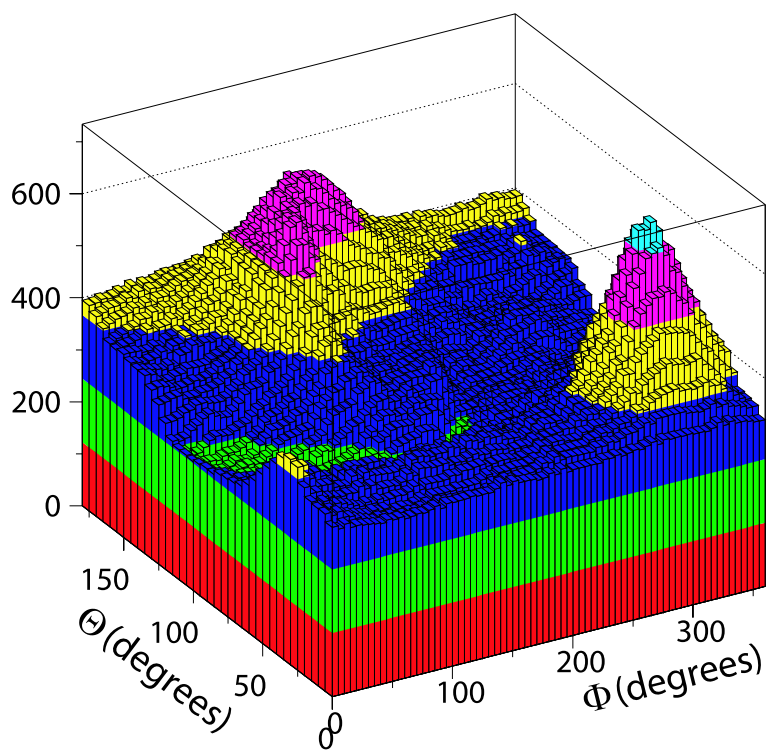
Figure A.2: Charge map from a Hough transformation algorithm for a typical two ring event. The peaks are the direction of the Cherenkov rings.

where $\mathcal{P}_i$ is the PDF for the ith evaluation function, and $(\mathcal{P}_i)_{multi(single)}$ is probability for multi-(single) ring events.

The ring counting process is repeated until no other rings are found. The maximum number of rings that the algorithm can find is set to five. More details can be found in References [77, 78].

A.3 Particle Identification

A particle identification (PID) program is applied to identify the final state particles. All of the Cherenkov rings are classified into two types: showering (e-like) or non-showering (μ-like). Due to the electromagnetic shower and multiple scatterings, electrons or gamma rays produce e-like rings, which diffused (fuzzier) ring patterns. Non-showering (μ-like) rings are produced by muons or charged pions (or in some cases, protons) and have sharper ring edges. Figure A.3 shows the event display of an electron and a muon neutrino MC event as an example. Each small circle in the figure represents a hit PMT, with the circle's size corresponding to the number of photons detected. In addition, the Cherenkov rings from electrons and gamma rays have a Cherenkov opening angle of 42°, but the Cherenkov rings from muons, pions, or protons, have smaller rings if they are not highly relativisitc ($\beta=v/c<<1$) and when they lose energy. The PID algorithm exploits these differences in the patterns and opening angles of the Cherenkov rings.

Using MC simulations, expected p.e. distributions and expected opening angle of Cherenkov rings from electrons and muons are calculated for each PMT by considering different vertex positions, light attenuation length, and PMT acceptance with different energies. By comparing the observed rings with the simulation, the probability for the ring pattern and the opening angle, ($P^{pattern}$(e or μ)) and (P^{angle}(e or μ)) can be determined. The probability functions of the PID for single ring and multi-ring events are defined as:

$$P_{single}(e,\mu) = P^{pattern}_{single}(e,\mu) \times P^{angle}_{single}(e,\mu) \tag{A.4}$$

$$P_{multi}(e,\mu) = P^{pattern}_{multi}(e,\mu) \tag{A.5}$$

where the subscripts indicate if the probability is for the single ring or multi-ring sample. For multi-ring events, $P^{pattern}_{multi}$(e or μ) is used because the angle is not precisely estimated. This algorithm was tested in a beam test experiment at KEK [79]. Figures A.4 and A.5 show the PID likelihood distributions for single ring and multi-ring events in SK-I and SK-II, respectively, where the likelihood is defined as $P_{PID} \equiv \sqrt{-\log P(\mu)} - \sqrt{-\log P(e)}$.

★ Super Kamiokande ★
NUM   3
RUN   999999
SUBRUN   99
EVENT   16
DATE   **-Feb-22
TIME   19: 3:47
TOT PE: 13433.
MAX PE: 52.8
NMHIT :   3839
ANT-PE: 65.3
ANT-MX: 8.5
NMHITA: 66

90/00/00:NoYet:NoYet
90/00/00:NoYet:NoYet
90/00/00:NoYet:NoYet
90/00/00:NoYet:NoYet
90/00/00:NoYet:NoYet
90/00/00:NoYet:NoYet
90/00/00:;R= 0:NoYet
    R   Z   PHI
  0.00: 0.00: 0.00:0.00
CANG : RTOT : AMOM : MS

RunMODE:MonteCar
TRG ID :00000011
T diff.:   0
FEVSK :80000003
nOD YK/LW: 3/ 1
SUB EV : 0/ 1
Dec-e: 0(0/ 0/
NO KEKGPS RED

Comnt;

★ Super Kamiokande ★
NUM   195
RUN   999999
SUBRUN   99
EVENT   1550
DATE   **-Feb-22
TIME   19: 4:32
TOT PE: 19375.
MAX PE: 52.5
NMHIT :   5622
ANT-PE: 59.0
ANT-MX: 5.1
NMHITA: 68

90/00/00:NoYet:NoYet
90/00/00:NoYet:NoYet
90/00/00:NoYet:NoYet
90/00/00:NoYet:NoYet
90/00/00:NoYet:NoYet
90/00/00:NoYet:NoYet
90/00/00:;R= 0:NoYet
    R   Z   PHI
  0.00: 0.00: 0.00:0.00
CANG : RTOT : AMOM : MS

RunMODE:MonteCar
TRG ID :00000011
T diff.:   0
FEVSK :80000003
nOD YK/LW: 2/ 1
SUB EV : 0/ 0
Dec-e: 0(0/ 0/
NO KEKGPS RED

Comnt;

Figure A.3: Event display for a single ring muon (top) and single ring electron (bottom) neutrino MC events. Each small circle represents a hit ID PMT, with the circle's size corresponding to the number of photons detected. Muon events have sharp ring edges while electron events have a diffuse ring pattern.
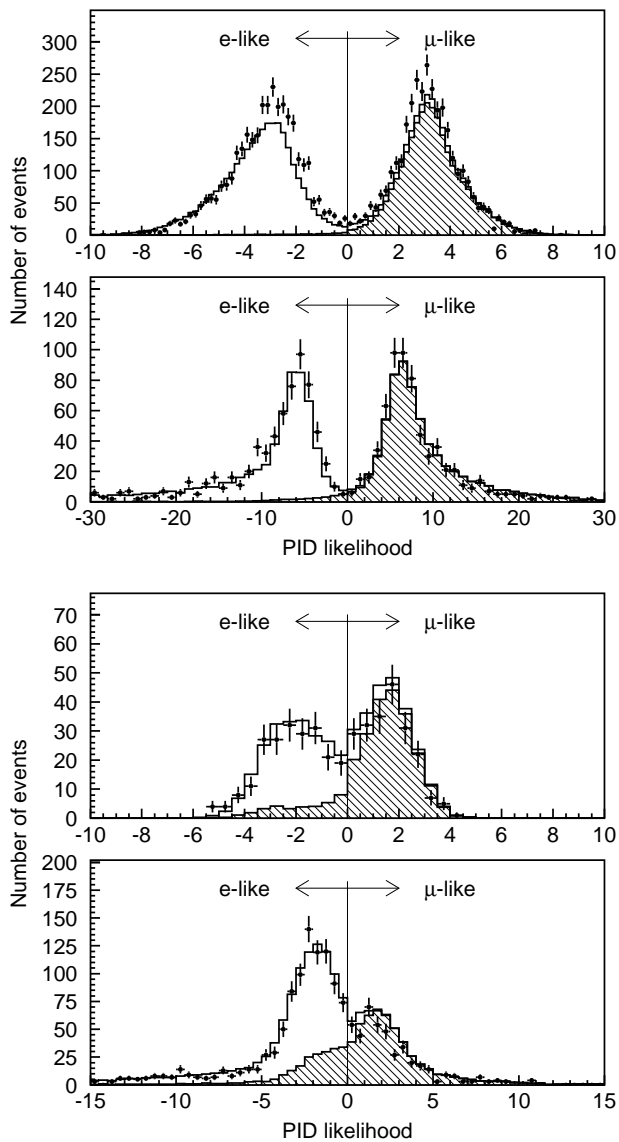
Figure A.4: SK-I PID likelihood distributions of sub-Gev and multi-GeV events for single-ring events (top) and multi-ring events (bottom). The points with error bars are SK-I data while the histograms are atmospheric neutrino MC oscillated with the SK-I best fit oscillation parameters $(\Delta m^2, \sin^2 2\theta) = (0.0021 \text{ eV}^2, 1.0)$. The hatched histograms are ν_μ CC interactions.
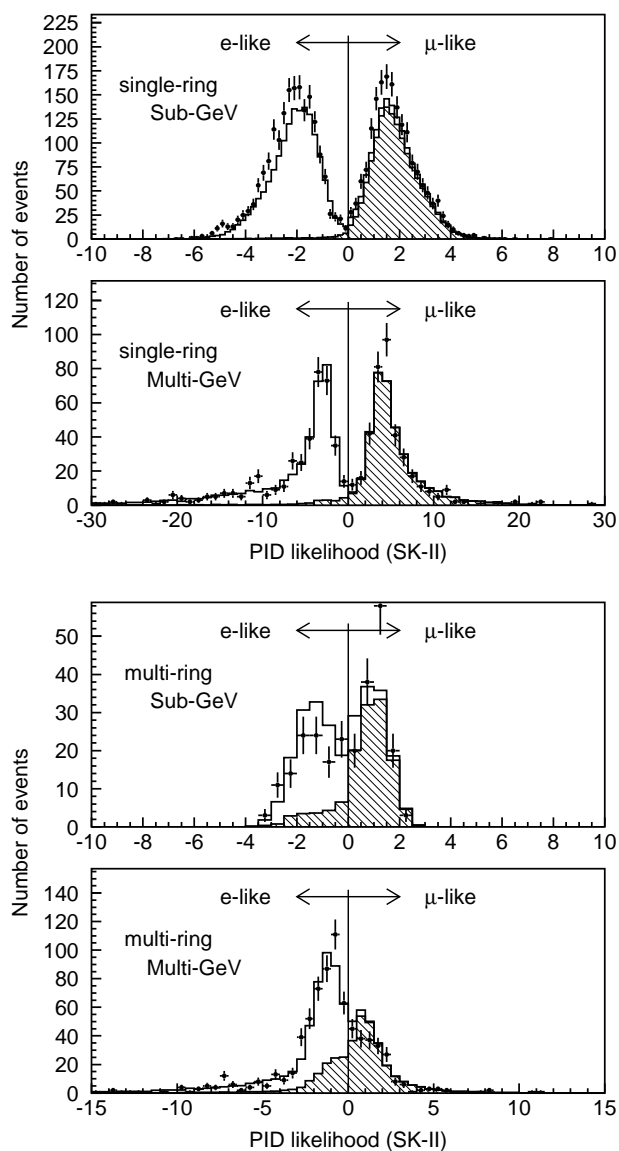
Figure A.5: SK-II PID likelihood distributions of sub-Gev and multi-GeV events for single-ring events (top) and multi-ring events (bottom). The points with error bars are SK-I+SK-II data while the histograms are atmospheric neutrino MC oscillated with the SK-I best fit oscillation parameters $(\Delta m^2, \sin^2 2\theta) = (0.0025 \text{ eV}^2, 1.0)$. The hatched histograms are ν_μ CC interactions.

A.4 Precise Vertex Fitting (MS-fit)

The vertex resolution in the longitudinal directions fitted by the vertex-fitting algorithm described in Section A.1 is not optimized for single ring events since it only uses the timing information. This can improved by refitting the vertex position using the ring pattern. The MS-fit modifies the vertex position and the particle direction by calculating the PID likelihood, and the vertex position is adjusted perpendicularly to the particle direction using the first vertex fitter with the timing information. This process is iterated until the changes in the vertex position and particle direction are less than 5cm and $0.5°$.

A.5 Momentum Resolution

The momentum of each particle is determined by summing all of the p.e.'s inside of a $70°$ half-angle cone, which is defined by the vertex position and particle direction of each ring. The total number of p.e.'s for each ring is corrected by taking into account the light attenuation and the PMT acceptance. The total p.e.'s are calcualted in a timing window from -50ns to +250ns of the event to avoid electrons from muon decays.

A.6 Ring Correction

As the last step in the event reconstruction process, the number of rings is corrected using the energy and angle information obtained for each ring, with mis-fit rings being removed. The criteria for the correction to remove the ith ring are:

The momentum of the ith ring is less than another ring, j ($p_i < p_j$; i≠j), the separation, θ_{ij} between the ith and jth rings is less than thirty degress, and the ith ring has a momentum less than 60MeV perpendicular to the jth ring direction ($p_i \cos \theta_{ij} < 50$MeV/$c$).

The momentum of the ith ring is less than 40MeV/c and also less than 5% of the total momentum

In SK-I, the momentum for the ring correction is determined without using the PID information, while for SK-II the PID information is used in the calculation.

Appendix B

Appendix B: Neutrino Interaction Simulation

The neutrino interaction simulation plays an important role both in estimating the expected number of neutrino interactions and in deriving the energy spectrum of neutrinos from the data. The Monte Carlo program simulates neutrino interactions with protons, oxygen, carbon and iron, which are the target materials of the neutrino detectors.

In the simulation program, the following charged and neutral current neutrion interactions are included: quasi-elastic scattering ($\nu\ N \to \ell\ N'$), single meson production ($\nu\ N \to \ell\ N'\ m$), coherent π production ($\nu\ {}^{16}O({}^{12}C,{}^{56}Fe) \to \ell\ \pi\ {}^{16}O({}^{12}C,{}^{56}Fe)$), and deep inelastic scattering ($\nu N\ \to \ell\ N'\ hadrons$). In these reactions, N and N' are the nucleons (proton or neutron), ℓ is the lepton, and m is the meson. For the single meson production processes, the K and η are simulated as well as the dominant π production processes. If the neutrino interaction occurs in oxygen or other nuclei, the re-interactions of the resulting particles with the remaining nucleons in the nucleus are also simulated.

B.1   Quasi-elastic scattering

The formalism of quasi-elastic scattering off a free neutron used in the simulation programs is described by Llewellyn-Smith [80]. For scattering off nucleons in the nucleus, the relativistic Fermi gas model of Smith and Moniz [81] is used. The nucleons are treated as quasi-free particles and the Fermi motion of nucleons and the Pauli exclusion principle are taken into account. The momentum distribution of the target nucleon is assumed to be flat up to a fixed Fermi surface momentum of 225 MeV/c (250 MeV/c)for carbon and oxygen (iron). The same Fermi momentum distribution is also used for all of the other nuclear interactions. The nuclear potential is set to 27 MeV for carbon and oxygen and 32 MeV for iron.

B.2 Single meson production

Rein and Sehgal's model is used to simulate the resonance production of single π, K and η [82, 83, 84]. This model divides the interaction into two parts. First there is the interaction

$$\nu + N \to \ell + N^*,$$

which is then followed by

$$N^* \to \pi(\text{ or K or } \eta) + \text{N}',$$

where N and N' are the nucleons, and N^* is the baryon resonance, such as $\Delta(1232)$. The mass of the intermediate resonance is restricted to be less than $2 \text{ GeV}/c^2$. To determine the direction of the pion in the final state, Rein and Sehgal's method for the dominant resonance $P_{33}(1232)$ is also used. For the other resonances, the directional distribution of the generated pion is set to be isotropic in the resonance rest frame. The angular distribution of π^+ has been measured for the $\nu p \to \mu^- p \pi^+$ mode [85] and the results agree well with the Monte Carlo prediction. The Pauli blocking effect in the decay of the baryon resonance is taken into account by requiring that the momentum of the nucleon should be larger than the Fermi surface momentum. In addition, pion-less Δ decay is considered. For these events there is no pion in the final state; only a lepton and nucleon are emitted [86] with its probability set to 20%. Single K and η productions are simulated using the same framework as for single π production processes.

Both the quasi-elastic and single-meson production models contain a phenomenological parameter (the axial vector mass, M_A), that must be determined by experiment. As the value of M_A increases, interactions with higher Q^2 values (and therefore larger scattering angles) are enhanced. The M_A parameters in the Monte Carlo simulation program are set to be 1.1 GeV for both the quasi-elastic and single-meson production channels based on the analysis of the near detector data [87].

Coherent single π production, the interaction between a neutrino and the entire nucleus, is simulated using the formalism developed by Rein and Sehgal [83]. Here, only the neutral current interactions are considered because the cross-section of the charged current coherent pion production was found to be very small at the K2K beam energy [51].

B.3   Deep inelastic scattering

To calculate the cross-section for deep inelastic scattering, the GRV94 parton distribution functions[88] are used. Additionally, the corrections in the small q^2 region developed by Bodek and Yang [89] has been included. In the calculation, the hadronic invariant mass, W, is required to be larger than 1.3 GeV/c^2. Also, the multiplicity of pions is restricted to be larger than or equal to two for 1.3<W<2.0 GeV/c^2, because single pion production is already taken into account as previously described. In order to generate events with multi-hadron final states, two models are used: for W between 1.3 and 2.0 GeV/c^2, a custom-made program [90] is employed while PYTHIA/JETSET [91] is used for the events whose W is larger than 2 GeV/c^2.

The total charged current cross sections including quasi-elastic scattering, single meson production and deep inelastic scattering are shown in Figure B.1 overlaid with data from several experiments.

B.4   Nuclear effects

The intra-nuclear interactions of the mesons and nucleons produced in neutrino interactions in the carbon, oxygen or iron nuclei are also important to consider for this analysis. Any absorption or change of kinematics of these particles will affect the event type classification. Therefore, the interactions of π, K, η and nucleons are also simulated in the program. These interactions are treated using a cascade model, and each of the particles is traced until it escapes from the nucleus.

Among all the interactions of mesons and nucleons, the interactions of pions are most important, since both the cross sections for pion production for neutrino energies above 1 GeV and also the interaction cross sections of pions in the nucleus are large. In the simulation program, the following pion interactions in nucleus are considered: inelastic scattering, charge exchange and absorption. The actual procedure to simulate these interactions is as follows: first the generated position of the pion in nucleus is set according to the Woods-Saxon nucleon density distribution [104]. Then, the interaction mode is determined by using the calculated mean free path of each interaction. The model described by Salcedo et al. [105] is adopted to sdescribe these mean free paths. The calculated mean free paths depend not only on the momentum of the pion but also on the position of pion in the nucleus.

If inelastic scattering or charge exchange occurs, the direction and momentum of pion are determined by using the results of a phase shift analysis
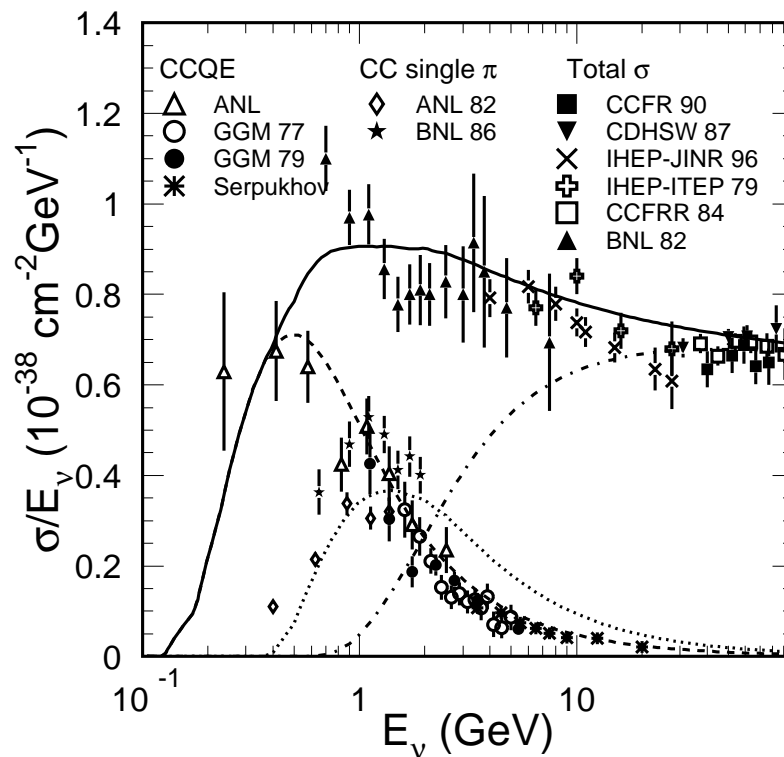
Figure B.1: Charged current total cross section divided by E_ν for neutrino nucleon charged current interactions. The solid line shows the calculated total cross section. The dashed, dot and dash-dotted lines show the calculated quasi-elastic, single-meson and deep-inelastic scatterings, respectively. The data points are taken from the following experiments: ($\triangle$) ANL [92], ($\bigcirc$) GGM 77 [93], ($\bullet$) GGM 79 [94, 95], ($*$) Sepukhov [96], ($\Diamond$) ANL 82 [97], ($\star$) BNL 86 [85], ($\blacksquare$) CCFR 90 [98], ($\blacktriangledown$) CDHSW 87 [99], ($\times$) IHEP-JINR 96 [100], ($+$) IHEP-ITEP [101], ($\square$) CCFRR 84 [102], and ($\blacktriangle$) BNL 82 [103].

Figure B.2: The π^0 momentum distributions for neutral current single π production processes off the water target and for the K2K neutrino beam at the near detector. The solid and dashed lines show the spectrum without and with the pion nuclear effects.
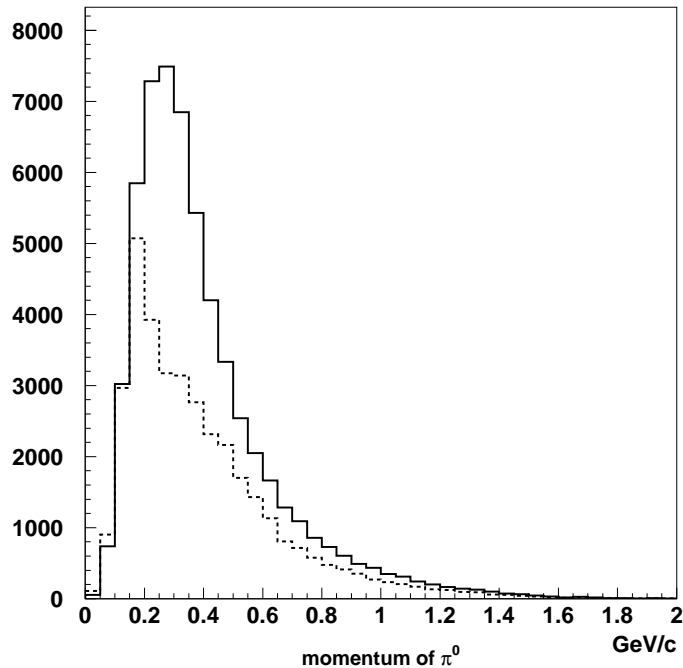
obtained from $\pi - N$ scattering experiments [106]. When calculating the pion scattering amplitude, the Pauli blocking effect is also taken into account by requiring the nucleon momentum after the interaction to be larger than the Fermi surface momentum at the interaction point.

This pion interaction simulation is tested by comparison with data using the following three interactions: π^{12}C scattering, π^{16}O scattering and pion photo-production $(\gamma + {}^{12}\text{C} \rightarrow \pi^- + X)$. The importance of including the proper treatment of nuclear effects is illustrated in Figure B.4 which shows the momentum distribution for neutral current single π^0 production in the water target both with and without having them applied.

The re-interactions of the recoil protons and neutrons produced in the neutrino interactions are also important, because the protron tracks are used to select quasi-elastic like events. This is done with the SciFi and SciBar near

detectors, and allows us to estimate the neutrino energy. Nucleon-nucleon interactions modify the outgoing nucleon's momentum and direction, which also affects whether the nucleon will be above detection threshold [107]. Both elastic scattering and pion production are considered. In order to simulate these interactions, a cascade model is again used and the generated particles in the nucleus are tracked using the same code as for the mesons.

Bibliography

[1] L.M. Brown, Phys. Today **31** (9), 23 (1978).

[2] E. Fermi, Z. Phys. **88**, 161 (1934).

[3] F. Reines and C.L. Cowan, Nature **178**, 446 (1956).

[4] C.L. Cowan, F. Reines, F.B. Harrison, H.W. Kruse, and A.D. McGuire, Science **124**, 103 (1956).

[5] G. Danby, J.M. Gaillard, K. Gouliano, L.M. Lederman, N.B. Mistry, M. Schwartz, and J. Steinberger, Phys. Rev. Lett. **9**, 36 (1962).

[6] M. L. Perl *et al.*, Phys. Rev. Lett. **35**, 1489 (1975).

[7] K. Kodama *et al.*, [The DONUT Collaboration], Phys. Lett. **B504**, 218 (2001) [arXiv:hep-ex/0012035].

[8] R. Davis, D. S. Harmer, and K.C. Hoffman, Phys. Rev. Lett. **20**, 1205 (1968).

[9] K.S. Hirata *et al.*, [The Kamiokande Collaboration], Phys. Rev. Lett. **58**, 1490 (1987).

[10] K.S. Hirata *et al.*, [The Kamiokande Collaboration], Phys. Rev. **D38**, 448 (1988).

[11] R. M. Bionta *et al.*, [The IMB Collaboration], Phys. Rev. Lett. **58**, 1494 (1987).

[12] R. M. Bionta *et al.*, [The IMB Collaboration], Phys. Rev. **D37**, 3361 (1988).

[13] W.M. Yao *et al.*, [Particle Data Group], J. Phys. **G33**, 1 (2006).

[14] M. Goldhaber *et al.*, Phys. Rev. **109**, 1015 (1958).

[15] Z. Maki, M. Nakagawa, and S. Sakata, Prog. Theor. Phys. **28**, 870 (1962).

[16] B. Pontecorvo, Sov. Phys. JETP. **6**, 429 (1957).

[17] T.K. Gaisser and M. Honda, Annu. Rev. Nucl. Part. Sci. **52**, 153 (2002).

[18] D. Casper *et al.*, [The IMB Collaboration], Phys. Rev. Lett. **66**, 2561 (1991).

[19] R. Becker-Szendy *et al.*, [The IMB Collaboration], Phys. Rev. **D46**, 3720 (1992).

[20] K.S. Hirata *et al.*, [The Kamiokande Collaboration], Phys. Lett. **B205**, 416 (1988).

[21] K.S. Hirata *et al.*, [The Kamiokande Collaboration], Phys. Lett. **B280**, 146 (1992).

[22] M. Aglietta *et al.*, [The NUSEX Collaboration], Euro. Phys. Lett. **8**, 611 (1989).

[23] K. Daum *et al.*, [The Fréjus Collaboration], Z. Phys. **C66**, 417 (1995).

[24] W. W. M. Allison *et al.*, [The Soudan 2 Collaboration], Phys. Lett. **B391**, 491 (1997).

[25] W. W. M. Allison *et al.*, [The Soudan 2 Collaboration], Phys. Lett. **B449**, 137 (1999).

[26] Y. Fukuda *et al.*, [The Super-Kamiokande Collaboration], Phys. Rev. Lett. **81**, 1562 (1998) [arXiv:hep-ex/9807003].

[27] Y. Ashie *et al.*, [The Super-Kamiokande Collaboration], Phys. Rev. **D71**, 112005 (2005) [arXiv:hep-ex/0501064].

[28] Y. Ashie *et al.*, [The Super-Kamiokande Collaboration], Phys. Rev. Lett. **93**, 101801 (2004) [arXiv:hep-ex/0404034].

[29] D.G. Michaels *et al.*, [The MINOS Collaboration], Phys. Rev. Lett. **97**, 191801 (2006) [arXiv:hep-ex/0607088].

[30] Y. Itow *et al.*, [arXiv:hep-ex/0106019].

[31] A. Weber, [The MINOS Collaboration], talk given at the EPS conference, Manchester, United Kingdom, July 2007.

[32] M. Guler *et al.*, [The OPERA Collaboration], CERN-SPSC-2000-028, CERN-SPSC-P-318, LNGS-P25-00.

[33] A. G. Cocco, [The OPERA Collaboration], Nucl. Phys. Proc. Suppl. **85**, 125 (2000).

[34] R. Acquafredda *et al.*, [The OPERA Collaboration], New J. Phys. **8**, 303 (2006) [arXiv:hep-ex/0611023].

[35] M.H. Ahn *et al.*, [The K2K Collaboration], Phys. Rev. **D74**, 072003 (2006) [arXiv:hep-ex/0606032].

[36] Becker-Szendy *et al.*, Nucl. Instrum. and Meth. **A324**, 363 (1993).

[37] H. Noumi *et al.*, Nucl. Instrum. Meth. **A398**, 399 (1997).

[38] A. Suzuki *et al.*, Nucl. Inst. and Meth. **A329**, 299 (1993).

[39] The Super-Kamiokande Collaboration, Nucl. Instrum. Meth. **A501**, 418-462 (2003).

[40] V. Bernard, L. Elouadrhiri, and U. G. Meissner, J. Phys. **G28**, R1 (2002) [arXiv:hep-ph/0107088].

[41] A. Suzuki *et al.*, [The K2K Collaboration], Nucl. Instrum. Meth. **A453**, 165 (2000) [arXiv:hep-ex/0004024].

[42] B.J. Kim *et al.*, Nucl. Instrum. Meth. **A501**, 418 (2003) [arXiv:hep-ex/0206041].

[43] S.H. Ahn *et al.*, Nucl. Instrum. Meth. **A451**, 558 (2000).

[44] M. Yoshida *et al.*, IEEE Trans. Nucl. Sci. **51**, 3-43 (2004).

[45] K. Nitta *et al.*, Nucl. Instrum. Meth. **A535**, 147 (2004), [arXiv:hep-ex/0406023].

[46] A. Glazov, I. Kisel, E. Konotopskaya, and G. Ososkov, Nucl. Instrum. Meth. **A329**, 262 (1993).

[47] S. Buontempo *et al.*, Nucl. Instrum. Meth. **A349**, 70 (1994).

[48] S. Kawabata *et al.*, Nucl. Instrum. Meth. **A270**, 11 (1988).

[49] F. James and M. Roos, Comput. Phys. Commun. **10**, 343 (1975).

[50] E. Aliu *et al.*, [The K2K Collaboration], Phys. Rev. Lett. **94**, 081802 (2005) [arXiv:hep-ex/0411038v3].

[51] M. Hasegawa *et al.*, [The K2K Collaboration], Phys. Rev. Lett. **95**, 252301 (2005) [arXiv:hep-ex/0506008].

[52] R. Brun, F. Bruyant, M. Maire, A. C. McPherson, and P. Zanarini (1987), CERN-DD/EE/84-1.

[53] J. Sanford and C. Wang, AGS Internal Report (unpublished) (1967).

[54] C. L. Wang. Phys. Rev. Lett. **25**, 1068 (1970).

[55] Y. Cho *et al.*, Phys. Rev. **D4**, 1967 (1971).

[56] M. G. Catanesi *et al.*, [The HARP Collaboration], Nucl. Phys. **B732**, 1 (2006) [arXiv:hep-ex/0510039].

[57] A. Yamamoto, KEK 81-13 (1981).

[58] T. A. Gabriel, J. D. Amburgey, and B. L. Bishop (1977), ORNL/TM-5619.

[59] C. Zeitnitz and T. A. Gabriel, Nucl. Instrum. Meth. **A349**, 106 (1994).

[60] A. Fasso, A. Ferrari, J. Ranft, and P. R. Sala (1993), given at the 4th International Conference on Calorimetry in High-energy Physics, Labiodela, Italy, 19-25 Sep 1993.

[61] E. D. Commins and P. H. Bucksbaum, *Weak interactions of leptons and quarks* (Cambridge University Press, 1983).

[62] H. Fesefeldt (1985), pITHA-85-02.

[63] M. Kohama, Master's thesis, Kobe University (1997), in Japanese.

[64] T. Maruyama, Ph. D. thesis, Tohoku University (2000).

[65] T. Inagaki, Ph. D. thesis, Kyoto University (2001).

[66] S. Nakayama *et al.*, [The K2K Collaboration], Phys. Lett. **B619**, 255 (2005), [arXiv:hep-ex/0408134].

[67] E. H. Monsay, Phys. Rev. Lett. **41**, 728 (1978).

[68] M. Shiozawa *et al.*, [The Super-Kamiokande Collaboration], Phys. Rev. Lett. **81**, 1158 (1998).

[69] K. Kobayashi *et al.*, [The Super-Kamiokande Collaboration], Phys. Rev. **D72**, 052007 (2005), [arXiv:hep-ex/0502026].

[70] J. Kameda, Ph. D. thesis, University of Tokyo (2002).

[71] M. C. Sanchez *et al.*, [The Soudan 2 Collaboration], Phys. Rev. **D68**, 113004 (2003), [arXiv:hep-ex/0307069].

[72] M. Ambrosio *et al.*, [The MACRO Collaboration], Phys. Lett. **B566**, 35 (2003), [arXiv:hep-ex/0304037].

[73] V. Barger *et al.*, Phys. Rev. **D74**, 073004 (2006), [arXiv:hep-ph/0607177].

[74] C.K. Jung, AIP Conf. Proc. **533**, 29 (2000), [arXiv:hep-ex/0005046].

[75] M. Apollonio *et al.*, Eur. Phys. J. **C27**, 331 (2003).

[76] E. R. Davies, *Machine Vision: Theory, Algorithms, Practicalities* (Academic Press, 1997).

[77] M. Ishitsuka, Ph. D. thesis, University of Tokyo (2004).

[78] S. T. Clark, Ph. D. thesis, Boston University (2007).

[79] S. Kasuga *et al.*, Phys. Lett. **B374**, 238 (1996).

[80] C. H. Llewellyn Smith, Phys. Rept. **3**, 261 (1972).

[81] R. A. Smith and E. J. Moniz, Nucl. Phys. **B43**, 605 (1972).

[82] D. Rein and L. M. Sehgal, Ann. Phys. **133**, 79 (1981).

[83] D. Rein and L. M. Sehgal, Nucl. Phys. **B223**, 29 (1983).

[84] D. Rein, Z. Phys. **C35**, 43 (1987).

[85] T. Kitagaki *et al.*, Phys. Rev. **D34**, 2554 (1986).

[86] S. K. Singh, M. J. Vicente-Vacas, and E. Oset, Phys. Lett. **B416**, 23 (1998).

[87] M.H. Ahn *et al.*, [The K2K Collaboration], Phys. Rev. Lett. **90**, 041801 (2003) [arXiv:hep-ex/0404034].

[88] M. Gluck, E. Reya, and A. Vogt, Z. Phys. **C67**, 433 (1995).

[89] A. Bodek and U. K. Yang, Nucl. Phys. Proc. Suppl. **112**, 70 (2002), [arXive:hep-ex/0203009].

[90] M. Nakahata *et al.*, [The Kamiokande Collaboration], J. Phys. Soc. Jap. **55**, 3786 (1986).

[91] T. Sjostrand, Comput. Phys. Commun. **82**, 74 (1994).

[92] S. J. Barish *et al.*, Phys. Rev. **D16**, 3103 (1977).

[93] S. Bonetti *et al.*, Nuovo Cim. **A38**, 260 (1977).

[94] S. Ciampolillo *et al.*, [The Gargamelle Neutrino Propane Collaboration], Phys. Lett. **B84**, 281 (1979).

[95] N. Aremenise *et al.*, Nucl. Phys. **B152**, 365 (1979).

[96] S. V. Belikov *et al.*, Z. Phys. **A320**, 625 (1985).

[97] G.M. Redecky *et al.*, Phys. Rev. **D25**, 1161 (1982).

[98] P.S. Auchincloss *et al.*, Z. Phys. **C70**, 29 (1996).

[99] J.P. Berge *et al.*, Z. Phys. **C35**, 443 (1987).

[100] V.B. Anikeev *et al.*, Z. Phys. **C70**, 39 (1996).

[101] A.S. Vovenko *et al.*, Sov. J. Nucl. Phys. **30**, 528 (1979).

[102] D. MacFarlane *et al.*, Z. Phys.**C26**, 1 (1984).

[103] N. Baker *et al.*, Phys. Rev. **D25**, 617 (1982).

[104] R. Woods, and D. Saxon, Phys. Rev. **95**, 577 (1954).

[105] L. L. Salcedo, E. Oset, M. J. Vicente-Vacas, and C. Garcia-Recio, Nucl. Phys. **A484**, 557 (1988).

[106] G. Rowe, M. Salomon, and R.H .Landau, Phys. Rev. **C18**, 584 (1978).

[107] C. W. Walter, Nucl. Phys. Proc. Suppl. **112**, 140 (2002).